

University of Alberta

Energetic Transitions of Magnetic Vortices

by

Jacob A. J. Burgess

A thesis submitted to the Faculty of Graduate Studies and Research
in partial fulfillment of the requirements for the degree of

Doctor of Philosophy

Department of Physics

©Jacob A. J. Burgess
Spring 2013
Edmonton, Alberta

Permission is hereby granted to the University of Alberta Libraries to reproduce single copies of this thesis and to lend or sell such copies for private, scholarly or scientific research purposes only. Where the thesis is converted to, or otherwise made available in digital form, the University of Alberta will advise potential users of the thesis of these terms.

The author reserves all other publication and other rights in association with the copyright in the thesis and, except as herein before provided, neither the thesis nor any substantial portion thereof may be printed or otherwise reproduced in any material form whatsoever without the author's prior written permission.

To my lovely wife.

Thank you for your love, support, help, and companionship.

Abstract

The vortex state in a magnetic disk contains a zero-dimensional domain wall, and consequently, is a system of interest for the study of fundamental physics. In particular, the disk geometry presents a prototypical system to study the properties of vortex states and to construct proof-of-concept magnetic logic devices. Here, work was performed to elevate the understanding of this system so that device development and experiments may be performed in a truly quantitative fashion. In order to achieve this, hysteretic transitions of the vortex state in thin-film magnetic disks were studied using a variety of techniques. The annihilation transition and its statistics arising from thermal dynamics were studied using a novel tool, AC magneto-optical Kerr effect susceptometry, that permits rapid acquisition of transition statistics. Much smaller hysteretic transitions were studied using extremely sensitive torsional magnetometry. Strong interactions between the core of the vortex and inhomogeneities in the thin-film were studied in 1D and 2D. The bistable states participating in hysteresis were found to exhibit low speed stochastic dynamics that allowed quantitative analysis of transition barriers. To aid in this work an improved analytical model describing the evolution of the vortex state with applied field was developed. In particular this model was demonstrated to be capable of correctly accounting for both the non-monotonic evolution of the magnetization and the vortex core position of the vortex state under a changing magnetic field in the presence of a pinning site. The combination of the model with the torsional magnetometer creates a powerful scanning vortex probe microscope, capable of imaging the energy landscape of the disk with a high spatial resolution. Concurrently, a time-resolved STM equipped with spin polarized tips was successfully constructed, and

applied to study *in situ* fabricated patterned magnetic disks. This attempt to observe magneto-dynamics on an unprecedented combination of spatial and temporal scales has not yet provided results, as magnetic contrast remains elusive. In developing novel high speed STM samples, cluster dynamics were discovered and studied in a metallic glass. In addition to equilibrium dynamics, the formation of a surface state of large clusters was directly observed as the film aged.

Acknowledgements

There are a great number of people to whom I would like to extend my most sincere thanks to for their assistance in this work. Throughout the process of performing research, a graduate student operates in an environment created by colleagues. I felt at home at the University of Alberta. Virtually everyone I worked with made me feel like they had the personal goal to help me succeed.

The technical team at the University of Alberta is an astonishing group. I cannot describe how much practical knowledge I obtained in working with them. I felt spoiled by, and will always be indebted to, their dedication to the research teams they support. I thank Greg Popowich and Don Mullin for teaching me everything I know about vacuum systems. Thanks to Tony Walford, Ken Marsh, Greg Popowich, Don Mullin, and Dave Fortin for teaching me how to machine (properly). Thanks to Dave, Greg, Don, Tony and Ken for all the equipment they built, and technical problems they helped me sort out.

I would like to offer a special thanks to the other half of the STM tag team. Thanks to Dave Fortin for suffering with me through my time using the Createc. Thanks for all of the Labview automation that allowed me to sleep at home most of the time. Thanks for all the beautiful 3D graphics. Thanks for all the trips to the gym, and the great conversations.

The staff at the University of Alberta Nanofab also deserves thanks for aiding me so much in development of various processes, and learning a broad range of nanofabrication techniques. Though he is not staff at the Nanofab, I would like to thank Vince Sauer for all his help.

I would like to thank all of my collaborators and co-authors on publications. There are too many to list in entirety, however I would like to thank a few in particular. Joe Losby was my go to guy for immediate discussion of problems, ideas, or sorting out scripts. Joe helped me in a lot of ways, and enhanced the lab work environment for me, both in productivity and fun. Zhu Daio joined our group later in my degree, but proved to be an invaluable in discussions of micromagnetics. Alastair Fraser proved to be a great collaborator. His diligence with and dedication to finicky experimental apparatuses made the work in Chapter 4 possible. Chris Holt provided me with invaluable help with nanofabrication, depositions, and support

in navigating the world of amorphous films. Prof. John Davis provided a very different perspective on the scientific process and fruitful collaboration. Doug Vick lent his expertise and skill in focused ion beam fabrication, enabling the development of critical components of the work Chapter 4 and Chapter 5.

Many people offered advice and help outside of official collaboration or classroom work. The Thursday beer crew, Joe, Zhu, and Allison, in particular, offered a great sounding board for ideas, problem solving, and, when necessary, problem forgetting. I would like to thank Prof. Frank Marsiglio for helpful discussions in confronting mathematical challenges. Prof. Frank Hegmann provided very useful insight into opto-electronics, and graciously allowed time on the RHK STM for the study of copper hafnium.

In finishing this thesis work, I called upon many to aid me. My emergency editing crew, Zhu Daio, Joe Losby, Allison Schultz, Chris Holt, my parents and Mark Freeman are to be commended on their speed, and accuracy in correcting my many typos. I would like to thank Prof. Robert Wolkow and Prof. Andrzej Czarnecki for their pre-reading of the thesis. I would also like to thank Mark Freeman, Joe Losby, John Davis, Alastair Fraser, and Doug Vick for extracting long forgotten data sets and figures from archives to provide some of the detailed background required in a thesis. A special thanks to Allison Schultz for assisting enormously with the entry of hundreds of references.

Funding came from a variety of sources through this project. I would personally like to thank NSERC for support through the CGS and PGS scholarship program, and thank the Alberta Ingenuity Foundation/Alberta Innovates/iCore for support through the Nanotechnology scholarship program. Additional thanks are due to the University of Alberta for support through the Walter H. Johns fellowship, and the Physics Department for the opportunity to participate in education through teaching assistantships.

In closing, I would like to offer my profound appreciation for my supervisor's guidance and the opportunities created for me. Prof. Mark Freeman, has been an ideal supervisor. The amount of freedom, and independence available to me as a student was remarkable. I feel that I have been prepared for, and that it was Mark's specific goal to do so, a career in research.

Contents

1	Introduction to Modern Magnetism	1
1.1	History	1
1.1.1	The Greeks to Maxwell	1
1.1.2	Domains and Quantum Mechanics	2
1.1.3	The Exchange Interaction	5
1.2	Micromagnetic Interactions	6
1.2.1	Exchange Interaction	7
1.2.2	Dipolar Interaction	8
1.2.3	External Field and Magnetocrystalline Anisotropy	10
1.2.4	The LLG Equation	11
1.2.5	Numerical Simulation	11
1.3	Technology and Spin Torque	12
1.3.1	Spintronics	12
1.4	The Search for New Physics	14
1.4.1	Quantum Tunneling	14
1.4.2	Ultrafast Dynamics	14
1.4.3	Sub-Nanoscale Dynamics	15
1.5	Goals	15
1.5.1	Long Time-Scale Behaviour	15
1.5.2	Detailed Interactions	16

1.5.3	Analytical Model of the Vortex	16
1.5.4	Combined Spatial and Temporal Imaging	16
1.6	Organization of this Thesis	17
2	The Magnetic Vortex	19
2.1	The Vortex State	20
2.1.1	Anatomy	20
2.1.2	Technological Importance	20
2.1.3	Quasi-static Behaviour: Evolution with Field	22
2.1.4	Quasi-static Behaviour: Annihilation and Creation of the Vortex State	25
2.1.5	Dynamical Behaviour	28
2.2	Historical Development of Models of the Vortex State	28
2.2.1	Motivation for a Two Parameter Model	30
2.3	The Rigid Vortex Model	30
2.3.1	Core Profile and Diameter	30
2.3.2	Vortex Displacement	31
2.3.3	Susceptibility Correction	34
2.4	The Two Vortex Model	35
2.4.1	The Two Vortex Two	37
2.4.2	Vortex Displacement	38
2.5	The Deformable Vortex Pinning Model	40
2.5.1	Coupling and Solution	41
2.6	Comparing the Models: The Ideal Disk	45
2.7	Pinning	47
2.7.1	Single Pinning Sites	49
2.7.2	Two Dimensional Pinning Site Array	51
2.8	Bistable Paths	54
2.9	Computation of Thermal Dynamics	54
2.10	Fitting to Magnetization Curves	57
2.11	Conclusion	57

3	Magneto-optical Study of Vortex Annihilation	59
3.1	The Magneto-optical Kerr Effect	59
3.1.1	Qualitative Description of MOKE	60
3.1.2	Applications	61
3.2	Thermal Driven Transitions in Magnetic Samples	64
3.2.1	Study of Arrays	66
3.3	Experimental Design	66
3.3.1	Sample	66
3.3.2	AC-MOKE Susceptometer	68
3.3.3	Optimization	69
3.4	Susceptibility of the Vortex State	73
3.4.1	Hysteretic Transitions	73
3.4.2	Analytical Model	76
3.4.3	Extraction of Physical Parameters	76
3.5	Annihilation Transition	77
3.5.1	Extracting the Distribution Peak	77
3.5.2	Temperature Dependence of the Saturation Magnetization	78
3.5.3	Temperature and Sweep Rate Dependence	79
3.6	Pinning in an Array	84
3.7	Revised Apparatus	84
3.8	Conclusion	86
4	Magnetic Vortex Pinning	89
4.1	Vortex Core Pinning	90
4.2	Torsional Magnetometry	91
4.2.1	Historical Application	92
4.2.2	Modern Micromechanical and Nanomechanical Magnetometers	93
4.3	Experimental Apparatus	93

4.3.1	Torsional Paddle	95
4.3.2	Interferometric Detection	96
4.3.3	The Apparatus	98
4.3.4	Simplified Analysis	101
4.3.5	The Magnetic Disk	102
4.4	Observation of the Nanoscale Barkhausen Effect	104
4.4.1	Analysis of the Major Loop	105
4.4.2	Emergence of Minor Hysteresis and Telegraph Noise	107
4.4.3	Instability	110
4.4.4	Two Dimensional Investigation	111
4.5	Extraction of the Pinning Potential	112
4.5.1	Fitting to 1D data	114
4.5.2	Limitations of Fitting	118
4.5.3	Fitting to Barrier Evolution	119
4.5.4	Pinning Potential in 2D	119
4.5.5	Supporting Micromagnetic Simulations	123
4.6	Artificial Pinning Sites	125
4.6.1	Ion Implantation	125
4.6.2	Artificial Bistable Sites	126
4.7	Conclusion	128
5	Time-Resolved Spin Polarized STM	131
5.1	Magnetodynamics and High Spatial and Temporal Resolution	132
5.2	Scanning Tunneling Microscopy	133
5.3	Time-Resolved STM	135
5.4	Spin Polarized STM	136
5.5	Theoretical Description of the STM	137
5.5.1	The Modified Bardeen Approach	138

5.5.2	SP-STM	142
5.6	Operation of a TR-STM	143
5.6.1	TR-SPSTM	146
5.7	Instrumental Design	146
5.7.1	Planned Design	148
5.7.2	The Createc STM	148
5.8	Pump Probe Scheme	150
5.8.1	Optical Pump Probe Scheme	150
5.8.2	Electronic Pump Probe Scheme	151
5.8.3	RF Switched JM-STM	153
5.9	Sample Preparation	155
5.9.1	Transmission Line Sample	155
5.9.2	Patterned Sample Fabrication <i>in situ</i> : Shadow Masking	156
5.9.3	Patterned Sample Fabrication <i>in situ</i> : UHV Deposition	158
5.9.4	Patterned Sample Fabrication <i>in situ</i> : Sample Transfer	159
5.9.5	Summary of Samples Made	159
5.10	Spin Polarized Tips	161
5.11	Proof-of-Principle Junction Mixing Results	163
5.11.1	Optimization of the Signal	163
5.11.2	Time Resolution	165
5.11.3	Spatial Contrast	166
5.11.4	Interpretation of Results	166
5.12	Challenges	169
5.12.1	Surface Roughness	169
5.12.2	Spin Polarization	169
5.12.3	Unanticipated Problems	171
5.13	Conclusion	172

6	Copper Hafnium:Structure and Dynamics	173
6.1	Metallic Glasses	173
6.2	STM Observations	174
6.3	Surface Structure	175
6.4	Surface Dynamics	177
6.4.1	Tunnel Current Dependence	180
6.5	Aging	180
6.5.1	Noise Analysis	181
6.6	Temperature Dependence	183
6.6.1	Measuring Cluster Lifetimes	183
6.6.2	Bandwidth Limitation for an Ensemble	184
6.7	Complementary Electron Microscopy	187
6.7.1	SEM: Surface Aging	187
6.7.2	SEM: Large Surface Changes	187
6.7.3	TEM: Hopping Clusters	189
6.7.4	Beam Influence	191
6.8	Cross Checks for Contamination	191
6.8.1	Identification of Hopping Clusters	191
6.8.2	Identification of Tip Artifacts	192
6.9	Surface preparation procedures unique to the study of amorphous films	193
6.9.1	Thermal Treatments	193
6.9.2	Current-Voltage Characteristics	193
6.9.3	Second STM	194
6.9.4	Argon from Sputter Cleaning	195
6.10	Conclusion	195
7	Summary	197

Bibliography	201
Appendices	
A Micromagnetic Simulations	217
A.1 LLG Software	217
A.2 Quasi-Static Simulations	218
A.2.1 Typical Simulation Parameters	218
A.2.2 Grid	218
A.2.3 Consequences of Over-Damping	219
A.2.4 Convergence	219
A.3 Dynamics	220
A.3.1 Thermal Stretching	220
B Electron Beam Evaporator	221
C Shadow Mask Fabrication	224
C.1 EBL Shadow Masks	224
C.2 FIB Shadow Masks	226
D Shadow Mask Deposition	229
E Vortex Creation	233
F Torsional Paddle Fabrication	236
G The Modified Bardeen Approach	240
H The UHV Suitcase	244
I GaAs Optoelectronic Switches	248
I.1 GaAs Photoswitches	248
I.2 GaAs Integrated Samples	251

J	Fabrication of Bulk Chromium Tips	252
J.1	Machining	252
J.2	Etching	254
J.3	Field Emission	255

List of Figures

1.1	A cartoon of the original Barkhausen apparatus.	3
1.2	Demagnetization charges on a uniformly magnetized element.	9
2.1	The magnetic vortex.	21
2.2	Deformation of a magnetic vortex state under an applied field in the absence of pinning.	24
2.3	Deformation of the magnetization of a magnetic vortex under an applied field in the presence of pinning.	26
2.4	The hysteresis loop of the vortex state.	27
2.5	Schematics of analytical models of the vortex state.	29
2.6	Plotting contours of constant magnetization for the RVM, TVM and simulation reveals the consistent underestimate of the magnetization intrinsic in the TVM for a displaced vortex core.	33
2.7	The susceptibility correction accounts for redistribution of demagnetization charges away from the edge of a magnetic element.	34
2.8	The RVM shows improved performance in predicting properties of the vortex state when incorporating the susceptibility correction.	36
2.9	The Deformable Vortex Pinning Model accounts for the qualitative change in the distortion of the magnetization when a vortex state has a pinned core.	40
2.10	Coupling of the TVM and RVM components of the DVPM requires consideration of the total demagnetization energy from each component.	42
2.11	Estimation of the optimal size of the size of the flexible region in the DVPM.	44
2.12	The DVPM provides good performance compared to the RVM and TVM in situations without pinning.	46
2.13	The 2D energy space defined by the two different types of vortex displacement: rigid and flexible, included in the DVPM.	48
2.14	The DVPM greatly outperforms the RVM in situations that include pinning.	50

2.15	Performance of the DVPM with pinning is robust for a wide range of disk sizes.	52
2.16	Computation of the 2D path of minimum energy, independent of field, permits generalization of the DVPM to 2D.	53
2.17	Multiple 2D paths of minimum energy creating a continuum of pinning sites.	55
2.18	Computation of energy barriers separating bistable states allows inclusion of thermal dynamics in the DVPM.	56
3.1	The Lorentz force can be used to qualitatively understand the shifts in ellipticity of linearly polarized light on reflection from a ferromagnet.	62
3.2	Magnetometers based on the magneto-optical Kerr effect.	63
3.3	Thermal dynamics and sweep rate affect the measured annihilation field for a vortex state.	65
3.4	The array of disks used to study the annihilation process.	67
3.5	The AC-MOKE susceptometer.	70
3.6	Optimization of MOKE signals depends strongly on the angle of the analyzing polarizer.	72
3.7	AC measured susceptibility can be acquired simultaneously with DC measured magnetization.	74
3.8	Contrast between AC measured susceptibility and DC measured magnetization provides insight into hysteretic transitions.	75
3.9	Vortex annihilation has a strong dependence on temperature correlated with $M_S(T)$.	81
3.10	A weak dependence of annihilation on sweep rate reveals thermal activation processes.	82
3.11	Pinning remains detectable in an array when measuring susceptibility using an AC-MOKE susceptometer.	85
3.12	Using a vacuum chamber to protect the sample, temperature range for the AC-MOKE susceptometer may be significantly expanded.	87
4.1	A torsional paddle provides the ideal platform to detect torque exerted on a magnet.	94
4.2	Resonant motion provides enhanced sensitivity to AC torques for magnetometers.	96
4.3	A paddle and mirror form an etalon, providing interferometric contrast dependent on the spacing of the paddle and mirror.	97
4.4	Permanent magnets shifted on rails provide stable magnetic fields applied as used in the torsional magnetometer.	100
4.5	Fabrication of permalloy disks on silicon nitride membranes enables a wide array of TEM inspection techniques.	103

4.6	Analysis of pinning using the RVM.	106
4.7	Weak pinning allows observable thermal dynamics.	108
4.8	Thermal dynamics allow experimental measurement of energy barriers separating bistable states.	110
4.9	Sweeping with two orthogonal bias fields allows a 2D inspection of pinning.	113
4.10	Single blind tests show that fitting the DVPM to magnetization curves provides an accurate extraction of the real pinning potential.	115
4.11	The torsional paddle with the DVPM allows very sensitive measurement of the pinning potential.	117
4.12	DVPM fitting can extract 2D constructed potentials that reproduce measured 2D magnetization data.	122
4.13	Simulations using random weak pinning mimic natural pinning.	124
4.14	Focused ion beam implantation can create precise, very influential, artificial pinning.	127
4.15	Varying implanted ion dosage points the way to 2D pinning potentials with very sensitive control of the pinning energy landscape.	129
5.1	The Besöcke Beetle scan head of the Createc STM.	134
5.2	A highly simplified picture of the STM tunnel junction under an applied bias voltage.	139
5.3	Spin-polarized STM uses tunneling magnetoresistance to detect magnetic contrast.	141
5.4	Nonlinear properties of the STM tunnel junction allow mixing of signals.	145
5.5	Opto-electronic Junction-Mixing STM designs use ultrafast lasers and photoswitches to apply pulses to the STM junction.	147
5.6	A time-resolved spin-polarized STM can be envisaged as using a smooth transmission line for both voltage and magnetic stimulus.	149
5.7	High-speed wiring was added to the Createc STM to allow all-electronic junction-mixing.	152
5.8	RF switched Junction Mixing STM.	154
5.9	The time-resolved STM sample transmission line and deposition process.	157
5.10	STM sample transfer process.	160
5.11	Permalloy disks observed via STM on a copper hafnium transmission line.	162
5.12	Bulk chromium STM tips.	164
5.13	Time delay scans acquired using RF switched JM-STM.	167
5.14	Time-resolved contrast observed between permalloy and copper hafnium.	168

5.15	Time-resolved contrast observed between surface regions on copper hafnium.	170
6.1	Surface structure of $\text{Cu}_x\text{Hf}_{1-x}$ strongly depends on concentration.	176
6.2	Surface clusters in $\text{Cu}_x\text{Hf}_{1-x}$ exhibit stochastic dynamics.	177
6.3	Initial scans on fresh areas of $\text{Cu}_x\text{Hf}_{1-x}$ exhibit stronger dynamics than heavily scanned areas.	178
6.4	Tip interactions on $\text{Cu}_x\text{Hf}_{1-x}$ surfaces influence hopping dynamics, and much larger surfaces changes.	179
6.5	Sputtering destroys the surface reconstruction of $\text{Cu}_x\text{Hf}_{1-x}$, which may be restored by scanning.	182
6.6	Cluster hopping on the $\text{Cu}_x\text{Hf}_{1-x}$ surface exhibits temperature dependence.	185
6.7	Rough areas of fresh $\text{Cu}_x\text{Hf}_{1-x}$ films exhibit a surface reconstruction under the influence of an SEM beam.	188
6.8	Large, spontaneous surface changes can be induced on $\text{Cu}_x\text{Hf}_{1-x}$ by SEM scanning.	189
6.9	TEM observations of $\text{Cu}_x\text{Hf}_{1-x}$ films on carbon nanotubes exhibit cluster hopping.	190
6.10	I-V spectroscopy on $\text{Cu}_x\text{Hf}_{1-x}$ shows that the films remain metallic.	194
B.1	The electron beam evaporator	223
C.1	The process flow for the electron beam lithography production of shadow masks.	225
C.2	Images of EBL defined holes etched in a membrane.	226
C.3	Production of shadow masks by focused ion beam milling.	228
D.1	Examples of samples made by shadow masking.	230
D.2	Geometric considerations for shadow masking.	231
D.3	Batsian style shadow mask manipulation and alignment.	232
E.1	Vortex creation distributions strongly depend on sweep rate.	234
F.1	The fabrication process for torsional paddles on SiN membranes.	237
F.2	Simulations showing the implantation profile of gallium ions into silicon nitride and permalloy.	238
H.1	The ultra high vacuum suitcase.	246

I.1	Example large area photoswitches.	250
I.2	Integrated circuit photoactive STM samples.	251
J.1	The hand machining process for bulk chromium STM tips.	253
J.2	Etching and field emitting chromium tips.	256

List of Symbols

A	The exchange stiffness of a magnetic material; usually between 1.0×10^{-11} and 1.3×10^{-11} J/m for permalloy.	31
A_o	The generalized attempt frequency used in the Arrhenius relation. For a vortex $A_o = f_o$, the gyrotropic mode, in this work.	79
E_F	The Fermi energy.	140
E_d	The demagnetization, or dipolar energy, of a magnetic element.	8
E_o	The energy scaling parameter used in describing the functional form of the energy barrier for a magnetic transition.	79
E_{Ex}	The total exchange energy of a magnetic element.	32
$F_1(L, R)$	An equivalent demagnetization factor describing volume demagnetization charges in the TVM.	39
$F_c(L, R)$	The susceptibility corrected average radial demagnetization factor for a cylinder uniformly magnetized in-plane.	32
$F_{nc}(L, R)$	The average demagnetization factor for a disk uniformly magnetized in-plane, with no susceptibility correction.	42
H' or H_{scaled}	A scaled field used to remove temperature dependence of saturation magnetization from magnetization measurements, but maintain reference to experimentally pertinent fields.	106
H_o	The critical field parameter used in describing the functional form of the energy barrier for a magnetic transition.	79
H_{AC}	Amplitude of the AC field applied to drive a torsional magnetometer resonance.	101
H_{Weiss}	Weiss' postulated molecular field responsible for ferromagnetism.	2
H_{eff}	The effective field used to describe precession in the LLG equation determined by the total energy interactions in a ferromagnetic sample.	11
I_R	The total moment of inertia of the torsional paddle.	101
J_{Ex}	The exchange integral.	6

L	The thickness of the magnetic film, or disk.....	31
M_S	The saturation magnetization describing the intensity of the magnetization, or, alternatively, the density of magnetic moments.....	7
N	A normalization factor used in describing the experimentally measured susceptibility of the vortex state.....	77
$P_G(x)$	The normalized cluster size distribution for a CuHf sample.....	186
Q	The quality factor of a resonant mode.....	101
Q_o	An offset factor used in describing the experimentally measured susceptibility of the quasi-single domain state.....	77
R	The physical radius of a disk.....	33
R_o	The exchange length, ~ 5.85 nm for permalloy films used in this work.....	31
$S(f)$	The noise power spectrum of thermally activated hopping with frequency.....	181
S_R	The magnetic field sweep rate.....	79
T_f	A fictitious temperature used to describe glassy dynamics as a glassy material ages. 181	
V_B	The bias voltage applied to the STM tunnel junction.....	137
$W_{\mu\nu}$	The transition probability per unit time between states ψ_μ and χ_ν	138
$Y(h)$	The magneto-optical signal signal measured in AC-MOKE proportional to the total susceptibility of sample under study.....	77
ΔE	The energy barrier preventing vortex annihilation.....	79
ΔH	Field step size for field sweeps using measurements made at discrete points.....	79
Δr	The vortex displacement from the centre of the disk.....	32
Δt	Added delay time per point for field sweeps using measurements made at discrete field points.....	79
Δ	The energy barrier describing diffusion in a metallic glass.....	181
$\Delta\theta(t)$	The angular deflection of a torsional paddle device.....	101
$\Delta\theta_0$	The angular amplitude of the motion of a driven torsional paddle.....	101
Γ	The transition rate of a thermally activated stochastic transition.....	185
Γ_{bw}	The limited bandwidth used in observing transitions of a thermally activated stochastic transition.....	185
Γ_{obs}	The bandwidth corrected observed transition rate of a thermally activated stochastic transition.....	185

Λ	A constant describing the aging process of a glassy material through a thermalization incorporating a fictitious temperature	181
α, α'	A constant defined for convenience to describe the combined exchange and demagnetization energies as a function of vortex displacement in the TVM, or for α' , the TVM component of the DVPM.	39
α_d	The exponent describing the process via which a magnetic transition occurs.	79
α_g	The damping parameter used in the LLG equation.	11
α_v	A parameter describing the surface area interaction strength of clusters.	186
β, β'	A constant defined for convenience to describe the combined exchange and demagnetization energies as a function of vortex displacement in the RVM, or for β' , the RVM component of the DVPM.	33
$\chi(h)$	The total relative susceptibility of a magnetic sample. For a disk, this is integrated over the volume, and then normalized.	77
χ_ν	A STM tip wave function.	138
$\delta\phi$	The phase difference between the motion of a driven torsional paddle, and the driving field, or the phase difference between two signals.	101
$\eta_\uparrow, \eta_\downarrow$	Respectively, the electronic spin up and spin down density of states at the Fermi level.	142
γ_o	The electron gyromagnetic ratio.	11
\hbar	The reduced Planck's constant.	137
κ	The displacement stiffness constant for a vortex core that governs the gyrotropic mode frequency.	28
$\mathbf{M}(\mathbf{r})$	The vector field describing the spatially varying magnetization over a ferromagnet.	7
$\mathbf{m}(\mathbf{r})$	The vector field describing the spatially varying magnetization over a ferromagnet normalized by M_S	8
μ_B	The Bohr magneton.	102
ν_R	The damping parameter for torsional motion.	101
ω_0	The resonant angular frequency of a torsional paddle.	101
ω_1, ω_2	Angular frequencies of example signals applied for mixing in a tunnel junction.	144
ω_d	Driving frequency of the AC field applied to drive a torsional resonance.	101
ϕ_w	The work function.	137
ψ_μ	A STM sample wave function.	138
ρ_T, ρ_S	The electronics density of states of the STM tip and sample respectively.	140

$\rho_d(\mathbf{r})$	The volume demagnetization charge distribution.	10
$\sigma(\mathbf{r})$	The distribution of demagnetization charges (uncompensated dipole moments). Usually σ only denotes surface charges, however since only 2D films are considered in this work, it is used to denote volume demagnetization charges as well.	32
σ_a	The standard deviation of the switching distribution for a magnetic transition. . .	77
τ	The lifetime of a thermally unstable state. Used here in describing vortex core pinning, vortex annihilation, and thermally activated cluster hopping in glassy films. 54	
τ_M	Magnetic torque of a field acting on a magnetic moment.	95
$\tau_M(t)$	The AC torque applied to drive torsional resonance of a magnetometer paddle using an AC magnetic field.	101
$\theta(\mathbf{r})$	A function used to describe the split between in-plane and out-of-plane magnetization in the RVM core profile.	31
θ_p	An angle defined by the size of the inner flexible region in the DVPM, describing the angle made by a line of constant vortex displacement makes with the b' axis. 47	
a, a'	A parameter describing vortex core displacement in the TVM, or for a' , the TVM component of the DVPM.	38
$a_o(h), a'_o(h)$	The normalized equilibrium vortex core displacement of a disk under an applied field according to the TVM, or for a'_o , the TVM component of the DVPM. 39	
b, b'	The normalized vortex displacement specifically in the RVM, or for b' , the RVM component of the DVPM.	32
$b_o(h), b'_o(h)$	The normalized equilibrium vortex core displacement of a disk under an applied field according to the RVM or for b'_o , the RVM component of the DVPM. 34	
d	The physical separation of the STM tip and sample: the tunnel gap.	137
e	Charge of an electron.	137
$f(E)$	The Fermi-Dirac distribution.	140
$f(z)$	A general function used to generate a magnetization distribution on the complex plane.	37
f_o	The gyrotropic mode frequency.	28
g	The coefficient in the Bloch $T^{3/2}$ law describing the variation of saturation magnetization with temperature.	78
$g(z)$	A general function used to describe different magnetization distributions in the complex plane.	37
h	The reduced magnetic field $h = H/M_S$	33

h_a or H_a	The annihilation field for the vortex state; $h_a = H_a/M_S$. For an array this is defined as the peak position of the annihilation distribution.	77
i, j	Coordinates transformed from b' and a' describing axes perpendicular and parallel to lines of constant vortex displacement in $b'-a'$ space in the DVPM.	47
k	A geometrical factor arising from the integration of volume demagnetization charges in the TVM.	39
k_F	A geometric constant for the self energy of the demagnetization charges induced by a vortex core on one face of the disk.	31
k_R	The stiffness constant of a torsional spring.	95
m_e	Mass of an electron.	137
$m_o(h)$	The normalized equilibrium magnetization of a disk under an applied field.	34
$o(z)$	An analytic conformal transformation used to distort a complex magnetization distribution to another form.	37
r_c	Radius of the maximum extent of the vortex core used in piecewise models of the core profile.	31
s	The normalized vortex displacement.	32
$\sigma_a(\mathbf{r})$	The surface demagnetization charge distribution.	9
AC-MOKE	Incorporation of a low speed AC field into a MOKE magnetometer to measure magnetic susceptibility optically.	64
AFM	Atomic Force Microscope.	67
Annihilation	The process of expulsion of the vortex core from the disk, and the transition from a vortex to a quasi-single domain state.	22
Bias Field	The DC field applied to induce shifts in sample magnetization.	99
Bistable Paths	Multiple solutions for the 2D path of minimum energy for the vortex core in a 2D pinning site distribution.	54
chirality	The direction of circulation, clockwise or counter-clockwise, of the vortex state magnetization distribution.	20
Creation	The transition process between a quasi-single domain state in a disk, to a vortex state.	22
CuHf	A shorthand form for $\text{Cu}_x\text{Hf}_{1-x}$	174
EBL	Electron beam lithography.	158
Electron Beam Evaporator	A deposition unit that evaporates a material using an accelerated electron beam for heating.	221

FIB	A focused ion beam uses an accelerated beam of ions (often Ga^+) to physically mill away material in samples. Implanted ions may also cause disruption of local material properties, including magnetism.	95
Glan-Thompson prism	A Glan-Thompson prism consists of two calcite wedges cemented together with their optical axes perpendicular. The beam transmitted through the prism, and the beam reflected from the interface of the wedges, have orthogonal polarizations.	69
Gyrotropic Mode	The lowest frequency excitation of the vortex state which results in a circular orbit for the vortex core.	28
JM-STM	Junction Mixing Scanning Tunneling Microscope/Microscopy.	135
Lorentz Microscopy	A transmission electron microscopy technique exploiting the Lorentz force on electrons passing through magnetic films to detect domains.	22
MFM	Magnetic force microscopy uses magnetic tipped cantilever to perform magnetic scanning probe microscopy.	93
MG	Metallic Glass.	173
MOKE	The magneto-optical Kerr effect consists of the rotation and elliptization of polarization of light on reflection from a magnetic sample.	59
Néel-Brown transition	A magnetic transition driven by thermal fluctuations, named in honour of the pioneering work by Néel and Brown.	65
Permalloy	A nickel-iron alloy. Here an alloy $\text{Ni}_{81}\text{Fe}_{19}$ by weight, the most common permalloy mixture.	59
Polarity	The direction of vortex core magnetization: into the plane (-1) or out of the plane (+1).	20
QSD	The quasi-single domain state is the approximately uniformly magnetized state observed in disk structures. It is entirely uniform, except for two edge defects.	25
RVM	The Rigid Vortex Model.	29
Skirt	The circularly symmetric, in-plane magnetized section of the vortex state magnetization distribution.	20
SQUIDS	Superconducting quantum interference devices that perform sensitive measurements of magnetic flux.	92
STM	Scanning Tunneling Microscope.	132
SVPM	Scanning Vortex Probe Microscope.	198
TEM	A transmission electron microscope.	91
Ti:Saph Laser	A laser using a titanium-doped sapphire crystal as the lasing medium that is pumped by a 532 nm pump laser. With a broad-band gain, it is possible to operate the laser as mode-locked, where where simultaneous phase-coherent emission from a large number of cavity modes yields ~ 100 s of femtosecond length pulses.	63

TMR	Tunneling Magneto-Resistance.....	136
TR-MOKE	A pump-probe technique to measure magnetization dynamics optically. . .	64
TR-STM	time-resolved Scanning Tunneling Microscope.....	132
TVM	The Two Vortex Model.....	29
UHV	Ultra-high vacuum, colloquially pressures that require significant baking of vacuum components to reach (below $\sim 1 \times 10^{-9}$ mbar.)	67
Winding Number	The winding number, or topological charge of a vortex like structure indicates the number of times the magnetization pattern circulates around the core. Half integer winding numbers arise for structures with symmetry broken by physical boundaries of magnetic elements.....	25

CHAPTER 1

Introduction to Modern Magnetism

1.1 History

1.1.1 The Greeks to Maxwell

Magnetic interactions have presented a fascinating and mysterious world to curious humans for millennia. Interactions between magnets are, perhaps, the prototypical example of Einstein's famous spooky action at a distance. Ancient civilizations pictured souls inhabiting magnetic rocks and giving rise to their unexplained behaviour. In fact, attributing magnetic properties of rocks to rock souls survived up to the 1600's with the work of William Gilbert.

The history of magnetism from the time of the ancients to more modern history is largely pontification on the philosophical nature of magnets, or the pragmatic application of magnetic effects. Progress would need to wait until inspiration was provided by concrete experimental results ¹.

The 1800s brought the golden age of classical physics and the theory of electromagnetic fields. Hans Christian Oersted famously discovered that a current carrying wire could deflect a compass needle. This discovery initiated an explosion of theoretical triumphs explaining ever more aspects of magnetism with contributions from classical greats such as Ampère, Gauss, Biot, Savart and Faraday. This body of work culminated in Maxwell's equations, and a comprehensive, tidy solution was at hand. The interaction of magnets could be described in terms of dipoles and the electro-magnetic fields generated by those dipoles.

¹An excellent account of early magnetic history may be found in the text by Mattis (*1*).

While the spooky action at a distance aspect of magnetism was resolved², magnetic behaviour continued to present challenging puzzles for new generations of scientists. The question still remained, even if interaction between ferromagnetic materials was understood, how were the materials magnetic in the first place?

Ampère presented a beautiful picture of microscopic current rings permeating magnetic materials, creating arrays of tiny dipoles which, when aligned, provided a magnetic moment for an object. This description provides a profoundly satisfying tie to the cartoon like picture of electrons orbiting atoms. Indeed, even up to the experiment of Einstein and de Haas in 1915, Ampèrian currents were thought to be the fundamental cause of magnetization in solids. Einstein felt his experiment offered definitive proof of the existence of Ampèrian currents (2). This was, of course, until a factor of two error was discovered in the analysis, meaning that the experiment was definitive proof that Ampèrian current loops (electron orbits) were not the root source of ferromagnetism. Compounding this issue, within the same time frame the Bohr-van Leeuwen (3,4) theorem showed that no classical ferromagnetism was possible. Fortunately, quantum mechanics soon provided the answer.

1.1.2 Domains and Quantum Mechanics

The framework for understanding ferromagnetism phenomenologically was laid down by Pierre Weiss in 1907 (5). Weiss proposed a solution to a number of puzzles concerning the nature of ferromagnetism with the postulation of a molecular field, H_{Weiss} , that existed only inside of ferromagnets. This field was introduced to explain how magnetic moments could be stably aligned under the influence of thermal fluctuations. Weiss also introduced the concept of sections of a magnet having separate magnetizations, a concept known as magnetic domains (Fig. 1.1). The domain viewpoint explained how a ferromagnetic sample could have a wide variety of net magnetic moments, including none, in zero field, despite the presence of a large intrinsic, internal field. These conjectures betray Weiss's profound insight into the nature of ferromagnets, as both would be justified in time.

Existence of Weiss' domains was verified experimentally in 1919 by Heinrich Barkhausen (6). The experiment employed a coil wound around a ferromagnet so that any shifts in the magnetization of the sample would induce a current spike in the coil. The coil was connected to a speaker providing an audible readout of the change in magnetization. A field was then applied to the magnet to induce reversal. Barkhausen found that the audio signal consisted of stochastic clicks and static, rather than a continuous tone. Thus indicated reversal was occurring by stick slip shifting of the boundaries between domains, and consequent jumps in the magnetization of the sample. Detection of domains marked the experimental beginnings

²Less rather than more, but for the purposes of this work it is safe to say it was well understood.

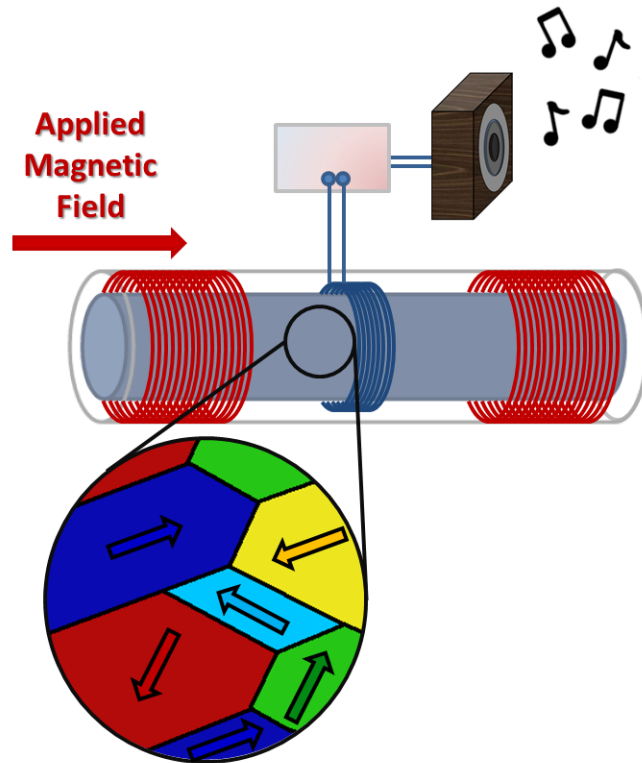


Figure 1.1: Barkhausen detected switching domains with induction coils connected to a loud speaker. Barkhausen obtained the first experimental evidence of domains from a magnetic rod under the influence of a swept applied field. As the field is increased the domain structure of the rod becomes energetically unfavourable, resulting in domain walls propagating up the rod, stochastically increasing magnetization. Coils wound around the rod pick up the changes in magnetic flux inductively, and output a characteristic clicking static noise.

of the study of micromagnetic phenomena. A working understanding of the underlying physics of domains still required some significant theoretical advances.

The possible existence of the Weiss molecular field raised many questions. The equivalent strength of the molecular field can be computed approximately from $\mu H = K_B T$, which for a single moment of magnitude μ_B , requires a field of order 10^9 A/m, orders of magnitude larger than experimentally accessible fields in the early 1900s (7). Dipolar interactions between electrons are of the order 10^5 A/m, far too low to offer an explanation. The source of the stabilizing interaction required a different explanation. Heisenberg resolved this conundrum in 1928 with the description of the exchange interaction applied to the intrinsic spin magnetic moment of electrons (8).

Investigation of the nature of the magnetic moments fundamentally responsible for the magnetic moment in ferromagnets provided essential clues in the discovery of the exchange interaction. A connection was predicted in 1908 (9) and investigated by Barnett (10), though, Barnett pointed out that much earlier Maxwell suspected a connection and even attempted experimental investigation (11, 12). In 1915, the connection was experimentally verified first by Barnett (13), who measured changes in magnetization induced by mechanical rotation, and subsequently by Einstein and de Haas (2, 14), who detected the inverse, rotation resulting from changing magnetization³.

One of the primary motivations of this work was to find proof that electron orbital motion was responsible for the magnetic moments by demonstrating a fundamental link between magnetic moments and orbital angular momentum⁴. This link was predicted to have the form $g' \mathbf{J} = \frac{2m_e}{e} \mathbf{M}$, where g' is the magneto-mechanical ratio. Given a measurement of the charge to mass ratio of the electron, the expectation was that $g = 1$ for orbital electron angular momentum.

Collaborating with de Haas, Einstein developed an apparatus that consisted of a magnetic rod suspended from a torsion spring. Reversing the magnetization of the suspended sample was found to induce a mechanical torque measurable with the torsion spring, confirming the suspected link. However, an error was made in the analysis resulting in a measured g' of one. Converse to this, Barnett measured the flux change correlated with rotation of a magnetic steel rod, and found $g = 2$. The inconsistency, the gyromagnetic anomaly, was resolved rapidly, as independent works (17, 18) verified the correct value was 2. This conclusively demonstrated that orbital motion could not entirely explain ferromagnetic phenomena⁵.

³Barnett, less famous than Einstein often is assigned less credit in the magneto-mechanical story. Here care is taken to include him and assign an equal or greater contribution as he was first, and moreover, obtained the correct result for g . He also took care to ensure his wife's contribution was acknowledged (15, 16), along with many of those who preceded him in this line of investigation.

⁴Note that spin had not yet been discovered, nor had the concept been developed formally.

⁵An excellent account of the early history of the Einstein-de Haas and Barnett effects is available in the work of Frenkel (19).

In their famous experiment Stern and Gerlach (20) showed that the magnetic moment of atoms was quantized. This coupled with the knowledge that the quantization could not be due to orbitals provides clear experimental motivation for the postulation of an additional magnetic moment that is also quantized. Pauli postulated such a system, along with the stipulation that it may be occupied by only one electron at a time (Pauli's Exclusion Principle) (21). Shortly thereafter, Uhlenbeck and Goudsmit introduced the concept of spin, describing such a system (22), with Pauli providing his famous spin matrices and the complete non-relativistic theory two years later (23). Electrons have been identified as fundamental carriers of angular momentum, and consequently magnetic moments. The spin of an electron was now well described by a two level system with a single half-integer quantum number ($\pm 1/2$).

1.1.3 The Exchange Interaction

The ingredients presented above were enough for Heisenberg to determine the nature of the Weiss molecular field. Heisenberg considered additional effects arising among interacting electrons when the exchange of the quantum states of two electrons is considered. The simplest case, and an illustrative one, is to consider two interacting particles occupying two separate states ψ_a and ψ_b . For particles of spin 1/2 obeying the Pauli Exclusion Principle (i.e. Fermions), particles fill states as pairs with opposite spin, up to an energy level related to the number of particles in the system. Additionally, fundamental quantum mechanical particles are indistinguishable. Therefore, a wave function for a system should be considered as a superposition of the wave functions for the electrons filling the states in one arrangement, and also for the exchanged arrangement.

$$\Psi_{tot} = \frac{1}{\sqrt{2}}(\psi_1(\mathbf{r}_1)\psi_2(\mathbf{r}_2) \pm \psi_1(\mathbf{r}_2)\psi_2(\mathbf{r}_1)) = \frac{1}{\sqrt{2}}(|1, 2 \rangle \pm |2, 1 \rangle) \quad (1.1)$$

For Fermions, the total wave function must be antisymmetric under particle exchange. This means, that for a spatially symmetric wave function (+ in equation 1.1) to be permitted, the component of the wave function representing the spin must be antisymmetric (opposite spins). Similarly the spin part must be symmetric, if the spatial wave function is anti-symmetric (- in equation 1.1). Now consider an interaction V_c between the two electrons, and compute the interaction term in the Hamiltonian, $E_{int} = \langle \Psi | V_c | \Psi \rangle$ for the spatially symmetric and anti-symmetric versions of the wave functions. The difference between E_{int} for the symmetric and anti-symmetric case is then $2 \langle 1, 2 | V_c | 2, 1 \rangle$. Recall that the symmetric and antisymmetric wave functions carry opposite spin. Therefore, depending on the wave function overlap, and sign of the interaction, spin arrangements with spins parallel or anti-parallel may be energetically favourable.

Heisenberg then expressed this as an interaction depending on the alignment of adjacent spins:

$$\hat{H}_{Heisenberg} = -2J_{Ex}\mathbf{S}_1 \cdot \mathbf{S}_2, \quad (1.2)$$

where $J_{Ex} = \langle 1, 2 | V_c | 2, 1 \rangle$ is the exchange integral, and \mathbf{S}_i represents the direction of the i th spin. Depending on the sign of the exchange integral, this interaction can cause adjacent spins to prefer parallel alignment, or anti-parallel, resulting in ferromagnetism and anti-ferromagnetism respectively.

1.2 Micromagnetic Interactions

Quantum mechanics provided the fundamental mechanisms required to understand magnetism in solids, however this opened the door to a massively complex area of study. Understanding a magnetic sample requires taking into account a wide variety of interactions between arrays of magnets, of the order $\sim N_A$ in number. Initial work by Ising tackled a 1D chain of two level sites incorporating intersite interactions (24, 25), while Bloch also took an atomistic approach attempting to solve for magnetic properties from a statistical perspective. Bloch had some success, most notably understanding the temperature dependence of the saturation magnetization via considering dynamic excitations in spin systems (spin waves), resulting in his famous $T^{3/2}$ law (26). However, these approaches did not provide a way to compute the structure of domains. This problem required a different perspective.

Amazingly, only 9 years after the description of the exchange mechanism, the fundamental framework enabling understanding of complex domain patterns, and even domain dynamics was introduced by Landau and Lifshitz (27). In their seminal 1935 paper, Landau and Lifshitz developed a cohesive picture of all of the magnetic interactions within a sample using a semi-classical description incorporating exchange, dipolar, and crystalline anisotropy energies.

The great achievement of Landau and Lifshitz was to regard the energetic problem as that of a continuous magnetization and not as discrete domains or individual spins. Formulating the energies in such terms enabled the accurate computation of the magnetization profile between domains with different magnetizations or, in other words, the magnetization profile of domain walls. Specifically, Landau and Lifshitz computed the form of walls with a magnetization that rotates out-of-plane in the transition region as is often the case for bulk samples or thick films. Bloch previously made attempts at this problem (28), and hence

the walls are known as Bloch walls ⁶ Solving this specific sounding problem unlocked the theoretical study of micromagnetic research.

A great deal of work must be devoted to understand the details of any particular system using the Landau and Lifshitz's framework. Conversely Landau and Lifshitz's theory has continually shown incredible flexibility in being extensible to incorporate newly discovered effects such as spin torque (30, 31). Effectively the present day micromagnetic community continues to describe magnetic phenomena almost exclusively using Landau and Lifshitz's original methods with few exceptions. The success and semi-classical nature of the theory has led to a subset of physicists in pursuit of non Landau and Lifshitz behaviour in the hopes of advancing the fundamental understanding of magnetic phenomena.

The first step to having a working understanding of Landau and Lifshitz's theory is categorizing each energetic interaction in a ferromagnet, and reformulating each in terms of a continuum description of the magnetization ⁷.

The direction of the magnetization, $\mathbf{M}(\mathbf{r})$, follows the local alignment of spins, with an intensity proportional to the spin density. Implicit in the continuum treatment is the assumption that the local magnetization always has the same intensity $|\mathbf{M}(\mathbf{r})| = M_S$, where M_S , is called the saturation magnetization.

1.2.1 Exchange Interaction

The inherent discrete nature of interactions considered in the Heisenberg Hamiltonian can be generalized to a continuous case. First the case where any adjacent pair is only slightly misaligned must be considered. This leads to the dot product of the spin vectors for two spins in an array indexed by i and j becoming:

$$\mathbf{S}_i \cdot \mathbf{S}_j = S^2 \cos(\theta_{ij}) \approx S^2(1 - \theta_{ij}^2). \quad (1.3)$$

Continuing in the small angle approximation, the difference between two magnetization vectors is related to the angular misalignment through the directional derivative, $M_S|\theta_{ij}| \approx |\mathbf{M}_i - \mathbf{M}_j| \approx |[(\mathbf{r}_i - \mathbf{r}_j) \cdot \nabla] \mathbf{M}(\mathbf{r})|$. The vectors \mathbf{r}_i and \mathbf{r}_j denote the positions of the sites i and j . This permits writing the sum of the total variation in exchange energy due to non-uniform alignment over the array as:

⁶The other common type of wall is the Néel wall, which has a magnetization profile that rotates in the plane of the film, was computed much later (29). Néel walls are commonly found in thin films.

⁷Readers seeking more detail are referred to treatments in Blundell (32), and Chickazumi (33) for clear treatments in MKSA units, or to Aharoni (34), for a detailed cgs unit treatment.

$$E_{Ex} = \frac{-J_{Ex}S^2}{2} \sum_{\langle i,j \rangle} \theta_{ij}^2 \approx -\frac{J_{Ex}S^2}{M_S^2} \sum_{i,j} |[(\mathbf{r}_i - \mathbf{r}_j) \cdot \nabla] \mathbf{M}(\mathbf{r})|^2 \quad (1.4)$$

where the sum is carried out only over nearest neighbours. Moving to the continuum limit, the sum may be converted to a volume integral over an energy density.

$$E_{Ex} = A \int_V \sum [\nabla \cdot \mathbf{m}(\mathbf{r})]^2 d^3\mathbf{r}, \quad (1.5)$$

where integral is performed over the volume of the element, the normalized magnetization $\mathbf{m}(\mathbf{r}) = \mathbf{M}(\mathbf{r})/M_S$ is introduced, and the constant $A = 2J_{Ex}S^2z_{nn}/a_l$ is the exchange stiffness constant, with z_{nn} accounting for the number of interacting nearest neighbours, and a_l the lattice constant. This continuum approximation permits computation of the exchange as a function from the magnetization distribution itself.

1.2.2 Dipolar Interaction

The most complicated and challenging energetic term in micromagnetic computations is the classical, very well understood dipolar interactions. The exchange interaction is short ranged, and easy to understand, while the long range field based interactions extend over a multitude of neighbours and non trivially depend on the boundaries of finite systems.

If a magnetization distribution is pictured as an array of dipoles (arrows), it is clear that in a uniform continuous distribution, the net dipolar interaction is canceled out by adjacent dipoles leading to no net dipolar contribution within the array. Uniform states, however, are not common in bulk samples, nor in microscopic samples. Bulk samples will tend to randomly organize into domains, while in microscopic samples, the boundaries tend to make a uniform magnetization unfavourable.

In a microscopic sample, consider spins as dipoles encountering a boundary. Along the boundary, neighbours are missing, leading to uncompensated dipoles and causing a net field. The magnetization distribution represents the distribution of dipoles through the volume, and so the density of uncompensated dipoles on a boundary is given by the dot product of $\mathbf{M}(\mathbf{r})$ with the normal vector of the boundary. For a uniformly magnetized sample, opposite edges terminate with opposite signs of the dot product. Thus the entire sample appears as a large dipole and with a corresponding net field. Within the sample itself, this field runs counter to the magnetization direction, and increases energy. Since the field is opposite the magnetization, this energy is often referred to as the Demagnetization Field. It leads to an energetic contribution: demagnetization energy, E_d :

$$E_d = \frac{\mu_0}{2} \int_V \mathbf{M}(\mathbf{r}) \cdot \mathbf{H}_d(\mathbf{r}) d^3\mathbf{r}. \quad (1.6)$$

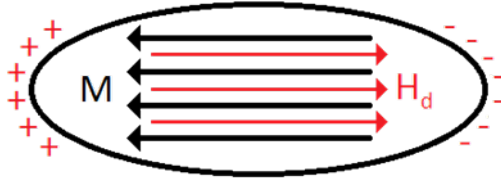


Figure 1.2: Demagnetization energy arises from the dipolar field of the sample magnetic moment. Uniform magnetization tends to exert a field counter to the magnetization of the sample, increasing energy and favouring a demagnetized sample. One method of computing a demagnetization field in a finite sample is to look at the ‘charge’ distribution on the surface. These charges represent the uncompensated dipoles contributing to the demagnetizing field.

A common approach to computing the demagnetization energy is to consider the dipoles as splittable into fictitious positive and negative magnetic charges with a Coulomb like interaction. This description lends itself well to considering boundaries. In an analogous way to electric dipoles, the charge distribution at a boundary, $\sigma_d(\mathbf{r})$, may be computed as:

$$\sigma_d(\mathbf{r}) = \mathbf{M}(\mathbf{r}) \cdot \hat{\mathbf{n}}(\mathbf{r}), \quad (1.7)$$

where $\hat{\mathbf{n}}$ is the surface normal of the boundary. With this charge distribution, two avenues may be taken to compute the demagnetization energy. A potential may be computed from the charge distribution, from which the demagnetization field can be computed. Alternatively, the self energy of the charge distribution may be computed with a fictitious Coulomb interaction. The former approach places more emphasis on the dipolar nature of the energy, and is preferred as a learning tool. It additionally is more amenable to inclusion in dynamical calculations where the net field is important. However the self energy of the charge distribution is often simpler to calculate. The self energy, or total demagnetization energy, E_d , may be computed as:

$$E_d = \frac{1}{2} \int_S \int_{S'} \frac{\sigma_d(\mathbf{r})\sigma_d(\mathbf{r}')}{|\mathbf{r} - \mathbf{r}'|} dS dS', \quad (1.8)$$

where the integrals are taken over the surface of the finite micromagnetic element. The boundaries of samples are not the only place demagnetization charges (uncompensated

dipoles) can develop. Partially uncompensated dipoles can exist inside a sample when there are continuous changes in the magnetization direction. These may be calculated as:

$$\rho_d(\mathbf{r}) = \nabla \cdot \mathbf{M}(\mathbf{r}), \quad (1.9)$$

where $\rho_d(\mathbf{r})$ denotes demagnetization charges arising from variation of the magnetization within the volume of the sample, often called volume demagnetization charges.

Computation of demagnetization energy is a difficult business. A general formalism is possible, but complicated. For uniformly magnetized samples, the demagnetization energy can be computed in terms of geometrical factors. These so-called demagnetization factors simplify the computation, but are limited in application. Once a factor is computed for a shape, the problem becomes easy, however computation of the factor is equivalent to the full calculation of the demagnetization energy. For computation of demagnetization energies and factors of arbitrary shapes, the reader is referred to the work of Beleggia and Tandon et al. (35–37).

As a final note on demagnetization energy, it should be emphasized that in the massive confusion often surrounding magnetic units, the demagnetization energy is very commonly the source of disagreements in factors of 4π between MKS and cgs unit systems.

1.2.3 External Field and Magnetocrystalline Anisotropy

The last of the important energy contributions are external field energy and energy due to anisotropies arising in crystal structure. The external field energy is not complicated to understand. In quite the usual way the energy is

$$E_H = -\mu_0 \mathbf{M} \cdot \mathbf{H} \quad (1.10)$$

where \mathbf{M} is the total magnetization and \mathbf{H} is the applied field. It can, however be challenging to compute the net magnetization of a complex distribution.

Magnetocrystalline anisotropy is potentially a very complicated contribution. In microscopic terms, the crystal structure of the sample will have an obvious influence on the exchange energy by virtue of determining the directions of strong orbital overlaps. This will create preferential directions for the magnetization relative to the crystal axes and provide additional complexity which must be taken into account in computing the equilibrium magnetization distribution. A good starting point for the inclusion of anisotropy in micro-magnetic calculations is the Stoner-Wolfarth model (38) of a uniformly magnetized particle with a single easy axis (uniaxial symmetry).

In this work, emphasis is placed on materials with low or zero crystalline anisotropy. In particular, the material of choice is permalloy, a nickel iron alloy. This material is popular for its low coercivity (low switching fields) and close to zero intrinsic anisotropy. Therefore, development of magnetocrystalline anisotropy shall not be discussed further.

1.2.4 The LLG Equation

The above descriptions of the energy in a ferromagnet can be unified into a single equation describing the physical evolution of the magnetization distribution. The original form of the equation followed from the treatment of precessional motion of the spins in the magnetization distribution under the action of an effective field (eg. $H_{eff} = H_{Weiss} + H_d + H_{ext}$). Damping of the precessional motion was a challenging issue for some time until a phenomenological damping was determined by Gilbert in 1951 (39). The resulting equation, the Landau-Lifshitz-Gilbert equation (LLG) can be written in a variety of forms, here, Gilbert's form is used.

$$\frac{d\mathbf{M}}{dt} = -\gamma_o(\mathbf{M} \times \mathbf{H}_{eff}) - \frac{\alpha_g}{M_S} \left(\mathbf{M} \times \frac{d\mathbf{M}}{dt} \right) \quad (1.11)$$

where γ_o is the electron gyromagnetic ratio, and α_g is the damping parameter.

The equation is reasonably simple looking, however, it should be apparent that it is an equation describing a 3D vector field under the influence of a horrendously complicated spatially and temporally varying effective magnetic field. With this in mind, it is no surprise that the bulk of computation performed with the LLG equation is performed using numerical simulation ⁸.

1.2.5 Numerical Simulation

With the advent of powerful, affordable computers, simulation has come to dominate the field of micromagnetics. The application of simulation to the LLG equation is easy to picture, and is, in a sense analogous to computing the evolution of an array of spins. Simulations are run using a finite difference (or finite element for more advanced simulation programs) approach. The sample is split up into a grid defining small volumes of magnetic material which are each treated as a single 'giant spin'. Under this approximation, the LLG equation is integrated in a discretized form, computing the effects of exchange interactions between neighbouring cells, dipolar interactions across the array and any other interaction

⁸A great deal of analytical work is done with simplified models, however, the use of models is not ubiquitous, nor are the models, in general, nearly as accurate as the simulations.

that is included. Proceeding with some numerical integration scheme permits computation of the time evolution of the sample magnetization. Appendix A contains the details of micromagnetic simulation programs and methodology used in this work.

Simulations tend to be so accurate that the results are treated as a direct substitute for experiment. This is not necessarily a problem, except in the sense that, as with all complex simulations, it is quite easy to tune simulation results over a wide range of parameters to create inaccurate results. Additionally, while simulation is obviously very useful to designing devices, and determining complicated, but understood interactions, it is not the best method of discovering new physics. This motivates the continued use and development of analytic micromagnetic models, particularly those covering quantum effects outside of the physics described by the LLG equation.

1.3 Technology and Spin Torque

Micromagnetism is a very active research field. The rich nature of magnetic interactions means that even within the confines of well-known samples described by the LLG equation a great deal of productive research can be performed. This richness also motivates a strong theme of technological applications. Over the past 70 or so years, micromagnetism has inexorably been linked to technological progress. In particular it has been linked to the storage of data through media such as tape drives, and hard drives.

Hard drives are a powerful force in driving micromagnetic research. Subfields are based on the development of ideal magnetic films to store data, while writing and reading data require understanding of magneto dynamics. Hard drives, however are an aging technology. New applications of magnetism, particularly those focusing on enhanced magnetic computing, have become the focus in the past decade.

1.3.1 Spintronics

Often magnetism is treated exclusively in the context of spins stationary at lattice sites. However, this overlooks the fact that many magnets are conductors and exhibit magnetic polarization in the spins of electrons occupying the conduction band. The theory of itinerant magnetism, which includes, but is not limited to conductors, is well developed (*40, 41*). However it is often left uncovered as considering magnetic moments at fixed sites is sufficient for qualitative understanding (*34*). Exploiting the polarization of the conduction electrons forms the basis of a great deal of current technologically motivated work. Collectively this field of research is known as spintronics.

Spintronics aims to replace electrical currents used to pass data and perform logic operations in computers with spin currents, or combined spin-charge currents (eg. reviews (42-44)). The non-volatile nature of magnetic storage, and fast time scale of magneto-dynamics make spintronics seem to be a promising field.

The importance of itinerant magnetism, in this work as well as in recent technology, centres on the existence of two spin populations on the propagation of current. The simplest situation to consider the effects of spin on current is that of a sandwich device with a non-magnetic spacer metal separating two ferromagnetic electrodes ⁹. Current passed through the sandwich exhibits different resistance depending on the scattering into the spin polarized states. For current passed perpendicularly through the sandwich, the current exits one ferromagnetic electrode polarized according to that electrode's magnetization. Similarly the magnetization of the other ferromagnet determine the polarization of the available states for conduction on the other side of the spacer. This leads to a situation where resistance perpendicular to the device is lowest when the magnetizations of the electrodes are aligned, and highest when they are anti-parallel. This is one of several geometries under which this effect, called Giant Magnetoresistance (GMR) can manifest. GMR, and its cousin Tunneling Magnetoresistance (TMR) are critical in read heads of hard drives and also form the basis of the gradually maturing field of spintronics. TMR is discussed in greater detail in Chapter 5 of this work.

A related effect allows switching of the magnetization of an electrode by injecting spins. The spin polarized current exerts a torque on the magnetic moments of the cathode. With a current of sufficient magnitude, the magnetization can be flipped (30, 31). Spin torque may be incorporated into the LLG equation. A fundamental issue challenges spintronic technologies. In reality, it is quite difficult and energetically expensive to switch the states of magnetic samples, requiring very high density currents. This issue may be conquered in time, particularly by changing the goal from complete magnetization reversal of a structure to a much smaller task of causing some other sort energetic transition in a sample. This line of reasoning has led to the exploitation of domain structures, such as walls, or more specifically vortices. High energy density of domain structures enhance local interactions, allowing domain walls to be pinned in particular locations, allowing much smaller energetic transitions to encode information (45). Pinning of vortex structures is discussed in great detail in Chapter 2 and Chapter 4 of this work.

Possible contribution to future technological advancement of spintronics provides significant practical motivation for the work described in this thesis. However, there is also significant motivation to look for magnetic behaviour outside the current realm of LLG description.

⁹The sandwich device featuring GMR, or TMR may be the situation that is easiest to understand, however the first magneto-resistive effect discovered was an intrinsic non spin related effect called simply magneto resistance, or Anisotropic Magnetoresistance (AMR).

1.4 The Search for New Physics

With the LLG equation accurately incorporating, exchange, demagnetization, spin torques and many other phenomena, it is challenging to determine new areas where behaviour may go beyond the semi-classical description. Two areas to work on involve the time scale extremes at which dynamics can be observed in magnets, respectively the fs and ms timescales ¹⁰. Additionally, there is significant interest in the observation of \sim ps dynamics at size scales approaching the atomic.

1.4.1 Quantum Tunneling

Tunneling of particles is, of course, a very well known quantum phenomenon. Less commonly covered is the tunneling of fields. Considering the magnetization of a particle to be a field, it is possible to envision switching pathways for ferromagnets based on tunneling. Typically tunneling is studied in the context of small clusters of magnetic atoms (46) or single molecule magnets (47) at temperatures sufficiently low that thermally activated switching no longer masks the quantum switching. Recent experimental results provide circumstantial evidence of quantum tunneling of vortex cores (48), while significant investigations in the mid 1990's showed evidence for tunneling affecting the switching processes of individual and arrays of small magnetic elements (49, 50). Tunneling of the magnetization has been considered for some time, however, it is only in more recent times that nanofabrication techniques and control of single molecule magnets have begun to deliver on the promise of manipulating magnetic elements on a scale pertinent to quantum tunneling.

1.4.2 Ultrafast Dynamics

In brief, the pursuit of non-LLG describable physics at the extreme fast time scale is attempting to push beyond the time scale for precession of magnetic moments (51). Femtosecond demagnetization of magnetic films is well established (52, 53) but controversy remains in the strict interpretation of the results (54–57). Significantly, extensive work has pointed to the influence of thermal effects (58, 59). Additional experiments postulate the existence of non-precessional switching in anti-ferromagnets (60, 61), and study ultra-fast switching through application of intense circularly polarized light (62, 63). No ultrafast experiments were performed in this work ¹¹.

¹⁰No doubt Geophysicists would quickly say that ms timescales are not at the extreme for long time scales, however from the perspective of magnetodynamics, it is beyond reasonable simulation time.

¹¹Although large area photoswitches were designed to work in tandem with the high amplitude regeneratively amplified lasers necessary for study of ultrafast demagnetization.

1.4.3 Sub-Nanoscale Dynamics

The LLG equation arises from a continuum treatment of a system that inherently consists of (at least partially) discrete particles. From this perspective there may be opportunities to find non-LLG dynamics on atomic size scales. This motivates the development of tools to investigate dynamics with as high spatial resolution as possible while maintaining temporal resolution. In particular, in the context of ultrafast dynamics, given some controversy of the ambiguity of results (54–57), it is possible obtaining spatial resolution might provide some clarity in this matter. Experimental observations in this regime have been limited to 100 nm resolution at X-ray facilities (64). Recent theoretical work on the dynamics of quantum vortices also suggests that quantum modifications to the LLG equation should lead to slight differences in dynamics (65–67). An instrument with \sim ps or better time resolution and sub-nm or atomic scale spatial resolution remains elusive despite extensive efforts using synchrotron X-ray sources (eg. review (68)).

1.5 Goals

A general theme unites the work described in this thesis. Each component consists of the development of a new tool for the study of magnetism, and the immediate application of those tools to extract technologically pertinent information. Particular emphasis is placed on making this information quantitative. However, the spirit of this work is primarily the pursuit of physics and each component also reflects this in the eventual applications of the tools developed to specific physics questions remaining in micromagnetism. Physics questions targeted include the observation of long time scale effects in the annihilation or pinning of domain wall structures (vortices), and an attempt to build an instrument capable of the observation of dynamics on the sub nm scale.

1.5.1 Long Time-Scale Behaviour

Study of vortex annihilation using magneto-optical techniques was the first experiment on long time scale vortex effects (69). The experiment was designed to enable a better understanding of the annihilation process by measuring the properties of the annihilation energy barrier. This study grew out of the observation that vortex decay of single disks exhibiting the vortex state might take as long as minutes (70) and with that comes potential technological ramifications for using disks as memory elements. There is also the opportunity to develop robust techniques to inspect decay distributions in preparation for studying vortex annihilation at temperatures low enough to observe quantum tunneling. Transfer of the apparatus to a liquid helium or lower temperature cryostat is left as future work.

1.5.2 Detailed Interactions

Vortex annihilation is not necessarily the best transition to examine at low temperature for quantum effects. The energy barrier for annihilation is quite large, meaning that quantum effects would only manifest just as vortices might annihilate. A more promising area of investigation is examination of very small energetic transitions such those which occur when defects pin the vortex state, trapping it in a local configuration.

Pinning effects were investigated extensively using nanomechanical torsion magnetometry (71), which was developed concurrently with this work (72–75). This technique enables detection of minute magnetization shifts and hence detection of interaction of the magnetic state with nanometer scale film defects. The energy barrier for transitions in the potential wells created by these defects create thermal dynamics observable at low temperatures. With close to defect free films or artificially tailored films, energy barriers should be reducible to quantum regimes.

Moreover, besides the observation of quantum depinning of domain structures, the study of pinning effects on minute scales is of critical importance to magnetic computing applications (42–44). Therefore study of pinning effects must be pursued independent of whether it eventually leads to the study of new quantum magnetism.

1.5.3 Analytical Model of the Vortex

Through the course of this work, in performing long time scale experiments or experiments with access only to magnetization, a need for a more capable analytical model of the vortex became apparent. Out of necessity, a more detailed analytical model of the vortex state, capable of accurate estimations of hysteretic transitions, was developed (71, 76). No exotic new physics was pursued to create this model, however a novel approach to computing the micromagnetic energies in the context of deforming, and difficult to compute magnetization distributions was developed. In a pragmatic sense the model serves to elevate experimental techniques to truly quantitative tools, and serves as a first order replacement for simulation in a limited range of applications.

1.5.4 Combined Spatial and Temporal Imaging

The most ambitious portion of this work aimed to develop the ultimate instrument for the study of magneto-dynamics. The highest spatial resolution form of magnetic microscopy possible, spin polarized scanning tunneling microscopy (SP-STM), was combined with pump-probe techniques designed to add time resolution. Infrastructure to enable time-resolved measurements was established.

1.6 Organization of this Thesis

The broad reach, and disparate, though complementary, nature of techniques applied in this work demands some forethought in organizing. Each chapter has its own somewhat extensive introduction. Preceding these, this introductory chapter serves as a spring board for any reader unfamiliar with the story of micromagnetism in the last century and a general introduction to the segments of the field necessary for a broad understanding of the following chapters.

Chapter 2 describes the development of analytical models of the vortex state. This work was performed throughout this thesis, motivated by various experimental advances. Collecting all analytical work into a single chapter not only makes sense, but it serves as a very thorough introduction of the vortex state.

Chapter 3 describes the magneto-optical experiments on arrays of disks studying the long time-scale decay of vortices. This chapter incorporates analytical modeling coupled with a novel application of AC-magneto optical susceptometry. It serves as a bridge chapter, demonstrating the power of analytical modeling coupled with new, sensitive techniques.

Chapter 4 describes the detection of pinning for an individual vortex. The model in Chapter 2 is applied to great effect, turning a vortex into a scanning probe microscope for potential energy wells in magnetic films. This chapter studies low speed thermal dynamics of a vortex core that are excellent candidates for observation of quantum effects given sufficiently weak potentials.

Chapter 5 describes a project pursued throughout the thesis work: the construction of the time-resolved spin polarized STM. It was hoped that this project would produce a revolutionary instrument with profound technological implications, with the potential to unlock a new regime of observation for magneto-dynamics. This chapter describes the work on the instrument, and its progress, but also the suspected reasons it did not produce results as of yet. The chapter is not based on published, or submitted work. For this reason, and also in the hope that someone continues the project, the chapter is written more as guide for a user of the microscope than a report of results.

Chapter 6 stands alone as a distinctly disparate offshoot of the main thesis work. The chapter is not directly related to magnetism and arose sheerly from one of those moments in scientific inquiry where curiosity can derail investigation to study something entirely unexpected. Chapter 6 could have been left out, however, as this thesis is to a certain extent a scientific story, that would be to ignore the colourful unexpected twists and the very nature of scientific investigation. The content covers dynamics of amorphous materials far below the glass transition temperature. The study grew out of dynamics discovered

while investigating a candidate material for a transmission line. Extensive study was made of these dynamics and remarkably, produced what may be the first movie of the aging of an amorphous solid on the sub-nm scale.

A large number of appendices are included. These are largely designed to remove the tedious details from the main body, and are intended to aid in the reproduction of this work.

CHAPTER 2

The Magnetic Vortex¹

As understanding of magnetic domain patterns advances, increasingly compact domain structures are investigated which leads inevitably to the magnetic vortex state. Arguably, the core of the vortex state is the most compact domain structure possible in a traditional micromagnetic element. It features interesting phenomenology based on its topological stability, its high energy density, and the tendency for the core to behave as if it is an unruly particle. Vortices arise in a wide range of magnetic elements, but a disk shaped magnetic film is the system that matches best with the symmetry of the vortex state. Therefore disks make attractive candidates for vortex state devices, and, perhaps more importantly, provide a prototypical environment to study vortex behaviour.

This chapter describes the development of an analytic model of a vortex in a disk that permits quantitative computations of magnetic vortex pinning effects. The chapter introduces the vortex state in a disk, including a detailed qualitative description of the evolution with field. Subsequently, a summary of work on modeling the vortex state with applied field is included to familiarize the reader with the historical approaches to this problem and the issues remaining with such models. This establishes the components necessary to create a two parameter, piecewise model that accurately describes the changes in vortex state evolution in the presence of pinning. This model serves as a powerful tool in the study of vortex properties by providing a method of extracting quantitative information about energetic pinning interactions from magnetization measurements. Additionally, the model can be solved on a time scale much faster than simulation, and it bolsters the intuitive understanding of the vortex state.

¹A version of this chapter has been prepared for publication (76).

2.1 The Vortex State

In zero field, the vortex state in a disk represents the ground state configuration (77–79) for a wide variety of disk aspect ratios (80).

2.1.1 Anatomy

The vortex state arises in a disk as a consequence of dipolar interactions (demagnetization energy). Over most of the disk, a circularly symmetric in-plane magnetization distribution maintains magnetization tangential to the disk boundary and reduces dipolar energy. This necessitates a higher exchange energy relative to the uniformly magnetized state and results in an out-of-plane magnetized core at the disk center with high energy density (Fig. 2.1).

The vortex state can be thought of as two components: the in-plane magnetization outside the core and the core itself. The core itself is equivalent to a zero dimensional domain wall. The in-plane magnetized region is referred to here as the skirt. Two parameters describe symmetry breaking in the vortex state: the direction of the circulation of the in-plane magnetization or the chirality of the vortex, and the direction of the magnetization of the core, or the polarity of the vortex.

In principle the polarity and chirality of a particular vortex are independent. However more recent work indicates that the two are coupled by the Dzyaloshinskii-Moriya mechanism in real disks (81, 82). This effect relates the polarity of the core to the chirality through edge interactions dependent on the edge profile. This results in a preferred polarity for a given chirality.

2.1.2 Technological Importance

Interest in magnetic vortices (77–79) in thin disks has grown dramatically over the past two decades, as these are fundamental physical systems with direct applications to technology (45). Topological structures such as vortices are stable, manipulable objects that show promise as logic elements or storage media in spintronics applications. Vortex containing disks have even been considered for cancer treatments (83) involving the selective chemical bonding of disks to cancer cells, and subsequent use of AC fields to physically actuate the disks, damaging the cell membranes.

While the geometry of a disk is optimal for the vortex state, vortices appear in many other micromagnetic systems. Particularly pertinent to technology is the existence of vortex domain walls in wires. For particular aspect ratios of ferromagnetic wires, oppositely

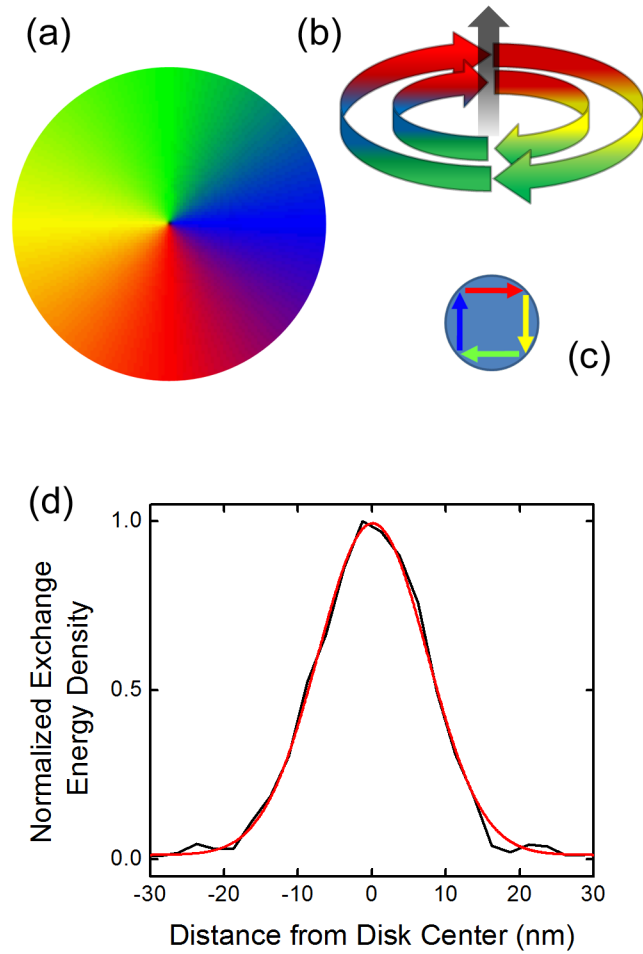


Figure 2.1: The vortex state consists of a circulating in-plane magnetization distribution surrounding an out-of-plane core. A simulation snapshot of a vortex in a disk is shown (a). It uses a colour encoding scheme to depict the direction of in-plane component of magnetization, with black used for out-of-plane magnetization. A cartoon of the vortex state (b) shows a vortex with clock-wise chirality, and positive polarity. A colour wheel (c) describes the mapping of colour to magnetization direction. The core of the vortex state is particularly interesting. A computation of the exchange energy density in profile across a core, computed from a simulation, is shown in (d). The high energy density in the core enhances local interactions like pinning.

magnetized domains will be separated by vortex domain walls rather than transverse (Néel)-like or Bloch-like walls (84). This leads to the opportunity of using the high exchange energy density of the vortex core in wire based devices (45).

The interaction of vortex cores or domain walls with film inhomogeneities has been a topic of significant recent interest. Geometric defects or magnetic impurities can increase or decrease the energetic cost of the topological structure (85), creating preferential locations or altering the magnetization distribution. In the disk system, direct observations of vortex state pinning have been made with Lorentz microscopy (86) while the effect on vortex dynamics has been observed with time-resolved magneto-optical Kerr effect microscopy (70, 87–91) and electronically (92).

The thin magnetically soft (low coercivity) disk, the prototypical system containing a vortex, has therefore become an extensively investigated system. Properties studied include structure (93–95), dynamical modes (87, 96, 97), annihilation (69, 98), and creation (73, 98–100). As each aspect of vortex physics is probed experimentally, and considered for technological applications, theoretical understanding via simulation and modeling is also advanced. Modeling is particularly important in the case of the thin ferromagnetic disk as it presents a well-defined system amenable to description by an analytical approach.

2.1.3 Quasi-static Behaviour: Evolution with Field

Usually, the magnetism community is focused on dynamical properties of magnetic systems, and quasi-static behaviour is regarded as less interesting. Consequently the vortex state is usually considered under the action of transient magnetic fields, or spin polarized currents that excite dynamical modes. However, evolution of the vortex state under applied field still presents a complex situation that is not fully understood analytically.

The changes induced by the applied field cause the section of the disk with magnetization aligned with the field to grow. For a thin disk, out-of-plane fields have a minimal effect. The core magnetization will grow or shrink slightly with the application of large (~ 10 kA/m) fields but this can almost always be neglected. In-plane fields will have a much larger effect. Under an in-plane field, it becomes energetically favourable for the section of the skirt aligned with the field to grow in size². The expansion can occur in two ways: the entire magnetization distribution may translate orthogonal to the field to create a larger section aligned with the field, or the region favored by the field direction may simply expand within the disk disrupting the circular symmetry of the magnetization distribution about the core

²Since the vortex is radially symmetric, there is no difference in which direction an in-plane field is applied unless the disk is composed of a material with crystalline anisotropy. Since this body of work considers polycrystalline permalloy, crystalline anisotropy may be neglected.

position. Both have energetic costs and will contribute to the increasing magnetization of the disk.

The competing exchange, dipolar, and field energies make the convolution of translation and distortion of the magnetization quite difficult to solve exactly. The complete physical picture of the vortex state under an applied field involves translation and a continuous deformation of the magnetization distribution from the core all the way out to the edge of the disk. The core and the boundary each have energetic interactions that reinforce circular symmetry locally. Near the edge, minimization of edge demagnetization energy favours the preservation of the tangential boundary condition for the magnetization distribution. Near the core, distortions of the magnetization distribution result in volume demagnetization energy as well as increased exchange energy³.

The bulk of the deformation can be considered as a widening of the section of the magnetization distribution aligned with the field. However, the maintenance of the tangential boundary condition means that this widening is more prominent near the center of the disk. This leads to curvature in the deformation, and also to core deflection. Conversely, the deformation of the magnetization distribution near the edges of the disk effectively boosts the component of the deflection that appears as rigid translation.

Examining a numerically simulated vortex state under an increasing field allows identification of each of these effects. The deformation can be visualized by considering contours of constant magnetization (eg. $|m_y| = 1$), which bend away from radial lines as the magnetization deforms from the circularly symmetric vortex state. Choosing two snapshots from the simulation at different fields and aligning the contours in various arrangements reveals deflection over the entire disk, true translation that induces edge demagnetization charges, and additional deflection of contours near the disk edge that contributes to an effective translation like shift (Fig. 2.2). Approximately aligning the contours near the edge of the disk demonstrates that the tangential boundary condition is violated and that true translation does occur. Plotting the two contour snapshots such that the locations of the vortex cores overlap reveals that gentle bending of the contours occurs over the entire disk from the core out to the edge, while more rapid bending takes place close to the disk edge. The gentle bending can be interpreted as the field induced enlargement of the aligned magnetization. The steeper bending effectively results in an additional translation of each part of the distribution inside the region of steeper bending. Note that hereafter discussion of translation includes both true translation, violating the tangential boundary condition, and effective translation due to strong deformation of the magnetization close to the edge of the disk.

³The overall exchange energy of the vortex state drops as the section aligned with the field, which has very low exchange energy density, grows. However, warping of the circular symmetry in the rest of the skirt represents an energetic cost.

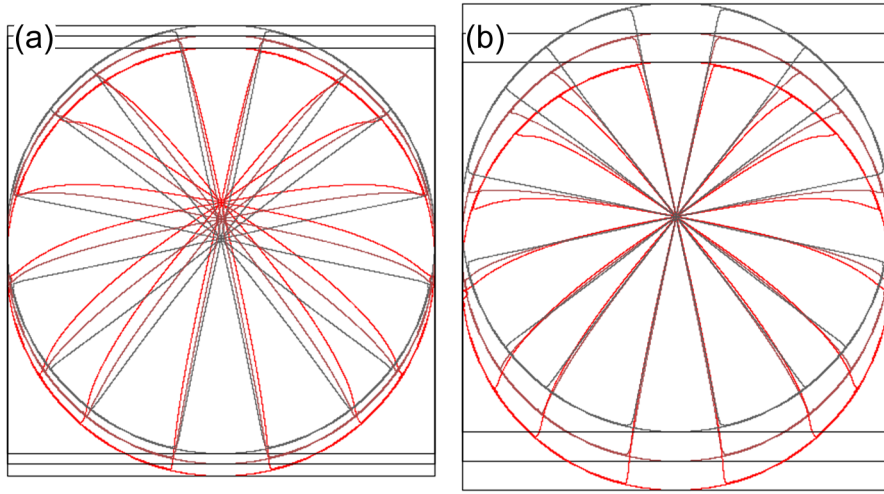


Figure 2.2: Contours of constant M_y magnetization show the presence of translation and deformation in the magnetization distribution of a disk under an applied field. Contours are shown for $|M_y/M_S| = 0.2, 0.4, 0.6,$ and 0.8 computed from three simulation snapshots under different fields (blue lowest, red highest) for a $1 \mu\text{m}$ diameter, 40 nm thick disk. In panel (a), the snapshots are overlapped such that the contour intersection with the disk edge approximately aligns for each snapshot. In order to do so, the disk boundaries must translate with respect to each other, demonstrating that true translation occurs. In panel (b), the snapshots are aligned such that the core position overlaps. The contours show steadily growing relative deflection throughout the entire disk, and a particularly strong increase in deflection near the disk edge.

In the absence of pinning, translation and deformation both increase monotonically under the influence of field. The entire distribution shifts, but the distribution is not rigid, and the core displaces an additional amount, ahead of the translation. However, the presence of a pinning site interaction with the vortex core means that the core position is no longer dictated solely by torques exerted on the core by the surrounding in-plane magnetization distribution and that there are preferential locations for the core in the disk. When the core is in a preferential site, the energy cost of further core displacement is increased and this necessarily influences the nature of the deformation.

With a pinned core, under increasing field, the magnetization of the disk will continue to grow despite the pinning. This results in the magnetic moment away from the core increasing preferentially, favoring the translational mode of displacement because it results in a larger magnetic moment near the edge of the disk. Simultaneously, the displacement of the core due to distortion decreases (relative to the translation), maintaining the core in the preferential location. This allows some of the circular symmetry of the initial magnetization

distribution to be restored.

The observation of the restoration of circular symmetry in micromagnetic simulations incorporating pinning verifies the applicability of the combined translation and deformation picture. Visualization is again accomplished by examining the contours of constant magnetization (Fig. 2.3). The widening of the section magnetized parallel to the field manifests as shifts in the angles of the contour lines, and an introduction of curvature. Near the center of the disk, the contours deflect only slightly, however this gentle deflection extends all the way out to the edge of the disk, showing a significant deformation-based core displacement. Near the edge of the disk, more extreme bending occurs. This is directly associated with the maintenance of the boundary condition and is significant in the reduction of the energetic cost of translation. Examination of the gentle bending near the centre reveals that the contours exhibit a deflection with a non-monotonic evolution as the vortex traverses the pinning site (Fig. 2.3 b). During pinning, the contours begin to return to the original (zero field) angles of deflection, partially restoring the circular symmetry of the magnetization distribution. The more extreme deformation near the disk edge maintains its growth, indicating translation continues during this time.

The change in deformation represents a significant energetic influence on the core. The flexible nature of the magnetization distribution acts as a combined dipole-exchange spring. The spring can absorb energy, allowing a core to jump ahead to a preferential site. Similarly, stored energy lowers as the core is trapped in the pinning site, permitting the core to stay in the site longer. This has a significant effect on observed hysteresis in pinning sites, as well as on computation of depinning energy barriers. This is the effect that the model developed in this chapter aims to describe.

2.1.4 Quasi-static Behaviour: Annihilation and Creation of the Vortex State

It is worth noting that, as a topological defect, the vortex core undergoes quite interesting transitions when the disk jumps from the vortex state to an approximately uniformly magnetized state and vice versa. Overall, this can be summed up in the statement: the winding number, or topological charge, of the vortex is conserved in annihilation and creation events (101). However this fails to convey the richness of the transitions.

Starting with a vortex ground state, the annihilation process occurs when the vortex core is pushed sufficiently close to the edge of the disk, that it hops out, and it annihilates (2.4). The annihilation process is examined in more detail in Chapter 3. In the context of winding number conservation, on annihilation of the vortex, the disk jumps to a quasi-single-domain state (QSD), but two defects are generated on the edge of the disk in the annihilation. Each

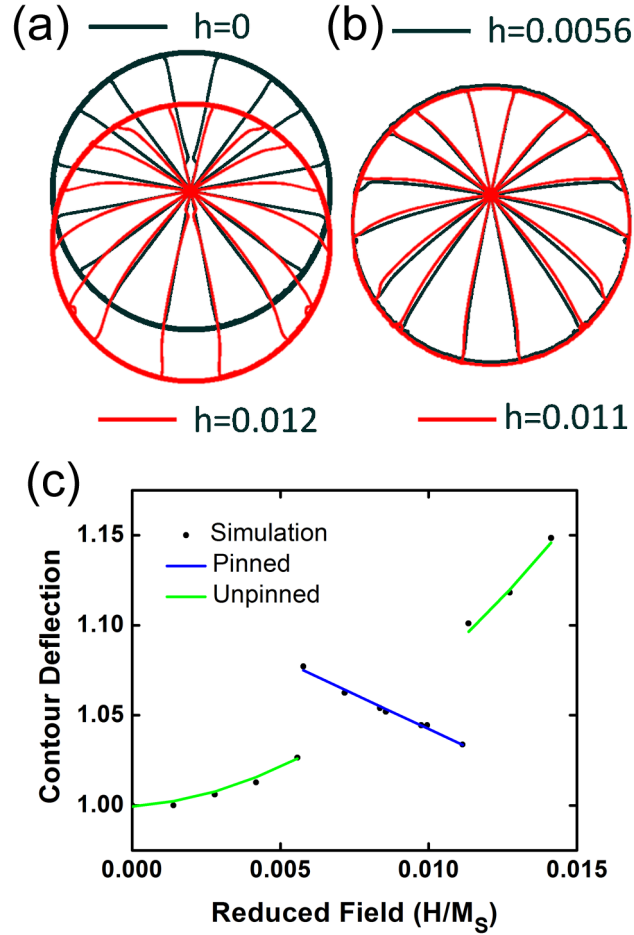


Figure 2.3: Contours of constant M_y magnetization ($|M_y| = 0.2, 0.4, 0.6,$ and 0.8) evolve non-monotonically during pinning. In panel a and b snapshots of the contours are shown from a simulation ($2R = 1 \mu\text{m}$ diameter, 40 nm thick disk) where vortex core is pushed through a single pinning site displaced by $0.22R$ from the disk centre. Snapshots with the core below and above the pinning site (a) show the same contour evolution as shown in Fig. 2.2. By contrast, comparing contour evolution during pinning reveals that the deflection actually decreases during pinning (b). In both panels the blue contour indicates the snapshot taken at a lower field. More quantitative analysis can be made by measuring the contour deflection near the vortex core. Specifically, one can measure the angle, away from the vertical, of lines drawn from the core to the intersection of the contours with a circle of radius $R/2$ centred on the core. Measuring the relative change of these angles for various fields, and averaging over contours in the upper right quadrant of the disk yields the plot in (c). When the core is pinned, the measured angles evolve in the opposite sense when compared to the unpinned evolution.

defect carries a ‘charge’ of $1/2$ where the vortex had a charge of 1. Physically, the defects provide a reduction in the demagnetization energy of the disk.

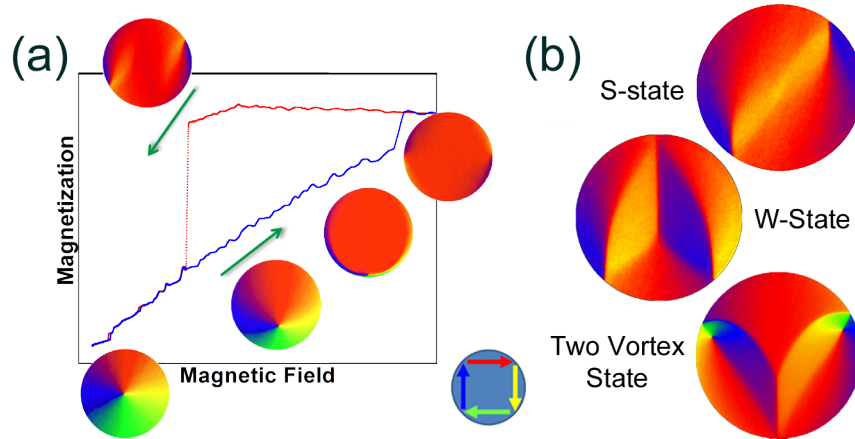


Figure 2.4: The rich switching behaviour and bistability of the vortex state creates a complex system that is challenging to study. Panel (a) shows an experimental measurement of a hysteresis loop for a single disk. Snapshots from a simulated hysteresis loop are included around the loop, showing the evolution from the vortex state to annihilation and the quasi-single domain state, and back again. The annihilation process proceeds similarly for all vortex states, however the creation process shows significant variability. Many intermediate (buckled) states can exist. In (b), a selected set of buckled states are shown along with the colloquial descriptive names of each buckled state.

In the inverse process, vortices are created in the disk. Whereas in the annihilation, one can consider all annihilation events to proceed the same way, with a vortex core escaping or annihilating near the edge of the disk, the creation process is much more complex. Simulations reveal that the defects on the edge play a strong role, often creating multiple vortices in an unstable configuration that eventually decays to a single vortex. The creation process is complicated by buckling events that occur as field is reduced. Intermediate domain patterns develop in the disk tied to the defects at the edge of the disk. Each buckling pattern undergoes a different subset of transitions back to the vortex state. The complexity of the creation process makes it challenging to study.

Any interested reader is directed to the work of (101) where the conservation rules are worked out for the case of wires and disks and to the work of Nori (102) where buckling states and the creation process are discussed.

2.1.5 Dynamical Behaviour

The dynamical response of the vortex state is rich. A wide variety of spin wave modes may be excited and a strong dependence on core polarity and vortex state chirality dictates what modes can be excited. The litany of dynamical modes including edge modes (103), core modes (70), radial modes (104), multi-vortex coupled modes (105), and multi-disk coupled modes (106) is beyond the scope of this work. References included here are in no way exhaustive, but may be helpful in starting a literature search on detailed vortex dynamics.

Here, only one vortex mode is of specific interest: the low frequency translational mode of the core known as the gyrotropic mode. In this mode, the vortex is displaced from its equilibrium position (at the centre in the case of zero field) and then relaxes back to the centre of the disk. As a consequence of the precessional term in the LLG equation, the relaxation will result in an gyroscopic force orthogonal to the direction of the core (107). This will result in a circular orbit for the core, which decays over time as the energy of the mode dissipates. Description of this mode is commonly accomplished through the collective coordinates approach (107–110), where the core coordinates are solved for as if the core is a particle in a potential. Using this approach, it may be shown that the gyrotropic mode frequency is $f_o = \kappa/2\pi G$ where $G = 2\pi LM_S/\gamma_o$ with $\gamma_o = 1.76 \times 10^{11} s^{-1} T^{-1}$, and $dE_{tot}/dr = \kappa r$ (108). The form of this solution, and appearance of the core's orbit in simulation promote the intuitive understanding of the vortex core as a separate particle. However it is important to remember that the core is part of the overall vortex state, and couples strongly to the skirt.

2.2 Historical Development of Models of the Vortex State

The solution for the minimum energy magnetization distribution of a cylindrically symmetric element was a challenging problem for a long period of time (eg. (111–113)). For thin magnetic disks, the vortex state ansatz was first developed by Aharoni in 1990 (93). Further work by Usov and Peschany (94) determined an exchange optimized functional form of the core magnetization profile. Good agreement between this model and simulation (114), as well as experimental observation (95), was found. This work considered the vortex ground state, at zero field. Computation of the evolution of the state with field presents a more challenging problem.

In constructing a simplified model that captures the field evolution, some assumptions must be made. The most successful models treat only one of the modes of core deflection, either

translation or deformation, and neglect the other. Thus far attempts to include both have resulted in models that make unphysical predictions (115).

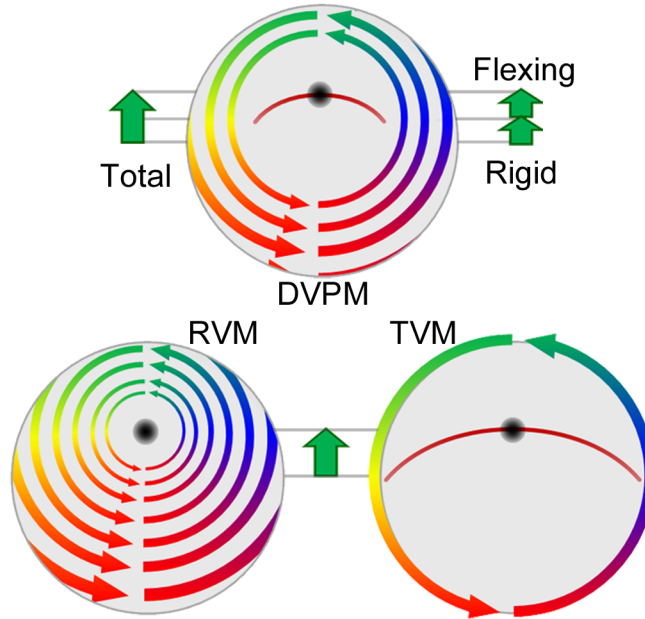


Figure 2.5: Schematic representations of the three vortex models discussed in this work. The Rigid Vortex Model (RVM) considers only rigid translation of the magnetization distribution on displacement of the core. The Two Vortex Model (TVM) assumes no change in the distribution at the boundary of the disk. The Deformable Vortex Pinning Model (DVPM) uses a combination of the RVM and TVM to provide a better energetic description of core displacement.

The translation has been addressed with the development of the Rigid Vortex Model (RVM) which is considered to originate with Usov and Peschanny's work. Subsequent work (116, 117) considered the displacement of the core with field, and annihilation field, using a model that rigidly translated the magnetization distribution developed by Usov and Peschany (Figure 2.5). This is known as the Rigid Vortex Model (RVM). Recent extensions of the RVM include higher order versions developed to describe the susceptibility of the displaced vortex analytically (69). Concurrently, models approximating the deformation of the magnetization distribution were developed (115, 118). This class of model is equivalent to the influence on the magnetization distribution of a second vortex moving from infinity to the edge of the disk, and is called the Two Vortex Model (TVM). Versions of this model have been applied to calculating the stability of the vortex state in a disk with moderate success (115, 118) and, with greater success, to predict frequencies of dynamic modes (108, 119, 120). The most successful version of this model is one that maintains a perfect tangential boundary

condition, prohibiting any translation of the magnetization distribution and considering only deformation. The other version of this model permits side demagnetization charges to develop while also displaying flexing. However solving this version of the TVM reveals that it incorrectly computes the energy, and predicts that, independent of disk size, a vortex will always annihilate at a displacement of $R/2$ where R is the disk radius.

2.2.1 Motivation for a Two Parameter Model

Both the RVM and TVM link the computed model magnetization directly to the vortex core displacement in the disk using only a single parameter⁴. So, although pinning may be added to the RVM (121), inherent errors are expected. This limitation renders the models incapable of computing, or even qualitatively describing the non-monotonic evolution of the deformation discussed previously. However a combination of these two models may be constructed, modeled after the observed magnetization distribution and incorporating both rigid translation and flexible deformation (Fig. 2.5). The following sections introduce the RVM and TVM in detail, and then, out of these two models construct a two parameter model that is capable of providing a good energetic description of pinning.

2.3 The Rigid Vortex Model

The first model necessary for the construction of a two parameter model that captures the changes during pinning is the Rigid Vortex Model (RVM).

2.3.1 Core Profile and Diameter

Work using the rigid approximation is generally considered to have started with the determination of the functional form of the core magnetization profile. The first attempt at this was by Aharoni (93), where various functional forms for the core profile were assumed and the resulting energies computed. Subsequently, Usov and Peschany improved on this using a variational approach to compute the exchange energy minimized core profile (94). The result was a piecewise distribution. This may be written in cylindrical coordinates as:

⁴The TVM uses a second parameter to describe distortions of the core profile under deflection, however this parameter does not have a significant influence on the overall disk magnetization or core displacement. It is therefore unsuitable for describing the influence of the skirt magnetization on the core.

$$\begin{aligned}
m_r &= 0, \\
m_\phi &= \begin{cases} \frac{2r_c r}{r^2 + r_c^2}, & \text{if } r \leq r_c \\ 1, & \text{if } r > r_c \end{cases} \\
m_z &= \begin{cases} \pm \frac{(r^2 - r_c^2)}{r^2 + r_c^2}, & \text{if } r \leq r_c \\ 0, & \text{if } r > r_c \end{cases}
\end{aligned} \tag{2.1}$$

where $\mathbf{m}(\mathbf{r}) = \mathbf{M}(\mathbf{r})/M_S = (\mathbf{m}_r(\mathbf{r}), \mathbf{m}_\phi(\mathbf{r}), \mathbf{m}_z(\mathbf{r}))$ is the the normalized magnetization distribution, r_c is a parameter describing the width of the vortex core, and (r, ϕ, z) are the usual cylindrical coordinates. The angle (θ) of the magnetization away from the vertical axis, z , out of the disk plane can be used for convenience. So that $m_\phi(\mathbf{r}) = \sin(\theta(\mathbf{r})) = 2r_c r / (r^2 + r_c^2)$ can be used, and $\mathbf{m}_z = \cos(\theta(\mathbf{r}))$. The angle is then a function of the radius only, for the vortex core centred in the disk. The computed optimum form yields a value for r_c dependent on the thickness of the disk. This may be written:

$$r_c = \left(\frac{R_o^2 L}{6k_F} \right), \tag{2.2}$$

where $R_o = \sqrt{2A/(\mu_0 M_S^2)}$ is the exchange length of the material, with A the exchange stiffness constant of the material, and L is the thickness of the disk, and $k_F \approx 0.0412$ is a geometric factor arising from the demagnetization energy of the core. It is important to note, that, while this parameter r_c is directly indicative of the core size, it is perhaps not what one would colloquially think of as width of the core. Interactions of the core with defects are dependent on the energy density of the core, which follows a similar profile to the z component of the magnetization. Therefore the effective radius will be comparable to the standard deviation, or half width half max of the exchange energy distribution, which is distinctly smaller than this r_c . For example $r_c \sim 17$ nm for the simulated disk from which Fig. 2.1 was extracted, and which has an exchange energy distribution standard deviation of 7.3 nm.

2.3.2 Vortex Displacement

The vortex displacement with field is derived for the RVM by considering the zero field vortex magnetization distribution ($93, 94$) to be immutable, and then translating that distribution relative to the physical boundary of the disk (Fig. 2.5). Changes in the energy and magnetization simply arise from the shift of the distribution with respect to the disk boundary, which serves as the limits of integration for the integrals for the various energies

in the model. Since the model is rigid, the contribution of the core itself does not change. Additionally the rigidity means that the translation may be described entirely with respect to the displacement of the vortex core. It is useful to express the energy relative to the zero field state.

Below, the exchange, demagnetization/dipolar, and external field energies are quoted for the RVM. Recall that this work treats magnetic devices composed of permalloy and considers the material to have zero crystalline anisotropy. For clarity with respect to subsequent sections where multiple vortex displacement parameters are used, in the formulas for the RVM the parameter b is used as $b = s = \Delta r/R$. The exchange energy, $E_{Ex} = A \int d^3\mathbf{r} \sum_i (\nabla m_i)^2$, may be computed following the work of Guslienko et al. (116, 117) continuing to use the angle of the magnetization away from the z axis, θ .

$$\frac{E_{Ex}(s)}{\mu_0 M_S^2 V} = \frac{R_o^2}{R^2} \int d^2\mathbf{r} \left[\left(\frac{d\theta}{dr} \right)^2 + \frac{\sin^2 \theta}{r^2} \right] = \frac{E_{Ex}(0)}{\mu_0 M_S^2 V} + \frac{R_o^2}{R^2} \ln(1 - b^2) \approx E_{Ex}(0) - \frac{R_o^2}{R^2} \frac{b^2}{2}, \quad (2.3)$$

Only the change in energy from the equilibrium $s = b = 0$ is of importance, therefore the constant term is dropped. The only contribution to the demagnetization energy comes from the edges of the disk. The effective charge distribution, $\sigma(\mathbf{r})$ may be computed at the edge by taking the dot product of the magnetization with the boundary.

$$\sigma(\mathbf{r}) = -\mu_0 M_S \frac{b \sin(\phi)}{\sqrt{1 + b^2 - 2b \cos(\phi)}}, \quad (2.4)$$

The demagnetization energy follows from this as the self energy of the charge distribution, E_d .

$$\frac{E_d(b)}{\mu_0 M_S^2 V} = \frac{1}{2} \int dS_1 \int dS_2 \frac{\sigma(\phi_1) \sigma(\phi_2)}{|\mathbf{r}_1 - \mathbf{r}_2|} \approx \frac{F_c(L, R)}{2} b^2, \quad (2.5)$$

where $F_c(L, R)$ is the average radial demagnetization factor corrected for the susceptibility of the material for a uniformly magnetized disk which can be computed in a variety of ways (35-37, 122-124).

Last, the external field energy is computed by the product of the field with the magnetization. The net magnetization is found by integrating the component of the magnetization parallel to the field (orthogonal to the core displacement) over the entire disk. The magnetization is computed to third order here, rather than stopping at the first order as in previous works (116). This minimal extension of the model enables the RVM to provide a good prediction of the susceptibility of the vortex state as a function of field.

$$\frac{E_h(b)}{\mu_0 M_S^2 V} = - \int_V d^3 \mathbf{r} \mathbf{m}(\mathbf{r}) \cdot \mathbf{h} \approx (-b + \frac{b^3}{8})h, \quad (2.6)$$

Here, a reduced field $h = H/M_S$ is used and all other symbols are as defined before.

With the energetic components for the RVM computed above in terms of the vortex displacement, the total normalized total energy for the 3rd order RVM (69) of a disk with a radius R and thickness L as a function of the reduced field h can be written as

$$\frac{E_{tot}(b)}{\mu_0 M_S^2 V} = \frac{\beta}{2} b^2 - h(b - \frac{b^3}{8}), \quad (2.7)$$

where the normalized core displacement $s = \Delta r/R$ is equal to b , $\beta = F_c(L, R) - R_o^2/R^2$ is a constant describing the demagnetization energy and exchange energy with $F_c(L, R)$ representing the susceptibility-corrected demagnetization factor computed for the uniformly magnetized disk (123), and R_o is as before. The energy is normalized by $\mu_0 M_S^2 V$ where V is the disk volume.

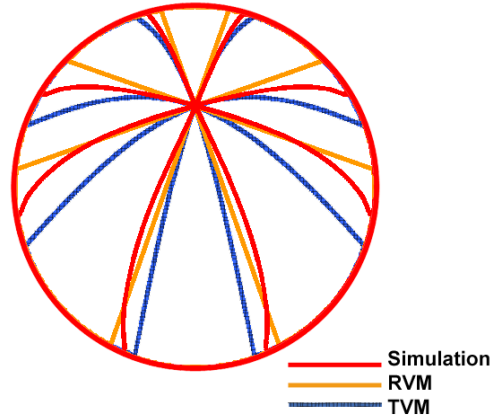


Figure 2.6: Contours of constant magnetization aid visualization of the magnetization distributions predicted for a displaced vortex core by the RVM and the TVM with no side charges. Here the contours for $|M_y/M_S| = 0.4$ and 0.8 are shown, compared against a simulation for a $1 \mu\text{m}$ diameter disk 40 nm thick. Both the RVM and TVM show disagreements with the simulation. In particular the TVM contours intersect the edge lagging the simulation, while the RVM contours lead by a similar amount. This demonstrates the over suppression of edge demagnetization charges in the TVM. Critically, the TVM contours lag behind the simulation everywhere, indicating an underestimate of the total magnetic moment. By contrast the RVM contours lead and lag the simulation contours, indicating a smaller error in the computed total magnetic moment.

Solving the model permits calculation of the vortex displacement as a function of field,

$$b_o(h) = \left(-4\beta + 2\sqrt{4\beta^2 + 6h^2} \right) / 3h. \quad (2.8)$$

From $b_o(h)$ the magnetization as a function of field may also be computed as $m_o(h) = M_o(h)/M_S = b_o - b_o^3/8$. Removing the third order term in the magnetization, and consequently the external field energy contributing to $b_o(h)$, reduces the model to the second order RVM (116, 117) with $m_o(h) = b_o(h) = h/\beta$. The gyrotropic mode constant for the RVM, κ is equal to β .

2.3.3 Susceptibility Correction

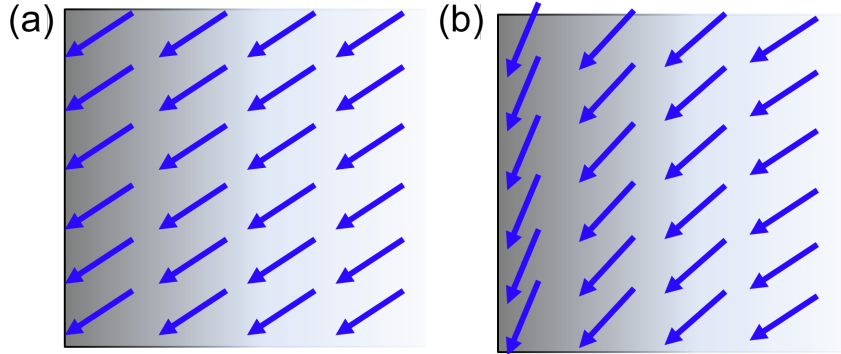


Figure 2.7: The susceptibility correction considers the effect of flexing of the magnetization distribution in the immediate vicinity of a boundary to avoid edge demagnetization charges. The effect is to distribute the charges into a larger volume near the edge, reducing the total self energy of the demagnetization charge distribution.

The incorporation of the susceptibility correction to the demagnetization factor, the so called μ^* correction (7, 33), is critical to the success of the RVM in application to a disk composed of a soft magnetic material, but has not previously been applied. Any inspection of displaced vortex magnetization distributions in simulated disks composed of permalloy or a similar soft material reveals the rigid assumption is flawed (Figure 2.6). The magnetic moments near the boundary of the disk will always rotate to a certain degree to partially maintain a tangential boundary condition and lower the total demagnetization energy by redistributing uncompensated edge dipoles into the volume (Fig. 2.7 a and b). In computation of the energy of uniformly magnetized particles, it is possible to account the net reduction by solving for the magnetic potential at the disk boundary taking into account a discontinuity in the rotational susceptibility of the material inside and outside of the disk.

The correction is applied only to the energy and does not explicitly compute the deformation of the magnetization. This correction is known as the μ^* correction (7, 33), and results in a constant factor applied to reduce the demagnetization energy.

The susceptibility correction was introduced to account for the overestimate of the demagnetization factor computed for a uniformly magnetized particle assuming a rigid magnetization. In reality, the magnetization in the particle will deform away from the uniform state, paying a small energy price for introducing volume demagnetization charges but causing a net energetic reduction by decreasing the edge demagnetization energy (Fig. 2.7 a and b). The cause of the net reduction, increasing separation of like effective demagnetization charges on either side of the particle, is made clear by equations 1.7 and 2.5. It is this reduction due to flexing that the correction takes into account.

In an ideal (permalloy-like) material, the susceptibility is considered as infinite. Typically low coercivity ferromagnets can be treated as having infinite susceptibility (>100). For permalloy, the maximum possible error in the demagnetization factor resulting from this treatment can be estimated as $< 0.8\%$ by considering the disk to have effective susceptibility equal to that of iron (~ 49) (7). With a value for the susceptibility, the corrected demagnetization factor may be computed (123), meaning that the correction gives back a fixed demagnetization factor for a known disk size. Therefore, the correction does not introduce an additional fit parameter. The logic of applying the correction to a rigid vortex distribution is borne out by the significant improvement in the performance of the RVM in predicting the vortex state magnetization and the core position (Fig. 2.8). The improvement in the performance of the RVM stemming from the susceptibility correction makes it clear that the correction parameterizes immediate bending of the magnetization near the edge of the disk, as well as deflection through the volume of the disk. This is what allows the corrected RVM to provide a good estimate of both net magnetization and total vortex core displacement despite treating only translation.

2.4 The Two Vortex Model

The TVM is derived by setting a boundary condition and computing the magnetization distribution that minimizes the exchange energy for a given vortex core displacement (118, 125). The model is solved by the computation magnetization distribution that exactly minimizes the exchange energy, while ignoring other contributions and maintaining boundary conditions. This approach was developed by Metlov (125), and applied to the problem of a magnetic disk by Metlov and Guslienko (115, 118).

The approach applied by Metlov is based on the observation that, for small particles, the dominant energetic contribution by density is the exchange energy. In real space, to compute

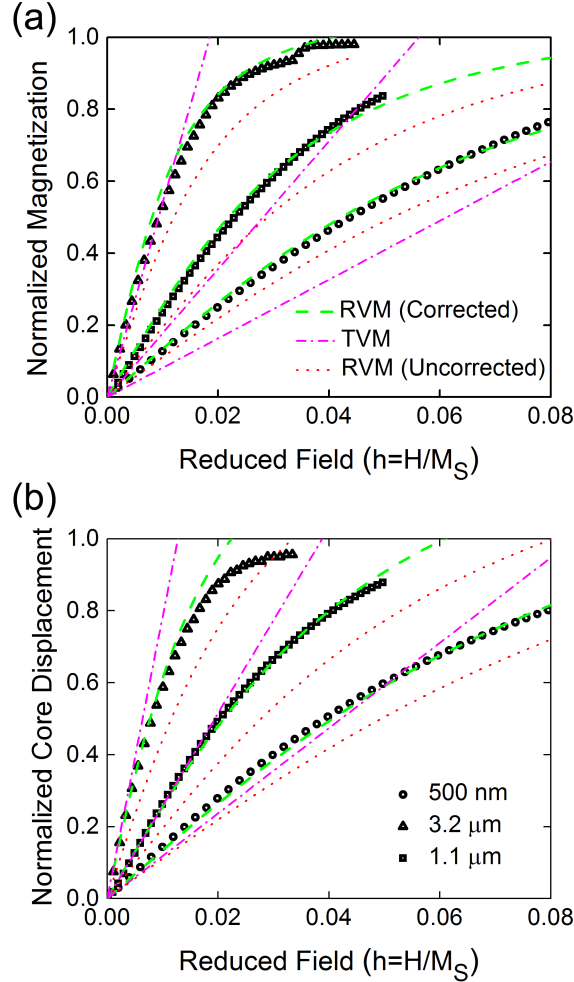


Figure 2.8: The RVM provides good predictions for the magnetization and vortex displacement referenced against micromagnetic simulation. Key to the performance of the RVM is the susceptibility correction to the demagnetization factor. This correction takes into account the flexing of the magnetization distribution near the edge to redistribute uncompensated dipoles arising at the edge into a larger volume, decreasing the demagnetization energy. Comparisons of the computed $m_o(h)$ (a) and $s_o(h)$ ($b_o(h)$ or $a_o(h)/2$) (b) to simulation for disks 500 nm, 1 μm, and 3.2 μm in diameter and 40 nm thick show that the susceptibility correction significantly improves RVM performance and that the TVM provides a reasonable vortex displacement estimate, but a poor prediction of magnetization.

the magnetization distribution, one then seeks to minimize the exchange energy rather than the total energy. Now, the problem is less intimidating, but an additional insight may enable a broad set of solutions to be developed rapidly. For thin magnetic film, sufficiently thin ($\sim 4R_o$) such that the magnetization distribution exhibits no 3D behaviour, the magnetization may be considered a 2D vector field. In this case, the magnetization distribution may be represented in the complex plane as a function $f(z)$ where $z = x + iy$ and $m_x = \Re(2f(z)/(1 + |f(z)|^2))$, $m_y = \Im(2f(z)/(1 + |f(z)|^2))$, and $m_z = \frac{1 - |f(z)|^2}{1 + |f(z)|^2}$. For instance, the piecewise zero field vortex core can be expressed using $g(z) = i(z/c)^{|\nu|}$ where $c = r_c/R$ to generate the functional form of $f(z)$ as:

$$f(z) = \begin{cases} g(z), & \text{if } |z| \leq c \\ \frac{g(z)}{|g(z)|}, & \text{if } |z| > c \end{cases}. \quad (2.9)$$

where ν is the vorticity (winding number, or topological charge) of the vortex. Given an initial distribution, such as Usov and Peschany's core profile, it may be shown that additional solutions providing a minimum in exchange energy may be generated from the initial solution using conformal transformations (125). The transformation $o(z)$ can be applied as $o(g(z))$ to generate the new $g(z)$ describing the distorted magnetization distribution. The only stipulation is that the conformal transformation must be an analytic function.

The broad choice of possible conformal transformations permits the description deformation of the vortex state magnetization under a variety of conditions. An obvious example is the use of a function $o(z) = z - a$ gives rise to the RVM. More complex transformations, chosen for maintenance of various boundary conditions, have been used to generate the class of models that describe the evolution of the displaced vortex state known collectively as the Two Vortex Model (TVM). The construction of the TVM is summarized in the following. More detail may be found in the works of Metlov and Guslienko (115, 118).

2.4.1 The Two Vortex Two

Two models have been developed using Metlov's conformal transformation approach applied to Usov and Peschany's zero field solution. The two models differ in the nature of the boundary conditions maintained in the transformations used. The more successful version of the model exactly maintains the tangential edge magnetization, resulting in no side demagnetization charges. The other flavour of TVM maintains only $d\mathbf{m}/d\mathbf{n} = 0$ along the boundary, permitting side charges to develop.

Implicit in the construction of the *no* side charges model is the very strong influence of demagnetization energy. Contrary to this, the side charge permitting version largely ignores demagnetization energy in determining the magnetization distribution. Note that the boundary condition imposed in the side charge model is contradictory in spirit with the susceptibility correction. It specifically prohibits additional flexing near the disk boundary, strongly favouring exchange minimization. This may be the reason that the side charge permitting model, despite appearing as the most physically accurate model, produces unphysical results such as predicting that the vortex core will always become unstable at displacements larger than $R/2$. The side charge version is generally not used in computation.

The no side charges version of the model can be generated using equation 2.9 with a function:

$$g(z) = \frac{1}{c} \left(iz + \frac{1}{2}(a - \bar{a}z^2) \right), \quad (2.10)$$

where the parameter a is related to the normalized vortex displacement as $s = \delta r/R = a/2$ for small displacements ⁵ and $c = r_c/R$. Solving for zeros of this function (points at which $m_z = 1$), yields two solutions: one inside the disk, and one outside. The outside point is interpreted as the centre of a virtual vortex, and the deformation of the magnetization distribution for a displaced core is considered to be the influence of the magnetization distribution of this second vortex moving in towards the edge of the disk from infinity. This interpretation gives the TVM models their name.

2.4.2 Vortex Displacement

Here the no side charges version of the model (108, 118) is applied and the magnetization is held tangential to the disk edge. Contributions from the core are neglected here, which is a reasonable approximation for disks with a radius significantly larger than the core radius (118). As with the RVM, solving for the core displacement requires computation of the exchange, demagnetization, and external field energies as a function of the core displacement.

The exchange energy may be computed as:

$$\frac{E_{Ex}(a)}{\mu_0 M_S^2 V} = \frac{R_o^2}{R^2} \left(2 - \ln \left(\frac{2c}{1 + \sqrt{1 - (a)^2}} \right) \right) \approx E_{Ex}(0) - \frac{R_o^2}{R^2} \frac{a^2}{4}, \quad (2.11)$$

⁵Note that references (118) and (108) use slightly different transforms thus the displacement parameter a is not consistent in all TVM based works

where a and c are as defined at the start of this section. As with the RVM, only the change from $s = 0$ is of importance, and the constant term is, again, dropped. Since the no side charges version of the TVM is under consideration here, there are no edge demagnetization charges to consider. However, the bending of the magnetization distribution inside the disk introduces volume demagnetization charges. The charge distribution may be computed in cylindrical coordinates:

$$\sigma(\mathbf{r}) = \mu_0 \nabla \cdot \mathbf{M}(\mathbf{r}) \approx \mu_0 M_S \frac{-a \cos(\phi)}{R}, \quad (2.12)$$

As before, the self energy of the demagnetization charge distribution may be computed to obtain the total dipolar energy of the model.

$$\frac{E_d(a)}{\mu_0 M_S^2 V} = \frac{1}{2} \int_V d^3 \mathbf{r}_1 \int_V d^3 \mathbf{r}_2 \frac{\sigma(\phi_1) \sigma(\phi_2)}{|\mathbf{r}_1 - \mathbf{r}_2|} \approx \frac{R F_1(L, R)}{2L} a^2. \quad (2.13)$$

The function $F_1(L, R)$ is an equivalent demagnetization factor describing the volume magnetostatic charges resulting from flexing of the magnetization distribution and is approximated as $k(L/R)^2$ with $k = 0.08827$.

Last, the magnetization may be computed for small displacements:

$$\frac{E_h(a)}{\mu_0 M_S^2 V} = - \int_V d^3 \mathbf{r} \mathbf{m}(\mathbf{r}) \cdot \mathbf{h} \approx -\xi h a, \quad (2.14)$$

where ξ is a constant ($\sim 10/29$).

The total normalized energy can now be written in the same form as used for the RVM,

$$\frac{E_{tot}(a)}{\mu_0 M_s^2 V} = \frac{\alpha}{2} a^2 - \xi h a, \quad (2.15)$$

where $\alpha = R F_1(L, R)/L - R_o^2/2R^2$ incorporates the demagnetization energy and exchange energy. As before, minimization with respect to a allows computation of the equilibrium values of a , $a_o(h) = \xi h/\alpha$, and the magnetization $m_o(h) = \xi a_o(h)$ as a function of field.

The TVM with a tangential boundary condition neglects the translation mode of displacement. There is, however, an overestimate of deformation that compensates, permitting good estimates of low field core displacement. The lack of translation introduces a pervasive underestimate of the magnetic moment that develops near the edge of the disk, leading to an underestimate of magnetic susceptibility (Fig. 2.8 a). For the TVM the constant determining the gyrotropic mode frequency, κ , is 4α .

2.5 The Deformable Vortex Pinning Model

With the two contributing models introduced, the composite model, the Deformable Vortex Pinning Model (DVPM) may now be constructed by dividing the disk into two regions, an outer annulus described by the RVM, and an inner disk of radius R_1 described by the TVM with no side charges. The RVM annulus provides a representation of the outer region magnetization with the capability of translating rigidly independent of the core position. The TVM central region shifts with the RVM outer annulus but provides a flexible region to permit the core to advance or to lag on account of pinning, while still directly coupling the in-plane magnetization to the core. In this construction, the RVM provides the increased magnetic moment from the outer sections of the disk, while the TVM core allows computation of the energy stored in the dipole-exchange spring and its effects on the core. The idea is that in the absence of pinning the RVM annulus translates and the TVM center deforms, recreating the physical situation apparent in simulation. When the core is in a pinning site, the rigid annulus continues to deflect, which leads to a reduction of the flexing inside the TVM core in order to maintain the approximate vortex position (Fig. 2.9).

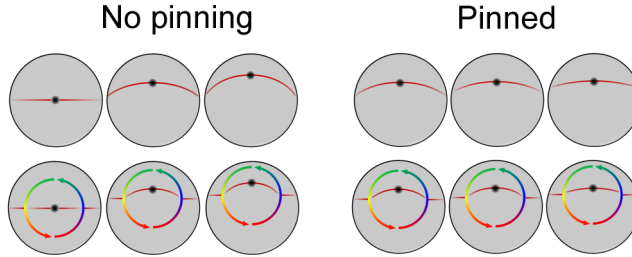


Figure 2.9: A cartoon depiction of how the DVPM mimics the flexing of the magnetization distribution in both unpinned and pinned situations. Each set of three snapshots show the evolution of the $|m_y| = 1$ contour in simulation (at top) and the DVPM (at bottom).

The use of the RVM for the outer region is motivated by the observation that a significant component of the magnetization distribution evolution can be described by translation. Additionally, the susceptibility correction means that the RVM is the best model for simultaneously predicting the net magnetization of the disk and the core position. Inside, the tangential boundary condition of the TVM maintains a piecewise continuity of the magnetization distribution ⁶. In the following sections, the model will be constructed and the

⁶Inverting the TVM and RVM, so that the TVM is outside the RVM will also result in the poor magnetization performance of the TVM dominating the model, an inability to restore circular symmetry and no natural boundary condition that can piecewise match the magnetization distributions between the two components.

details of coupling the two components of the model will be presented. Subsequent to that, the performance of the model will be evaluated, verifying the quantitative accuracy of the model.

2.5.1 Coupling and Solution

The clear challenge in developing this piecewise model, is modifying the coupling between the two models such that a reduced central flexible region correctly describes the energetics of flexing over the entire disk. The correct computation of the total energetic capacity of the dipole-exchange spring for a given core displacement will be critical to the model's ability to compute the influence of the spring and any consequent changes during pinning. It is also important to correctly compute the energetic cost of translation. Effectively, the optimal coupling of the two models will compute the correct proportion of translational displacement, and deformation based displacement while also computing the correct energetic cost of the deformation.

As previously noted, the two contributing models represent the limiting cases of translation only, and of no translation. The RVM uses the susceptibility correction to take into account the displacement due to deformation, while the TVM overestimates displacement due to deformation, compensating for the lack of translation. A combined model, with no changes to either component results in artificially increased predicted values of both the positional and magnetic susceptibilities of the vortex state. Therefore, the energetic cost of displacement (and consequent increase in magnetic moment) must be increased for both of the components to compensate. The reduced size of the TVM region already represents a reduced flexing potential. Exacerbating this makes little sense. Therefore the energetic cost of the rigid annulus should be also increased.

The magnitude of this correction for the outer annulus may be computed by considering the demagnetization energy, which provides the dominant energy contributions in each model. Inside the TVM region, the vortex is displaced in an energetic well, dominated by the volume demagnetization charges. The spring force governing the core position in this well is approximately given by the coefficient of the derivative of the energy of the induced volumetric demagnetization charges with respect to the displacement parameter $a/2$. The ability to move the vortex via the RVM shell must be reduced by an equivalent amount by increasing the stiffness of the well constraining rigid translation. This may be incorporated by an equivalent increase in the demagnetization factor of the outer shell. The equivalent change of the RVM shell demagnetization factor necessary to rebalance the energetic cost of vortex displacement is an increase of $(R_1/R)^2(2R_1/L)F_1(R_1, L)$.

The physical accuracy of this coupling approach may be grounded by considering the fun-

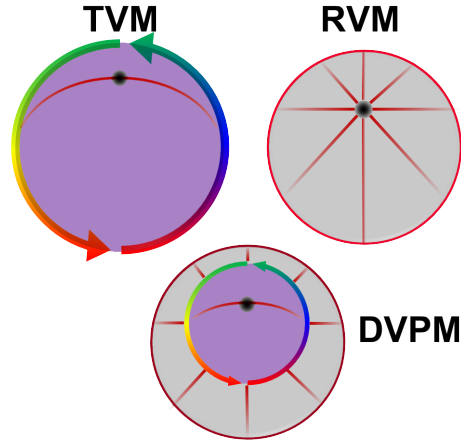


Figure 2.10: In the TVM, only volume demagnetization charges (depicted with purple shading) contribute to the total demagnetization energy. In the RVM, there are only edge charges (depicted with the red boundary). In the DVPM, both components are present. However, the susceptibility corrected RVM accurately accounts for the total demagnetization energy, meaning that it parameterizes some volume demagnetization charges. The inclusion of additional demagnetization charges within the flexible centre of the DVPM means that the RVM no longer needs to parameterize all of the volume charges, or the all of the flexible displacement. Consequently, the computed density of edge charges of the RVM shell must be modified for use in the DVPM.

damental meaning of the susceptibility correction incorporated into the RVM. The susceptibility correction implicitly couples the two sections through the demagnetization energy. In the RVM, the susceptibility correction uses material susceptibility to estimate the net decrease of the demagnetization energy due to the reduction of side charges, and the introduction of volume charges parameterizing the real world magnetization flexing. However, the TVM is already flexible, and therefore including the susceptibility correction for the shell, in addition to a central TVM region, reduces the demagnetization cost of translating the magnetization distribution too much. Ideally, the central region would parameterize only the gentle bending of the contours that leads to the deformation displacement, while the steeper edge bending that reduces translation cost would still be parameterized by the susceptibility correction. This implies that the susceptibility correction should be decreased in magnitude proportionally to the size of the TVM region. Comparing a linear interpolation between the corrected (F_c) and uncorrected (F_{nc}) demagnetization factors of the form $F(L, R, R_1) = (1 - R_1/R)F_c(L, R) + (R_1/R)F_{nc}(L, R)$ to the computed change in the RVM shell demagnetization accuracy above shows that the deviation between the two does not exceed 10% over the range $R_1/R = 0$ to 1. This corroborates the application of

susceptibility correction and its physical interpretation in the context of a rigid model. For computations from here on, the interpolation is chosen over the estimated rebalancing energy to maintain the limiting values at the susceptibility-corrected demagnetization factor and the uncorrected value.

Using the interpolated demagnetization factor, the energy of the combined piecewise model may be written,

$$\frac{E_{tot}(b', a')}{\mu_0 M_s^2 V} = \frac{\beta'}{2} b'^2 - h(b' - \frac{b'^3}{8}) + \gamma(\frac{\alpha'}{2} a'^2 - \xi h a'), \quad (2.16)$$

where $\beta' = F(L, R, R_1) - R_o^2/R^2$ and $\alpha' = R_1 F_1(L, R_1)/L - R_o^2/2R_1^2$. Here b' is the normalized displacement of the outer RVM shell, and $a'/2 = \Delta r_1/R_1$ is the central TVM core displacement normalized to R_1 . The factor $\gamma = R_1^2/R^2$ scales the energy contributions accordingly. All other symbols remain as before. The total core displacement is $s = \Delta r/R + \Delta r_1/R = b' + R_1 a'/2R$ with the same expressions for $b'_o(h)$ and $a'_o(h)$ as before, but with β' and α' replacing β and α respectively. The corresponding magnetization is $m_o(h) = b'_o(h) - b'_o(h)^3/8 + \gamma \xi a'_o(h)$. For small displacements, the third order terms for the RVM shell may be dropped to make a simplified version of the model. For the DVPM, κ may be computed in the unpinned and zero field case as

$$\kappa = \frac{4(\alpha' + \gamma \xi^2 \beta') \beta' \alpha'}{(2\alpha' + \rho \xi \beta')^2}. \quad (2.17)$$

Only one free parameter remains, the radius of the inner TVM section. The influence of R_1 is mitigated by the coupling of the models using the susceptibility correction, however the choice of R_1 is not entirely arbitrary. The susceptibility correction interpolation maintains the energetic cost of total vortex displacement, but R_1 still determines how much of the deformation based displacement is explicitly accounted for by the inner region and how much is attributed to the shell, via the remaining correction. The constructed model can behave as the RVM in one limit ($R_1 = 0$), or the TVM in the other limit ($R_1 = R$). Consequently, the model can exhibit the failings (and successes) of the RVM in one limit, and the TVM in the other. Optimal computation of the properties of the vortex state require an intermediate R_1 . This can be estimated by minimizing the deviation of the DVPM from the successful predictions of the RVM ($m(h)$, $s(h)$) and the TVM (gyrotropic frequency, f_o). More precisely, for comparison of $m(h)$, the initial susceptibility $\chi_0 = dm/dh$ at $h = 0$ may be used, and similarly, the initial positional susceptibility, ds/dh at $h = 0$, of the core may be used. The error optimization can be visualized by plotting the surfaces of relative error ($|q_{DVPM}(0) - q_{RVM}(0)|/q_{RVM}$ or $|q_{DVPM} - q_{TVM}|/q_{TVM}$) for the three metrics of interest as a function of the disk radius and the inner region radius (Fig. 2.11). For

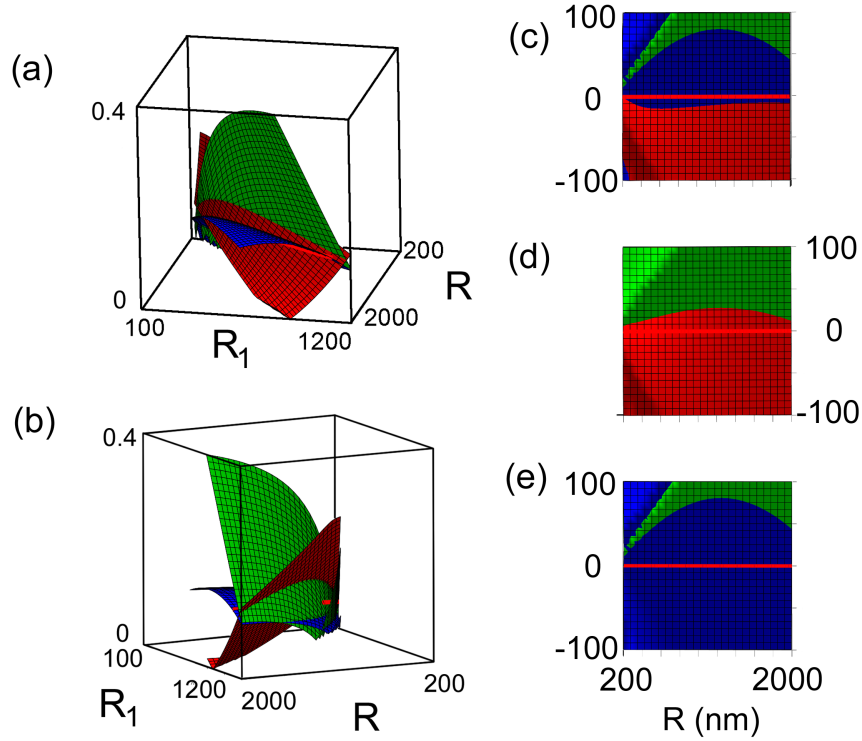


Figure 2.11: Plotting the absolute value of errors in DVPM predictions compared to RVM and TVM predictions provides a solution for optimal coupling parameters. Planes defined by $|q_{DVPM}(0) - q_{RVM}(0)|/q_{RVM}$ or $|q_{DVPM} - q_{TVM}|/q_{TVM}$ where q represents the gyrotropic frequency (green), initial susceptibility (red), or initial positional susceptibility (blue), and plotted as a function of disk radius R and inner region radius R_1 give solution at a line defined by the near intersection of the planes. Two views of the raw 3D-plot show the intersection. An added red line shows the solution $R_1 = R(0.6 - (5/3)(L/R))$ which tracks the intersection. In the 3D view, the red line is challenging to see. At left, three views of the planes from below are shown, plotted as functions of R and $R_1 + R(0.6 - (5/3)(L/R))$ so that the x axis defines the solution $R_1 = R(0.6 - (5/3)(L/R))$. The x axis highlighted in red, and is much easier to see than in the 3D plots, allowing proper comparison of the solution and plane intersections. This provides an alternative method of visualizing the intersection.

example, one surface is defined by plotting $|\chi_{DVPM}(h=0) - \chi_{RVM}(h=0)|/\chi_{RVM}(h=0)$ as a function of R and R_1 . The three planes indicate an approximate solution at the near intersection. Solving for this optimal $R_1(R)$, in general, a reasonable agreement with all three parameters can be found for R_1 values of approximately $R/2$. In more detail, the optimal R_1 has a weak dependence on the radius of the disk. Semi-empirically, the optimal

$R_1 = R(0.6 - (5/3)(L/R))$ was computed for disks of varying radius and 40 nm thickness. It is important to note that this R_1 value is determined by comparison to models with known flaws. Therefore, one cannot be confident that this is the true optimal R_1 that correctly computes the strength of the dipole-exchange spring effects in pinning without comparison to simulation. This will be done in a subsequent section.

2.6 Comparing the Models: The Ideal Disk

Previous sections have introduced the energy balances necessary for the solution of three models the RVM, the TVM with no side charges, and the DVPM. The first step in evaluating the DVPM is to compare its performance against simulation as well as the TVM and RVM.

From Equations 2.7, 2.15, and 2.16 the ideal disk behaviour of each model may be computed and compared to Landau-Lifshitz-Gilbert micromagnetic simulation⁷. To mimic quasistatic behaviour, time integration with a damping factor of 1.0 was used. All simulations were performed on a 2-D 5 nm × 5 nm grid using an exchange stiffness constant of 1.05×10^{-11} J/m, with M_S values between 700 kA/m and 800 kA/m and either 20 nm or 40 nm thickness. See appendix A for more detail on simulations. All calculations with the model used an exchange length of 5.85 nm and M_S values matching the simulations.

Comparison of the $m(h) = M(H/M_S)/(\mu_o M_S)$ and $s(h) = \Delta r(H/M_S)/R$ curves are shown in Figures 2.12 a and b. Clearly the susceptibility-corrected 3rd order RVM provides the best estimate of both magnetization and vortex displacement as a function of field, while the uncorrected version exhibits the poorest performance. Both the DVPM and TVM provide good estimates of vortex position with field for displacements up to $R/2$, but of those two, only the DVPM simultaneously gives a good description of the magnetization.

Two other metrics have been applied to evaluate the performance of the analytical models near zero field in past work: initial susceptibility, and the frequency of the lowest order excitation mode of gyrotropic vortex motion. Both of these parameters primarily depend on the aspect ratio of the disks. Comparisons between simulation and computed results for initial susceptibility and gyrotropic mode frequency are shown in Fig. 2.12 c and d. Dynamic simulations were performed using a realistic damping factor (0.02) but otherwise matched the parameters used in the previous simulations. The poor performances for magnetization description of the TVM and uncorrected RVM manifest as incorrect estimations of the initial susceptibility. However, both approach the simulation results for squat disks, corroborating previous results (108, 116) and demonstrating the general utility of these models. By

⁷All simulations were performed using version 2.56d of the LLG Micromagnetics software package <http://llgmicro.home.mindspring.com/>.

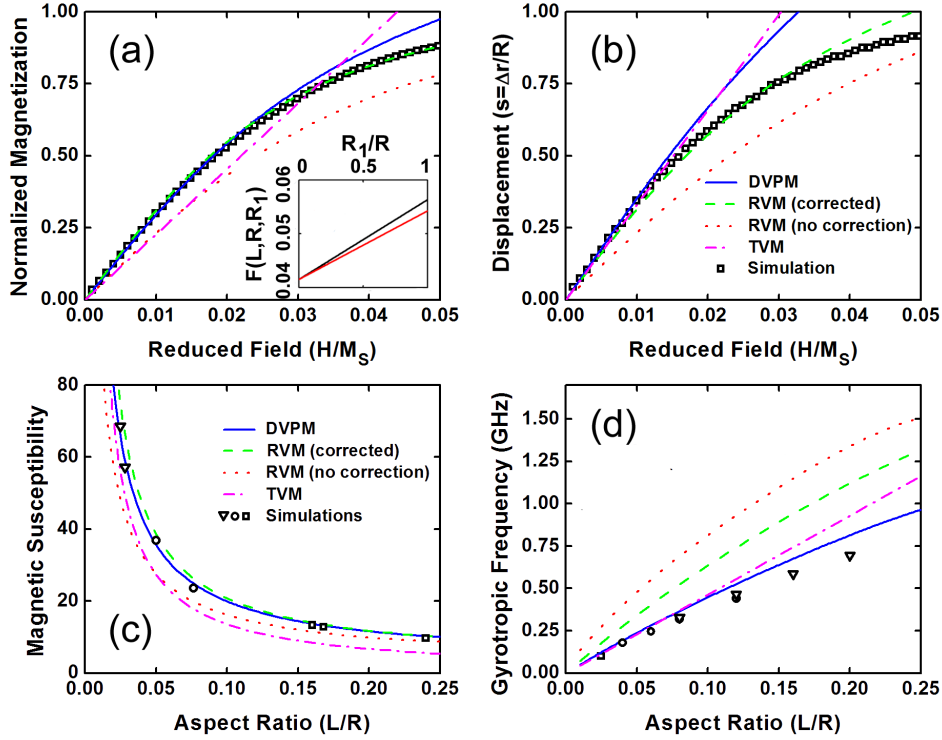


Figure 2.12: (a) The computed m-h curves from four models (RVM corrected and uncorrected, DVPM, TVM) are compared against a simulation of a $1\ \mu\text{m}$ diameter, $30\ \text{nm}$ thick disk with $M_S=800\ \text{kA/m}$. (b) The computed normalized vortex displacement as a function of field is compared against the simulation. The legend inset in panel (b) applies to both (a) and (b). Only the RVM with a susceptibility-corrected demagnetization factor and the DVPM describe both position and magnetization accurately for displacement $s < 1/2$. Inset in (a) is a comparison of corrected demagnetization factor as a function of R_1 used in the DVPM computed by interpolation (solid red) and from demagnetization energies (black). (c) The computed initial susceptibility is compared against simulation for disks varying radius (R) and thickness (L). Squares denote $R = 250\ \text{nm}$, circles $R = 500\ \text{nm}$, and triangles $R = 1800\ \text{nm}$. All simulations use $M_S = 800\ \text{kA/m}$ except the $R = 1.8\ \mu\text{m}$ which use $M_S = 715\ \text{kA/m}$. (d) Using the same simulation parameters the frequency of the gyrotropic mode was computed. The legend in (c) applies to panel (d) as well. Only the DVPM agrees well with both the initial susceptibility and the gyrotropic frequency. For (c) and (d) calculations were performed holding $R = 500\ \text{nm}$ with variable thickness. All DVPM calculations in panels a-d use $R_1 = R/2$.

comparison, the DVPM and corrected RVM provide excellent estimates of initial susceptibility for all aspect ratios investigated. Previously, only the TVM has provided reasonable estimates for the gyrotropic frequency of the vortex state while the RVM has provided poor estimates. The success of the TVM is reproduced here, as is the failure of the uncorrected RVM. The susceptibility correction improves the RVM prediction, however it fails to match the performance of the TVM in the prediction of f_o . However, the DVPM provides comparable performance to the TVM for low aspect ratios and improved performance with more squat ideal disks.

2.7 Pinning

In the previous section, the DVPM was shown to provide excellent predictions for a variety of properties that analytical models have been used to compute previously. That section alone, however, does not provide a compelling reason for switching away from the RVM and TVM to the DVPM. To see that, the treatment of pinning must be examined. In this section, pinning sites are added to the DVPM and to the RVM. In principle, pinning sites may be added to the TVM as well, however the behaviour will not be qualitatively different than that of the RVM.

Adding pinning to the models is accomplished by adding functions of the form $E_p(b' + R_1 a' / 2R - X_p)$ for a pinning site located at X_p to equation 2.16, or of the form $E_p(b - X_p)$ for the RVM in equation 2.7. For the RVM case, simply solving for the minima in energy permits a full solution of the problem. For the DVPM, the 2-D optimization required makes the problem more complicated, however this is critical to the success of the model. Plotting the pinning energy, pinning sites appear as linear troughs in $b' - R_1 a' / (2R)$ space (Figure 2.13 a). This permits a simplification of the optimization process by the consideration of pinning site coordinates defined by $b' = i \sin(\theta_p) + j \cos(\theta_p)$ and $a' = i \cos(\theta_p) - j \sin(\theta_p)$ for $\theta_p = \tan^{-1}(2R/R_1)$. Switching to i and j coordinates allows independent minimization and simplifies the problem. The position and existence of local minima inside and outside of pinning sites evolves with changing applied field (Figure 2.13). Sometimes bistable states exist, and when they do, there is inevitably a transition pathway between the two extant minima that passes over a saddle point. Applying a 2D optimization repeatedly while changing the field permits computation of the values of b' and a' for all minima and saddle points. This in turn permits computation of the quasistatic pinned and unpinned magnetization and vortex position, while locating the saddle points separating minima allows computation of the energy barriers separating bistable states.

The critical feature of this minimization process is that the coordinate a' may evolve non-monotonically with increasing field, matching the qualitative non-monotonic evolution of

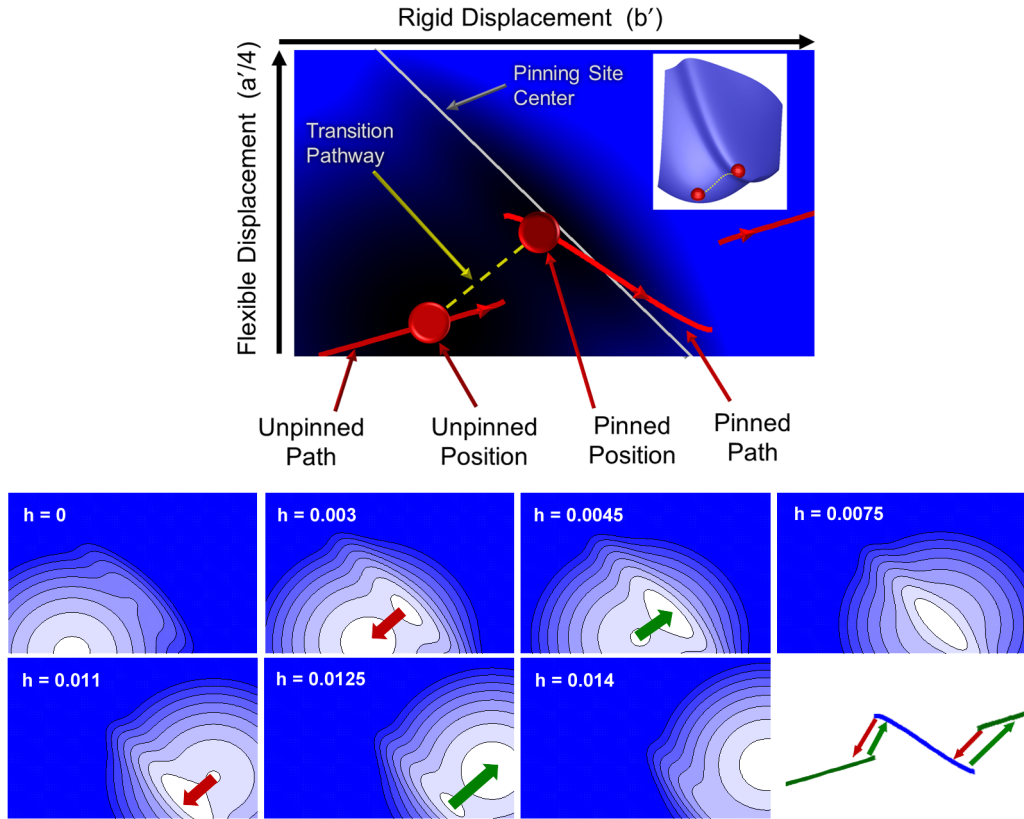


Figure 2.13: A 2D plot of the energy landscape (colour gradient) in the DVPM computed for a $1\ \mu\text{m}$ diameter, $40\ \text{nm}$ thick disk is shown as a function of both rigid displacement of the RVM annulus (b') and flexible displacement of the central TVM region ($a'/4$ for $R_1 = R/2$). The energy is computed for a fixed field value of $h = 0.025$ using an $M_S = 800\ \text{kA/m}$. This is the 2D landscape that must be solved to find the lowest energy combination of b' and $a'/4$ for a particular vortex displacement. The energy landscape chosen features a single pinning site at $b' + a'/4 = 0.21$. At $h = 0.025$, two local minima exist, one inside the pinning site, one outside. Inset at top right is a 3D representation of the potential at $h = 0.025$, the two local minima and the transition pathway. As field is changed, the positions of these minima shift along the paths displayed above, allowing the DVPM to describe flexing and rigid displacement in unpinned and pinned situations. At bottom, a sequence of images depicting the 2D energy potential for an increasing field is shown. Evolution of the minima positions determine the magnetization computed in the model. Transition points into and out of the pinning site are indicated by arrows (green up sweep, red down sweep). Field dependent asymmetry in the energy barrier separating the sites results in a hysteric path for a complete up and down sweep, as shown in the final panel.

the flexing of the magnetization distribution visible in simulation.

Micromagnetic simulations were used to evaluate the pinning performance of the DVPM and, for comparison, the corrected RVM. The same simulation parameters were used as in the previous simulations. Pinning sites are mimicked using approximately circular regions of depressed saturation magnetization to modify the energy landscape of the disk (Fig. 2.14 c inset). This leads to two contributions to pinning energy, the reduced exchange energy of the core in the low M_S region, as well as reduced demagnetization energy when the core is centered on the site. The energetic profile of the pinning site can be approximated by considering the convolution of a 2-D Gaussian at various offsets with the profile of the M_S variation (Fig. 2.14a, inset). The Gaussian effectively approximates the exchange energy density of the core, as well as the M_z profile, providing an estimate of how the two energy contributions change as the core shifts relative to the pinning site. Here a full width half max of 17.2 nm is used for the Gaussian approximation.

2.7.1 Single Pinning Sites

The performance can be evaluated by three metrics: the pinning site position error, the width of the minor hysteresis loops associated with pinning and depinning, and the combined computed pinned differential magnetic and positional susceptibilities. Figure 2.14 a-d show results for a 1 micron diameter, 40 nm thick, disk compared to the DVPM and the 3rd order RVM. The DVPM accurately captures both differential susceptibilities while the RVM fails to capture the positional slope. Both models feature effective position shifts of the pinning site. The DVPM agrees best with the simulation for a pinning site shifted 2.5 nm further from center than the actual simulation (107.5 nm instead of 105 nm), while a shift greater than 10 nm is best for the RVM (at 115 nm instead of 105 nm). Most importantly however, the computed entrance and exit hysteresis loops agree closely for the DVPM, but are almost non-existent for the RVM. The deformation allowed by the DVPM permits the vortex to move ahead into the site, and linger in the site at a lower energy cost than the rigid model.

Disk sizes between 500 nm diameter/40 nm thick and 2000 nm diameter/20 nm thick were simulated with identical M_S variation pinning sites (Fig. 2.15). The value of R_1 used makes a significant difference in computing pinning effects in comparison to unpinned behavior. Changing R_1 has a weak influence on the computed m-h and r-h curves, mitigated by the coupling approach used. More importantly, the value R_1 dictates the energetic cost of displacing the core via the exchange-demagnetization spring. Reducing the proportional value of R_1 stiffens the spring. This in turn has a significant effect on pinning and depinning barriers. In the previous section, errors between the DVPM and its component models were analyzed to determine the optimal R_1 , providing an R_1 estimate independent of simulations.

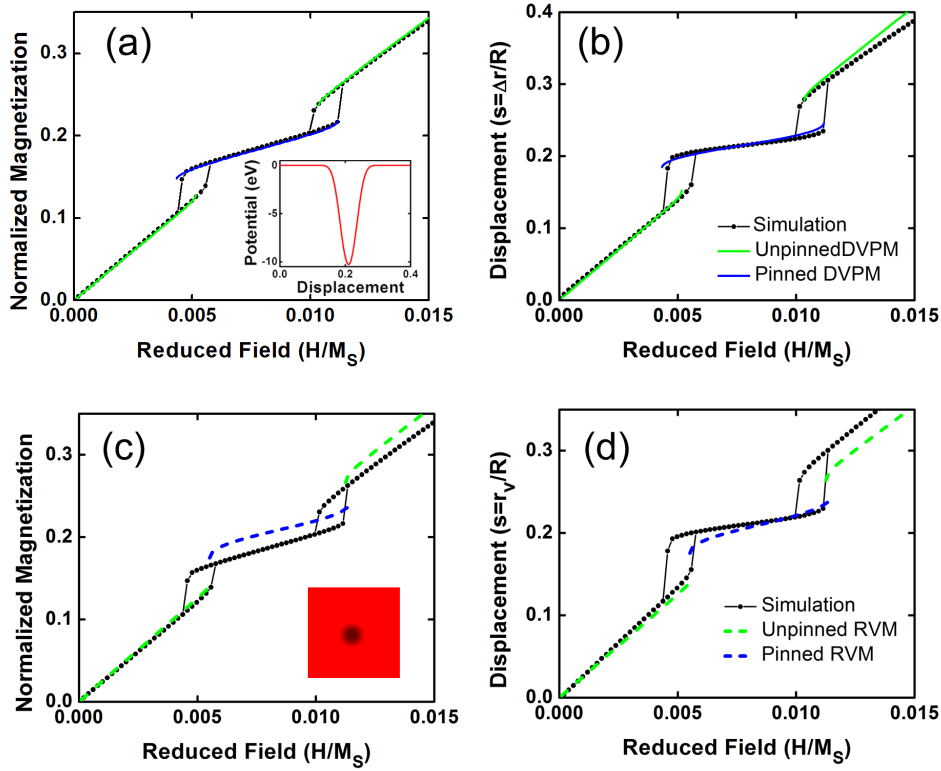


Figure 2.14: The m-h (a) and s-h (b) curves for a field sweep up and down are compared against simulation for a $1\mu\text{m}$ diameter, 40nm thick disk with a single pinning site located at 105nm with an energy profile estimated from the simulation (inset in (a)). For comparison, the same pinning site is added to the susceptibility corrected, one parameter RVM. The computed m-h (c) and s-h (d) curves provide much worse agreement including a larger ($> 10\text{nm}$) positional error, and more importantly, a complete absence of hysteresis on entrance and exit from the pinning site. In the simulation the pinning site is included as a region of suppressed M_S (inset in panel (c)) with diameter 40nm , where at the center $M_S = 550\text{ kA/m}$.

In the case of pinning, however, no model is adequate for comparison, and consequently it is best to determine an optimal R_1 value by comparison to well-defined pinning simulations. As in the comparison made to the RVM and TVM, in general the value $R_1 = R/2$ provides reasonable results. However, for disks below $1\mu\text{m}$ in diameter (for 40 nm thickness), reduced R_1 values provide better pinning performance, reflecting the increasing rigidity of smaller disks. A comparison between the optimal R_1 values computed by error minimization against the RVM and TVM, and also by comparison with simulation, is shown in the inset of figure 2.15c. Each optimization method returns the same qualitative trend of decreasing R_1/R with the value of R .

The DVPM was found to give good estimates of hysteresis width and vortex position for all disk sizes when an optimized value of R_1 was used. For disks significantly larger than $1\mu\text{m}$ in diameter, at 40 nm thickness, the pinned magnetic differential susceptibility was found to be underestimated. Figure 2.15 shows a 500 nm and 1500 nm diameter result for comparison. The R_1 from error minimization provides a reasonable estimate for situations where simulation is not possible, however reference to a known simulation is preferable. For large and thin disks, $R_1 = R/2$ provides better agreement with simulation. This reflects the fact that in low aspect ratio disks, large compared to the exchange length, the character of flexing in the magnetization distribution will change to include more complex deformations beyond the scope of the TVM approximation used. It should be noted that for a given disk aspect ratio, once the optimal R_1 is computed from a single simulation with well known pinning parameters, the R_1 value is then fixed. This permits computation of the effects of arbitrary pinning potentials or even fitting magnetization curves to extract information about the pinning potentials.

2.7.2 Two Dimensional Pinning Site Array

The DVPM provides excellent performance in the description of ideal disk behavior and pinning for idealized simulations. However, in application to real samples, the treatment of pinning sites located centred directly along the pathway followed by the vortex as it is deflected by field is limiting. As noted in recent numerical simulation work on pinning (126), a more realistic case is to consider pinning sites near, but not centered on, the field-defined path. This can be incorporated into the 1-D model presented here by computing the 1-D equivalent potential of the actual 2-D path followed by the vortex. Deviations orthogonal to the path defined by the applied field have an energy cost approximated by $\kappa\Delta x^2$ where the value of κ is given by equation 2.17. Since the magnetization induced by these deviations is orthogonal to the applied field, the energy is effectively static and can be summed with a 2-D distribution of pinning sites to form a trough guiding the vortex through the 2-D energy landscape. It is then possible to compute the minimum energy pathway $\Delta x_o(\Delta r)$ that

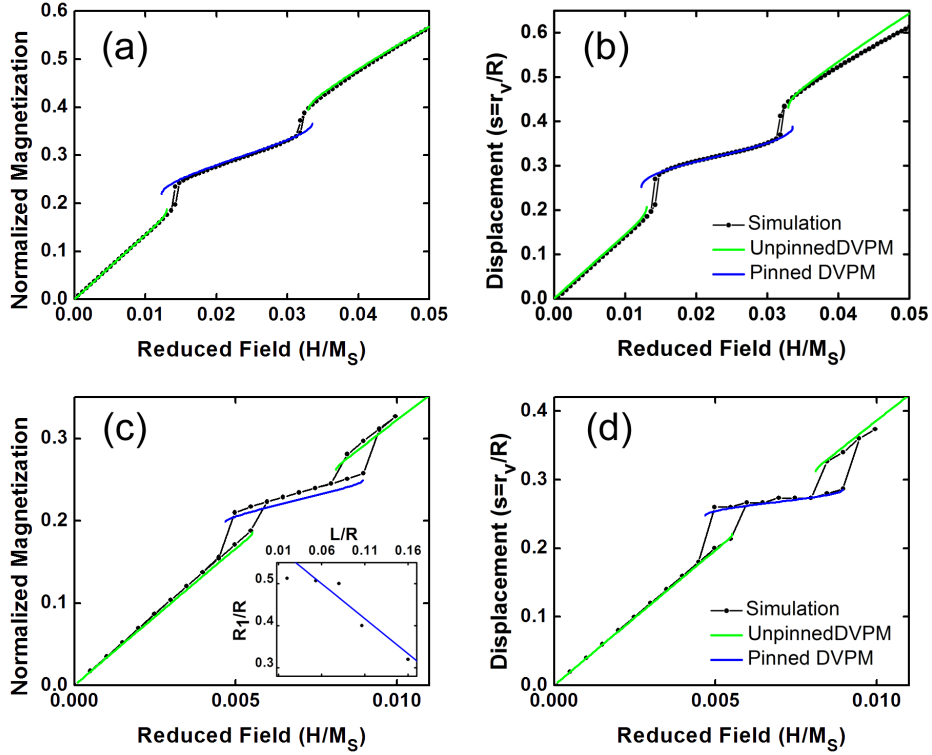


Figure 2.15: (a) The DVPM m-h result is compared to a simulation of a 500 nm diameter, 40 nm thick disk with $M_S = 700$ kA/m and a single pinning site located 80 nm away from the centre. (b) The computed normalized displacements are compared for the same simulation. For this comparison with $R = 250$ nm, $R_1 = 80$ nm provides the best estimate of hysteresis loop width. The inset shows a plot of the optimal R_1 value found by comparison to simulation as a function of aspect ratio (black points). The blue line is the optimal R_1 value computed by minimizing deviation of the DVPM from the RVM and TVM for initial susceptibility, ds/dh and gyrotropic mode computed for 40 nm thick disks. (c) Comparison to a simulated 1500 nm diameter, 40 nm thick disk with a single pinning site at 200 nm from center shows that the DVPM begins to underestimate the magnetization as disk size increases. (d) The computation of the vortex position and hysteresis loop width remains accurate. For $R = 750$ nm, an R_1 value of 375 nm was used.

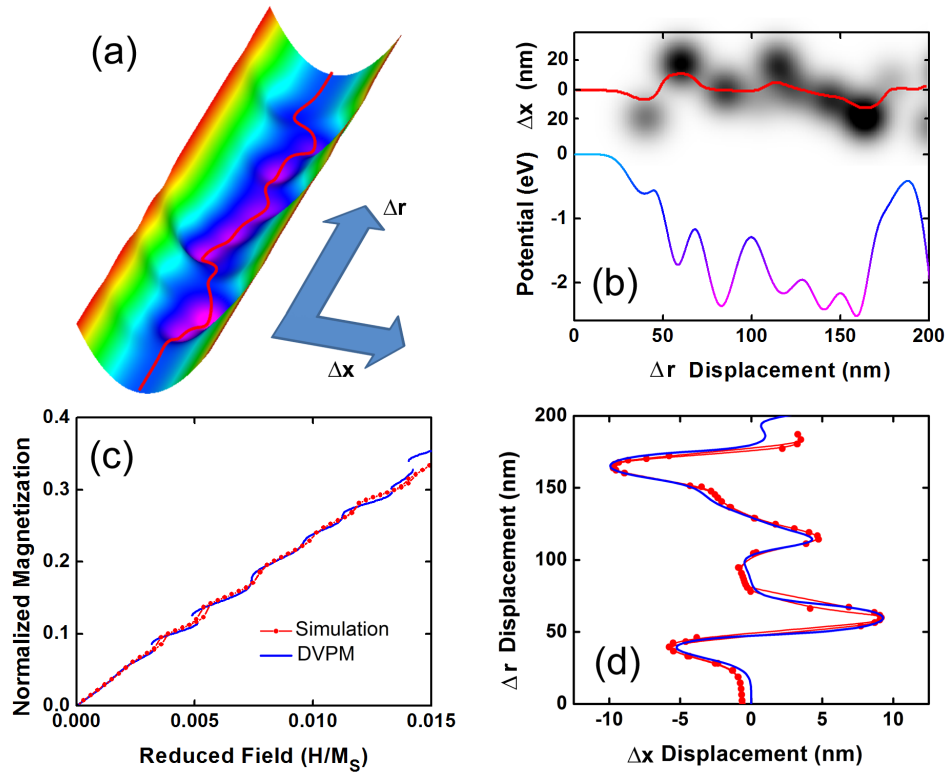


Figure 2.16: (a) A 3-D plot shows the pinning site potential combined with the harmonic potential for deviations orthogonal to the path defined by the applied field. The computed path of minimum energy, $\Delta x(\Delta r)$ is plotted as a red thread. (b) At top the 2-D pinning potential is plotted with the computed minimum energy path (red line). Below, the equivalent 1-D potential is presented. The equivalent potential incorporates contributions from both the pinning potential and harmonic trough. The colour gradient on the potential line matches the colour scale in panel (a). (c) The magnetization curve computed from the potential in (b) is compared against a simulated curve incorporating M_S suppressed regions with the same 2-D distribution. The depth of the 2-D potential used in the model calculations is estimated from the simulation. Agreement is very close, though some deviations show up as the vortex displacement increases and a large energy change is encountered. (d) The simulated $\Delta x(\Delta r)$ is compared to the computed minimum path showing excellent agreement.

the vortex will follow as it is deflected (Figure 2.16a). Computing the total static energy, pinning plus the trough energy, $E(\Delta x_o)$ yields an equivalent 1-D potential as a function of Δr (Figure 2.16b). This potential can then be summed, as the Gaussian pinning sites were previously, with the potential for a perfect disk including field. Solving for minima, as before, allows computation of the evolution of the magnetization and vortex position in the 2-D potential.

This approach is applied to a simulation that incorporates a 2-D distribution of 10 nm diameter pinning sites with various values of suppressed M_S near the field-defined path. As before, the pinning sites are incorporated into the model as Gaussian wells with depths estimated from the simulation and profiles computed by convolving a Gaussian with the profile of the M_S variation. The computed 2-D path agrees well with the vortex position extracted from simulation, as does the computed magnetization (Figure 2.16 c and d). Some disagreement is noted as the deflection increases close to the effective $R/2$ limit of the model, and the vortex passes over a large barrier.

2.8 Bistable Paths

In the computation in the previous section, a sparse 2-D distribution of sites ensures a unique $\Delta x_o(\Delta r)$. However, in principle this approach can be extended to bistable states in Δx by consideration of multiple vortex tracks (Fig. 2.17), or bistable paths. Due to the complexity and opportunity for multiple switching paths, computation of the exact energy barriers separating tracks, however, would require a more complete minimization. Useful information can still be extracted from simple situations. For two bistable paths with a continuum of transition pathways, approximate ranges of barriers can be investigated by looking at energy profiles along likely hopping paths. One additional effect to keep in mind is the sensitivity of possible transition pathways to the offset of the path. For instance, if a 2D field is applied, with one field acting as the primary field, and a second one adding a small offset to tune the 2D position of the path, this may strongly affect observed energy barriers (Fig. 2.17).

2.9 Computation of Thermal Dynamics

For transitions between bistable states with one transition pathway, the effect of thermal dynamics may be included in the model. Classical thermal dynamics for stochastic transitions may be computed using an Arrhenius relation $\tau = f_o^{-1} \exp(\Delta E/k_B T)$ where the barrier ΔE is the barrier computed from the model computation describing the bistable states. This

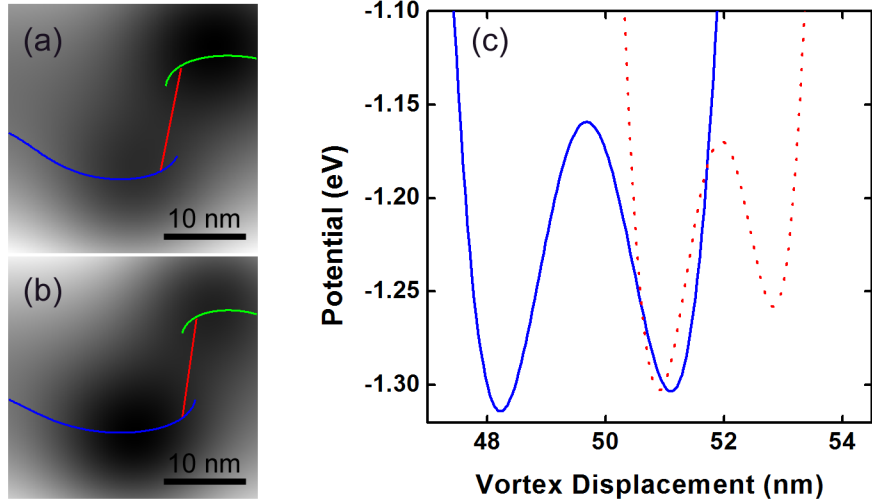


Figure 2.17: Two pinning sites create bistable paths. Effectively these may be considered to be a continuum of bistable states with a wide range of transition paths. In a simple situation like this, estimated transition paths can still be useful for estimating energetic transition pathways. Using the same two pinning sites, two different paths are shown in (a) and (b). The only change is the consideration of a ~ 2 nm offset in the path relative to the pinning sites. The greyscale potential shows a shift, as do the main energy minimum paths (blue and green). The estimated optimal hopping paths (red) shift more significantly. Examining the barrier profiles along each in panel (c) shows that the barrier becomes smaller and asymmetric for panel (b) (dotted red line) when compared to panel (a) (solid blue line).

allows computation of lifetime distributions for telegraph noise, and the influence of thermal dynamics on observed magnetization in real experimental situations.

In a hysteresis loop, particularly a small hysteresis loop resulting from a small energetic transition, the point of transition may be affected significantly by thermal dynamics. Switching will happen before the energetic barrier involved in the transition is zero, effectively narrowing hysteresis loops. This is included in the model by determining the energy barrier at which the average time for a transition to occur is equal to the experimental bandwidth of the instrument used to acquire the data: $1 = \Delta t_{BW} f_o \exp(-\Delta E/k_B T)$. Plotting the number of transitions expected within the band width provides a nice exponential function to indicate a realistic location for switching to occur (Fig. 2.18). Previous data in this chapter concern simulations at effectively zero temperature, thus thermal transitions were not considered.

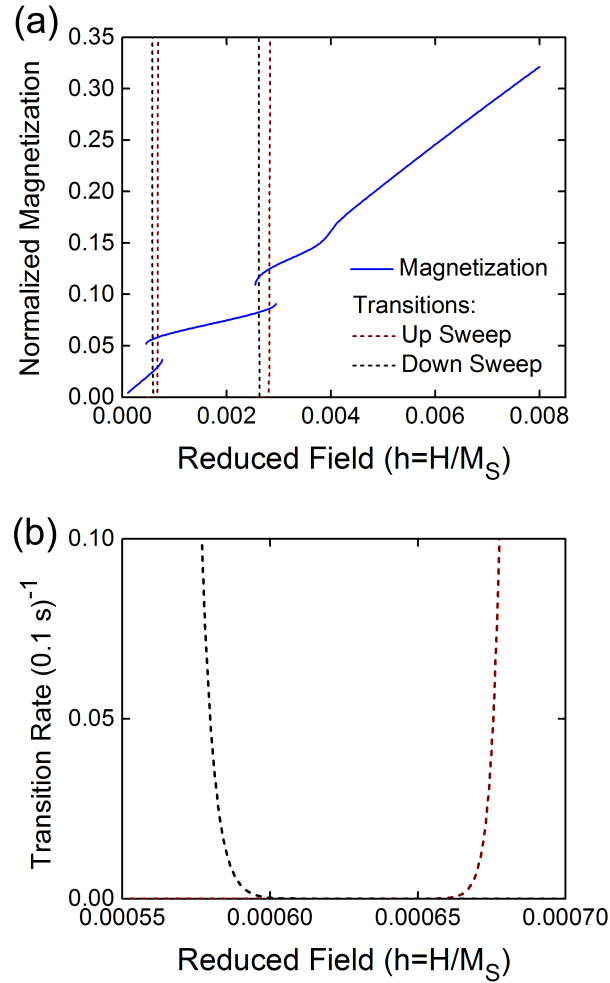


Figure 2.18: Thermal dynamics affect the width of hysteresis loops. An example computation including thermal dynamics is shown here (a). Transitions out of bistable states occur before the states become energetically unstable (are no longer local minima). Transition points are computed by plotting the number of transitions expected to occur within a set amount of time, here 0.1 s. The actual point of transition will depend on field sweep rate, and the bandwidth of the observation used in experiment. The exponential nature of the transition rate (b) provides a steep transition profile that provides a convenient graphical method of indicating the transition point.

2.10 Fitting to Magnetization Curves

The model is extremely useful as a tool for computing what will happen in a realistic, or artificially modified disk. It is faster than simulation and provides intuition useful for understanding what is happening to the vortex state. However, these applications are really secondary. The most powerful application of the model is as an analysis tool for experimental data (71). Given a magnetization curve in a well characterized disk, the model is capable of extraction of a pinning potential with accurate positions. Application of the model to real experimental data is covered in Chapter 4. In comparison to experimental data, inclusion of thermal dynamics in fitting is very important.

2.11 Conclusion

The piecewise approach applied to develop the DVPM yields a highly functional analytic model that makes quantitatively accurate predictions of a wide variety of properties of a vortex in a disk. Most notably, it provides a powerful description of vortex core pinning and provides greater physical insight into the behavior of the vortex during pinning. The model holds promise as a tool in probing the modification of pinning in technologically pertinent thin films to better understand effects such as ion damage. The piecewise approach demonstrated may, in future, be generalized to other geometries, permitting quantitative computation of device behavior without cumbersome simulation.

CHAPTER 3

Magneto-optical Study of Vortex Annihilation¹

The prototypical nature of the vortex state in a thin magnetic disk makes it an ideal system to pursue detailed studies of vortex behaviour. In particular the technological potential of the vortex state (eg. (45)) demands careful understanding of the stability of the vortex state and energetic transitions such as vortex creation and annihilation. This motivates study to elucidate the nature, reproducibility, and methods to control these transitions in the well understood experimental arena of the thin disk.

This chapter details the development of an experiment to capture statistics of vortex annihilation in an array of permalloy disks. The goal of the experiment included the study of the long time scale stability of vortices close to their annihilation fields. This enables the study of thermal activation, and the mechanism of the decay process. To do so required the development of a magneto-optical susceptometer capable of rapidly extracting the decay distributions of the sample array with the capability of tuning sample temperature and field sweep rate. A thorough introduction of the magneto-optical Kerr effect (MOKE) is provided for unfamiliar readers, including an abbreviated historical narrative of MOKE, as well as an overview of popular applications of MOKE in modern science. A full description of the experiment follows, including an additional, unpublished, section describing upgrades made to the instrument for future work, as well as preliminary data.

3.1 The Magneto-optical Kerr Effect

Initially discovered by Reverend John Kerr in 1876 (127–130), the magneto-optical Kerr effect (MOKE) describes the rotation and ellipticity of the polarization of light after reflection from a magnetic material. Remarkably, Kerr detected polarization rotation of light

¹A version of this chapter was published in Physical Review B (69).

with nothing more than a collimated paraffin lamp, two Nicol Prisms, and the polished end of a horseshoe magnet (128). The simplicity of the experiment and rudimentary nature² of the available equipment serves as a testament to Kerr's astounding experimental ability, but it also hints at a puzzle which would stand for over 75 years following Kerr's initial discovery. Namely, how is the coupling between the light and the magnet strong enough to be detected at all? This question remained unanswered until Argyres (132) developed a complete quantum mechanical theory incorporating spin-orbit interactions. Up to that point, classical theories provided a good explanation of the qualitative behaviour observed, but failed to capture the observed magnitude of the rotation.

3.1.1 Qualitative Description of MOKE

Kerr's discovery came at a time when Maxwell's theory of electromagnetism (11, 12) was well developed and allowed a very accurate understanding of optical effects. It was also preceded by the analogous effect for transmission: the Faraday effect (133). Classical descriptions of these effects in ferromagnets failed to explain the magnitude of the effect.

In principle, both effects can be described in classical terms via interaction of a magnetic field with electrons in the material induced to oscillate when exposed to the light (134). An intuitive understanding of MOKE may be developed by considering an electron induced to oscillate on a surface by an incident oscillating electric field (Figure 3.1). Any added magnetic field will result in a Lorentz force applied to the electron inducing a distortion in the electron oscillation path. Therefore, re-radiated light that has interacted with an electron in the sample supporting the magnetic field will show a distortion in its polarization. This simplistic picture permits a robust understanding of the qualitative behaviour observed for all orientations and polarizations of incident light on a magnet with a magnetization in any direction. The version easiest to picture is the polar effect, where the magnetization of the sample is perpendicular to the plane of the sample, and the optimal angle of incidence for light is normal to the surface. Picturing the polarization of the light, the Lorentz force induced will be orthogonal to the light electric field, and of opposite sign for positive and negative portions of the wave. Thus it will induce a rotation of the polarization for light re-radiated (reflected) following interactions with electrons. All combinations of incident polarization direction and sample magnetization direction lead to different types of MOKE. Figure 3.1 provides a visual explanation using the rudimentary Lorentz force picture of all

²Originally, this sentence commented on the crudeness of Kerr's apparatus. However, this excerpt from a 1935 biography of Kerr by Gray motivated a change: (131) "...Lord Lister said: 'It has been a matter of admiration and wonder to subsequent investigators that Dr. Kerr should have been able to learn so much with the comparatively simple and ineffective apparatus at his disposal'. It is related that Dr. Kerr, then seventy-four years old, was much peeved at Lister's remarks: 'Simple it may be,' he protested, 'but not ineffective; rude but not crude'.". With this in mind, the apparatus is, perhaps, best described as rudimentary rather than crude.

of the effects. The most important version to understand for the remainder of this work is longitudinal MOKE with magnetization perpendicular to the incident polarization.

More formally, the polarization effects may be computed for all flavours of MOKE using a generalized dielectric tensor for the magnetic material. This is equivalent to considering different indices of refraction for right and left hand circularly polarized light. A full treatment may be found in the work of Freiser (135). This framework using the dielectric tensor is useful for both classical and quantum descriptions of magneto-optical effects. The only difference for full quantum mechanical treatment is that the computation of the tensor components must be approached quantum mechanically to incorporate the effect of the spin orbit coupling. Argyres (132) provides a detailed description of the polar version of MOKE for the interested reader.

While it is important to understand the origin of magneto-optical effects, in general the qualitative description provided by the Lorentz force picture is adequate for understanding most research performed using MOKE. Typically, calibration of MOKE apparatuses for quantitative measurements is challenging. Hence data is usually presented in terms of normalized magnetization for any particular sample. This makes a detailed understanding of the magnitude of the effect unnecessary as long as the effect remains linear.

3.1.2 Applications

The Kerr effect has found great application in the study of magnetic films and has made a significant contribution to advances in the understanding of magnetism.

Most commonly, MOKE is applied in magnetometry. The typical modern MOKE magnetometer (Figure 3.2) employs a laser light source, a magnet, optics to control the orientation of the polarization of the laser, and an analyzing polarizer to detect shifts in the polarization on reflection from the sample. This basic design can be modified to improve sensitivity in many ways including optimization of the angle of the analyzing polarizer (136,137), the addition of a photo-elastic modulator (138), and additions of dielectric coatings to samples (139). As an optical technique, MOKE lends itself to applications in microscopy. Addition of a objective lens and a camera can enable imaging of domains (140). Modern versions of imaging microscopes are capable of video rate imaging of domain switching (141). More common now are scanning versions of laser magnetometers. In this geometry, no camera is used and spatial resolution is obtained by shifting either the sample or the objective on an automated stage. With a high numerical aperture objective and a laser operated at high power (142), or extensive number of averages (143), this technique permits the study of individual nanoscale magnetic elements.

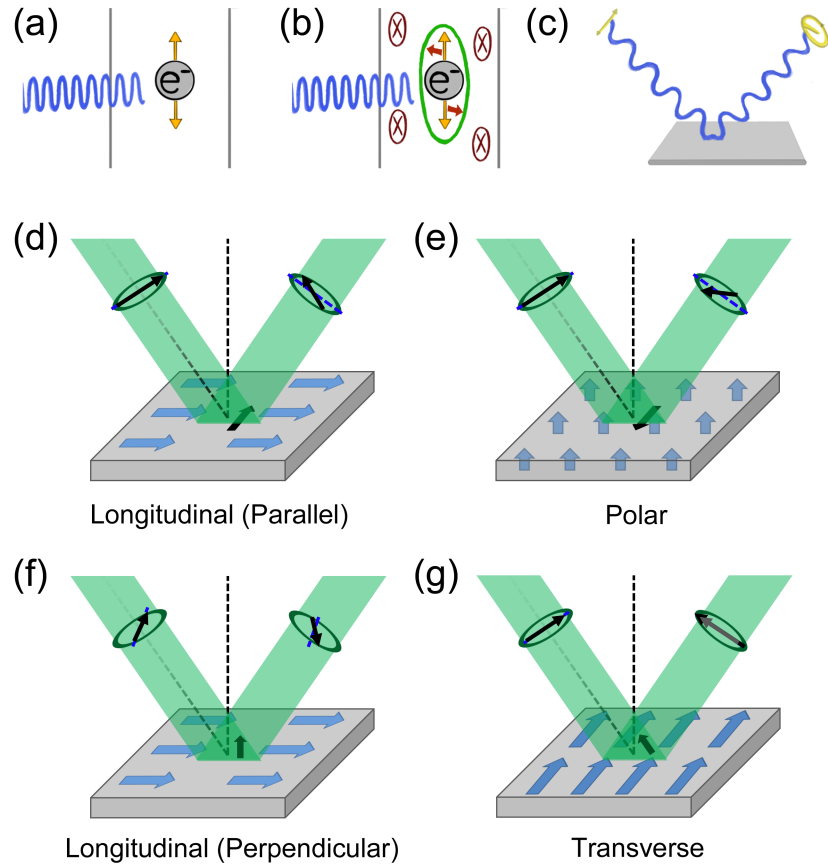


Figure 3.1: Panels a to c provide a cartoon representation of the classical Lorentz force view of the magneto-optical Kerr effect. The polar version is represented. Panels d to g show the four different types of MOKE effect. The incident and reflected polarization are represented by the arrows in the beams (ellipticity is not), while the magnetization of the sample is shown using the blue arrows in the plane. The direction of the Lorentz force is shown with the black arrow on the sample surface. The two longitudinal effects and the transverse effect require non zero angles of incidence, while the polar effect is largest for normal incidence. The two types of longitudinal effect are distinguished by the polarization being either parallel to the plane of incidence (and magnetization), or perpendicular.

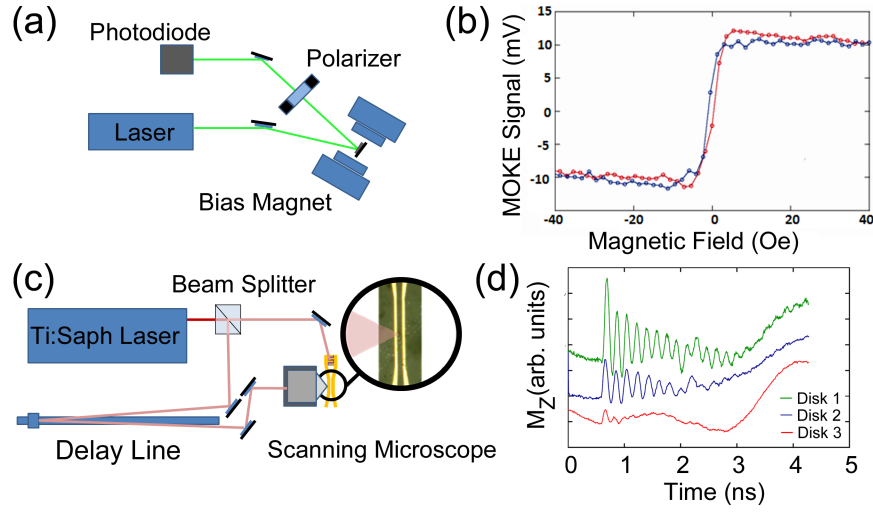


Figure 3.2: Basic schematics of the most common types of MOKE magnetometers are shown. At top a simple magnetometer operating in longitudinal mode is shown. The laser is polarized, and shifts in the polarization after reflection from the sample are converted to intensity variations by an analyzing polarizer. Many other elements can be added to the magnetometer, such a half-wave plates to control the laser polarization. Data taken from a 15 nm thick permalloy film using such an apparatus is shown in (b). Below, a simplified image of a TR-MOKE apparatus is shown. The laser pulses from the Ti:Saph laser are split. One set of pulses triggers a magnetic stimulus. In this case, a current pulse is launched down two coplanar transmission lines to apply a transient out-of-plane field between the lines. The other pulse is directed down a delay line, providing variable path length and hence, tunable time delay. This pulse is then directed through a scanning microscope objective and focused onto the magnetic sample. The reflection is collected and analyzed using a polarizer (not shown). Panel (d) shows the magnetic response of $2 \mu\text{m}$ diameter, 55 nm thick disks to a H_z pulse measured by changing the delay length. Dynamical modes excited by the pulse contribute oscillations in the measured magnetization.

Arguably, the most important application of MOKE now is the use of stroboscopic techniques to access information about the dynamics of magnets. First implemented in 1969 (144), time-resolved MOKE (TR-MOKE) was re-developed in the early 1990's (145), and popularized over the next decade (146–148). At the core of the technique is the application of a pulsed, usually titanium sapphire (Ti:Saph), laser to create a series of ultrafast pulses. Two trains of pulses are split generated, one pulse generates a pump stimulus that disturbs the magnetization of the sample, the second pulse arrives on the sample at a tunable delay providing a measurement of the magnetization at a particular time (Fig. 3.2). Tuning the delay results in time trace of the magnetization response to the stimulus. Clearly this technique functions most effectively with repeatable stimuli. TR-MOKE is now ubiquitous in the study of magnetodynamics. Particularly important to this thesis is the application of TR-MOKE to the vortex state in a disk (70, 87–90).

A more uncommon application of MOKE, but one particularly important to this chapter, is the use of AC fields to measure the susceptibility of samples. This approach, known as AC-MOKE, is typically used to study temperature driven magnetic phase transitions (31, 149) in samples, since $\chi = dM/dH$ is a divergent quantity at the critical temperature (150).

3.2 Thermal Driven Transitions in Magnetic Samples

The influence of temperature on magnetic samples is a rich field of study. Initial work by Brown (151) and Néel (152) resulted in a model of thermal activation very similar to the widely applied Arrhenius relation. This model is applied to the study of switching events of many systems. In particular, various thermal properties of vortices have been measured including temperature masked vortex pinning (153) in permalloy disks, thermally accessible vortex states in cobalt disks (154) and in rectangular ellipsoidal permalloy elements (155). These experiments yielded results that suggest, respectively, depinning and vortex creation are best described by a Néel-Brown (152) thermal transition. More recent work, applied directly to vortex annihilation, has found that at high temperature annihilation behaviour is dominated by variation of the saturation magnetization with temperature while a thermal activation description is applied at low temperatures (99). However, concurrent work has shown that the influence of field sweep rate supports thermal activation as the decay channel for vortices at room temperature (73).

Extensive investigation of switching in small single domain (\sim uniformly magnetized) elements was performed in the 1990's, where domain wall nucleation and magnetization reversal in small single domain particles were each investigated using sweep rate and temperature in the same experiment (49, 50). That work tested, and verified theoretical predictions for the switching distribution as a function sweep rate (156, 157) as well as the shape of the energy

barrier as a function of applied field. This previous work identifies a powerful method of investigating thermally activated transitions. Given an array of nominally identical magnetic elements, applying a field swept at a constant rate, random thermal fluctuations will induce individual elements to switch producing a switching distribution as a function of the field value (Fig. 3.3). The combined temperature and sweep rate dependence of the position of the distribution peak can be studied to extract energetic parameters such as energy barriers, as well as information about the method of switching.

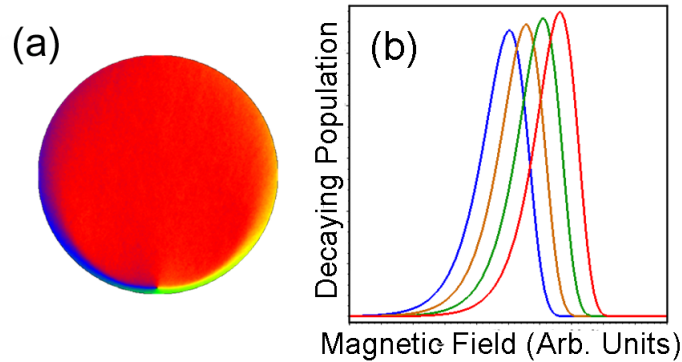


Figure 3.3: The annihilation process occurs when the vortex is very close to the edge of the disk (a). Close to the annihilation the quasi-single domain (QSD) is lower energy, however there is still an energy barrier related to expulsion of the core from the disk which must be overcome either by the application of more field, by thermal fluctuations, or by some other stimulus. For a typical bias field sweep on the sample, temperature and sweep rate can play a large role. The decay distribution for an element for a swept (from low to high) magnetic field is slightly asymmetric. Example decay curves computed for 4 arbitrary temperatures (Red low, Blue high) are shown in panel (b).

The recent works suggesting room temperature annihilation depends on material parameters (99) and on thermal activation (73) each present only half of the story. One tunes only temperature, the other sweep rate. The experiment described in this chapter aims to fill in the gap between the two using measurements of the decay distribution of an array of vortex state permalloy disks. Both sweep rate and temperature are changed to extract information about the annihilation energy barrier at temperatures near room temperature in order to clarify the role of the saturation magnetization and potential Néel-Brown transition in the annihilation process.

3.2.1 Study of Arrays

The prevailing approach for the study of magnetic micro and nano-elements has been to move from arrays to single objects. The motivation for this change is obvious: shifts in the sample can be interpreted much more clearly when this signal is not averaged over thousands of contributing elements. In this experiment, an array was chosen for two primary reasons. Even with a well-optimized MOKE magnetometer, it is challenging to acquire data from a single object in the micron size range. Typically, non time-resolved MOKE experiments on single objects use high powered lenses to focus high power onto the target (142), resulting in excessive sample heating. Clearly this would not be ideal for the study of thermal activation. More importantly, in the case where statistically significant sampling of events is important, an array massively enhances the efficiency of data acquisition, providing that all samples are behaving approximately identically. In the present case the vortex state can be confirmed as the ground state for the array, therefore each disk should proceed through a very similar annihilation on the field sweep from low field to high field. However, simulation showed that multiple vortex creation pathways were possible for $2\ \mu\text{m}$ disks. Therefore the array approach applied here is only applicable to the study of the annihilation transition.

An approximately simultaneous experiment was performed on a single disk using torsional magnetometry (73). This experiment was designed as a complement in order to study vortex creation. Pertinent to this discussion, is the fact that creation was found to be highly variable even in a single $1\ \mu\text{m}$ disk, further suggesting creation should not be studied by arrays. By contrast, annihilation events exhibited low variation, and a tight switching distribution. More details on this experiment may be found in Appendix E.

3.3 Experimental Design

In order to study the annihilation transition of the vortex state in a statistically significant way, an AC-MOKE susceptometer was constructed and applied to measure an array of permalloy disks. Using the high signal-to-noise provided by AC-MOKE, as well as an array, allowed single measurements to extract the annihilation peak without need of averaging to get a distribution, or to improve signal-to noise. This enables a significant quantity of data to be collected and permits a thorough investigation of annihilation.

3.3.1 Sample

The sample observed consists of an array of 15,000 $2\ \mu\text{m}$ diameter disks composed of permalloy. A large centre-to-centre spacing of $4\ \mu\text{m}$ ensures that the dipolar interactions

between individual disks are negligible. The disks were prepared by use of a silicon nitride shadow mask (158) and collimated electron beam deposition under UHV pressures ($\sim 9 \times 10^{-10}$ mbar). The masking process gives each disk a linearly sloped edge shape as seen in previous work employing shadow masks (159). See appendices B and D for more information on the evaporator and shadow masking process respectively. Film thickness is approximately 32 nm based on atomic force microscope (AFM) inspection (See Fig. 3.4b) while the observed linear slope in the disk edge profile is quite broad at an average 230 nm wide parallel and perpendicular to the fast scan direction. This breadth implies that the slope cannot be a tip radius imaging artifact in the AFM imaging. The disks have been deposited on a thermally oxidized silicon substrate with a 100 nm thick oxide layer.

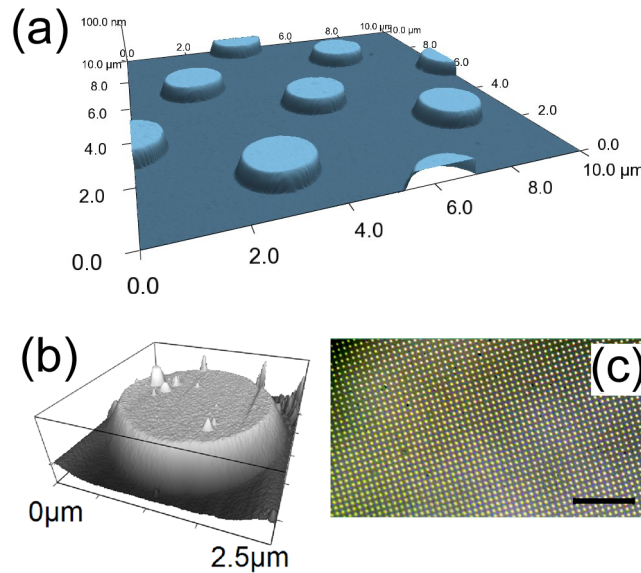


Figure 3.4: (a) An AFM image of a set of $2 \mu\text{m}$ in diameter permalloy, 55 nm thick disks prepared by shadow masking, and imaged immediately afterwards. The disks featured in this panel are identical, except for thickness, to those on the sample studied in this experiment. (b) An AFM image of a disk on the actual sample used is shown along with (c) an optical micrograph of the sample. The disks are $(1.98 \pm 0.01) \mu\text{m}$ in diameter, $(32 \pm 3) \text{nm}$ tall and are separated by a center to center spacing of $4 \mu\text{m}$. The scale bar on the optical image is $40 \mu\text{m}$ long. The height is exaggerated in the AFM data to show the approximately linear edge profile with a measured slope angle of $\sim 8^\circ$ over an edge width of $\sim 230 \text{nm}$. This is a side effect of the shadow masking deposition process. The small defects are dust which settled on the sample over the course of measurements; AFM images of fresh samples (panel a) show no significant defects.

3.3.2 AC-MOKE Susceptometer

The apparatus is a MOKE magnetometer that operates using the perpendicular longitudinal version of MOKE to measure the in plane magnetization response of the sample to an applied bias field. The MOKE apparatus uses a 532 nm laser (Coherent Verdi 5W) operated at 145 mW incident on the sample at an angle 55° from normal. A custom built collimating telescope is used to reduce the spot diameter on the sample to approximately $110 \mu\text{m}$. This results in a sampling of 1200 disks near the centre of the array. It was noted that any focusing effect of the telescope could have a significant effect on the measured MOKE signal therefore care was taken to ensure that the mean showed minimal divergence exiting from the telescope. The beam diameter was estimated by computing the transmission of a Gaussian beam through a set of pinholes of various sizes in comparison to the transmitted power.

The sample holder is composed of an aluminum slab bolted to a thermally insulating block. The sample chip is clamped onto the aluminum slab such that the array lines up over a pre-drilled hole in the aluminum slab³. Mounted behind the sample slab is an L shaped aluminum arm with a machine slot that holds a Hall probe (Senis C-H3A-2m e3d-2.5khz-1%-0.2T) in such away that the active area of the probe is aligned in two spatial dimensions with the hole sample slab, and is precisely 9.75 mm behind the sample. The insulating block holding the slab and L piece is then mounted on a three axis stage, allowing alignment of the sample to a fixed beam line, and also allowing the hall probe to be translated forward so that it is in exactly the same location as the sample for calibration purposes.

A thermal resistor may be mounted to the back of the slab and connected to a pulsed current supply with a temperature controller (Omega CN132). The slab is fitted with a thermocouple so that the temperature of the sample holder may be monitored. Even at 145 mW, the sample holder temperature was noted to increase a few degrees ($\sim 2^\circ\text{C}$). In order to confirm that the sample was not at a highly elevated temperature, a worst case finite element calculation of the heat sinking in the sample was performed. This assumed all 145 mW of laser power was absorbed into a $100 \mu\text{m}$ in diameter circle on top of a cylindrical section of silicon wafer 3 mm in diameter and 0.5 mm thick. This mimics the section of sample over the hole in the aluminum sample slab. The boundary condition at the edge of 3 mm section was fixed at a chosen temperature. It was found that even in this extreme case, heating of the sample over and above the rest of the Si wafer was minimal, and confined only to the immediate vicinity of the beam. Therefore, while there might be a small offset in sample temperature from the measured holder temperature, it is indeed very small, and will also be a constant offset present for all sample holder temperatures.

³The hole was originally included for transparent (sapphire) substrates to allow the active area of the sample to be backed by an index matching oil to prevent reflections from the back face of the sample substrate.

The bias field is applied in the plane of the sample and parallel to the plane of incidence of the laser, yielding a measurement of the in-plane magnetization through the longitudinal variation of MOKE (134). Rather than using an electromagnet to apply a bias field, a pair of permanent magnets are employed, one stationary and one mounted on a rail (Velmex Unislide MB2527CJ-S2.5) equipped with stepper motor (Vexta PK264-02A) (See Fig. 3.5a). To perform a hysteresis measurement, the rail mounted magnet is simply stepped through a cycle on the rail. Calibration was determined by shifting the hall probe forward to be in the sample position, and then calibrating the field as a function of steps taken by the stepper motor. Through careful positioning of the two magnets a sweep of -400 A/m to $+16,000$ A/m in x , while maintaining the y and z fields at (-200 ± 40) A/m and (160 ± 40) A/m respectively, is possible. The z axis is perpendicular to the sample plane. The sweeps have exceptional repeatability, the stepper motor was never found to ‘lose steps’, and there was no measurable degradation in the strength of the magnets over several months. Another benefit of mobile permanent magnets over electromagnets is the lack of heating, which can cause extraneous drift or unwanted temperature shifts. In this way stability and reproducibility of the magnetic field sweeps unobtainable with the typical electromagnet and power supply are achieved.

In order to attain the signal-to-noise needed to study very small shifts in the vortex annihilation field at sufficiently small optical powers that sample heating can be neglected, a lock-in technique known as AC-MOKE (31, 150) is employed. Typically AC-MOKE is used to probe the susceptibility of samples near temperature-driven phase transitions or in other low signal scenarios (150). A low frequency, 525 Hz, AC field is applied along the \hat{x} direction using a coil.

This provides a sensitive measurement of the sample susceptibility which reveals, directly, any hysteretic changes in the sample including vortex annihilation and creation. To study the annihilation field, a rectangular wave dither, with an offset so that the dither field ranges from -320 A/m to $+0$ A/m, is applied. This waveform is chosen to prevent the dither from increasing the total applied magnetic field beyond the bias field value and significantly influencing the decay behavior. The amplitude is well above recently reported values of switching distribution widths for single disks (73) meaning that decays are only likely during the 0 A/m portion of the dither. Use of a coil with inductance such that its cut off frequency is ~ 1.2 kHz ensures that the dither remains interpretable as a quasistatic applied field. The low frequency prevents any activation of dynamical magnetic behavior.

3.3.3 Optimization

The MOKE magnetometer is operated in a differential configuration. The reflected beam is passed through a Glan-Thompson prism (Thorlabs GT10-A) mounted on a precision

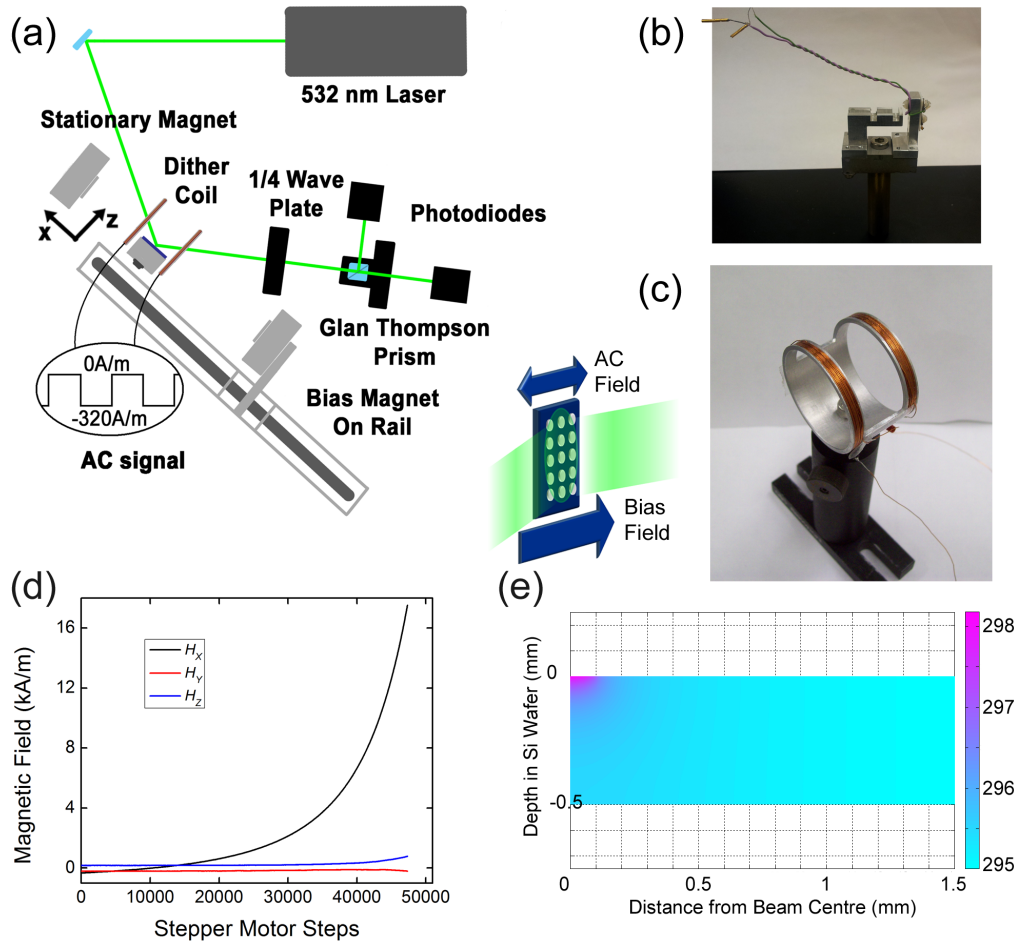


Figure 3.5: (a) The apparatus diagram is shown at top. A differential measurement scheme using the reflected beam from a Glan-Thompson prism as a reference scaled and subtracted from the transmitted signal beam. The sample holder consists of an aluminum block with an L-shaped Hall probe mount behind it (b). A small air core coil is used to apply a low frequency magnetic field in the plane of the sample and introduce an AC component in the measured MOKE signal (c). The transmitted signal is fed into a lock-in amplifier to detect the AC response while the DC signal is recorded simultaneously using a standard DAC board. Inset near the coil is a schematic of the typical asymmetric rectangular AC drive signal used. The bias field is provided by a permanent magnet mounted on a rail driven by a stepper motor. The field is primarily in x with minimal y and z components that vary minimally (d). Solving the heat equation for the sample wafer with a worst case scenario (complete absorption) treatment of the incident laser beam shows that the sample area will be heated minimally (e). The beam is incident at $(0, 0)$ on the silicon wafer. The calculation is performed on a reduced cylindrical representation of the wafer 1.5 mm in radius. The boundary condition at the radial edge is held constant at 295 K, representing heat sinking of the wafer to the aluminum block.

rotatable mount (Thorlabs PRM1 GL10) aligned such that the transmitted (signal) beam is close to being minimized, while the bulk of the power in the specular reflection is redirected to the reflected ray (the reference beam). Each beam is detected using a large area silicon photodiode (Thor Labs SM1PD1A) connected to a low noise dual input preamplifier (SRS SR560) operated in differential mode; subtracting the reflected signal from the transmitted. The preamp output is recorded using a DAC (National Instruments USB 6221) as well as fed into a lock-in amplifier (SRS SR830) to detect the AC signal. Each photodiode is connected in parallel with variable resistor to providing various levels of transimpedance gain⁴. Additionally a variable neutral density filter (New Focus 5215) is placed on the reflected beam path. Tuning transimpedance gain and the neutral density filter allows approximate balancing of the signal and reference levels to reduce drift.

Optimization of the MOKE signal is quite an important topic for MOKE magnetometry. It was first mentioned by Rhigli (*136*) that the best signal can be obtained by tuning the axis of the polarizing prism such that the transmitted signal is very close to, but not quite at the minimum. Transmission through the polarizing prism follows Mallus' Law, so that the transmitted power follows a square cosine relation as a function of the angle between the beam polarization and the transmission axis of the polarizer. Logically, one might expect that, particularly in light of the differential mode, that the optimum angle would be 45° from minimum transmission. However this is not the case in a practical apparatus where the noise level of the system also increases. This means the optimal signal-to-noise occurs for a small, finite rotation of the polarizing prism away from minimum transmission. Additionally, the ellipticity introduced into the reflected signal may be converted into additional rotation by use of a quarter wave plate. Here such a plate was used. A full treatment of the problem is given by Allwood et al. (*137*).

In practice it is easiest to experimentally determine the optimal angle for signal-to-noise. This is particularly easy to do with an AC-MOKE susceptometer where signal-to-noise is proportional to the ratio of the lock-in signal and fluctuations in the recorded DC signal. It is then simple to determine the approximate optimal angle (Figure 3.6). In this experiment it was found that the optimal angle was usually between 1 to 5° depending on the termination resistor used for transimpedance gain. Optimization of the quarter wave plate was performed prior to optimization of the Glan-Thompson prism.

Subtleties in the process of changing the prism angle make this process time consuming. These include repositioning optics for the reflected ray and adjusting the neutral density filter and transimpedance gains to avoid saturating the photodiodes. A particular point is the avoidance of reflections. In particular reflections inside the Glan-Thompson prism

⁴Photodiodes operate as current sources with limited voltage output and current output proportional to the incident optical power. Therefore changing a shunt resistance tunes the sensitivity of the photodiode.

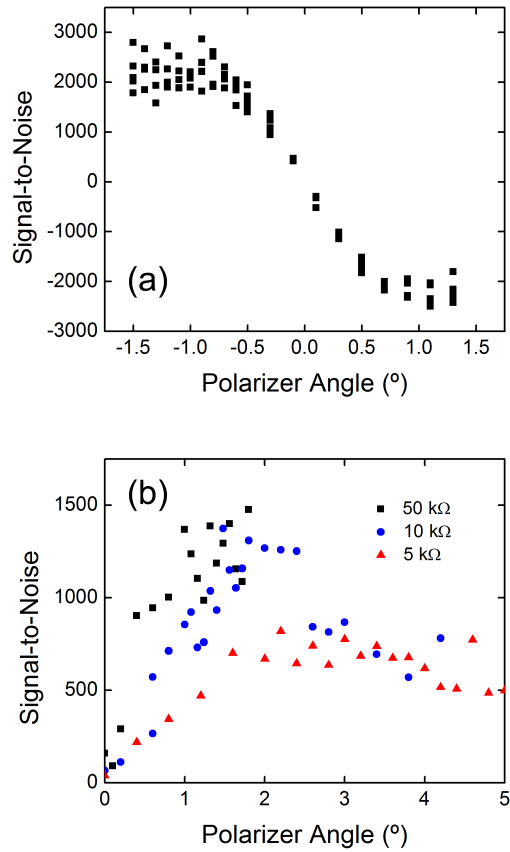


Figure 3.6: Optimization of the MOKE signal is very important. The signal is generally weak, and can be challenging to detect. Optimization is driven primarily by the angle of the analyzing polarizer away from the point of minimum transmission. In panel (a) a measurement of the signal-to-noise for the AC signal is shown (computed as $S/N = \text{AC Signal}/\text{Std. Err. in AC signal}$). This measurement was performed with a $50 \text{ k}\Omega$ termination resistor. There is a clear plateau in the signal-to-noise. In panel (b) three other optimization curves are shown for transimpedance gain resistors of 50, 10, and $5 \text{ k}\Omega$. The lower resistance curves extend to larger polarizer angles because the photodiode output is saturated for lower angles.

appear to cause an interference effect that modulates the signal-to-noise. Therefore the use of irises or other beam blockers is recommended to mitigate this problem.

3.4 Susceptibility of the Vortex State

In the vortex state, the disk shows a reasonably high degree of susceptibility. As the field biases the disk, and shifts the core, the potential confining the vortex to its equilibrium position stiffens, reducing susceptibility. The AC-MOKE signal directly measures this susceptibility. Figure 3.7a shows the simultaneously recorded DC-MOKE signal, proportional to the net magnetization, M_x . The sample exhibits a classic vortex hysteresis loop showing a transition to the quasi single-domain (QSD) state at ~ 12.4 kA/m and the nucleation of the low remanence vortex state at ~ 3 kA/m. The AC signal reveals a complementary loop (See Fig. 3.7b) showing a steadily decreasing susceptibility of the vortex state as the vortex is pushed closer to the disk edge, followed by a drop off in signal as disks in the array switch to the QSD state. On the reverse sweep the AC signal shows a kink preceding the rise in signal corresponding to vortex creation. This feature may be a signature of a buckled transition state (102) preceding the nucleation of the vortex state. Investigation using single disk measurements and simulation are required to further elucidate the nature of this kink.

3.4.1 Hysteretic Transitions

In application of AC-MOKE to micromagnetic samples, part of the technique's power is revealed by taking the numerical derivative of the DC signal for comparison to the AC measured susceptibility (Fig. 3.8). Deviations between the two immediately indicate irreversible changes. In a hysteretic response, the jump due to the event shows up in the DC signal, while in the AC signal the hysteretic shift will not respond to the AC dither. In particular over the annihilation field range the distribution of annihilation fields can be extracted by noting that a surviving vortex has a non-zero susceptibility which is measured by the AC signal, while the QSD state has a negligible AC response. Thus, though the DC-MOKE slope increases, the drop off in the lock-in signal is linearly proportional to the number of decayed vortices in the sample. This property gives AC-MOKE the ability to quickly map out hysteretic changes. Slight deviations which do not appear consistent with vortex annihilation precede the nominal annihilation range. These may indicate the observation of minor hysteresis processes as recently reported for single disks (99). Experiments on this sample, with minor hysteresis loops near annihilation, failed to confirm this.

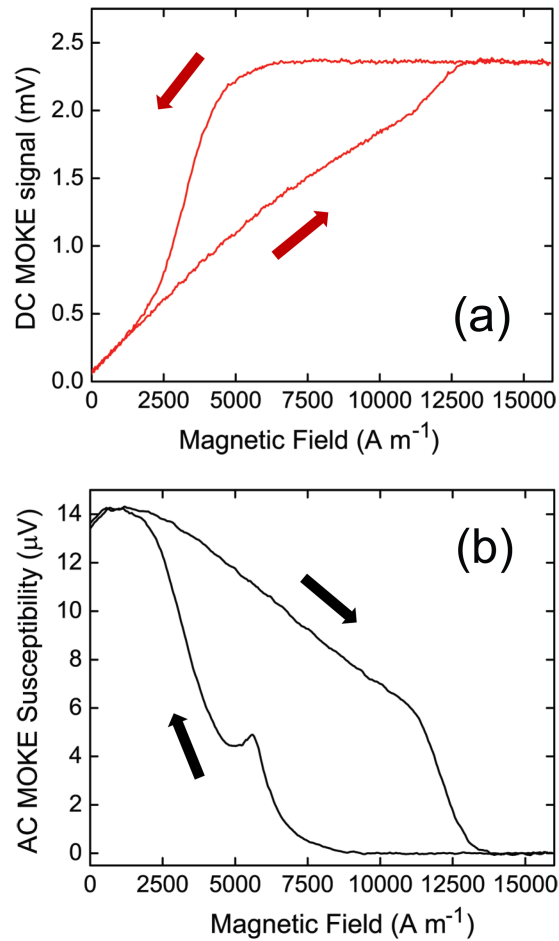


Figure 3.7: (a) The DC-MOKE signal exhibits a typical single-sided hysteresis loop indicating the presence of a vortex state. The measured Kerr signal is linearly proportional to the magnetization of the sample. The slight offset from zero is arbitrary and is introduced by the preamplifiers in the differential measurement process. This loop is the average of 100 measurements. (b) The AC-MOKE signal is proportional to the susceptibility of the sample. This data was acquired with a 240 A/m peak to peak sinusoidal AC field with a frequency of 525 Hz in a single measurement.

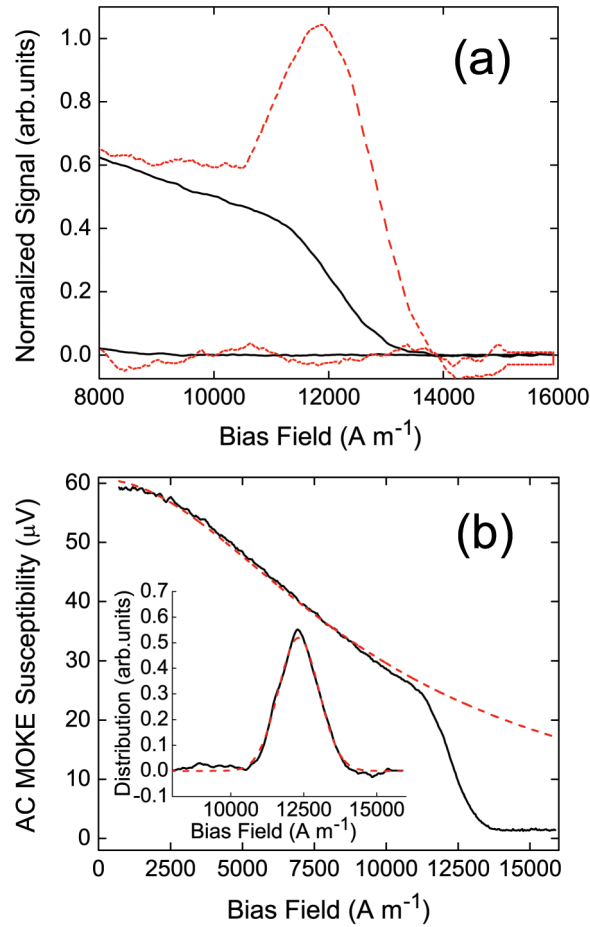


Figure 3.8: (a) The numerical derivative of the DC MOKE signal (dashed red line) is plotted with the measured susceptibility signal (black solid line) over the annihilation range. The irreversible processes are immediately highlighted by the disagreement where a vortex annihilation appears as an increased signal in the DC derivative, and a drop in the AC. (b) The analytical rigid vortex model allows extrapolation of the response of the disks into the annihilation region. The experimental data (solid black line) was acquired with an asymmetric $320 A/m$ square AC field while the fit (dashed red line) uses a saturation magnetization of $715 kA/m$, a demagnetization factor of 0.0168 and an exchange length of $5.85 nm$. Inset below is the extracted experimental distribution (solid black line) with a Gaussian fit (dashed red line). Panel (b) shows the sample holder with the L-shaped Hall probe holder, while (c) shows the AC coil. Panel (d) shows the field calibration with stepper motor position. The results of a finite element computation of sample holder heating due to the laser are shown in (e).

3.4.2 Analytical Model

In order to accurately fit the measured susceptibility data, an analytical model was needed. In this instance the usual micromagnetic simulations are inadequate as it has been demonstrated that vortex decay can occur on extremely long time scales well beyond feasible numerical simulation (70). Hence it is important to employ analytical theory for interpretation of the influence of the micromagnetic state. This provided this initial motivation to develop the analytical models described in Chapter 2, in particular the third order extension of the Rigid Vortex Model (RVM). Details of the derivation and result will not be repeated here, however it will be reiterated that this model is capable of extrapolating the magnetization and susceptibility of the sample accurately out to the vortex annihilation field. Moreover, it depends on real physical parameters of the the sample. The susceptibility may be expressed as $\chi(h) = dm(h)/dh$ where $m(h) = m(s_o(h) - s_o(h)^3/8$ and $s_o(h)v = \Delta r(h)/R$ is given by equation 2.8 in Chapter 2.

3.4.3 Extraction of Physical Parameters

The presence of physical parameters such as saturation magnetization (M_S), and demagnetization factor ($F(L, R)$) allows extraction of information about the properties of the disks in the array from the fit. It is important to note that fitting here must be approached cautiously as the demagnetization factor and saturation magnetization are coupled, and affect the susceptibility curves in similar ways. Subtle differences in the curvature caused by each parameter aid determination of the parameters somewhat, but confident determination of parameters remains a challenge. In this case, an estimate of saturation magnetization was available from TR-MOKE measurements on disks made with the same evaporator providing a starting point for room temperature (M_S) of 700 kA/m (See Figure 3.2 for example data). Starting from this point, initial fits required an M_S close to this value, a fit exchange length equal to the exchange length calculated from the fit (M_S). This resulted in parameter values of (715 ± 5) kA/m for M_S and (0.0168 ± 0.0002) for the demagnetization factor. These values provide an excellent description of these disks. The fit exchange length was 5.85 nm, equal to one calculated from M_S assuming an exchange constant of 1.1×10^{-11} J/m. A disk radius of 990 nm was used.

The demagnetization factor extracted from the fit was initially regarded as surprisingly low. This work was performed prior to the incorporation of a susceptibility correction into the demagnetization factor. The expected, non-susceptibility corrected demagnetization factor was 0.026 (123, 124). At the time, it was speculated that the large sloped edges of the disk resulting from shadow masking may account for this difference based on the work of Pütter et al. (160). However relative difference of 0.32 is quite large. Comparing demagnetization

energies of simulations of disks run with and without sloped edges suggest corrections up to 0.1 or even 0.2 could be possible depending on the slope and disk size. This was therefore an optimistic speculation. However, if one computes the susceptibility corrected value (123,124) for the demagnetization factor, it is approximately 0.0175. The remaining difference between the fit value and the susceptibility corrected value is then easily explained by the influence of the sloped edges. This provides a rough empirical verification of the applicability of the susceptibility correction in addition to the simulated evidence presented in Chapter 2.

3.5 Annihilation Transition

The decay of the AC-MOKE signal as vortices annihilate, combined with an analytical model that remains applicable from $h = 0$ out to the annihilation field for the estimation of $m(h)$ and $\chi(h)$ allows a very convenient extraction of the vortex annihilation distribution.

3.5.1 Extracting the Distribution Peak

Using the extrapolated susceptibility the switching distribution can be extracted. Taking the difference between the extrapolated susceptibility and the data at each field, and normalizing by the extrapolated value, as a representation of what the AC susceptibility would be if all vortices were still present, yields the cumulative switching distribution of the vortex population in the array. Differentiating with respect to applied field then yields the switching distribution which agrees very well with a Gaussian decay profile (See Fig.3.8b). This suggests that the decay profile is dominated by disk size and shape variation within the array, since an asymmetric distribution is expected for a switching spread dominated by thermal switching (157, 161). Knowing that a Gaussian distribution is then appropriate, a function describing the measured susceptibility over the full field range (Equation 3.1) may be fit to the signal directly to extract the mean annihilation field and standard deviation:

$$Y(h) = \frac{N}{2} [\chi(h) (1 - \text{erf}(h, h_a, \sigma_a)) + Q_o (\text{erf}(h, h_a, \sigma_a))], \quad (3.1)$$

where $Y(h)$ is the signal, $\chi(h)$ is the normalized susceptibility calculated from the third order model, h_a is the mean and σ_a is the standard deviation of decay distribution. In the fit procedure a normalization factor was employed, N , and an offset, Q_o , to account for the response of the QSD state of the disks to the dither. Any field dependence of the AC response of the QSD is imperceptible in the raw data. A small decrease as the QSD becomes more rigid at high field is expected, but could easily be canceled by a small angular misalignment of the dither coil. The fit parameters are effectively determined by separate

parts of the curve. The values of M_S , $F_c(L, R)$ and R_o used in χ are taken from the previous fit of the RVM to the susceptibility curve measured up to the start of annihilation while the normalization factor and offset are effectively fixed by the sections of the curve before and after the annihilation range. This results in an equivalent two parameter fit for the mean and standard deviation of the decay distribution.

For the nominal standard sweep rate of 40 A/m-s at room temperature, the approximate peak value is (12370 ± 30) A/m and the standard deviation is (635 ± 15) A/m. The standard deviation is significantly larger than recently measured decay distribution widths (~ 80 A/m) for single disks (73). This further suggests that the decay distribution *width* is dominated by variations between disks.

The combination of the lock-in technique, the use of an array, a highly stable MOKE apparatus and the developed model enables a large number of experiments to be performed to test the change in the switching distribution as sweep rate and temperature are tuned. As a standard approach, a four parameter fit is used to extract the mean and standard deviation, while allowing the scale factor to vary in order to compensate for inter-run drift. The offset was allowed to vary on some fits to account for variable noise fluctuations in the low signal QSD region, though the fit value typically remained constant at a value approximately two orders of magnitude smaller than the zero field vortex response. The fitting procedure provides highly stable results for the mean annihilation field, while power fluctuations, particularly during very long runs where power could drift as much as 10 mW over several hours, introduced more scatter into fit values of the standard deviation. Long term runs show variation in the standard deviation of up to 50 A/m compared to the more stable, fast runs used to calculate the measured standard deviations stated above.

3.5.2 Temperature Dependence of the Saturation Magnetization

The only exception to this fitting procedure is in the temperature variable results where M_S must be determined individually for each data point in order to maintain a good fit of the calculated RVM susceptibility to the data. This enables an experimental measurement of the appropriate $M_S(T)$ for this sample. The general trend showed a decreasing M_S with increasing T and allowed the extraction of a coefficient for the Bloch $T^{3/2}$ law (26) where $M_S(T) = M_S(0)(1 - gT^{3/2})$ with $g = (2.1 \pm 0.2) \times 10^{-5} K^{-3/2}$ and $M_S(0) = 805$ kA/m (See Fig. 3.9a). This is a relatively large coefficient, approximately double the expected value for permalloy (99, 162, 163). Calculating individual M_S values for runs with no temperature variation showed no change in M_S with changing sweep rate. From the fits of equation 3.1 to the data, an additional decrease in the fit standard deviation with increasing temperature was found. The fit standard deviation was (610 ± 15) A/m at 50°C, significantly lower

than the room temperature value. This runs counter to the model of thermally activated decay, which would suggest increasing standard deviation (50), but does make sense within the context of an array. As the temperature rises, pinning sites on individual disks which contribute to variation in annihilation statistics, become less effective and hence one might expect the array distribution to decrease. This suggests strongly that pinning sites, and consequently depinning like processes, play a prominent role in the annihilation.

3.5.3 Temperature and Sweep Rate Dependence

The extracted means allow examination of shifts of the distribution peak with both temperature and sweep rate. In turn this allows comparison of results to the semi-empirical model for a switching process governed by an Arrhenius relation under a continuously swept field developed in previous work (156, 157, 161). Comparison to the model is valid despite the presence of the array. The disk spacing is double the disk radius, easily satisfying the previously derived condition (116) under which dipolar coupling can be neglected for calculation of the annihilation field. This means the disks are effectively independent. The expected peak shift is given

$$H_a = H_o \left\{ 1 - \left[\frac{k_B T}{E_o} \ln \left(\frac{S_R E_o}{k_B T H_o A_o} \right) \right]^{\frac{1}{\alpha_d}} \right\} \quad (3.2)$$

where H_a is the peak position, A_o is the constant attempt frequency in the Arrhenius expression, S_R is the sweep rate of the field, and the energy barrier used is $\Delta E = E_o (1 - H/H_o)^{\alpha_d}$ with empirical values for the critical field H_o and initial energy barrier, E_o extracted from the model fit. The exponent α_d has been previously identified as 3/2 for domain walls depinning (157), and 2 for flipping of single domain particles (50) although other integer and half integer values are possibilities (161). Previously this model was applied to low temperature results where M_S may be considered constant with temperature (49) and as such, must be modified by the introduction of the Bloch $T^{3/2}$ law. A variation of $H_o(1 - gT^{3/2})$ is assumed, reflecting the dependence of the calculated annihilation field on M_S (116). The value of the coefficient g is $2.1 \times 10^{-5} \text{ K}^{-3/2}$ determined from the measured $M_S(T)$. An additional temperature dependence of the energy barrier on M_S is considered. It is based on the typical energy normalization with respect to $\mu_0 M_S^2 V$ used in the RVM yielding $E_o(T) = E_o(0)(1 - gT^{3/2})^2$. For the attempt frequency, a value of $A_o = 50 \text{ MHz}$ is used as an approximation of the gyrotropic frequency of the disk; the fit, however, is relatively insensitive to the specific value of A_o . The sweep rate is varied by adding wait times at each data point. The effective sweep rate is calculated as $S_R = \Delta H / (\Delta t / 2)$ where ΔH is the step size between data points and Δt is the added wait time. The factor of two takes

into account the influence of the AC field reflecting the assumption that vortex decays only occur with reasonable probability on the 0 A/m half of the AC square wave.

To obtain the peak shift with temperature, a feedback loop is used to control the sample holder temperature while taking field sweeps over the annihilation range. Since the sample was kept in atmosphere, experiments were limited to a narrow temperature range ($\Delta T \sim 29^\circ\text{C}$) to avoid condensation and oxidation. Measurements employed a sweep rate of 40 A/m·s with step sizes of 40 A/m and 8 A/m to take multiple sets of data.

Fitting equation 3.2 to the temperature data alone is challenging (See Fig. 3.9b). The slope is affected by g and E_o , however with the large value of g from fit M_S data, the slope effectively matches the peak shift within error only telling us that the energy barrier is large. With the slope dominated by g , the energy barrier and critical field effectively both offset the fit curve vertically without significantly impacting the slope, precluding the extraction of either accurately.

Changing the sweep rate provides a key companion plot (See Fig. 3.10). In the case of constant temperature, the slope on a log plot of the peak shift against sweep rate is determined effectively by the energy barrier alone. This allows us to determine the energy barrier from the sweep rate slope, g from the $M_s(T)$ data and H_o from the temperature data. Combining these three plots is critical to constraining the fit to extract accurate values for E_o and H_o for a chosen α_d . Simultaneously fitting both plots gives good agreement using an exponent of $\alpha_d = 3/2$ for an energy barrier of $E_o(0) = (8.5 \pm 1.0) \times 10^{-18}$ J and a critical field of $H_o(0) = (14500 \pm 60)$ A/m. This corresponds to a room temperature $E_o = (6.8 \pm 1.0) \times 10^{-18}$ J and $H_o = (12950 \pm 60)$ A/m. In Figures 3.9b and 3.10, five different curves are shown. Three curves are created by varying energy barriers, the remaining two curves used varied critical fields. The curves are color coded identically in both figures so that together, they show the error range and overlap of the two data sets. Using the extracted parameters, the calculated switching distribution full width half maximum for a single disk was ~ 60 A/m, compatible with the observation that array variation dominates the distribution width. A ~ 50 A/m offset exists between the temperature data and the delay data. This might be attributable to subtle shifts of the beam position on the sample. Slight random shifts were noted on an approximate several day to week time scale. Much more infrequent larger hysteretic shifts correlated with realigning optics; allowing identification of beam position as the cause of the shifts. Each set of data acquired as a function of magnetic field sweep rate was taken within the same time period where no significant shifts occurred, with temperature data taken both before and after this time period. Slight shifts, probably due to thermal expansion in temperature cycling the sample holder, separate the temperature data at room temperature and the sweep rate data at 40 A/m·s as a result of non-simultaneous data acquisition.

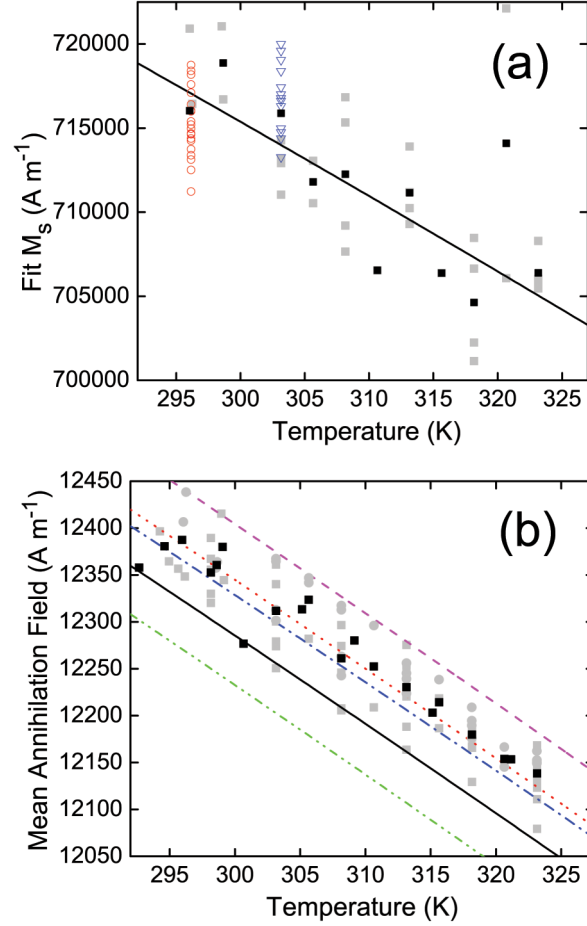


Figure 3.9: (a) The fit results for the saturation magnetization as a function of temperature. The black squares indicate results from rapid temperature sweeps performed within one day, while the open red circles and open blue triangles are results from longer term delay measurements performed at fixed temperatures of 23°C and 30°C respectively. The fit line uses a coefficient of $g = 2.1 \times 10^{-5} \text{ K}^{-3/2}$. (b) The fitted mean annihilation field as a function of temperature shows a distinct trend. Averaged data binned in 0.7°C bins is shown with black squares, while the raw data is shown as light grey points. Five fit curves are shown. In order from bottom to top, the green (double dot dashed), black (solid) and blue (single dot dashed) lines use energy barriers of $E_o(0) = 7.5 \times 10^{-18} \text{ J}$, $8.5 \times 10^{-18} \text{ J}$ and $9.5 \times 10^{-18} \text{ J}$ respectively in conjunction with a critical field of 14300 A/m , while the red (dots) and magenta (dashed) lines use critical fields of 14500 A/m and 14570 A/m with an energy barrier of $8.5 \times 10^{-18} \text{ J}$.

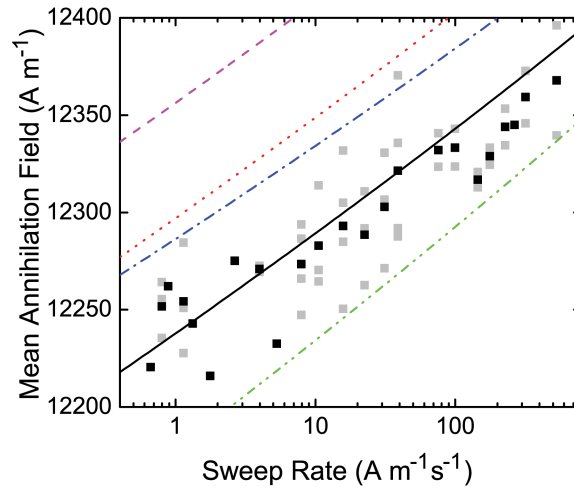


Figure 3.10: Changing the sweep rate by adding delays at each data point results in a decrease in mean annihilation field. The trend is logarithmic, in agreement with the applied model. The temperature and sweep rate results agree with the same parameters within a 50 A/m offset. Averaged data is shown with black datapoints, while the raw data is shown as light grey data points. The five fit curves shown are color coded to match the fit curves on the temperature plot. In order from bottom to top, the green (double dot dashed), black (solid) and blue (single dot dashed) lines use energy barriers of $E_o(0) = 7.5 \times 10^{-18}$ J, 8.5×10^{-18} J and 9.5×10^{-18} J respectively in conjunction with a critical field of 14300 A/m, while the red (dots) and magenta (dashed) lines use critical fields of 14500 A/m and 14570 A/m with an energy barrier of 8.5×10^{-18} J.

Other models were considered in fitting this data. If the effects of $M_s(T)$ on H_o and E_o are neglected, the result is a highly simplified Arrhenius model. To capture the slope of the peak shift with temperature in this case, E_o must be decreased over an order of magnitude. This then gives a fit curve for the sweep rate results with a much steeper slope than is seen experimentally. This supports the conclusion that at high temperatures, the variation of $M_S(T)$ cannot be neglected. This effectively resolves the potential conflict between previous results (73,99), revealing that the decay channel follows thermal activation, but is constrained by the overall energetics of the disk. At high temperatures, due to the large change in M_S , which sets the overall energy level and is manifest primarily through the empirical critical field, the thermal activation channel is very difficult to extract from temperature results alone. In the integration of the $M_S(T)$ data, the expected effects on the energy barrier are also included, however the qualitative properties of the fit are not significantly affected by neglecting this possibility and taking only $H_o(T)$ into account. The temperature range probed is not large enough to verify the form of temperature dependence of $E_o(T)$.

Recognizing the generality of a power law model for the energy barrier, slight variations of the power law scaling were investigated using different values of α as well as the energy barrier extrapolated from the third order RVM. Using equations 2.8 and 2.7 from Chapter2, it is simple to calculate an energy barrier for annihilation ($s_o=1$) as a function of h . For the disk size used in this experiment, the expected peak switching field is found to be 19.2 kA/m. The calculated energy barrier is large and has a gentle slope with an energy barrier approximately an order of magnitude larger than those attained for the power law model. This is much too large a barrier to explain the present results. This does not call into question the validity of the RVM or the extrapolation, rather it demonstrates that the excitation is not over the whole disk and must be triggered by a local process with the energy scaling given by M_S . This is not surprising given the size of the disks.

It is valuable to attempt to determine the appropriate α_d as this may shed light on the local excitation process. Different values of α_d including a linear barrier, $\alpha_d = 2$, and $\alpha_d = 5/2$, give good fits to the data. As with previous results (49), it is difficult to distinguish which fit is best. Fitting with $\alpha_d = 1$ results in a best fit energy barrier of $E_o(0) = (2.8 \pm 1.0) \times 10^{-18}$ J and a critical field of $H_o(0) = (14240 \pm 60)$ A/m while $\alpha = 2$ yields $E_o(0) = (2.5 \pm 1.0) \times 10^{-17}$ J and $H_o(0) = (14580 \pm 60)$ A/m, finally, $\alpha = 5/2$ gives $E_o(0) = (6.1 \pm 1.0) \times 10^{-17}$ J and $H_o(0) = (14780 \pm 60)$ A/m. In the consideration of a local process, the concept of an activation volume can be valuable. Converting the energy barrier to a volume by $\mu_o M_s^2 V$ cylinders of diameter ~ 13 nm, ~ 23 nm, ~ 40 nm, and ~ 60 nm are obtained for $\alpha = 1, 3/2, 2$, and $5/2$ respectively for these 32 nm thick disks. However qualitative considerations argue that the exponent $3/2$ is physically the most compelling choice since it is clear that pinning sites play a prominent role in the annihilation process. Other recent results have confirmed

the prominence of pinning in annihilation with single disk observations (73). Previously, an exponent of $3/2$ was found to describe a domain wall depinning based magnetization reversal (49, 157) and based on the trends seen here, it may be conjectured that this process is analogous to vortex annihilation. A local depinning event is a good candidate for the local lower energy process which triggers the annihilation.

For experimental verification of the power law exponent and determination of the temperature dependence of the energy barrier, a significantly larger range of temperatures should be probed.

3.6 Pinning in an Array

The data taken in this experiment clearly contains information about vortex creation, and less obviously, about pinning effects. However, due to the use of an array, interpretation of this data is inherently speculative. Appendix E describes concurrent work using a single disk to study the creation process. The observation of pinning effects in an array is surprising. It also provided some experimental motivation for the study of suppressed susceptibility during pinning which is covered in Chapter 2 and Chapter 4.

AC-MOKE susceptometry is, compared to regular MOKE magnetometry, a high signal-to-noise technique. In fact, it was noted that the noise pattern in some data sets was persistent from data run to data run under varied experimental conditions (Fig. 3.11). The reproducibility of the minute changes in susceptibility are interpreted as the effect of a certain number of vortex cores within the array being pinned, and therefore having suppressed susceptibility. Normally one would not expect to see this effect in an array, however, the susceptibility is very sensitive to pinning. For the typical signal-to-noise seen in the measured susceptibility changes in the number of disks exhibiting pinning at any one time as small as 10 disks might be resolved. This effect was only visible with small amplitude AC fields, corroborating its interpretation as pinning.

Some interesting information may have been accessible using MOKE susceptometry, however it is not the optimal way to study and understand pinning of the vortex state in a disk. Chapter 4 is devoted to studies of single disks and the pinning effects observed.

3.7 Revised Apparatus

The MOKE susceptometer developed proved to be a powerful tool in studying vortex decay. However it is clear that more could have been learned about annihilation if a greater

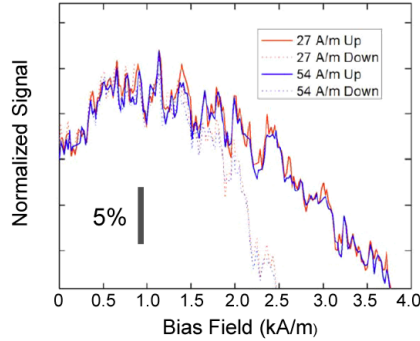


Figure 3.11: Two different hysteresis loops taken with differing, low amplitude sinusoidal AC fields are overlaid. The two noise patterns match closely. The noise was also found to be robust with field sweep rate and from day to day. No matching noise pattern was found in the measured bias field. The reproducible noise is attributed to fluctuations in the number of disks exhibiting pinning at any one time. The inset scale bar indicates the amplitude of the magnetization response normalized to the maximum signal value.

temperature range was accessible. Therefore a small vacuum chamber was built to house the sample on a cold finger.

The chamber is a simple design (Fig. 3.12), made primarily of non-magnetic⁵ stainless steel. A custom window was made with no glass to metal seal and instead uses o-ring seals. The sample sits on a copper plate, that is screwed down to two stacked thermo-electric Peltier cells (TE Technology VT-127-1.4-1.15-71R). These cells in turn sit on top of a copper cold finger that has a continuous flow of liquid nitrogen, or some other cryogen (methanol/dry ice slurries and chilled water were also used). The Peltier cells provide limited cooling capacity (negligible for low temperatures). However they can provide effective heating when current is reversed. They are therefore useful for gentle cryogen free cooling near room temperature as well as providing tunable temperature via heating when a cryogen is being used. The cells are driven by DC power supplies (BK Precision 9120A and 1788). The chamber is held at vacuum by a Varian 8L/s ion pump with a Varian Microvac controller. At the pump inlet, the chamber pressure is $\sim 5 \times 10^{-7}$ mbar, however due to conductance limited pumping down the long bellows, the chamber head will be much closer to $\sim 1 \times 10^{-4}$ mbar.

An important detail is the placing of the AC coil. It is best to include a small coil inside the chamber rather than outside. Outside the chamber, the AC coil will cause a Faraday effect

⁵Non-magnetic stainless steel is not a fair thing to say. Even with alloys that are supposedly completely non-magnetic, one may encounter residual magnetism. Each component of this chamber was selected for minimal magnetic response.

in the glass window which will dominate the response of the sample and complicate analysis. With the coil inside the chamber, only a small stray field affects the glass. A unique design of coil, employing an angular split in the coil (coils are not parallel) was used. This allows the coil to be lower profile, as well as to allow greater optical access for the laser. The field of the coil cannot be computed easily, though it is reasonable easy to measure, and the coil geometry introduces some out of plane field. The out of plane field has little effect on an in plane vortex state and its transitions.

Preliminary testing on the chamber showed it was functional between 100 K up to room temperature. However there were some significant challenges. The cold finger is mounted on thin walled stainless steel to minimize thermal conductivity to the chamber, however heat transfer to the chamber will occur. This combined with thermal contraction in the cryogen lines tends to cause a tilt in the chamber. This can be avoided with an aluminum brace to support the cold finger sidewall and prevent the tilting. An additional copper ring with thermal resistors may be attached to the chamber to provide heating near the attachment point of the stainless steel tubing.

The above problems were solved, however two problems remain. The temperature control for the cold finger is poor at best. The problem is that the chamber relies on boil off pressure in a dewar of liquid nitrogen. This provides an inconsistent flow. A cryogen source with a controlled flow rate should solve this problem. The other issue is the thermal contraction of the cold finger. The sample is slowly shifted as the cold finger expands and contracts. To correct this, the sample position must be corrected for at each temperature. This would be annoying, but not impossible to deal with if a constant temperature could be maintained for the cold finger, however it proves insurmountable combined with the poor flow control. Significant work and some new equipment could allow the susceptometer to become a very powerful instrument.

Despite the issues, the chamber provided some useful data. Measurements of the annihilation distribution peak showed a cross over in behaviour. This indicates a change in the dominant influence on the temperature dependence of the annihilation peak field. This is a cross over from the effect of the temperature dependence of the saturation magnetization, to a regime where saturation magnetization is approximately constant, and thermal activation remains. This cross over was previously found in the work of Mihajlovic et al. (99), though that work ignored the influence thermal activation at temperatures above this cross over point.

3.8 Conclusion

AC-MOKE was applied in a novel fashion to study the switching properties of arrays of micrometer scale thin film ferromagnetic disks. This technique was exploited to extract a

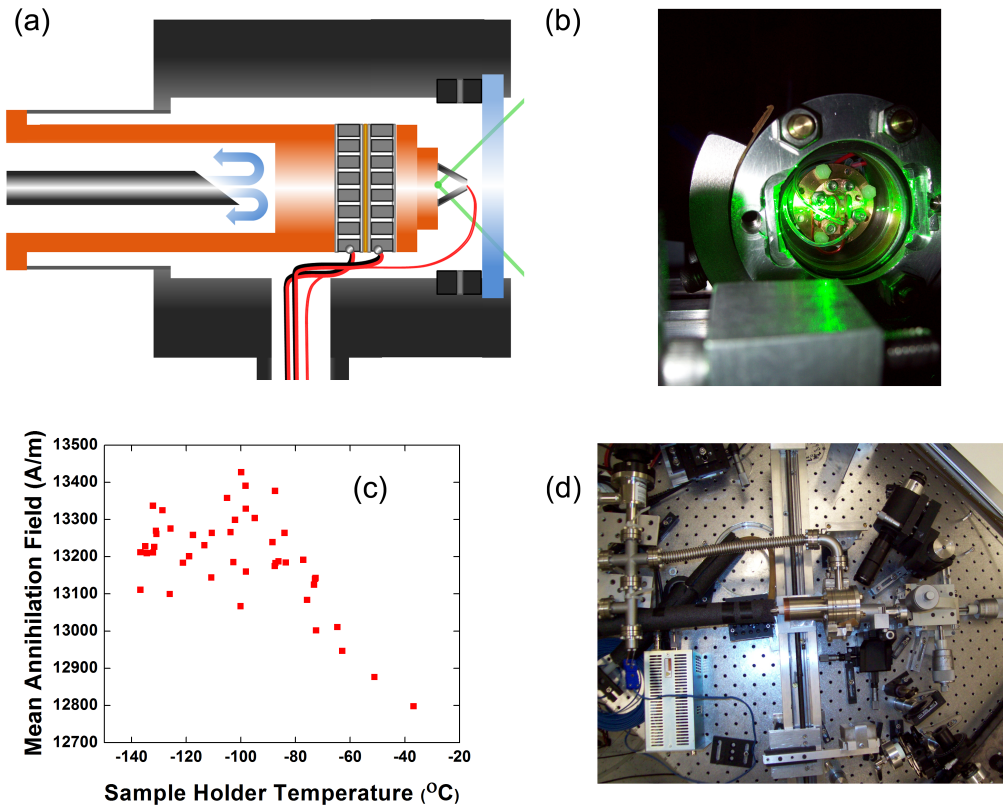


Figure 3.12: The vacuum chamber for the AC MOKE susceptometer. Panel (a) shows a bottom view schematic of the vacuum chamber including the cold finger, cryogen flow, thermo-electric cells, the copper sample stage, the AC field coil, laser path, and o-ring clamped window. A front view of the chamber is shown in (b) with the laser on. Panel (c) shows the trend in the evolution of the annihilation field at low temperature. The declining influence of the variation of the saturation magnetization with temperature is clearly visible. The data is very noisy in large part due to the poor control of the cryogen flow rate, and consequently, the temperature. Panel (d) shows a top view of the entire chamber, including the flexible bellows connecting the chamber head to a electronic feed-throughs (instrumentation, and thermocouple) as well as an 8L/s ion pump.

large set of statistics on the thermal switching properties of the magnetic disks. Extension of the rigid vortex model for non-interacting disks to third order enabled reliable extraction of statistics as well as fundamental parameters such as saturation magnetization. The compiled results reveal that the typical Néel-Brown model in conjunction with the Bloch $T^{3/2}$ law give a good description of the annihilation process. The results indicate that pinning sites strongly influence the decay process and therefore suggests that the most appropriate form for the annihilation energy barrier is one modeled after domain wall depinning, using a power law exponent of $\alpha_d = 3/2$. This experiment highlights the importance of continued use of arrays in switching experiments in order to allow acquisition of large data sets for statistical analysis. Ideally simultaneous experiments using both single disk techniques and array techniques to explore individual switching pathways and bulk statistics, respectively, should be used to shed further light on this problem. The chamber apparatus constructed has the potential to continue combined temperature and sweep rate investigations of transitions to provide a better understanding of the annihilation transition. However, the stability concerns must be resolved first.

CHAPTER 4

Torsional Magnetometry Applied to Magnetic Vortex Pinning¹

Transitions of the vortex state on annihilation or creation of the vortex exhibit large energetic costs. Much smaller transitions occur without annihilating the vortex state when the core interacts with inhomogeneities in the magnetic film. Detection of these transitions requires an apparatus with very high sensitivity, and since the inhomogeneities are randomly distributed, is best done with a single magnetic element.

This chapter describes a highly detailed study of vortex core pinning in a single disk using a nano-scale torsional magnetometer. Applying the resurgent technique of torsional magnetometry with modern enhancements allows very sensitive measurements to measure core pinning and depinning events as well as low speed thermal dynamics associated with these transitions. The experimental data presented in this chapter is inherently tied to the model described in Chapter 2. The model was directly motivated by the desire to produce pinning site maps from hysteretic magnetometer data with quantitative accuracy in energy and in vortex position. Combining the experimental power of torsional magnetometry with the model developed in Chapter 2 enables a complete description of classical pinning behaviour in the device.

The approach and results presented in this chapter demonstrate the potential of a disk on a torsional magnetometer as a platform for studying physics of pinning. This includes an initial proof of concept study of pinning sites added to the device via focused ion beam. In addition to making the physics power of the model/disk/torsional magnetometer combined

¹A version of this chapter has been published in Science Magazine (71). It is available online at [10.1126/science.1231390](https://doi.org/10.1126/science.1231390).

platform apparent, these induced pinning sites are also strongly suggestive of direct magneto-mechanical devices for integration in technological applications.

4.1 Vortex Core Pinning

One can consider the beginning of experimental micromagnetic work to be the discovery of the Barkhausen effect, where switching of individual domains was detected for the first time. The Barkhausen effect refers to the stochastic jumps in magnetization resulting from the pinning of magnetic domain patterns. Since the discovery of the Barkhausen effect in 1919 (6), detection of Barkhausen jumps in novel systems has been an important step in understanding ferromagnetic systems as investigation has progressed to smaller size scales. Of interest now is how the nature of the phenomenon itself is modified at the smallest scale, and the consequent technological implications. Once again, thin-film magnetic disks exhibiting a ground state vortex (77–79) and offer a convenient platform to study single vortex behaviour and present a system in which to observe, arguably, the ultimate in small scale Barkhausen effects. The magnetic vortex core is equivalent to a zero dimensional domain wall and is often restricted to a radius of less than ten nanometers (95). In a permalloy disk, the radius is often larger, 10 – 20 nm, but it may be tuned with disk aspect ratio. The high density of exchange energy within the core enhances local interactions with any variation in disk structure, including thickness, crystal structure, or grain boundaries (85, 121, 164). As the smallest stable domain structure considered in classical micromagnetism, the vortex core presents an opportunity to observe Barkhausen phenomena at extraordinarily low energy scales, and with an elegant, tidy system. In summary, a single point-like pinning site, together with a vortex core constitutes the simplest system to exhibit the Barkhausen effect.

Pinning of the vortex core has become a great interest due to technological considerations as covered in the introduction to Chapter 2. Technologically, domain wall pinning, and consequently Barkhausen effects, present an opportunity to enhance spintronic memory (45) and construct magnetic logic devices (43, 165, 166). In wire geometries, film imperfections have been found to influence domain wall velocity and energy loss (167), while thermal motion of wall structures in wire kinks has been exploited to learn about non-adiabatic spin torque (168). Previous work studying pinning exclusively with the goal of understanding the phenomenon has shown indirect signs of the Barkhausen effect for the vortex state. Local variation in films have been found to cause a stick-slip motion (86), and to increase the frequencies of dynamic modes of the vortex (88–92).

As is typical with micromagnetic investigations, dynamics have been the focus of most pinning investigation. The work of Uhlig et al. (86), represents the most prominent quasi-

static investigation, and it is worth noting a few details. The study used a transmission electron microscope (TEM) to track the evolution of the domain pattern of the vortex state as field was increased. The stated result was an observation of core position during pinning as a bright spot near the centre of the disk. However, the observations were made using the Fresnel version of Lorentz imaging to visualize the domain patterns, which means this bright spot is really an effect of the skirt magnetization, and not the actual core position. This lead Uhlig et al. to identify a complete immobilization of the core during pinning. This disagrees with simulation, as well as analytic computation. The results of Uhlig still provide a powerful view of pinning. However, beyond the confirmation of the existence of pinning effects the observations do not offer much insight.

A direct observation of the core position, via magnetic scanning probe microscopy, or high resolution X-ray imaging would provide a better approach. However these methods are exceedingly challenging. This is a contributing reason to the fact that that the most progress has been made using measurement of the effect of pinning on the dynamical modes of the vortex. Another good observable quantity is the total magnetization of the disk. Coupled with an accurate analytical model relating vortex position to magnetization, highly sensitive magnetization measurements can serve as a sort of scanning vortex probe microscopy. This approach is highly complementary to dynamical measurements. Nanomechanical torque magnetometry (eg. (74, 169)) provides an ideal method of measuring tiny magnetization (M) changes with minimal influence on the sample.

4.2 Torsional Magnetometry

Torsional magnetometry is an old stalwart in the suite of techniques to measure magnetic phenomena. The essential design of a torsional magnetometer consists of a magnetic object attached to a torsion spring. Any field that is applied, induces a torque on the magnetic moment, and, assuming the direction of the torque is aligned with the torsion spring, a mechanical restoring torque develops (Fig. 4.1). In the micromagnetic community, it had largely fallen by the wayside and given way to newer more sensitive techniques suited to smaller samples, while, in other fields, such as geomagnetism, torsional magnetometers continued to be prominent. However in the past 25 years torsional magnetometry is making a resurgence in the condensed matter community, fueled by the rise of micro and nano-mechanical devices.

4.2.1 Historical Application

The phrase torsional magnetometry is, for good reason, associated with geomagnetism. Arguably the true first torsional magnetometer was a compass, where the torque on a magnetic needle deflects the needle so that it is in equilibrium with the local magnetic field. More formally, however, geomagnetic torsional magnetometers have been in use at least since the mid 1600's (170). Their use continues today in geophysical prospecting, and monitoring the Earth's magnetic field.

The beginning of torsional magnetometry in the study of condensed matter can be directly identified as the discovery of the Einstein de Haas effect (2). Einstein and de Haas' experiment proved the fundamental link between magnetic angular momentum and mechanical by measuring the conversion of spin angular momentum into mechanical momentum. In other words, if a magnet connected to a support is torqued by a field, the support will torque to compensate, conserving the total angular momentum of the system ². Measurement of the deflection of the support then provides a measurement of the change in the magnetic moment in the magnet. Just before the discovery of the Einstein de Haas effect, the inverse effect (the Barnett Effect) of transferring angular momentum to a magnetic sample via rotation was discovered (13). The immediate importance of this work was the verification that spin angular momentum is equivalent to mechanical angular momentum, and the verification that something like Ampère's molecular currents existed. Thus, the experiments contributed directly to the understanding of magnetism within solids and the narrative of discovery described in the introduction.

Following the groundbreaking revelations of the equivalence of mechanical angular momentum and spin, torsional magnetometers settled into a workhorse role. Experimentalists refined and improved the design and adapted the device to measure magnetic properties of a wide variety of samples suspended from torsion springs (171). Of particular note torsional magnetometry provides a useful way of measuring anisotropy constants since it is simple to vary the angle of the applied field to the sample and the torsion axis (172).

Over time torsional magnetometers were exploited in a less widespread capacity as more advanced magneto-optical magnetometers (using lasers) and superconducting quantum interference devices (SQUIDs) became prominent. Torsional magnetometers continued to be used in some applications, such as high field environments (173, 174) where other magnetometers fail. A revitalization of the technique would have to wait until micromachining created torsional devices on a massively smaller size scale with a suite of concomitant advantages (175).

²A vivid analogy is the classic undergraduate demonstration of a physics professor standing on a rotatable support with a spinning bicycle wheel held with its axis of rotation aligned to that of the support. Upon rotation of the wheel's axis by π , the formerly stationary professor begins to spin. Bicycle tires and professors are extremely similar though, so this is unsurprising.

4.2.2 Modern Micromechanical and Nanomechanical Magnetometers

Over the past 30 or so years, micro and nano fabrication advances have led to the rapid development of micro/nano electro-mechanical systems (MEMS/NEMS) (176, 177). These devices exploit fabrication techniques developed primarily for computer technology to produce mechanical systems on extremely small scales. MEMS are now ubiquitous in modern technology, most commonly as force sensors or orientation sensors. Basic designs include cantilevers, bridges, and torsional paddles (176, 178).

Perhaps the most prominent integration of magnetism and micromachined cantilevers is the magnetic force microscope (MFM) (179). Strictly speaking, the MFM is not a torsional magnetometer as it is sensitive to the force exerted on the magnetic tip of the cantilever by gradient fields. A more recent and similar approach, with much higher sensitivity, is magnetic resonance force microscopy, which employs a cantilever to detect nuclear spins directly (180–182).

Scanning probe microscopes are prominent integrations of fabrication technology and magnetism, however the concept of having a magnetometer on a chip or enhancing magnetometers using the sensitivity of micromachined chips is also very appealing. In the mid 1990's the approach of shrinking and studying resonant properties of torsional magnetometers appeared in applications to high field sensors (173, 174). These smaller (mm scale) resonant torsional magnetometers foreshadowed the development of micromechanical devices (Figs. 4.1 and 4.2). This technology was rapidly integrated into the concept of torsional magnetometry, with various MEMS and NEMS devices replacing the torsion spring in the traditional design. Integrated devices with fabricated micromagnets became popular in the late 1990's (183–185). The flexibility of the torsional magnetometer platform enabled a wide variety of experiments (169). Notably, magnetic resonance detection in samples mounted on a magnetometer was performed very early on (186). Later, resonances were excited by magnetic devices in vapour beams (187). Fittingly, one of the most elegant early experiments detected the Einstein-de Haas effect in a micron scale device (188).

4.3 Experimental Apparatus

To study the magnetization of a micron scale disk, a relatively simple torsional paddle design was used. At its core, the paddle design consists of a platform suspended from supports by torsion bars. On the platform, a single magnetic disk composed of permalloy, and exhibiting a vortex ground state, is fabricated. This enables a magnetic field to be applied, inducing a torque on the magnet proportional to the magnetization, which deflects the

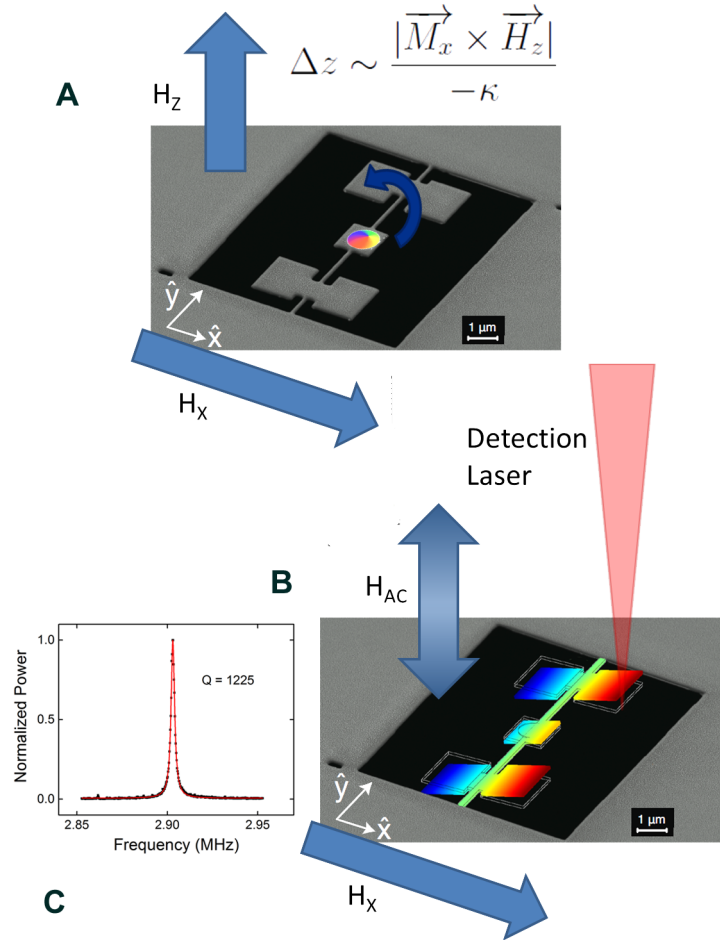


Figure 4.1: A schematic detection of vortex magnetization by torsional magnetometry. A magnetic moment is induced in the disk with an in-plane bias field (A). Using an out of plane secondary field, a torque is applied to the magnetic moment. Due to the strong shape anisotropy of the disk, torque is transferred to the paddle causing mechanical deflection. The out-of-plane field is an AC field operated at the fundamental torsional resonance frequency of the paddle (B). This enhances the amplitude of the motion of the paddle, which is a high quality resonator, increasing signal detection. At 77K, the quality factor of the paddle is 1225.

paddle. Detection of the deflection of the paddle, and hence the torque proportional to the magnetization, is accomplished by a laser interferometer. In the following sections, the full apparatus is described, including the torsional paddle, its fabrication, and the measurement apparatus.

4.3.1 Torsional Paddle

The device used in this experiment was fabricated on a 100 nm thick silicon nitride membrane suspended over a silicon frame (189). Magnetic disks with a nominal diameter of 1 μm and thickness 42 nm were deposited onto the membrane by shadow masking, ensuring a magnetic film with no contamination by organic resist. After this, the resonators were milled into the membrane around the magnetic disks using a focused ion beam (FIB) taking care to avoid any exposure of the magnetic film to the ion beam. Details of the fabrication process can be found in Appendix F.

To detect the magnetization of the disk, the paddle is actuated by an AC stimulus, here, an out of plane magnetic field. This provides signal enhancement when the AC stimulus is operated at a frequency that matches one of the mechanical resonant modes of the device. Since the disk is in the vortex state, in order to do this, an in-plane magnetization must be induced first. An in-plane quasi-static field is applied perpendicular to the torsion rod supports of the paddle. As field is increased, the vortex core is deflected orthogonally to the field, moving it through the film and increasing magnetization. If an out-of-plane field is applied, this applies a torque to the induced in-plane magnetic moment that may be written $\tau_{\mathbf{M}} = \mathbf{M} \times \mathbf{H}$. As a thin film device, the shape anisotropy maintains the magnetization of the disk in-plane (except for the core). As such, the torque of the magnetic moment is transferred directly to the mechanical paddle, and results in a measurable deflection of the paddle rather than a canting of the magnetization. The deflection of the paddle is given by $\delta\theta = -\tau_M/k_R$ with k_R the stiffness constant of the torsional spring.

Tuning the frequency of the AC out-of-plane field to one of the mechanical resonances of the paddle resonantly enhances the deflection and allows the use of a lock-in amplifier providing significant improvements in signal-to-noise in the measurement. Since the AC field specifically exerts a torque on the device, and since the in-plane field is orthogonal to the torsion bar, the torsional resonances of the device are very efficiently, and selectively, actuated in this scheme (72). The paddle device actually consists of three paddles, one small central paddle holding the magnetic device, and two larger paddles in a wing shaped design. The outer paddles are designed to provide isolation of the central paddle from the membrane. In practice, however, the best sensitivity was achieved using the first torsional mode of the device where all three paddles deflect in unison. The other modes of the device

were explored in previous work (72). Here, discussion is limited to this first torsional mode which has a resonant frequency of 2.9 MHz.

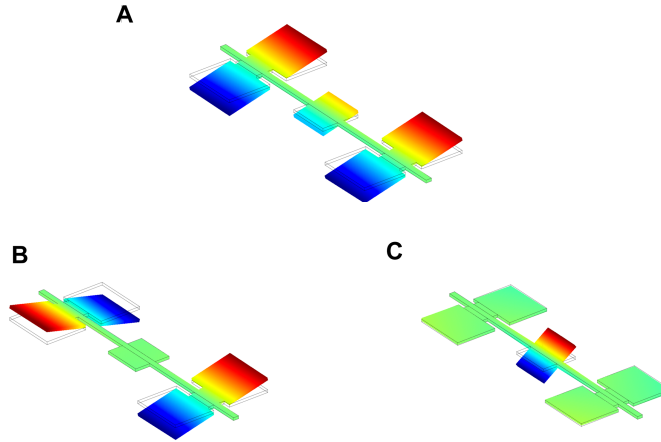


Figure 4.2: Finite element simulations showing the first three torsional resonant modes of the torsional paddle design. At top is the fundamental torsional mode (A), which is used for detection here. Below are the second torsional modes. In theory, the mode confined to the central paddle (C) would be useful for detection, however in practice, due to the smaller paddle size, signal-to-noise is lower.

4.3.2 Interferometric Detection

Though the physical deflection of the paddle is easy to understand, it is still very small (~ 100 pm) and consequently requires forethought to measure. Interferometric detection is a powerful method that can provide a non-invasive, high bandwidth, and sensitive method of detecting MEMS motion (190–192). Here a CW HeNe (632 nm, Melles Griot 05-LHP-141) laser source is used with a microscope objective to form a scanning interferometric microscope that requires very low optical power (Fig. 4.3).

Following completion of the fabrication of the device, the sample is mounted on a clean, bare silicon wafer which serves as a reflective substrate. An ultra thin U-shaped piece adhesive tape (3M Adhesive Transfer Tape 9400 Series) is applied to the silicon wafer prior to the sample being mounted. The sample is mounted membrane side down with the devices over the cut out section of the U and the frame secured onto the tape. This results in the membrane being suspended ~ 30 μ m above the substrate. Additional securing of the wafer using BeCu clips, or adhesive kapton strips helps to reduce drift. This sandwiching of the

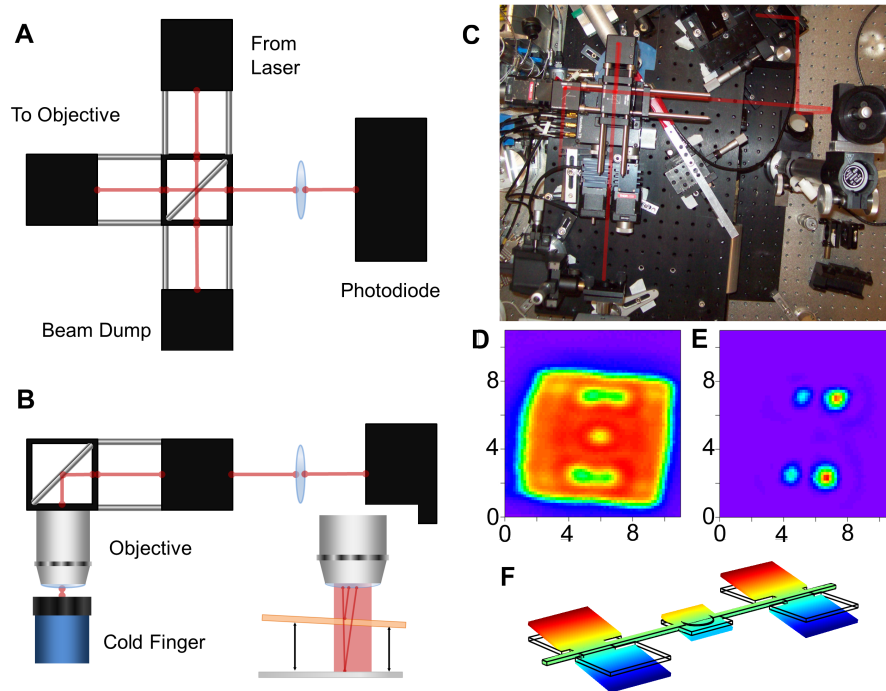


Figure 4.3: The torsional magnetometer uses a custom interferometer to measure the paddle deflection. A cage mount system is used to mount a long working distance objective lens on a piezo-electric scanning stage over top of the sample cold finger (A-C). Though the cage system appears to lend itself to a Michelson design, the interferometric cavity is formed by the paddle itself and a reflective backing mirror (B inset). Tilt on the paddle due to tape mounting contributes to spatial variation of the signal. Reflected signal is not affected by the tilt (D), while the AC signal from the first torsional mode (E) shows variation independent of the symmetry of the mode (F). Scales on D and E are in microns.

membrane chip and the Si wafer, with a spacer, creates a low finesse Fabry-Pérot cavity (an etalon) between the two, and this results in interference, modulating the reflected power based on the change in the gap (Fig. 4.3).

At first glance, considering the requirement for the path length difference for interference, the haphazard mounting of the sample on tape may appear like it is doomed to fail. However, the reality is that the interference is robust, and the the potential for random alignment actually is beneficial in the flip-chip design. The gap is uncertain on a larger scale than the wavelength of the light used, meaning a good interference condition is not guaranteed. However there is invariably some degree of tilt to the sample on the adhesive, leading to a wedge shaped gap. A tilt of 9.8° is sufficient to give the paddle a one wavelength degree of tilt over the breadth of the wing shaped paddles. In practice, this means that one of the four outer edges of the large wings will have a good interference condition and a correspondingly large signal (Fig. 4.3). This is one reason that the first torsional mode of the paddle, where the wings and central paddle oscillate in phase is used. Another reason, of course, is that the interferometer detects displacement, not angular displacement. The more expansive wings simply displace more than the central paddle. The last reason for using the wings as detection points, is that if there is any heating from the laser to be concerned with, measurement of a large paddle weakly thermally linked to the disk by a thin rod mitigates any thermal effects on the magnetic material.

4.3.3 The Apparatus

The paddle device and silicon substrate is mounted on the cold finger of a Oxford Instruments Microstat cold-finger cryostat (P.N. 9747). This cryostat is vacuum evacuated ($\sim 1 \times 10^{-5}$ mbar) using a vibration isolated turbo pumping station (Varian MiniTask AG-81) and a continuous flow cryogen system permits cooling to \sim K with liquid nitrogen, or down to 3 K with liquid helium³. In practice, it was too expensive (and wasteful) to run the cryostat with liquid helium, limiting observations to higher temperatures, a new helium recycling system has been purchased and installed which will make helium temperature measurements more practical in future.

Over top of the sample, with the device centred, a 3 mm diameter coil wound with 30 turns is used to apply the AC out-of-plane field to drive the resonance. The laser beam is focused in the middle of the coil, using a Mitutoyo 20X long working distance objective lens (numerical aperture 0.42, focal length 10 mm). The detection beam is fed into the

³The continuous flow is effected by a vacuum pump. This means the supply of cryogen is effectively pumped on, permitting a lowering of the vapour pressure in the storage vessel, and consequently reducing the boiling point of the cryogenic liquid. Hence the cryostat can reach temperatures below the usual boiling temperatures for liquid helium and nitrogen.

objective from a uni-body cage interferometer set-up that is mounted on a piezo driven optical stage (Thorlabs Nanomax-TS) that can also be coarsely stepped with micro-stepper motors (Thorlabs DRV001). The HeNe laser is mounted off of the interferometer stage and is passed through a strong attenuator (Newport 925B) to reduce the beam power to between 3 and $5\ \mu\text{W}$. Entering the interferometer cage, the beam passes through a beam expander before hitting a beam splitter that redirects light to the objective. After reflection from the paddle and substrate, the light passes through the beam splitter again, the transmitted light is then collected with a lens and focused onto a high bandwidth (125 MHz) photodetector (New Focus Model 1801). The photodetector signal is passed through a pre-amplifier (SRS SR445) and then into an RF lock-in (SRS SR844) referenced to a function generator (SRS DS345) used to feed the RF amplifier (EIN Model 310L) driving the AC coil. This permits measurement of the amplitude of the periodic resonance of the paddle. In alignment and optimization, a spectrum analyzer (HP 8594E) is used to locate the resonance peak as the resonant frequency does shift with temperature. Simultaneously, the DC reflected light, independent of frequency is recorded to provide an image of the sample.

The end of the cryostat is entirely non-magnetic. The quasi-static in-plane field (bias field) is applied in the same manner as the MOKE susceptometer described in Chapter 3. A stepper motor powered rail shifts a permanent magnet relative to the sample providing a very stable magnetic field. The rail, stepper motor model, controller model, field calibration method are all the same as those described in Chapter 3, however two differences exist. First a diametrically magnetized cylindrical magnet is used mounted with the dipole axis orthogonal to the direction of translation along the rail. This permits rotation of the magnet by 180 degrees to flip the applied field (Fig. 4.4). A second stepper motor was included to automate this rotation, though typically it was not needed due to the infrequency of magnet flips. The second difference is that a backing magnet was not used to attain zero field in light of the ability to flip the field.

Optimization of the signal is an art form. This is in part due to uncertainty in the cavity, drift in the tape, changes in the gap, changes in the location of the maximum signal, and the dependence of the signal on the focus. In practice, the coarse stepper is used to locate the paddle by focusing on the membrane and scanning periodically. Once the paddle is located, the focus is adjusted to optimize the signal on one of the four wings. Then the optimal wing is found by a 2D scan looking at the AC lock-in signal. Then, after moving to the maximum signal point, the signal is re-optimized through the focus. Additional tuning of the driving frequency may be used as well, to compensate for any changes in the resonant frequency.

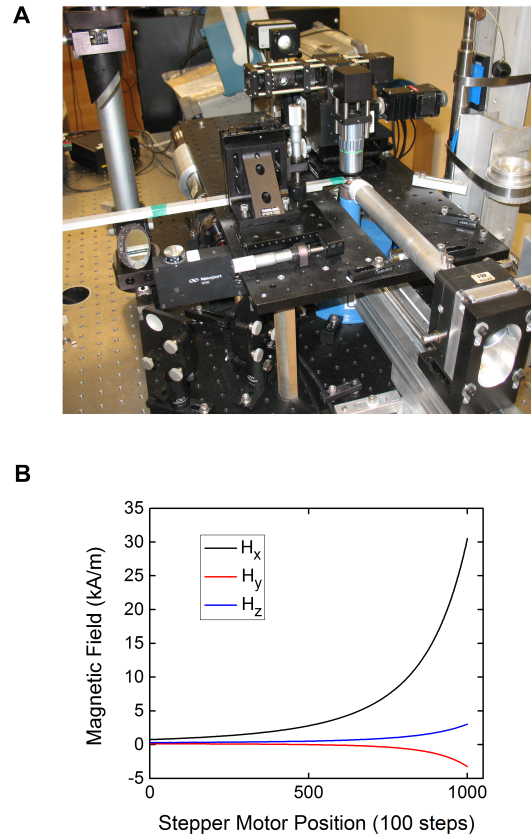


Figure 4.4: The bias field is applied to the torsional resonator using a permanent magnet mounted on a stepper motor powered rail. The bias magnet is mounted on a rigid aluminum support to permit close approach of the magnet to the sample cold finger (A). The cylindrical magnet is mounted axial with the aluminum support, but is diametrically magnetized. This allows reversal of the applied field by rotating the cylinder. Calibration is performed by shifting a hall probe mounted on a two axis stage directly over the sample. At high field, stray y and z components of the field are applied to the sample, however in experimentally pertinent ranges, variation in secondary field components is minimal (B).

4.3.4 Simplified Analysis

Using the first torsional mode of the device, and using the apparatus to extract only information about the normalized magnetization enables a very simple conversion of the measured magnetization to be applied by considering the device to be a driven damped harmonic oscillator (eg. (193)). The driving torque exerted by the AC field is, as before, $\tau_{\mathbf{M}}(t) = \mathbf{M} \times \mathbf{H}_{\text{AC}} \cos \omega_d t = \tau_M \cos \omega_d t$. Where τ_M is the magnitude of the torque exerted at the peak applied AC field. The equation describing the motion of the resonator is then:

$$I_R \frac{d^2 \Delta\theta}{dt^2} + \nu_R \frac{d\Delta\theta}{dt} + k_R \Delta\theta = -\tau_M(t), \quad (4.1)$$

where I_R is the total moment of inertia of the device, ν_R is the damping parameter, and other symbols are as defined before. This equation has a well-known steady state solution of the form $\Delta\theta(t) = \Delta\theta_0 \cos(\omega t + \delta\phi)$ where $\Delta\theta_0$ is the angular amplitude of the motion and $\delta\phi$ is the phase difference between the motion and the drive. The amplitude and phase may be solved for as a function of the drive frequency leading to a classic Lorentzian peak:

$$\Delta\theta_0^2(\omega_d) = \frac{\left(\frac{\tau_M}{I_R \omega_0^2}\right)^2}{\left(\frac{\omega_0^2 - \omega_d^2}{\omega_0^2}\right)^2 + \left(\frac{\omega_d}{Q\omega_0}\right)^2}, \quad (4.2)$$

$$\delta\phi = \tan^{-1} \left(\frac{-\omega_d \omega_0}{Q(\omega_0^2 - \omega_d^2)} \right), \quad (4.3)$$

where the resonance frequency is $\omega_0 = \sqrt{k_R/I_R}$ and the quality factor of the device is $Q = \omega_0 I_R / \nu_R$. The angular amplitude is linearly proportional to the driving torque, which in turn is linearly proportional to the magnetization. For small angular displacements, this means the absolute displacement, measured by the interferometer, is directly proportional to the magnetization.

This means that the measured signal is linearly proportional to the magnetization of the disk. The above treatment of the torsional resonator is highly simplified for clarity, but it is also sufficient for the experiment presented. Starting in the vortex state at zero bias field, the response of the magnetometer is zero. As the bias field, and magnetization increases, the response increases. When the vortex annihilates, the disk switches to the quasi-single domain state with an approximately saturated magnetization. This provides a reference signal value for $m \sim 1$ for the normalized total magnetization of the disk. Since the response is linear in the magnetization, these two points are sufficient for relative calibration of the apparatus. A full analysis of the device is possible, and absolute calibration of the sensitivity of the magnetometer can result (75), but this is not necessary here.

To directly extract quantitative information requires a careful calibration of the measured deflection of the device. However, one may place an estimate on the upper bound of the sensitivity of the device by considering the minimum magnetization step measurable, and the signal amplitude at the maximum magnetic moment of the disk at saturation. If the volume of magnetic material is computed, and assumed to be completely saturated, the minimum normalized signal can be converted into a normalized magnetization, and then into an absolute magnetization. This provides a reasonable estimate of the device sensitivity. In this case the sensitivity is found to be $\sim 6 \times 10^7 \mu_B$.

Second order effects, such as effective stiffening of the torsional response by the application of the field do not distort the signal significantly at low (experimentally pertinent) fields. When these effects do become measurable, the constant magnetization of the quasi-single domain state has been attained already. A slight decrease in the measured signal becomes visible despite the lack of change in the actual magnetization. With the $1 \mu\text{m}$ diameter, 42 nm thick permalloy disk, these effects are not noticeable. This is supported by the use of a constant AC drive frequency, independent of field, throughout this experiment. Other effects, such as the breakdown of the reliance on the shape anisotropy of thin film to maintain the the magnetization of the disk in plane with the paddle, rather than being aligned with the bias field, are similarly too small to detect. One would expect the shape anisotropy of the thin film to be sufficient up to fields significantly greater than 100 kA/m . Similarly, nonlinear effects in the resonant motion do not manifest for the low amplitudes used in this study. For the interested reader, a full non-linear treatment is available in reference (194).

4.3.5 The Magnetic Disk

A description of the torsional paddle is important for understanding the method of the experiment, but the object of interest, physically is actually the magnetic disk. A number of interesting aspects of the disk arise due to the fabrication methods.

The silicon nitride membrane provides a number of advantages. For instance, it is somewhat electron transparent. This permits TEM inspection of the edge of the deposited disk (the centre of the disk is too thick) to observe the grain structure. It also permits Lorentz microscopy to be performed, confirming the vortex state. The Frensel (out-of-focus) mode of Lorentz microscopy is used to observe a bright spot at the centre of the disk which arises from the Lorentz force exerted on the electron beam as it passes through the in plane circulating magnetization of the vortex state (Fig. 4.5).

The disk is formed using shadow masking, which means that it develops a unique edge shape (159). This will have a significant influence on the shape anisotropy properties, or more precisely the demagnetization factor. The sloped edge of the disk will result in

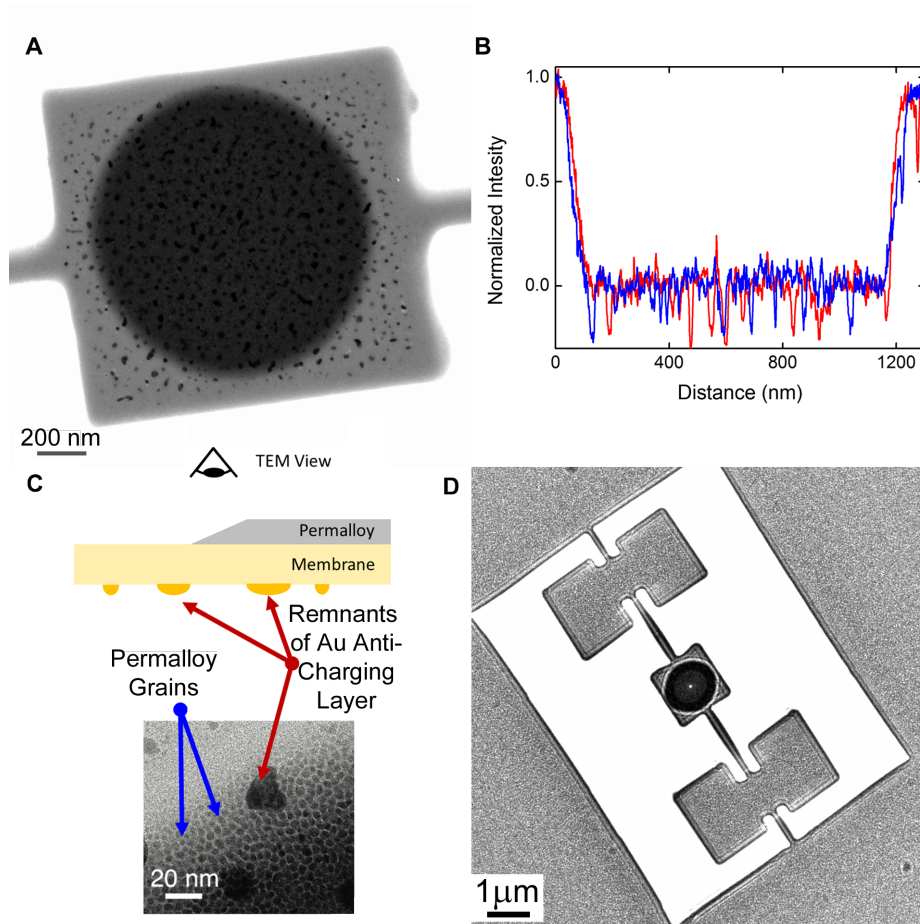


Figure 4.5: Fabricating the torsional paddle out of a silicon nitride membrane permits TEM inspection of the disk (A) including, by the measured transmission, a relative estimate of the thickness (B). Profile cuts through the bright field data show a flat topped disk with strongly sloped edges. In the thinner sloped edge, the permalloy is sufficiently thin to allow inspection grain structure (C). Lorentz imaging allows direct confirmation of the vortex state. The bright spot coincides with the vortex core position (only at zero field), but does not reflect the polarity of the core. Rather, the bright spot represents the chirality (CW); the opposite chirality (CCW) would feature a dark spot. Panel D courtesy of J. Davis and P. Li.

edge demagnetization charges being distributed farther apart and yield a reduction in the demagnetization factor⁴. This effect is difficult to quantize, as the true extent of the slope for the disk on the resonator is not known. AFM inspection cannot be applied to the disk on the resonator and variation in the gap between the shadow mask and membrane will have a significant effect on the edge profile. Minimum bounds on the width of the sloped region may be placed by TEM inspection which suggests a slope > 100 nm wide. High resolution TEM imaging (Fig. 4.5) can be directly applied to the disk on the resonator, but is limited by the relative opaqueness of the disk away from the edge. Using a profile cut to measure the contrast in the TEM image provides an approximate relative measurement of the slope profile, however it may be subject to a saturation in contrast when the disk effectively becomes opaque. The TEM inspection demonstrates that the disk has a diameter at top of ~ 980 nm and at bottom of ~ 1200 nm. AFM inspection of disks deposited onto the frame of the membrane holding the resonator show that the deposition thickness was 42 nm.

The grain structure of the films produced by the UHV evaporator (Appendix B) was consistently found to be extremely small and uniform. The disk studied in this Chapter proved to be no exception. Grains were found to be roughly 5 nm in width, and very uniformly distributed with only single \sim nm scale variation. AFM measurements reveal a thickness variation in the surfaces of disks from the same deposition of ~ 0.3 nm RMS.

4.4 Observation of the Nanoscale Barkhausen Effect

Measuring the magnetization response of the disk to field reveals the effect of the intrinsic structure of the film. Energetic interactions between the core and imperfections in the film – thickness variations, grain boundaries, or material impurities – alter the energy cost of shifting the core, leading to concomitant variations in the differential magnetic susceptibility, dM/dH (Fig. 4.6 and Fig. 4.11). During pinning the differential susceptibility is suppressed, but crucially, does not vanish. By comparison, transitions between pinning sites appear as steep sections.

A great deal of information may be extracted by analyzing the detailed slope variations and jumps exhibited in the measured magnetization using the model developed in Chapter 2. However, prior to analysis of the pinning interactions, some analysis must be performed on the full hysteresis loop to fix fit parameters and learn more about the disk. The following sections provide a thorough introduction of the experiment, the analysis to extract the overall disk parameters, and finally analysis using the DVPM. In order to build a cohesive

⁴This is similar, in a sense, to the susceptibility correction in that it reduces the demagnetization energy by spacing the effective demagnetization charges out.

narrative, the data presented exhibiting telegraph noise and minor hysteresis presented was all obtained from the same minor hysteresis loop (the lower loop near 1.6 to 1.8 kA/m in Fig. 4.6 and Fig. 4.11). This is important to keep in mind; each method of investigating provides different insight into the pinning sites involved.

4.4.1 Analysis of the Major Loop

The accuracy of the pinning model is highly dependent on the parameters that describe the overall disk. Particularly in light of the uncertainty in the disk edge shape, and possible uncertainty in the disk thickness this makes independent determination of the demagnetization factor necessary. Of course, the other primary fit factor is the saturation magnetization, however from data in Chapter 3 and additional data taken using a time-resolved MOKE microscope on these films (195), a good estimate for the saturation magnetization can be made as between 700 and 715 kA/m at room temperature. An application of the susceptibility corrected, 3rd order RVM enables an extraction of the demagnetization factor.

Prior to fitting the 3rd order RVM to data taken at 77 K and at room temperature (295 K), an additional constraint can be placed on the fit. The experiment described in Chapter 3 and a concurrent experiment (99) both indicate that the shift of hysteretic features with temperature is dominated by the change in the saturation magnetization $M_S(T)$. This implies that, by lining up features in the curves, the scaling constant in the Bloch $T^{3/2}$ law may be determined where the law is expressed as $M_S(T) = M_S(0)(1 - gT^{3/2})$. Additionally, if a single scaling factor lines up all, or almost all features on the curves, this implies that the path followed by the vortex does not change significantly with temperature. Good agreement on the positions of virtually all features was found for $g = 1.5 \times 10^{-5}$, a value half way between the typical bulk permalloy g and the value found in the previous chapter. Armed with the value of g , curves from multiple temperatures may be fit simultaneously using a single demagnetization factor and saturation magnetization value. In principle, this implies that with multiple temperature datasets (> 2) the value of $M_S(T)$ could be extracted objectively by fitting the the demagnetization factor and saturation magnetization to best match the curvature of the hysteresis curve. In practice, however, in an $M - H$ plot the curvature of the vortex loop is very subtle, much more so than the $\chi - H$ curve measured in Chapter 3. Hence very little actual information may be gleaned in this manner. It is best to proceed with an independent estimate, as discussed previously, of M_S .

Fitting yields a demagnetization factor of 0.0225 (Fig. 4.6). For the sake of posterity, attempting to fit the curvature of the curves with multiple temperatures implies a $M_S(0) = 750$ kA/m for optimal agreement. In subsequent fits, a value of 700 kA/m for room temperature and 750 kA/m ($M_S(0) = 758$ kA/m) for 77 K, was used, in accordance

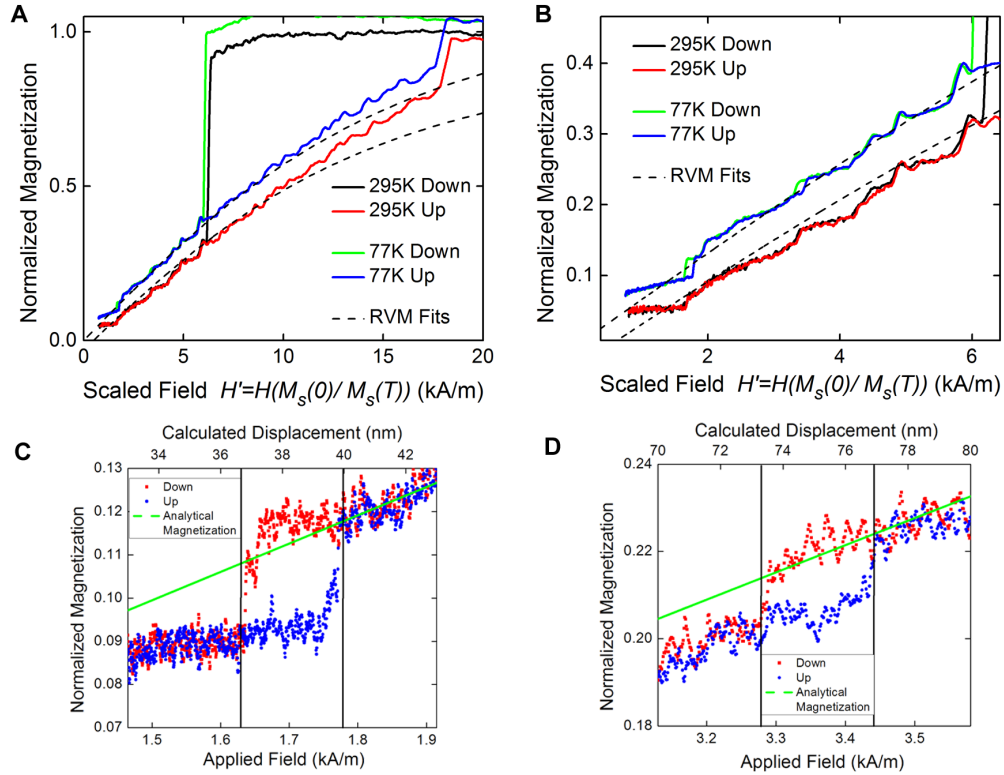


Figure 4.6: Analysis of vortex data using the RVM allows extraction of overall disk parameters and rough estimates of pinning effects. Given a good estimate of saturation magnetization, fitting to the overall hysteresis loops allows extraction of a demagnetization factor (A). Plotting data from room temperature and low temperature against a scaled field ($H' = H_{scaled} = H(M_S(T = 0)/M_S(T))$) demonstrates that features in curves from separate temperatures align (B). Some features become hysteretic at low temperatures indicating jumps (C and D). Estimations based on the field width of the loops, and magnetization jumps suggest hop distances of 4-10 nm for the vortex core.

with the lower range of the value estimated from the previous work. Error on the demagnetization value can be estimated to be ± 0.002 and for the $M_S(0)$ value, 20 kA/m. The error ranges for these values are linked. Since the slope of the computed $M - H$ curve is affected similarly by both M_S and $F_c(L, R)$, an error in one can be compensated for by an corresponding error in the other. Assuming a perfectly known M_S value, the demagnetization error is closer to 0.00002, however, M_S is not known to such precision.

4.4.2 Emergence of Minor Hysteresis and Telegraph Noise

At room temperature all inter-site transitions appear to be continuous and reversible, however at $T = 77$ K, some transition states become minor hysteresis loops (Fig. 4.6). This immediately identifies a temperature dependent process that masks bistability at high temperature. Though $M_S(T)$ changes and energies will scale as M_S^2 , a $\sim 13\%$ change in the energy value will not eliminate barriers between bistable states (in general).

The obvious explanation is that the energy barriers between the bistable (or multi-stable) states are sufficiently low that at room temperature thermally activated noise masks the presence of the two states and results in a thermally averaged sloped transition region instead. This can be simply understood. When the hopping rate exceeds the measurement bandwidth (~ 10 -30 Hz), a time-averaged magnetization weighted by the occupancy of the participating states is recorded. Picturing a Boltzmann type distribution determining the occupancy of the states by their relative energy, it is clear that as field increases (decreases) the state with larger (smaller) magnetization will have a more rapidly decreasing (increasing) relative energy, and consequently, will have an increasing (decreasing) proportion of the occupancy. Since individual transitions occur too quickly to observe, the measured signal will show a smooth transition with a positive slope, spanning the region of bistability (Fig. 4.6).

Initial analysis using the third order RVM permits estimation of the vortex core hopping distance via two methods: the field width of the loop provides one estimate, while the magnetization change provides another (Fig. 4.6 B and C). Using these two approaches, hopping distances were initially estimated to be between 4 and 10 nm. However, Chapter 2 has demonstrated the inherent flaws in using the RVM as an indication of pinned vortex position, and more robust analysis was pursued subsequently.

Investigation at intermediate temperatures directly shows the convergence of the experimental bandwidth and the hopping frequency as the thermal noise slows (Fig. 4.7). This verifies the dynamical explanation for the absence of hysteresis at room temperature. Altering (slowing) the sweep rate also provides an method of enhancing the chance of observing the stochastic transitions.

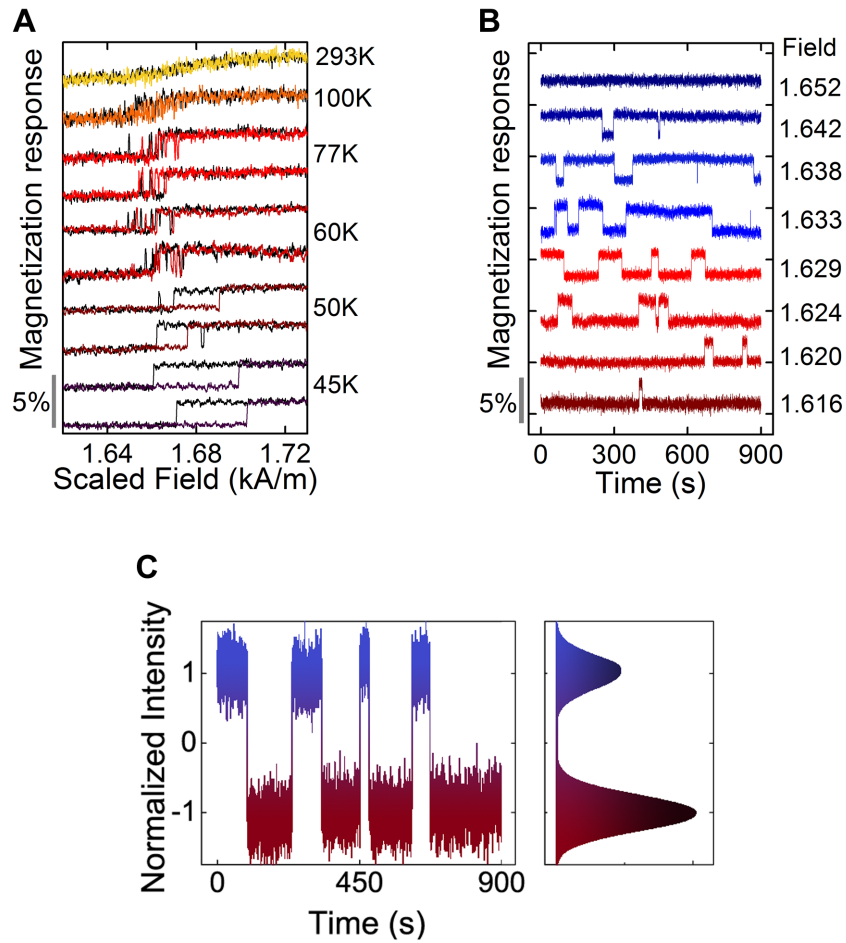


Figure 4.7: Barkhausen telegraph noise across a bistable transition. The strong temperature dependence (A) of minor hysteresis is probed over a bistable state (the first minor loop in Fig. 4.6) with a field sweep rate of $0.45 \text{ Am}^{-1}\text{s}^{-1}$. At 77 K and various fixed fields (labeled in kA/m), telegraph noise traces show strong field dependence (B). The gray bar indicates the normalized magnetization scale. Binning the experimental magnetization data from telegraph noise into a histogram indicates that only two states participate in the hopping processes (C).

Stopping at fixed fields around the hysteresis loop field allows traces of Barkhausen telegraph noise to be captured (Fig. 4.7). This data provides the classic view of a two level bistable system with stochastic transitions. Additionally, examining the occupancy distribution of this data provides a good method to search for multiple states participating in the dynamics. The telegraph noise traces can be binned according to the measured signal value (proportional to the magnetization). This shows the occupancy distribution of the different states blurred out by a Gaussian representing the noise level of the apparatus. Only two level distributions were observed; no multiple state dynamics were found.

Incrementing the field demonstrates that the lifetimes of the states involved in the hopping have strong field dependence as would be expected from the field dependence of the occupancy. The rate of hopping is determined primarily by the energy barrier separating the sites in conjunction with the temperature, while the magnetization jump gives a rough indication of how far the vortex core hops in the transition. The field evolution of the energy barrier also provides information about how far apart the sites involved in the hopping are. The evolution of the relative energies of the sites is determined by the change in magnetization induced during the hop. Additionally, the barrier height evolves in much the same way. Picturing a simple, classical transition with a single pathway, the energy barrier is determined by the location that the vortex core must pass through that has the highest energy. Just as with any other core location, there is a corresponding magnetization for the vortex to be located at this high energy point, and consequently the energy will also evolve with field. The separation⁵ of the pinned state and the barrier locations/magnetizations directly determines the rate of barrier evolution with field. This leads to two interesting points. First, it is entirely possible to have asymmetric barrier evolution with field for unequal spacings of barrier and pinned sites. Second, the smaller the separation, the slower the evolution of the barrier will be. This directly implies that thermal dynamics will only be detectable for a window of field inversely proportional to the site separation. Only sites spaced closely together, with low energy barriers will have detectable thermal dynamics. A full analysis of the hopping barrier evolution requires detailed fitting using the DVPM and is discussed subsequently.

Clearly, there are sites satisfying the above criteria in the sample. For those sites, a simplified analysis can be performed using an Arrhenius relation to describe the hopping. Computation of the lifetimes of the states from telegraph noise traces for varied temperatures and fields enables calculation of energy barriers separating bistable states by using an Arrhenius relation, $\tau = f_o^{-1} \exp(\Delta E/k_B T)$. The attempt frequency value $f_o = 200$ MHz is used as an approximation of the gyrotropic mode frequency. Note that as before, the attempt fre-

⁵For the sake of brevity, here separation is used as a loose term for physical hopping distance and magnetization change. As demonstrated in Chapter 2, these are inexorably linked, but not necessarily trivially.

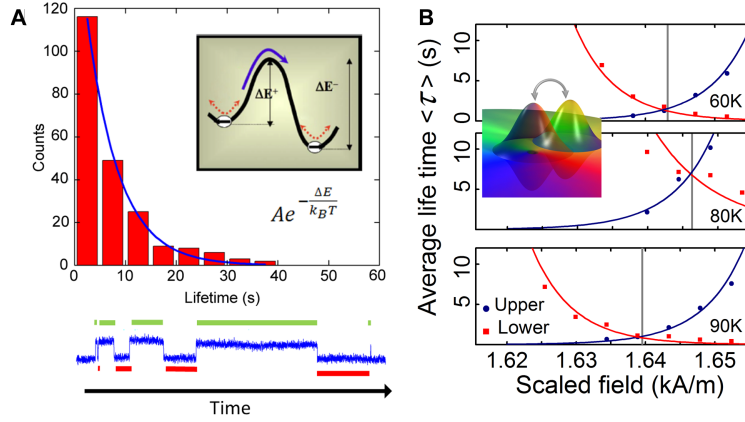


Figure 4.8: Arrhenius analysis allows empirical study of hopping energy barriers. Capturing telegraph noise traces and extracting the lifetime distributions for the up and down states allows computation of the energy barriers involved in the decay by fits to the lifetime distribution (A). For three temperatures the average lifetimes of the upper and lower states are calculated as a function of field (B). Analytical estimates of the lifetimes computed from the vortex pinning model show that the two sites are separated by ~ 10 nm in y . For equal state occupancy, the barriers range between 100 and 140 meV. Inset is a cartoon depicting the hopping process.

quency is not critical, an order of magnitude estimate is sufficient. For each site inspected, the same general pattern of evolution was found (Fig. 4.8). The lifetimes, occupancies, and energy barriers for the bistable states feature a crossing point as one state goes from being lower energy to higher energy (and vice versa). Both symmetrical and asymmetrical barrier evolution were found, as expected, and barriers were computed to be quite low, ranging between 100 and 150 meV. The barriers are quoted as the 50 – 50 dwell time barriers, ie the energy barrier at the cross over point where occupancy of and transition rate from both sites are equal. Since the lifetimes and barrier are effectively equivalent, data presented here are retained in the experimentally grounded lifetime, while fits and theory are converted from energy, to lifetime using the Arrhenius relation stated previously.

4.4.3 Instability

The data for thermal transitions was extremely difficult to acquire ⁶. Various sources of instability in the apparatus lead to significant drift with temperature. The most notable causes are thermal shifts in the microstat cold finger, as well as in the adhesive mounting for the sample. Initially long traces of telegraph noise were captured and corrected for drift

⁶Most data acquisition was performed by a colleague, Alastair Fraser.

using polynomial subtractions and rescalings. However, it proved to be more efficient to capture multiple shorter noise traces separated by re-optimizations of the signal. The drift and instability of the apparatus hindered data acquisition, however it does not necessitate any additional analysis besides the occasional drift correction. Note that drift correction, in this case, should be considered as a multiplicative factor, rather than an offset. A shift in the beam location, or drift in the paddle-mirror gap will modulate the amplitude of the signal, it will not induce an offset.

Additional instability that was found to be uncorrelated with apparatus issues was found⁷. For separate data runs, the measured energy barrier and hysteresis loop position changed slightly, indicating instability in the hopping pathway on a very fine scale. In the example traces shown in Fig. 4.8, the barrier at which occupancy of the two sites is equal is found to be ~ 0.14 eV in the 80 and 90 K traces, while it is 0.1 eV in the 60 K. These types of shifts were often associated with a refreshing of the vortex (annihilation and recreation), or other large changes in magnetic field sweeping the vortex far away from the telegraph noise region, and then back again. For optimization of the signal, annihilation of the vortex provided the best result as it returns the disk to the quite consistent, and easily detected quasi-single domain state. Data sets for the evolution of lifetimes with field required enormous amounts of time. Consequently, single blocks of 30-40 hours of data acquisition permitted only single temperatures to be tested thoroughly. Each of the data-sets presented comes from a single ‘day’ of observation and therefore is separated from the other data sets by vortex annihilation.

The nature of this instability was not made clear until the analysis of the data was complete. The effect was attributed to the vortex following very slightly different paths in the disk. Therefore for each day, a different pathway separating the same two sites could be observed. To understand this more clearly, the opportunities for different paths must be investigated in 2D.

4.4.4 Two Dimensional Investigation

In a perfect disk the deflection of the core by the applied bias field would lead to a straight path orthogonal to the field. However, the imperfections that introduce pinning and telegraph noise also present the possibility of 2D deviations from the idealized path. Adding a second in-plane orthogonal field, H_y , to the primary bias field, H_x , allows 2D measurements (Figs. 4.9 and 4.12). Using secondary field values equivalent to path shifts on the nanometer scale to explore the lower hysteresis loop near 1.7 kA/m shows how strongly the interaction

⁷The only explanation related to the apparatus would be some sort of imp that periodically hit the magnet with a hammer changing the calibration. Though suspicions have long been held that a *Lab Kaiju* exists, this was never substantiated and the calibration was found to be stable.

of the core with pinning sites can be affected by the 2D distribution. On the low field side of the loop, a single site with a clear circular interaction profile dominates the pinning. On the high field side, multiple pinning sites can be identified by counting the distinct magnetization levels in the minor hysteresis loops. Looking at the circular symmetry of the dominant lower site, the regions of interaction with adjacent sites can be identified (Fig. 4.9). Under the assumption that all sites have circular symmetry due to convolution with the vortex core, ranges of interaction for each site can be drawn on. This draws the eye to curvature in the hysteresis loop positions that suggests a circular interaction profile for all sites. However this is speculative. It remains a useful exercise in preparation for quantitative analysis.

Immediately visible is the fact that with zero H_y applied, the vortex path only weakly interacts with the edge of the lower site. This implies the possibility that multiple low energy hopping pathways, possibly hopping to different pinning sites, may exist in this region. This motivates quantitative analysis to determine if this explains the instability observed when looking at the telegraph noise statistics for the hysteresis loop near 1.7 kA/m. Note that the long data trace presented in Fig 4.6 has a small H_y offset (-110 A/m) owing to a slightly different calibration, which registers it away from the $H_y = 0$ region in the 2D region. Shifts in the position and strength of the loop match well with the H_y offset.

4.5 Extraction of the Pinning Potential

The data presented in the previous section provide a detailed look at pinning phenomenon in a magnetic disk. However, beyond computing the energy barriers from the Arrhenius data, and estimating hopping distances with the RVM, little can be done that is not qualitative. This is the purpose of the Deformable Vortex Pinning Model (DVPM) developed in Chapter 2. The model is applied by fitting to the measured magnetization data in order to extract a quantitative pinning potential. This model captures both the field dependence of the core position and the flexing of the disk magnetization in response to the presence of imperfections - whether they are strong enough to locally trap the vortex or merely modify its progression across the disk. This means the extracted potential presents the real potential in terms of the vortex position. This contrasts with approaches that use the computed idealized core position describe extracted potentials (90). As noted in simulation work (164) the vortex position is not ideally determined by field, and there is a warping in the mapping. This can be resolved with the DVPM.

Fitting to the data is non-trivial. In addition to the disk fit parameters (M_S and $F_c(L, R)$), the entire pinning potential must be fit as well. This creates significant flexibility in the fit that must be constrained if an accurate pinning potential is to be extracted. This is the reason care was taken to ensure the overall fit parameters were fit with the 3rd order RVM

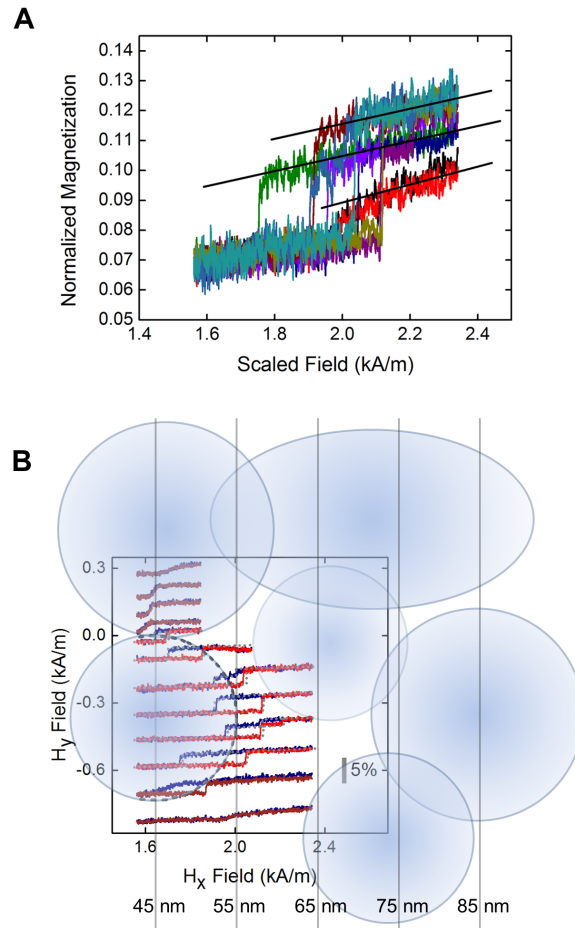


Figure 4.9: Examination of the magnetization levels for an array of 2D loops as well as an approximate 2D plotting of the loops allows estimation of the number and location of distinct pinning sites. A subset of loops from a 2D data set (A) show at least 3 pinning sites interacting with another site (the lower site). The three upper sites are indicated in magnetization level by black lines. Examining the full 2D distribution, estimation of the 2D positions and interaction radii of the participating sites is possible (B). Pinning sites are represented by the blue circles and ellipses overlaid on the magnetization traces. The estimates are quite rough, but are very useful as starting points for constructing 2D potentials.

prior to considering fitting with the DVPM. Several types of data set have been discussed in the previous section, each must be fit in a different manner. The first set of data that will be discussed is the fitting to long, single magnetization loop traces (1D data).

4.5.1 Fitting to 1D data

For a single trace, fitting is accomplished by creating 1D sum of Gaussian potentials that results in a computed curve that closely agrees with the experimental data. Effectively, the process may be thought of as a Levenberg-Marquardt fit process transformed through the model computation fit to the experimental data. In practice, the fit is applied manually. The reason for this is primarily the flexibility of the code in the model calculator. The initial implementation of the model calculator was made in high level symbolic mathematics program (Maple 15). This means that the algorithms called to compute the critical points of the 2D (rigid displacement axis and flexible displacement axis) energy space, which represents the base of the model, are fixed functions built into the program and not custom coded. The challenge in fitting to the experimental data primarily arises in fitting to the hysteresis loops, but simultaneously the slopes and magnetization level must also be accurate. Fitting to two curves (up and down) simultaneously, and fitting to transition points for the hysteresis loops is beyond the built in functions capability meaning that custom coding is required for automation. Since a limited number of data sets required detailed fitting, it was deemed more efficient to fit manually. The manual fit was accomplished by fitting individual pinning sites with a Gaussian profile and therefore a position, a width and a depth. This process constructs a smooth potential that reproduces the steps and hysteresis loops observed. Pinning site position is determined by the measured magnetization level the pinning feature appears at, while depth and width contribute to the slope and breadth (in field) of the measured suppression of susceptibility. Significant experience with fitting allows excellent guesses of the location, width and depth making fitting much easier, however it should be emphasized that the fit procedure is very time consuming and is never easy.

The influence of depth and width on both the slope and range of hysteretic interaction calls into question the uniqueness of the fit. In principle, there is sufficient information to uniquely define the fit potential by virtue of interaction of adjacent sites constraining the widths and depths of neighbors. To test this, single blind fits were performed and it was found that, indeed, the extracted potential is uniquely extractable. Artificial potentials were constructed by hand, by an individual selected for impartial disposition bordering on cruelty, passed off to a second person, who formatted the data as it would appear from experiment, including incorporation of a realistic M_S value, and finally provided the data to the third person who performed the fits. Certain values were known to the fitter, such as the demagnetization factor, and the temperature for computing dynamics. The M_S value

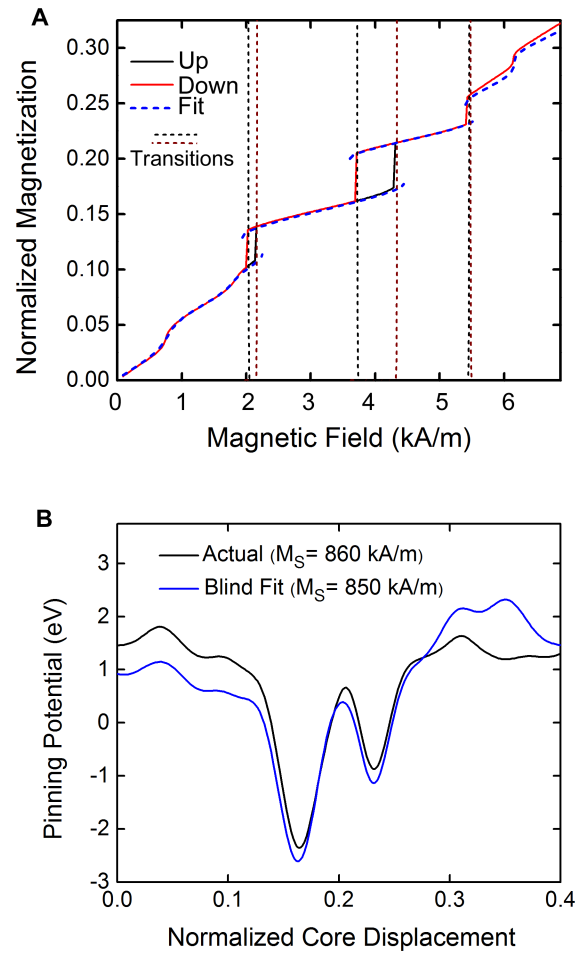


Figure 4.10: Single blind testing demonstrates that fitting to magnetization traces yields a good representation of the pinning potential. Fitting to a magnetization curve generated by a concealed potential was performed, including temperature effects which affects the transition points of the hysteretic loops (A). The extracted potential compared well with the original potential (B). The largest error was in the fit saturation magnetization, which was slightly off. This introduces a slope in the fit potential relative to the generating potential.

was not, nor was the pinning potential. The unknown M_S value is equivalent to an unknown demagnetization factor as seen in experiments. Additionally, temperature was always known for the experiments. The extracted potential was then passed back to the first person for comparison with the input potential. The agreement was found to be very good (Fig. 4.10). The largest disagreement is a slight slope caused by an error in the fit M_S . This manifests as a compensating slope in the constructed pinning potential. This testing laid to rest fears about the uniqueness of fitting to long, single hysteresis loops. This is a general theme in the fitting procedure. Any error in the overall fit parameters will manifest in the slope. Similarly, systematic variation, where the DVPM deviates slightly from simulated curves, for instance, will also result in offsets in the fit values. For instance, at large displacements, $> R/2$, pinning site positions will tend to be over estimated in order to have the computed magnetization level agree with a measurement.

Fitting was performed to the data acquired at liquid nitrogen temperatures. Following the procedure outlined above, a reconstruction of the pinning potential encountered by the core as a function of the real, pinned position of the core for the particular path that it followed in this measurement. From this extraction, typical pinning site energies between 0.6 and 2.0 eV are found. It is important to note that these fits are strictly 1D, the computed potential is displayed as a function of the displacement in the direction defined by the field only. It is also important to know the specific field calibration for each measurement set presented here. This data set features a slightly different calibration than the subsequent data sets presented (most notably the 2D data). The primary bias field (H_x) is properly calibrated, so the plots do not change much, however there is a small, -110 kA/m H_y offset. The offset is constant over the range presented ($\sim \pm 20$ kA/m).

Uniqueness was verified for long data traces, however this does not mean that *every* fit will be unique. In particular, when fitting to only two sites in a single hysteresis loop, it is possible to compute a variety of combinations of the two sites that results in a good fit. This directly results from the influence of the width and depth on the hysteresis loop. To get a unique fit, the dataset must include either sufficient information on the evolution of the magnetization within the site, providing a good slope estimate over a broad field range, or feature interaction with pinning sites both above and below. A broad slope gives a good indication of the curvature of the site leading up to a transition to an adjacent site, thus demanding a minimum width to the site and preventing the use of very narrow shallow sites that only capture the approximate energy barrier of the hysteretic transition. Similarly, interactions with neighbouring sites demand sufficient width that the overlap with both neighbours leads to the correct barrier for transition. For a site that has a good slope estimation over a broad field range, but no interaction on one side, the information about the site remains inherently incomplete and one side of the pinning site remains unknown.

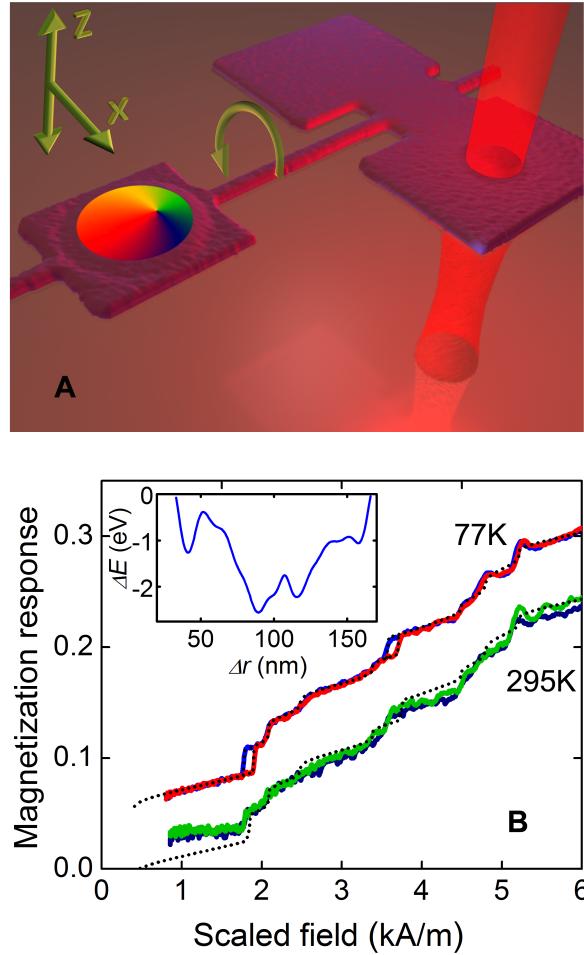


Figure 4.11: Device schematic and magnetization curves showing the Barkhausen effect. A rendering of the torsional paddle device with 3D shape and texture generated from SEM data shows the function of the paddle device, as discussed previously (A). Low field M - H loops show the influence of pinning sites on dM/dH . At 77 K, bistable states appear in the up (red) and down (blue) sweeps, while at 295 K (offset for clarity) up (green) and down (blue) sweeps are identical. Magnetic field is rescaled as $H_{scaled} = H(M_S(T = 0)/M_S(T))$ to normalize the field position of features independently of temperature (69, 99). An analytic fit (dotted line), including thermal effects, to the 77 K data is used to extract the disorder potential (inset). Recomputing using the same potential at room temperature, the hopping rates exceed the measurement bandwidth and mask the bistability.

In two cases limited hysteresis loops were analyzed with fits: the telegraph noise evolution with field, and the 2D data. In each of these cases issues of uniqueness were carefully considered. In the case of the telegraph noise data, the issue is not with the shapes of the pinning sites, relative depths, or site/barrier curvature (i.e. width and depth convolution). The field evolution places strict requirements on the relative separation of the pinning sites and the barrier, which in turn constrains the depth and width. Rather, the position of the sites, and the absolute depth of the sites are ambiguous. Here absolute depth is used to refer to a constant offset that affects both sites, not the depths of the sites that affects the curvature. This is not really an issue however, as complementary hysteresis measurements can provide good estimates of the specific site location. In the case of the 2D data, the problem was initially considered impossible to resolve, however the ambiguity of the fit can be removed if one of the two pinning sites is completely characterized and offers no flexibility in fit parameters. This was the development that motivated the construction of the 2D extension of the DVPM. Use of data from long $M - H$ traces provided specific location, depth, and width parameters for the lower pinning site in the 2D data. Assuming the site is symmetric in 2D, this allows a complete elimination of that pinning site from the fit and permits extraction of 1D equivalent potentials from the small hysteresis loops acquired in using the H_y coil. This is the first step in reconstruction the pinning potential in 2D. Reproducing these 1D equivalents using the 2D model and a 2D distribution of pinning sites is a different matter, discussed in a subsequent section.

4.5.2 Limitations of Fitting

A point that should be brought up explicitly is what information analysis with the DVPM cannot provide. Effectively, the model is incapable of probing areas that the vortex will only transiently access, with the exception of the peak barriers. The probed potential is limited to measurements of pinned locations, and the transition peaks between those locations. Given a pinning potential, everything can be computed, but this is not the case for a fit. This is an unfair criticism of the DVPM specifically though. This is true of all analyses using dynamical data or static data and using a model to reconstruct the potential. This is because the measurements are, themselves, limited to the pinning sites and rapid transitions between those sites. The DVPM still offers the advantage of providing the correct locations and curvature information for the pinning sites as well as better estimates for the barriers. It is not, however, a magic model that can be used to extract information that does not really exist in the experimental data. One must be cautious not to overstate the conclusions drawn about the pinning potential in regions not probed by the vortex.

4.5.3 Fitting to Barrier Evolution

The hopping barriers for the telegraph noise can be fit with a potential formed by two sites approximated as Gaussians. The dominant fit parameters are the separation of the two sites from the barrier peak, which determines the rate of the energy barrier change with the application of field, and the widths of the two pinning sites, which influences the height of the barrier. The depths of the sites are also clearly important, however, the overall depths and positions of the sites determine the field position of the hysteretic feature corresponding to the telegraph noise in the overall field trace, allowing constraints to be applied. The possibility of diagonal hopping paths that are not detected in 1D field sweeps means that the widths of sites must be determined from the telegraph noise data. For a site that is symmetric (with the barrier equidistant between the two pinning sites), fitting is simplified since the widths of the two sites are equal. This gives an end fit that results in a good description of the energy pathway from one hopping site to the other. For an asymmetric site, the widths are not equal making fitting more challenging and error prone. Of the examples presented in Fig. 2C, the 60K and 90K data are symmetric, while the 80K data is asymmetric.

Fitting to the telegraph noise evolution with field (Fig. 4.8) reveals a pinning site configuration that is, in 1D, impossible. It suggests two pinning sites spaced out by approximately 10 nm with a steep separating barrier. The two fit sites required standard deviations below 6 nm to fit the data. This violates the minimum size expected of a pinning site convolved with the core. Even a point like pinning site will have an apparent standard deviation equal to the standard deviation of the core energy density profile (~ 7.3 nm). Considering these size limitations, this implies a diagonal hopping path⁸. Since the telegraph noise presented here is all for the minor loop located at 1.7 kA/m, and since the 2D data reveals a weak interaction for $H_y = 0$, it is then fairly obvious that the core hopping pathways are diagonally to the upper right in Fig. 4.9. Fitting in 2D is covered in the next section.

4.5.4 Pinning Potential in 2D

The starting point for the 2D fit is the complete characterization of the lower site that dominates pinning in the 2D data. This is the same pinning site that forms the lower half of the telegraph noise data, and the lower half of the minor hysteresis loop at 1.7 kA/m in the long $M - H$ curves. The fit parameters for this site include a displacement from the disk centre equal to 45 nm, a standard deviation of 7.4 nm and a depth of 1.6 eV. From the 2D data, the assumption that the circular symmetry of the lower site implies that the site is

⁸Diagonal here means the start and end points of the path are separated by a diagonal straight line. The hopping trajectory will preferentially follow the path of lowest energy, and may be s-shaped.

circularly symmetric in reality is a key point. Note that this is quite a reasonable assumption, since all pinning sites will exhibit some degree of circular symmetry due to convolution with the core. Then the equivalent Δy offset computed from H_y provides a good estimate of the y position of the site at -10 nm. The known 2D location allows computation of the full depth (1.9 eV) of the site and standard deviation (8 nm). For each H_y value used to acquire a loop for the 2D dataset, a 1D equivalent of the lower pinning site may be computed and used in a 1D fit to that particular loop. This procedure is challenging, and must be followed rigorously to ensure no biases are introduced in to the fits. Additionally, this approach may only be applied to loops where one is completely confident that the lower half of the pinning site is due to the well characterized pinning site at 45 nm. Any others must be ignored as a unique fit cannot be guaranteed.

Despite fixing the lower half of each measured loop, the pinning situation remains complicated. Five pinning sites participate. Some sites participate as intermediate sites, others have more subtle effects. The important consideration is that with one half of the potential fixed, the other half is still constrained by necessarily reproducing the barrier shape, even if more than one pinning site must be added to the unknown side. Fits were performed individually, however greater efficiency was realized by noting that the same pinning sites appear in multiple adjacent curves, hence speeding up the fitting process by providing good guesses for site position. Only the central five hysteresis loops were fit as those were the only loops that showed definitive dominance of the 45 nm site on the lower side. (Fig. 4.9)

The next step of reproducing the 2D pinning potential is to fit the array of 1D equivalents with a 2D array. The 2D array has minimum paths ($\Delta x_o(y, H_y)$) for each H_y , and each of these minimum paths has an computed 1D equivalent. The 2D distribution must provide 1D equivalents that match as closely as possible those extracted from the fits to experimental data. Motivated by the qualitative identification of the pinning sites, the 2D construction is restricted to five pinning sites (in addition to the one at 45 nm), and y positions of those pinning sites are taken from the 1D equivalent fits. The detail necessary in the fits means that the transition pathways between bistable sections of the computed minimum path should be investigated in detail (See Chapter 2 for a discussion of bistable paths). The transition pathways are the sections over which the barrier must be computed, therefore the potentials along the transition pathways must be considered as part of the 1D equivalent. This adds an additional layer of complexity, and in the case where a single transition path way cannot be identified, or computed, uncertainty.

A better idea of the morphology of the natural pinning may be gleaned from the 2D data. The strongest individual sites used in the reconstruction are 2.0 to 2.5 eV deep, while the weakest are approximately 0.3 eV, deep corroborating the range found in the 1D fit. Site sizes range from 7 to 10 nm in standard deviation, matching closely with the 7.3 nm standard

deviation of the simulated exchange energy distribution of a vortex core in this size of disk. Since any defect profile will be convolved with the energy profile of the core, this demonstrates that the pinning sites are typically very small; effectively point-like up to a few nm in width.

The constructed 2D potential, and the paths followed by the core through this section of the disk reveal the enormous complexity that exists in the detailed core behaviour (Fig. 4.12). It also explains why periodic instability in the properties, and positions of the hysteresis were observed from data run to data run. Most H_y values have bistable paths. It appears that the lower pinning site, rather than describing a jump between two large pinning sites, describes the transition of the core through smaller pinning sites that surround a large repulsive site. Numerous H_y values features paths that diverge to the sides of the repulsive site, symmetrically around the $H_y = 0$ path. This is seen in figure 4.12 in the $H_y = -430$ A/m and $H_y = -200$ A/m loops where the solutions provide particularly clear jumps around the central repulsive site.

Minor hysteresis can rise for transitions between bistable positions along the same path, or between separate paths. Along the same continuous path, this is just the jumping ahead of the core to a preferable point over a barrier on that path. The two local minima exist transiently in field. Transitions between coexisting paths are more complex. Each path has its own energetic profile, and consequently transitions between bistable points on separate paths for a particular field value are, in general, diagonal. Exact computation of the 2D transition pathway is not performed here. This would require a 4D optimization in an $x - y$ space with x and y each described by a rigid and flexible coordinate. Rather estimates of the transition paths are made based on the appearance of saddle points, indicating a preferred transition path in between coexisting paths. Since transitions are linked to, and in some case dominated by thermal dynamics, identification of an exact path that is followed for every transition can be misleading.

Transitional paths are mostly well defined, with small regions of bistable paths indicating approximately where the transition will occur. However, in the region that corresponds to the telegraph noise ($x = 0, y = 50$ nm) in the loop, a broad overlap of bistable paths exists for the $H_y = 0$ path. This indicates that a large number of possible transition paths can exist. Exploring possible hopping paths reveals a range of energy barriers in the correct range 100-200 meV. This provides an explanation for the inconsistent hopping energy barriers observed. Minute differences in the path the core follows may affect the energetic costs of each of these hopping trajectories changing which one is accessed for a given field sweep. With a broad range of transition paths available for a single path, this is not surprising. What is more surprising is the fact that for given data runs, the hopping trajectory remained stable at all. This implies some detail in the transition process that has not been uncovered

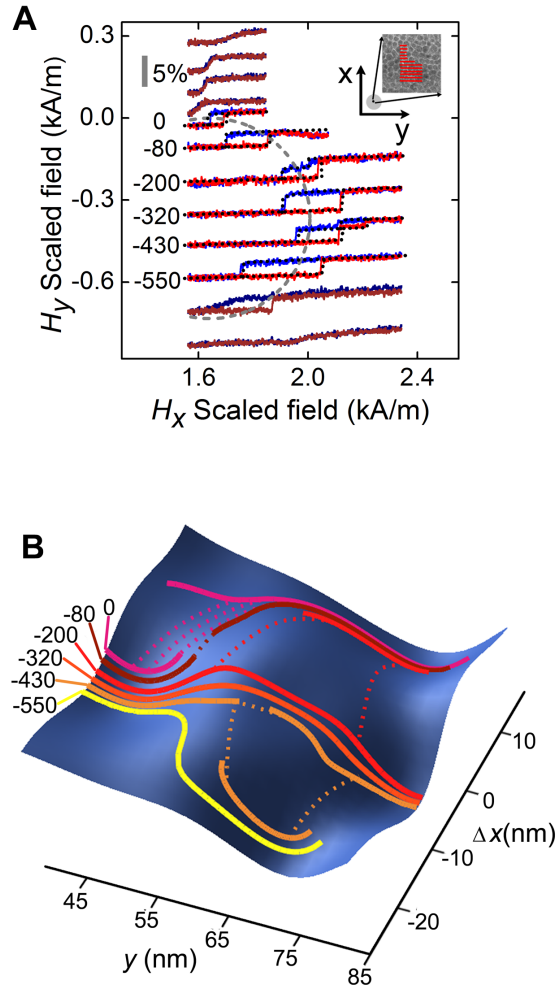


Figure 4.12: Quantitative 2D mapping of the pinning potential. Field sweeps taken with various secondary, H_y , field values (labeled in A/m) probe the landscape around a strong pinning site (A). The circular profile of the central site is clearly visible; a dashed line indicates a circle with radius 10 nm computed analytically assuming no pinning. Inset is a cartoon of the idealized paths overlaid on a representative 50 nm square TEM image showing the grain structure of the Permalloy disk. The gray bar indicates the normalized magnetization scale. A 2D potential is constructed (B) that yields minimum energy paths (solid lines) and estimated hopping trajectories (dashed lines) with profiles matching those extracted from the hysteresis loops in panel A. The field values are labeled in A/m. For the $H_y = 0$ path, the broad overlap of bistable paths provides a multitude of diagonal hopping paths with energy barriers in the 100-200 meV range, consistent with Fig. 4.8.

here. In principle, the stability has been detected, but insufficient data prevents identifying the cause directly. The instability of the temperature control, and the challenge in acquiring the telegraph noise data (in particular), and data in general makes pursuing this problem impractical. A revised apparatus with better temperature stability, and automatic drift correction is under development and will serve as a more capable replacement.

It is necessary to confront the question of uniqueness of the constructed 2D potential. In this case, it is not reasonable to offer a guarantee that the potential is unique. It is possible that the reconstruction is missing features, or has positional errors. For instance, one could picture a washboard potential, with grooves parallel to the y axis that each define a minimum path matching exactly those defined by the H_y values and within the washboard, \sim 1D potentials exactly matching the 1D equivalents extracted from the data. However, the restriction on size and steepness of the pinning sites applies in 2D, and, in conjunction with the constraints applied during fitting: restricting fitting to the number of qualitative sites identified, and using y positions identified in the 1D fits, lends credence to this construction being an accurate representation of reality. To improve the 2D fit to an absolutely confident, unique potential, the torsional magnetometer should provide both M_x and M_y .

4.5.5 Supporting Micromagnetic Simulations

To investigate the effect of the intrinsic variations in an as-deposited film on the magnetic hysteresis of a disk, a random map of regions ranging in size from 5 nm to 15 nm was generated using the Voronoi plug-in for GIMP 2.6. This was used to apply a random variation to the saturation magnetization in regions of the disk. Due to the energy scaling of the problem, variation of the saturation magnetization mimics variations in the thickness of the disk. This allows inclusion of the effect of topographic roughness of the disk in a single layer simulation.

A rectangular grid of cells 5 nm square in plane and 42 nm tall was used with a disk 1100 nm in diameter. Due to the aspect ratio of the disk, 3D properties of the magnetization are expected to be negligible allowing an extended z dimension to be used. Integration of a hysteresis loop was performed through sequential equilibration of the magnetization distribution via time integration at steps of 80 A/m beginning with a vortex state at 0 field. Material parameters matching those used to model the disk were applied. The exchange stiffness constant was 1.05×10^{-11} J/m, and anisotropy was neglected. Using the random map of regions, variations in saturation magnetization between 610 kA/m and 750 kA/m were applied, simulating thickness variations of up to ± 4 nm. The resulting magnetization curve exhibits steps and deviations from the idealized magnetization curve very similar to those observed experimentally (Fig. 4.13). This corroborates the interpretation that the

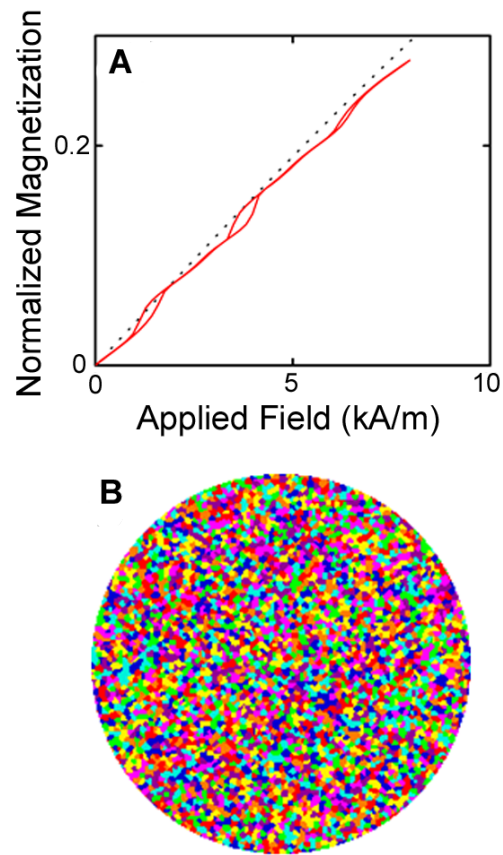


Figure 4.13: Randomized saturation magnetization patterns included in simulation mimic the natural pinning potential of a lumpy polycrystalline disk. The normalized magnetization as a function of the applied field computed in a simulation of a vortex on a grid with randomized saturation magnetization in regions approximately 15 nm in size is shown (A). Small hysteresis loops and deviations from the ideal magnetization trace, very similar to the experiment, are identifiable. For comparison, the black dots are an analytic curve calculated using the RVM for a disk the same size as the simulated disk (demagnetization factor of 0.0381) with a saturation magnetization equal to the average used in the simulation (680 kA/m). The Voronoi map generated to apply the randomized magnetization map is shown (B). Each color represents a variation in saturation magnetization of up to 70 kA/m. This is equivalent to film thickness variations of approximately 10%, much rougher than the disk used in this experiment.

roughness of the deposited film and thickness variations can result in this type of intrinsic pinning (91). In this case, witness disks show RMS roughness measured via AFM to be 0.3 nm, much less than that required to explain the variation. This suggests additional pinning mechanisms.

It may be conjectured, that, despite the smoothness of the films used in this study, the film structure still provides a hint of the cause of pinning. Details of the electron beam deposition are given in appendix B. Important here, is the fact that the design of the electron gun ensures that Ni and Fe are issued from the gun as accelerated (sub 1 keV) and arrive collimated at the substrate. The TEM data presented showing the edges of the disk reveals that the film has well ordered columnar grains. The charged nature of the ions, and the fact that each ion arrives with a reasonable amount of energy leaves open the possibility that the grain structure arises by repulsion of like charged ions diffusing on the film surface, and the subtle resputtering at the sample caused by newly arrived ions. The sputtering may create voids below the surface of the film (196), and repulsion could lead to spacings between grains. This has obvious effects on the saturation magnetization in the film, simply by reducing the density of magnetic material agreeing with the suppressed M_S extracted from the devices made with these films. Intergrain exchange effects would also be expected to be suppressed, making inter grain locations attractive pinning sites for the core. Substantiating this conjecture would require a robust 2D mapping, as constructed in the previous section, along with TEM data providing a map of the local grain structure. This was not possible, as the paddle device and disk were not sufficiently electron transparent near the middle of the disk.

4.6 Artificial Pinning Sites

4.6.1 Ion Implantation

The detailed understanding of the quasistatic and low speed stochastic dynamics of the vortex core in its natural pinning potential motivates detailed exploration of artificial texturing of the local magnetic energy for novel device functionality. Artificial control of pinning potentials will be important for device applications (166) and focused ion beam modification (197) is emerging as a leading technique of tailoring pinning potentials in prototype magnetic logic or memory devices. The effects of ion implantation are not fully understood. Implanted ions remove magnetic material on impact, dilute the magnetic material, change anisotropy, can create sub surface voids (196), and may have additional effects such as disrupting exchange interactions. The exact mechanisms behind conjectured effects such as the suppression of exchange energy are not understood, for instance, the aforementioned

voids would obviously have an effect on exchange interactions in the immediate vicinity of the void. Reviews of ion implantation in magnetic films provide a good overview of possible effects (198–200).

The torsional magnetometry platform presents an interesting possibility for integrated devices. NEMS are considered a promising platform for integration into standard computing technology (176, 177), or photonic technology (201) as a lower power device platform. Combined with the introduction of very weak pinning potentials, this suggests the opportunity to create low power magnetic devices.

4.6.2 Artificial Bistable Sites

The concept is demonstrated here by the addition of three pinning sites, much stronger than the natural pinning potential, introduced by ion milling fine dimples into the surface. This was done through very low current (0.3 pA), fast-shuttered (40 ms) point exposures of a focused gallium ion beam ($\sim 70,000$ Ga⁺ ions) onto the disk. This is a very much scaled-down version of the “antidots” (holes) in a vortex disk studied earlier by Rahm (202, 203). One dimple was placed ~ 110 nm from the disk center while on the opposite side of the disk two dimples were placed at ~ 200 and 280 nm to enable identification of the chirality of the vortex state. All dimples were placed along the y axis where previous measurements had thoroughly characterized the natural pinning potential.

The dramatically modified magnetization response as the core passes through the pinning site is shown in Figure 4.14A. Even at room temperature, strong minor hysteresis loops mark the entrance and exit points of the vortex from the dimple. This contrasts with the pre-dimple room temperature measurements along this path that showed only thermally smoothed features. Exploring the opposite side of the disk, similarly dramatic changes occur (Fig. 4.14B), including clean minor hysteresis from direct transitions between the proximal dimples. The strong pinning sites also emphasize the non-zero differential susceptibility, a key characteristic of the nanoscale Barkhausen effect. Applying the model, good fits are found for Gaussian pinning sites at 110 nm, 215 nm, and 300 nm, with depths between 17 and 21 eV and a common standard deviation of 18 nm. Recall that at displacements greater than $R/2$ the model begins to return fit values larger than the actual positions of the pinning sites due to systematics in the model.

If the maximum energy density possible in the film is considered to be $\mu_0 M_S^2$, this pinning site strength is equivalent to the complete suppression of magnetization in a volume equivalent to a cylinder ~ 6 nm in radius through the thickness of the disk. The physical thinning of the disk at the dimple (~ 2 nm depth by AFM), or dilution of magnetic material by Ga is insufficient. This suggests that the Ga⁺ ions disrupt the exchange interaction.

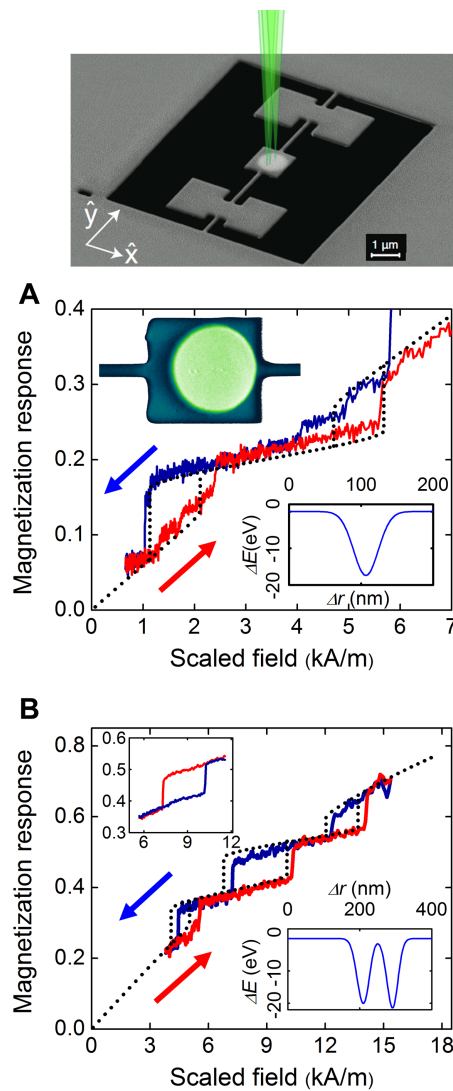


Figure 4.14: Control of the Barkhausen Effect. Point exposures of Ga^+ ions disrupt ordering in the permalloy film, creating strongly interacting artificial pinning sites (A). The three added pinning sites are visible with a linear remapping of the greyscale to a color scale in a contrast enhanced SEM image of the torsional paddle (inset top left). The modified magnetization response exhibits prominent hysteresis between the up (red) and down (blue) field sweeps as the vortex is driven over the single dimple. The observed pinning is modeled accurately (dotted black line) by a Gaussian pinning potential (inset bottom right). The double dimple also shows strong artificially induced bistability (B), including hysteretic transitions directly from dimple to dimple (inset top left). The two dimples may be modeled as Gaussian sites (inset bottom right) with width and depths very similar to the single dimple.

Assuming linear response, the efficacy of magnetic potential well excavation is ~ 0.3 meV per implanted ion. Recent work demonstrates methods of reducing or eliminating exchange effects (204) and the flexibility of very weak pinning (166). The previously noted columnar structure of the grains in the disk makes the view of Ga ions diffusing along grain boundaries, down further into the disk than would be expected by ion implantation, an attractive possibility. However this is an unsubstantiated theory. Further speculation on the nature of this suppression, as well as substantiation of the assumed linear scaling down to single ion effects, requires more data.

The limited set of pinning sites probed here provides some insight into the nature of ion damage, but it is not sufficient to resolve any mysteries. The work done here provides a blueprint for subsequent studies where dosing effects or additional materials beside permalloy are explored. Initial dose tests on plain films (not on torsional devices) have been performed indicating that pinning sites over an order of magnitude smaller can be accessed (Fig. 4.15). This raises the possibility of sculpting the potential on the same scale as the natural disorder, or more interestingly, making extremely simplified pinning situations in single crystalline materials. Further investigation of the pinning effects combined with shifting devices to an entirely on chip photonic detection scheme that uses lower power, and has much higher sensitivity, makes pursuit of technology based applications for these devices an eminently practical goal.

4.7 Conclusion

The work presented in this chapter outlines the development of a technique capable of probing nanometer scale properties of magnetic films with nm precision and quantitative energetic accuracy on the meV scale. The combined usage of the DVPM and hysteretic magnetic data presented here will be a powerful tool moving forward in quantitative understanding of micromagnetics.

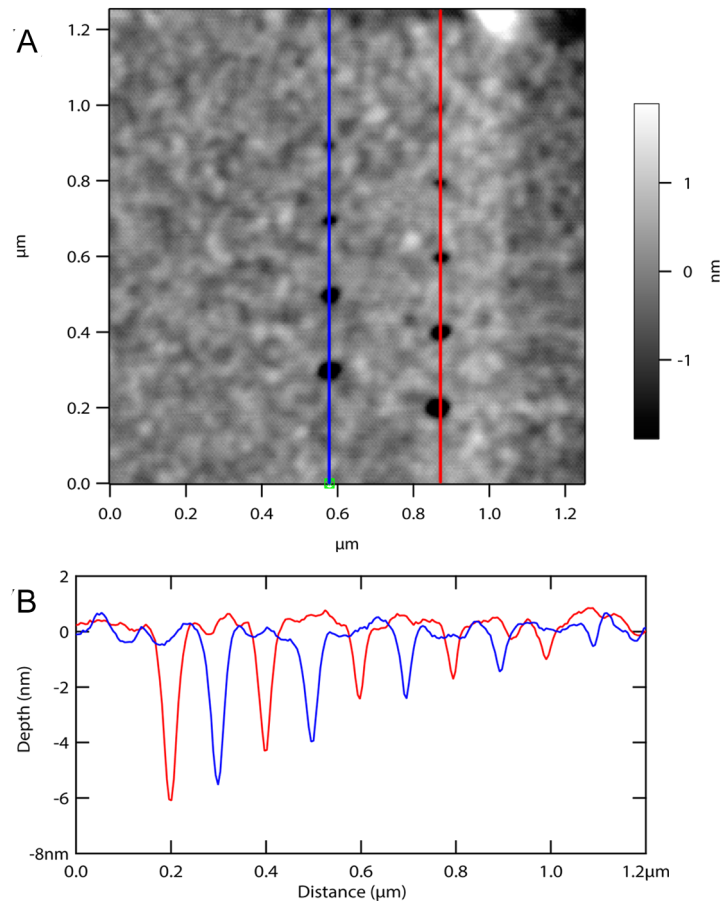


Figure 4.15: Variable dose FIB point exposures demonstrate the possibility of variable texturing of magnetic films in a pointillist fashion. AFM data (A) of a witness film showing a FIB dose test for a line of point exposures. Dosage times range from 5 ms to 1280 ms for dimples along the blue profile, and 10 ms to 2560 ms for the red. (B) Profile data shows the physical depth of each dimple. Dimples with an exposure of 40 ms dimple were reliably visible in SEM inspection.

CHAPTER 5

Time-Resolved Spin Polarized STM: A Route to Simultaneous Temporal and Spatial Resolution

A consistent theme throughout the work presented thus far is the desire to know exactly where the vortex core is, and what it is doing. This provided much of the initial motivation for the development model in Chapter 2, which allows the mapping of pinning sites presented in Chapter 4. This approach is robust and provides a great deal of information beyond the position of the vortex, however benchmarking of the model is still necessary against simulation. Current experimental approaches applied to fabricated micromagnetic devices that might lead to an experimental tracking of the core position fail for reasons such as applying stray field to the sample, insufficient resolution, or providing a systematically incorrect core position. This points out the potential importance of a technique that provides sub-nm resolved measurements of the vortex core position. Such a technique could also provide new information about structural changes of the vortex core during pinning.

The work in Chapters 2, 3 and 4 focuses almost entirely on the quasi-static behaviour of the vortex core. However, magnetodynamics can provide a great deal of complementary information (eg. (70, 87–90, 92)). Complementary dynamics measurements focusing on pinning, thus far, are limited to ~ 100 's of nm resolution. In principle, measurements of magnetic hysteresis combined with dynamical measurements would provide the same improved core position estimate as was obtained for the torsional magnetometry data in Chapter 4. This alludes to potentials for combined dynamic and static magnetometry based investigations of pinning. However, as with the application of the model to quasi-statics, experimental verification of the core position, independent of simulation or modeling, is still desirable. Furthermore, combining conventional dynamics techniques with quasi-statics and the model will not provide new insight into deformations of the core due to pinned dynamics.

This begs the question, if one developed the instrument alluded to in the first paragraph, with high spatial resolution, could it also be made with temporal resolution to enable nm scale observation of dynamics?

This chapter describes the development of an instrument designed to resolve the vortex core position and dynamics with combined sub-nm spatial and sub-ns temporal resolution. The base of the instrument is an ultra-high vacuum (UHV) low temperature scanning tunneling microscope (STM). To this base a large number of components must be added including: wiring upgrades for high-speed operation, a magnetic tip, and a system for preparing fabricated samples *in situ*.

At the time of this writing, the instrument is a time-resolved STM (TR-STM) with \sim nm spatial resolution and \sim 500 ps temporal resolution. It also happens to use a tip that is, in principle, spin polarized, and therefore should provide magnetic contrast. However, magnetic contrast has not yet been observed. Thus the ingredients to create a time-resolved spin polarized STM (TR-SPSTM) exist, however practical challenges remain. The details of development of the system, its supporting infrastructure, its operation, and challenges remaining in its application to the problem of a vortex are described in the following chapter.

5.1 Magnetodynamics and High Spatial and Temporal Resolution

The development of an instrument capable of simultaneous high spatial resolution and temporal resolution is a long standing goal in the micromagnetics community. As discussed in the introduction, this is one of the most prominent avenues of investigation that may lead to the observation of non-LLG quantum magnetic behaviour.

The current state-of-the-art in simultaneous space and time resolution is provided by synchrotron based x-ray laser sources (eg. Advanced Light Source Berkley). There, x-ray pulses are generated on the synchrotron beam line, and then passed to microscopes that employ x-ray optics to image samples. A variety of techniques can be used, including direct imaging with the x-rays (205, 206), or using scanning x-ray microscopes (97). Magnetic contrast can be obtained by use of x-ray magnetic circular dichroism to measure differences in absorption of right and left hand circularly polarized x-rays in the sample. Two issues exist with this technique. The first is that, until bright table top x-ray sources become affordable, this is only a viable approach for large-scale synchrotron institutions. Second, and more importantly, the optics for the x-ray beam lines are very challenging to produce. The optics consist of nanometer scale metal gratings fabricated on silicon nitride membranes (207). Current technology is pushing the limits of conventional lithography (sub 10 nm feature

size). Despite extraordinarily fine optics, spatial resolution is still limited to ~ 12 nm in proof-of-principle work (208) and ~ 20 nm in practical realization (209). Temporal resolution is limited to by the synchrotron itself at ~ 70 ps (205, 206, 209). Recent reviews provide more information (68). This means that imaging time response is averaged over millions of events, as with any other pump probe technique. Other imaging techniques have very fast temporal resolution, such as TR-MOKE microscopy, but limited spatial resolution. An important detail to keep in mind is that these time-resolved techniques, both synchrotron and magneto-optical, are pump-probe experiments, that is, they are stroboscopic. While high resolution scanning probe microscopies such as MFM, and spin polarized STM, traditionally have millisecond, at best, temporal resolution.

5.2 Scanning Tunneling Microscopy

Scanning tunneling microscopes revolutionized microscopy of solid state systems in 1981 (210–213). The working principle of the STM is vacuum tunneling of electrons between electrodes separated by a very small gap. It is well known that the rate of tunneling transitions between the electrodes depends exponentially on the gap. This permits, with uniform electrodes, the use of the tunnel current as a sensitive probe of sample topography. Moreover, the nature of the tunneling process reveals a great deal of information about the density of electronic states in the electrodes.

The STM was made possible by advances in piezo-electric technologies that permitted \sim pm positioning accuracy for the tip. The basic design of the instrument consists of a sharp (typically atomically sharp) conductive tip mounted on a piezo tube that provides three axes of translation (Fig. 5.1). The tip is brought near, and held extremely close to the sample, so that the vacuum tails of the conduction electron wave functions in the tip and sample have a non zero overlap. This allows direct tunneling between the tip and sample. The tip is connected to the inner conductor of a highly shielded coaxial cable which carries the tunneling current to a sensitive current-to-voltage converting pre-amplifier. Typically the microscope is operated with a feed-back loop that controls the position of the tip, and consequently the width of the gap, in order to maintain a constant tunnel current. Less commonly, in situations where the sample is sufficiently flat, and the microscope is stable, the feed-back loop may be turned off and the tip can be scanned at constant height while the variation in the tunnel current is recorded.

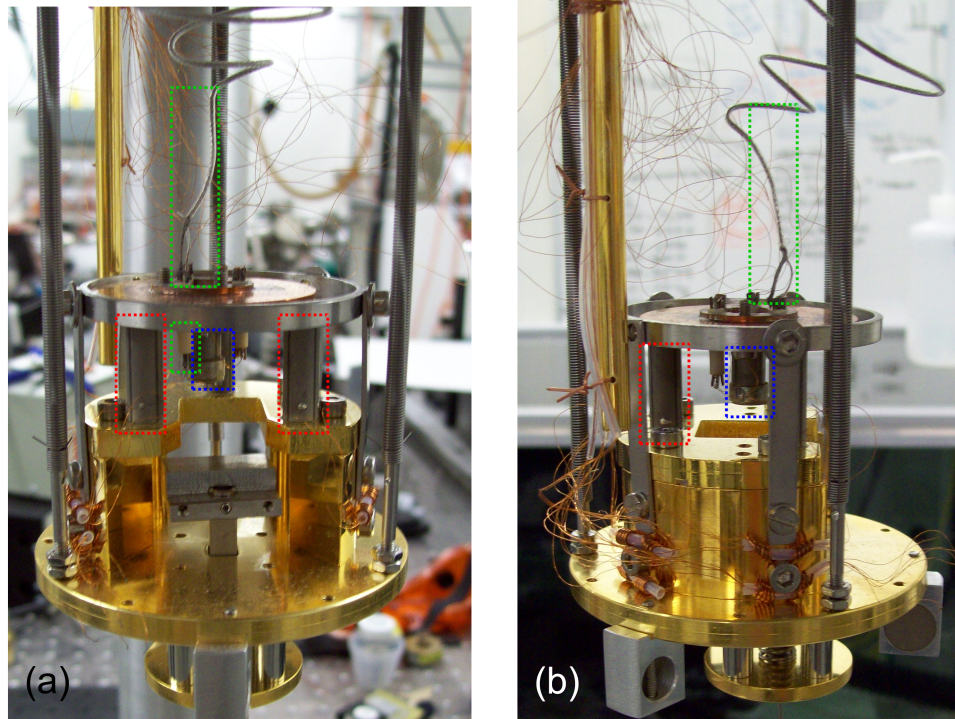


Figure 5.1: The Besöcke Beetle scan head of the STM. The tip is mounted on a scan tube which is in turned mounted on a copper ramp with radial sloped sections machined into it. The copper ramp sits on three additional piezo tubes (one for each sloped section) tipped with sapphire balls. These outer tubes can shift in X and Y , pushing the ramp around via stick-slip motion. The outer tubes can also raise and lower the ramp by rotation. Fine scanning is performed using the more sensitive scan piezo. The coarse piezo tubes are highlighted by a dotted red outline in the above, while a blue outline identifies the fine scan piezo. The tunnel current wire, both above and below the ramp, is outlined in green.

5.3 Time-Resolved STM

The STM has a design that effectively prohibits any significant natural time resolution. Most prominently, the minute tunnel currents detected (fA to nA) demand extremely high quality pre-amplifiers which ubiquitously have high input impedances and very low bandwidth. Compounding this is the fact that scanning almost always requires a feed-back-loop which also operates in the kHz range. In principle, the intrinsic time resolution of the junction is very fast, although shot noise from the discrete tunneling current would be an issue on short time-scales. In the early 1990s a variety of approaches were taken in order to enable pump-probe time resolution in STM. These approaches used various methods of circumventing the band width limitations, while the common pump-probe arrangement assures shot noise is not an issue by averaging over a large number of events. Success was found using modulation of the tunnel gap via application of a signal to the scan piezo (214), and by application of voltage pulses to a transmission line style sample, modulating the bias (215). Initially promising was the use of a photoswitch attached to the tip to gate the tunnel current (216), however this was quickly shown to exhibit charging effects (217). Effectively the tip was charging up according to the capacitance of the tip and sample, and then discharging when the photoswitch was triggered. In other words, the information contained in the measured tunnel current no longer represented only information from the actual tunnel junction at the apex of the tip, placing a fundamental limit on the resolution and information attainable with this technique. By contrast, use of voltage pulses applied with photoswitches has been shown to have no capacitive nature, and to provide actual tunneling information (218).

Of the other two successful approaches, the electronic approach offers far superior time resolution¹. Tunnel distance modulation is fundamentally limited by the response of the piezos used for scanning, making the best time resolution attainable ~ 1 ns. By contrast, initial work in using voltage pulses permitted ps time resolution. Since its invention, sporadic work has been performed advancing JM-STM (215, 219–222), demonstrating spatial resolution down to 1 nm (222, 223) and temporal resolution as fast as 8 ps (223). The use of opto-electronic switches is not a key feature of JM-STM; an all electronic version, replacing photoswitches with electronic pulse generators, has been demonstrated, with temporal resolution of 100 ps and atomic spatial resolution (224). Very recent work has resulted in an all optical approach, mixing optical pumps with plasmon modes excited by THz pulses in a manner very similar to JM-STM (225). This work has demonstrated 700 fs time resolution with 2 nm spatial resolution, however it has only been demonstrated operating in field emission mode, not as a true STM. Additional work on all optical techniques has been pursued in the last decade. Shaken Pulse Paired STM (SPP-STM) uses two different wave-length

¹In addition to the peace of mind that comes with not jiggling the tip up and down as fast as is permitted by the scan piezo.

optical pulses to excite carriers in semi conductors, and then probe the population of carriers and the excited dynamics (226–228).

Pervasive in the works directly advancing JM-STM is the limited scope of investigation. Virtually all time-resolved STM experiments are proof-of-principle works and fail to measure physically interesting phenomena. The classic experiment is the measurement of a voltage spike. Exceptions above include the use of pulse paired STM to investigate carrier dynamics on the nano-scale in photoexcited semiconductors (228), and examination of charging dynamics in quantum dots with the THz technique (225). This relatively limited set of applications betrays the fundamental difficulty in operating a TR-STM. Practically, it is very challenging to develop a high bandwidth microscope that can be applied to general samples.

The lack of physical meaning in TR-STM work has effectively been rectified with recent work examining magnetic systems (46, 229). In this work the dynamics of single spins excited by tunnel current pulses was examined using an all electronic variation of TR-STM, similar in some ways to JM-STM. The use of tunnel current pulses as both the pump and probe stimulus limits this technique to point-like measurements (or arrays of point-like measurements), and also limits time resolution (~ 1 ns) by the use of the tunnel current wire which may exhibit ringing, however it also permits application of TR-STM to any sample. Thus far it has been used to examine the effect of engineered local anisotropy on spin decay times (229), and also as a switching mechanism for chains of stable spins (46).

5.4 Spin Polarized STM

Spin-dependent tunneling was observed in thin film tunnel junction devices over 35 years ago (230). In a thin film sandwich, composed of a ferromagnet, a non-magnetic insulator, and another ferromagnet, for current passed through the device perpendicular to the layers,² the effective resistance of the device depends on the relative alignment of the two ferromagnets. This effect, known as Tunneling Magneto-Resistance (TMR), has been well investigated as one of the key components of the field of spintronics (eg. review (44)). In the past decade, TMR has been incorporated into hard drive read heads meaning the effect is now ubiquitous in the life of the typical computer user.

The sandwich geometry described in the context of TMR is identical to a STM with a magnetic sample and tip. This immediately motivates the thought that spatial magnetic contrast may be obtained. This technique, Spin polarized Scanning Tunneling Microscopy

²Particularly in sandwich devices with a conductor replacing the insulator, there are very well known effects for current passed in one of the ferromagnetic planes dependent on the relative magnetization of the other plane. However, here only the perpendicular case, analogous to the STM junction, is considered.

(SP-STM), is an increasingly common form of non-invasive magnetic microscopy. SP-STM was first developed for a UHV STM in 1990 (231–233). Since then it has been used extensively for the inspection of atomic scale magnetism in systems ranging from the usual, large single crystal STM samples down to individual atoms (eg. (234–237)). It is a clear candidate form of magnetic microscopy that has the necessary resolution (\sim atomic) to determine the core position and examine the core structure. Imaging performed on single crystal iron nano islands has already provided the highest resolution inspection of the vortex state ever performed (95). Inspection of more technologically pertinent elements, composed of polycrystalline permalloy has not been performed in any meaningful way. A key part of the challenge is the fact that SP-STM (and STM in general) is usually applied only to atomically flat samples such as single crystals, individual atoms, or magnetic molecules. Scanning a rough polycrystalline surface presents a challenge.

5.5 Theoretical Description of the STM

The tunnel current is exponentially dependent on the gap. It is typically introduced as a standard problem of plane waves being transmitted through a finite tunnel barrier, as can be found to varying degrees of complexity in a wide variety of undergraduate or graduate physics textbooks (238, 239). In summary, the problem may be solved by computing the transmission coefficient for plane waves of energy E , and then integrating total transmission over the density of states for these plane waves. The limits of integration are set by considering the density of states available for tunneling, those occupied on one side, and unoccupied on the other. In a real sample, the Fermi energies at the junction will naturally equalize by equilibrium tunneling, and asymmetry providing constant current will arise only when a bias voltage creates a persistent inequality. This is taken into consideration here by only integrating over energies in a range defined by the bias voltage. Describing the barrier as a rectangular barrier with energy ϕ_w equal to the sample work function, and considering electrons at energies $E \leq \phi_w$, solutions an expression for the tunnel current may be written down:

$$I = \frac{e^2 V_B \sqrt{2m_e \phi_w}}{16\pi^3 \hbar^2} e^{-2\sqrt{2m_e \phi_w} d}, \quad (5.1)$$

where V_B is the bias voltage, and e , m_e and \hbar are the electron charge, mass and Planck's Constant respectively. This formula, considered in the context of a continuum of free electron gas states for the two sides of the barrier, and for an applied bias voltage constitutes the simple expression for the tunnel current which is usually used in introductory STM theory. It accurately conveys the the exponential dependence on d , demonstrates the exponential

dependence of the tunnel current on the gap width and therefore topography of the sample. However, the dependence on the density of states in the tip and sample is not explicitly highlighted. An approach to describing the STM that provides an intuitive understanding of the importance of the density of states is provided by the Modified Bardeen Approach (MBA) as summarized in the next section.

5.5.1 The Modified Bardeen Approach

Commonly, the STM is given a rudimentary theoretical treatment focusing on the exponential gap and considering only a free electron gas on either side of a barrier. This gives a good idea of the sensitivity of the microscope to the gap and the nature of the current, however it fails to capture the richness of information available in the tunneling current. Of particular importance here is understanding the role of the density of states in determining the tunnel current. A more complex, but also more rewarding and accurate treatment can be derived from time dependent perturbation theory following Bardeen's treatment of a vacuum gap (240).

In this section, the goal is to provide a computation that relates the rate of electron tunneling to the tip and sample wave functions, the applied bias voltage, and the occupancy of states in the tip and sample (ie. the density of states). This derivation, as applied to an STM is known as the Modified Bardeen Approach (241) first applied in the famous work of Tersoff and Hamann (242) and built upon by Chen (243). A brief overview of the concept of the MBA is included here. A more detailed derivation is available in Appendix G or in Chen's text.

In effect, the MBA treats the presence of the tip as a perturbing potential introduced at time $t = 0$. Under the assumptions that tunneling rates are slow, and that the overlap of the tip and sample wave functions is small, it may be shown that the approximate tunneling rate follows Fermi's Golden rule:

$$W_{\mu\nu} = \frac{2\pi}{\hbar} |M_{\mu\nu}|^2 \delta(E_\nu - E_\mu), \quad (5.2)$$

where $W_{\mu\nu}$ is the tunneling rate per unit time between the sample state ψ_μ and the tip state χ_ν that have energies E_μ and E_ν respectively. The matrix element $|M_{\mu\nu}|^2 = \langle \chi_\nu | U_T | \psi_\mu \rangle$ describes the overlap of the tip and sample wave functions while the delta function enforces an elastic tunneling condition. Note that, in this description, the exponential dependence on the tunnel gap is contained within $M_{\nu\mu}$. In this work, it is sufficient to understand that the exponential dependence exist, as shown from the simple transmission through a barrier treatment, and further details on evaluation of the matrix element are left undiscussed. The

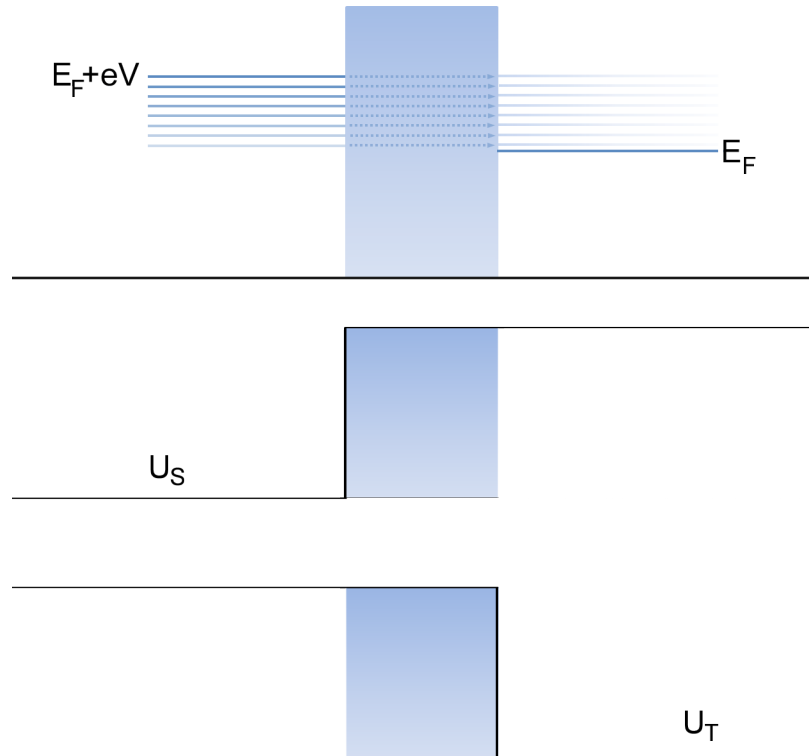


Figure 5.2: The tunnel junction of an STM can be represented in rudimentary form as a square finite barrier tunneling problem. The junction is in chemical equilibrium so that the Fermi energies of the tip and sample are equal. Applying a bias, elevates the energy of one side, enabling tunneling between occupied states and unoccupied states. In the modified Bardeen treatment, the potential defining the well is divided into tip and sample portions.

reader is referred to Chen's detailed and clear description on the complexities of actually evaluating $M_{\nu\mu}$ for realistic wave functions.

Once the Golden Rule can be written down for any two states, an expression for the total tunnel current may be obtained by integrating over all states available to participate in the tunneling process. In order to do so, it is assumed that the tip and sample are in chemical equilibrium (equal Fermi energies E_F). Without further additions to the problem, the net tunneling rate would then be zero. Introducing a bias voltage across the junction shifts the Fermi level of one electrode. For this description, it is subsequently assumed the energy in the sample is raised as if a negative bias was applied to the sample. This creates an imbalance across the junction, permitting occupied states in the sample to tunnel to the tip, creating a steady (on long time scales) current that depends on the transition probability ($\sim |M_{\mu\nu}|^2$) and the number of states participating in the tunneling ($\sim V$).

Considering a generalized density of states for the tip $\rho_T(E)$ and sample $\rho_S(E)$ a generalized form for the expected tunnel current may be written down:

$$I = \frac{4\pi e}{\hbar} \int_{-\infty}^{\infty} [f(E_F - eV_B + \epsilon) - f(E_F + \epsilon)] \rho_S(E_F - eV + \epsilon) \rho_T(E_F + \epsilon) |M|^2 d\epsilon \quad (5.3)$$

where $f(E) = 1 / \left(1 + e^{\frac{E - E_F}{k_B T}} \right)$ denotes the Fermi-Dirac Distribution. This may be simplified by considering the use of a small bias, so that $|M_{\mu\nu}|$ is approximately constant, and low temperature, so that the Fermi-Dirac Distributions become effective step functions. The tunneling current then becomes:

$$I = \frac{4\pi e |M|^2}{\hbar} \int_0^{eV_B} \rho_S(E_F - eV + \epsilon) \rho_T(E_F + \epsilon) d\epsilon \quad (5.4)$$

This expression makes the influence of the density of states of both the tip and sample on the tunnel current eminently clear. Commonly, this is exploited in order to image the density of states of the sample. Considering the derivative of the current with respect to the voltage, and assuming a relatively boring tip density of states (approximately constant), $dI/dV \sim \rho_S(E_F - eV)$. This demonstrates how useful tunnel current spectroscopy can be. Fundamentally dI/dV spectroscopy is the basis of Junction Mixing STM and most other forms of time-resolved STM. It is also the basis of Spin Polarized STM.

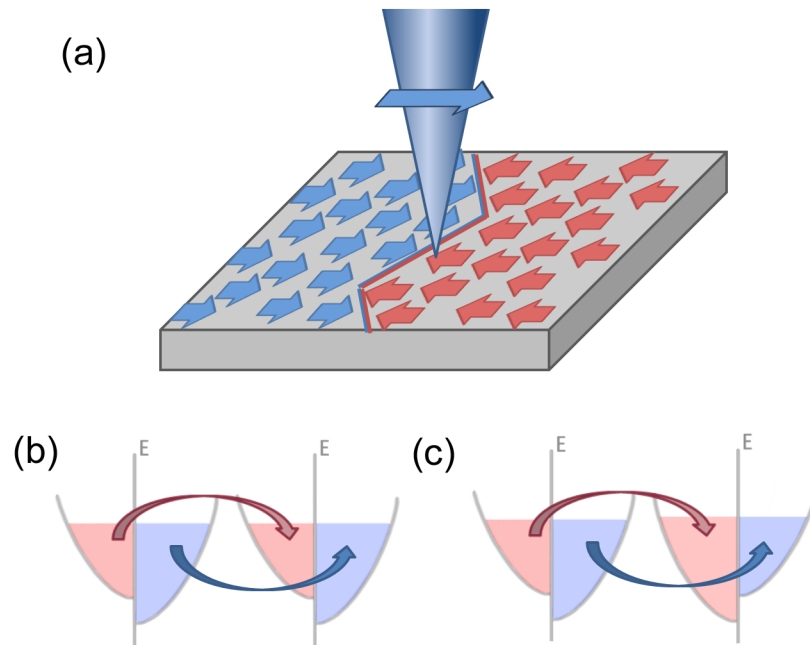


Figure 5.3: A spin polarized STM detects magnetic contrast by variation of the polarization of the sample conduction electrons, using the polarization of the tip itself. Contrast arises as the direction of the sample magnetization changes relative to the constant tip magnetization (a). The influence of the density of states on the tunnel current causes the contrast by virtue of modulating the net conductivity of the junction depending on the match of spin up and spin down states in the tip and sample (b). The density of states of a free electron gas is used here as a simplified representation of the tip and sample.

5.5.2 SP-STM

The use of the Bardeen approach makes the influence of the density of states of both the tip and sample on the tunneling current obvious. This immediately motivates the use of spectroscopy as discussed in the previous section. For magnetic samples, it also immediately implies that the magnetization can be probed via the spin split density of states, ρ_\uparrow and ρ_\downarrow , that exists in ferromagnets (Fig. 5.3). For no spin flips during tunneling (very reasonable for elastic tunneling), the tunnel current be described as two components, representing tunneling in up and down spins ³. The tunnel current expression becomes:

$$I = \frac{4\pi e|M|^2}{\hbar} \int_0^{eV_B} (\rho_{S\uparrow}(E_F eV + \epsilon)\rho_{T\uparrow}(E_F + \epsilon) + \rho_{S\downarrow}(E_F eV + \epsilon)\rho_{T\downarrow}(E_F + \epsilon)) d\epsilon. \quad (5.5)$$

This leaves the sum of the products of the up and down densities of states forming the integrand of the tunnel current. The more closely the magnetizations or spin populations of the tip and sample are aligned, the larger the tunnel current will be, and vice versa. In general the magnetizations of the tip and sample will have imperfect alignment. A general treatment of the tunnel barrier problem with spin may be pursued (244). It is useful to define a quantity describing the spin populations of the conduction electrons in the tip and sample called the polarization (P) (eg. (244)). Usually polarization is defined as $\frac{\eta_\uparrow - \eta_\downarrow}{\eta_\uparrow + \eta_\downarrow}$ by the density of up and down spins at the Fermi level (η_\uparrow or η_\downarrow). In this case however, it makes sense to consider the polarization of all states participating in tunneling.

$$P = \frac{\int_0^{eV} (\rho_\uparrow - \rho_\downarrow) dE}{\int_0^{eV_B} (\rho_\uparrow + \rho_\downarrow) dE} \quad (5.6)$$

The conductivity of the junction can then be re-expressed in terms of the the polarizations of the two electrodes (P_S and P_T), and on the angle between the magnetizations (θ_{ST}) as:

$$\frac{dI}{dV} \sim (1 + P_S P_T \cos(\theta_{ST})). \quad (5.7)$$

While it is clear that there are many elements of the SP-STM subject to more complexity in realistic situations, the above results provide a working qualitative knowledge of SPSTM.

³Up and down defined by the magnetization of either the tip or the sample

5.6 Operation of a TR-STM

Similarly to the SP-STM, the operation of the most successful time-resolved STMs depends on the presence of the density of states in the tunnel current expression. Specifically, the classic Junction Mixing approach depends on the nonlinearity of the density of states of the metallic sample. The non-linear properties of the tunnel current can be described using a full solution to the tunneling barrier problem considering free electron gases. This solution is generally known as the Simmons model (245, 246), though contributions were made by Sommerfeld (247) and by Holm (248), special cases were covered by Fowler and Nordheim (249), and Bardeen's general formalism would also lead to the same general result with the appropriately evaluated matrix element. In approximation, the total I-V dependence for a metal-insulator-metal junction has the form:

$$I \sim Z_1 V_B + Z_2 V_B^3 \quad (5.8)$$

where Z_1 and Z_2 are coefficients specific to any particular type of junction. The non-linearity is critical to the extraction of time-resolved information from the STM. The critical limitation is the time resolution of the highly sensitive pre-amplifiers necessary for measuring tunnel currents. Overcoming this limitation requires the use of a pump-probe technique. Proof-of-principle results (215, 219, 220, 222) and applications to physically interesting systems (229) have so far used voltage pulses. If the effect of two voltages is considered separately, the total current $I(V_1) + I(V_2)$ is less than the current under the summed voltage $I(V_1 + V_2)$ (Fig. 5.4). This is equivalent to considering the effect of two sets of voltage pulses applied to the junction. If the pulses do not overlap, increases in tunnel current are simply the effect the voltage pulses separately. If the pulses do overlap, the non-linearity guarantees an additional excess in the tunnel current pulses. To measure the time response, it is simply a matter of changing the delay time between the pump and the probe.

Accessing the excess component of the current requires some forethought. Due to the pre-amplifier bandwidth, pulses are not resolvable above the kHz range. This means the charge carried in the tunnel current pulses will be integrated into apparent DC tunnel current contributions. In principle, the excess tunnel current would still be measurable, however due to the usual operation of an STM with a feedback loop maintaining a tunnel current set-point, this is not generally practical. Even working with an exceptionally stable STM in constant height mode (no feedback), time-resolved contributions to the current could not be separated from spatial contributions. The simplest approach to measuring the excess is to apply a chopping signal to either the probe pulse train, turning it on and off periodically at a frequency below the bandwidth of the pre-amp, but above the bandwidth of the feedback

loop. The chopped signal is detectable with a lock-in amplifier and represents the total contribution of the probe pulses: both the time-resolved excess current, and the contribution of the probe pulse alone. The offset from the solitary probe pulse contribution is not critical. This type of instrument was used by Loth et al. in recent work (46, 229).

In the original opto-electronic Junction Mixing experiments (215) the non-linearity was additionally used to convert the tunnel junction into a mixing electronic element. Consider two time dependent signals included in the bias voltage. For simplicity, consider two sinusoidal voltages $A_1 \sin(\omega_1 t)$ and $A_2 \sin(\omega_2 t + \delta\phi)$. The third order expression may be expanded $V_B^3 = (V_{DC} + V_1(t) + V_2(t))^3$. In the expansion, the terms with the product $V_{DC}V_1(t)V_2(t)$ is of particular interest.

$$V_{DC}V_1(t)V_2(t) \sim \sin(\omega_1 t)\sin(\omega_2 t + \delta\phi) = \frac{1}{2} [\cos((\omega_1 - \omega_2)t) - \cos((\omega_1 + \omega_2)t)] \quad (5.9)$$

The nonlinearity acts to create products of the time-resolved signals, generating mixing terms. This leads to a spectrum of mixed signal peaks in the tunnel current (Fig. 5.4), most notably including the sum frequency. Lock-in detection of the sum frequency enables measurement of the excess tunnel current resulting from the overlap of the two signals guaranteeing only time-resolved information. This approach has the advantage of detecting only the excess current, and cutting down on the chances of detecting any spurious signals.

In practical application, the mixed signals are more complex than simple sinusoids. To obtain fast time resolution, pulses ranging from the μs to ps scales can be used. In the above calculation, the frequencies of the signals used in the mixing must provide a detection (mixed) frequency that is within the preamplifier bandwidth. Any attempt to use low repetition rates to accomplish this will result in virtually eliminating the excess current signal simply by the duty cycle of the input pulse trains. In principle, the difference frequency could be used to down-mix the time-resolved signal into the bandwidth range, however maintaining two pulse trains with repetition rates in the MHz or GHz with a frequency difference in the ~ 100 Hz range is challenging and likely to lead to poor signal-to-noise. It is easier to apply fast pulses for the pump and probe using equal repetition rates, and then to chop the input pump and probe pulse trains at two separate frequencies. In this sense, with the low bandwidth of the current preamplifier, the pulse trains are treated as effective DC voltages, though time-resolved information still exists dependent on whether the pump and probe overlap. The chopping frequencies can then be chosen for convenience so that ω_1 and ω_2 are within the feedback bandwidth, while the sum frequency is above the feedback bandwidth, but still within the preamplifier's bandwidth. This allows the feedback to mask the influence of the separate pump and probe frequency peaks as contributions to the DC

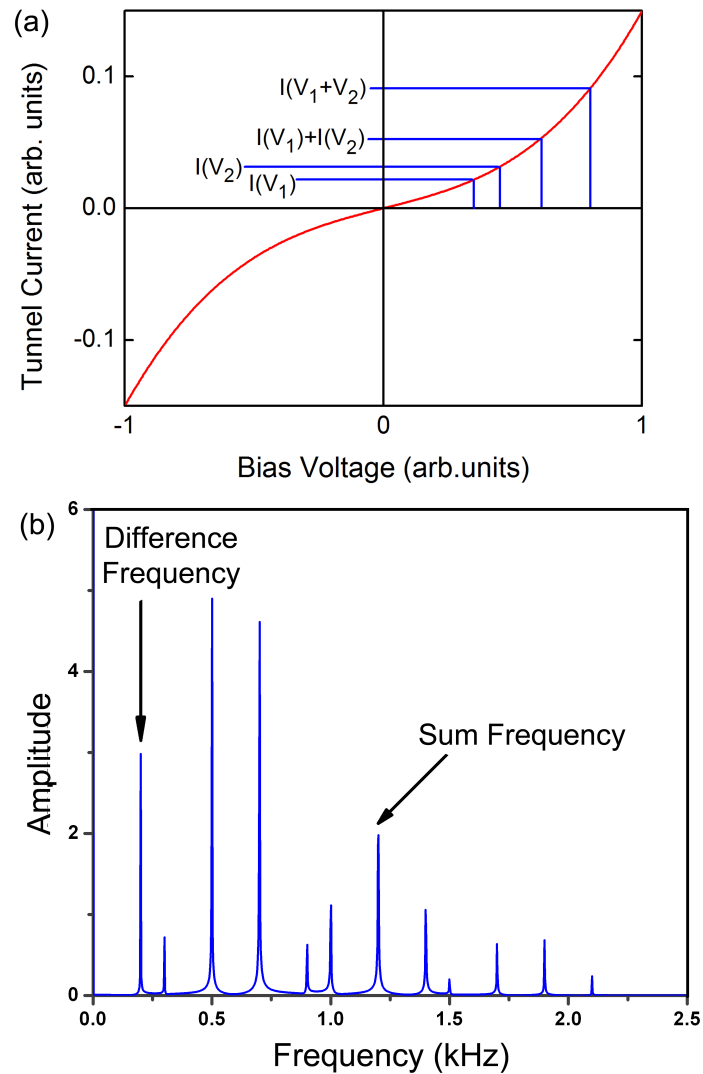


Figure 5.4: The I-V properties of a metal-insulator-metal tunnel junction are non-linear. The sum of two currents induced by two separate voltages in a tunnel junction is less than the current caused by the sum of the voltages (a). The nonlinear terms in the current expression permit the mixing of signals input in the bias voltage or sample density of states, resulting in a spectrum of mixed peaks including the sum and difference frequencies (b). The sum frequency represents the excess tunnel current contributed by the overlap of the input signals.

bias. Alternatively, if the signals are undesirable in the measured topography⁴, the signal frequencies can be increased to exceed the feedback bandwidth.

An advantage of the original JM-STM approach, besides the possibility of improved signal-to-noise, is the flexibility of the of the technique for different methods of pulse application. The technique is designed to work well with opto-electronic photoswitches that directly apply voltage pulses to the tunnel junction using a Ti:Saph laser with an optical delay line as a the pump-probe apparatus (Fig. 5.5). Chopping of the signals is accomplished by optical chopping wheels that mechanically block the signal periodically. The technique works well adapted to an all electronic apparatus (224).

5.6.1 TR-SPSTM

Other stimuli besides voltage pulses will also easily mix as long as there is an influence on the density of states. Equation 5.4 make the possibility of generating product terms with mixed stimuli clear, as long as those stimuli affect the density of states. With the actual mixing performed on the chopping signals, the form of the stimuli are unimportant. Quite simply, the interaction of the probe with the sample response caused by the pump will have a certain magnitude dependent on delay. By virtue of the product terms generated in the tunneling current expression, the chopped signals will still generate mixing terms as long as the interaction is non-zero.

Consulting equation 5.5, and considering the connection of the conduction electron polarization to the magnetization of the sample, it is clear that pumps that excite magnetodynamics will provide a modulation in the density of states that can mix with a voltage pulse probe.

5.7 Instrumental Design

In order to construct a TR-SPSTM capable of observing vortex dynamics in a fabricated disk a great deal of infrastructure was developed. Starting with a commercial UHV STM, two modifications were necessary: the introduction of a pump-probe scheme to the microscope (either optical or electronic) and the development of compatible spin-polarized tips. Additionally a method of sample preparation that yielded clean magnetic elements on a smooth transmission line was required. Complicating this aspect of the project is the incompatibility of the usual methods of STM sample preparation with nano-scale fabricated elements that may diffuse or undergo undesirable structural transitions under high heat.

⁴This is extremely unlikely. The scan rate is likely to be set so that one pixel in a scanned image is equal to $>$ one lock-in time constant ($\sim > 30$ ms at a minimum). Therefore, even for a few 100 Hz signals, multiple cycles of each pump and probe chopping signal would be averaged into a single pixel.

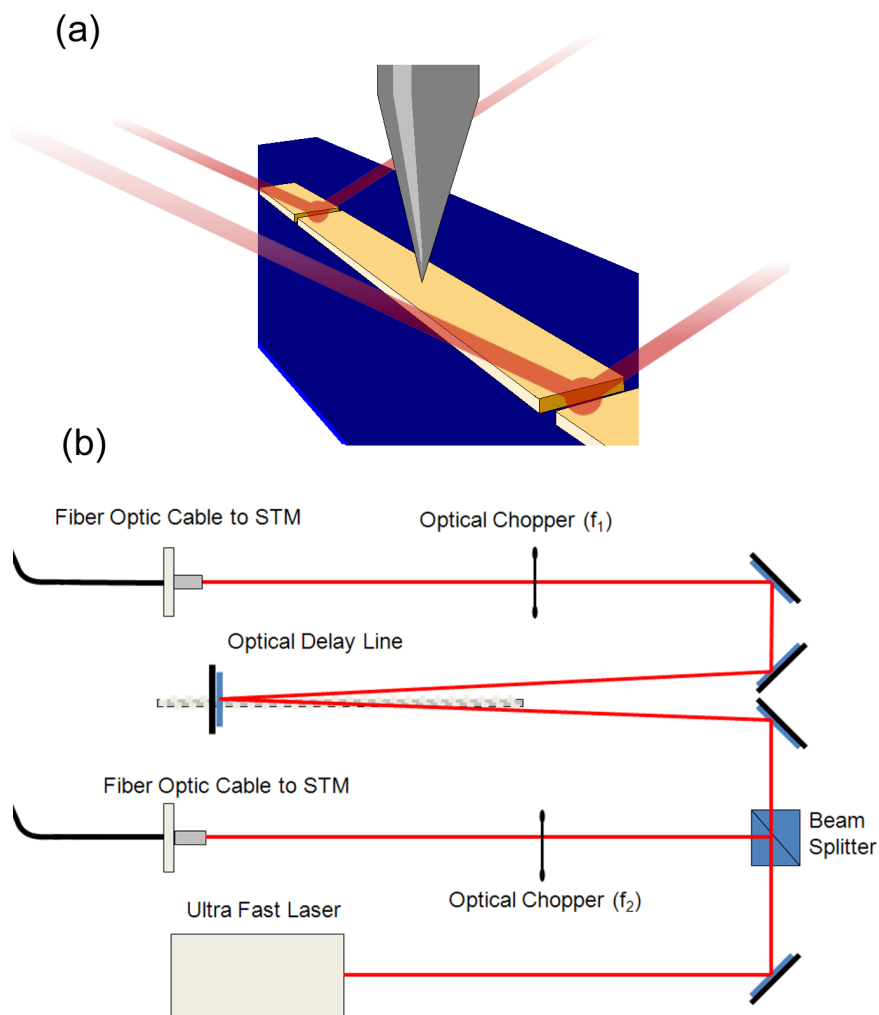


Figure 5.5: The original JM-STM instruments were operated with an optical pump-probe scheme. A Ti:Saph laser generates a train of short optical pulses. The train is split, with a portion of the power being diverted to an alternative path incorporating a delay line with a mobile mirror. Each path passes the beam through an optical chopper, chopping the fast pulse train into a slow square wave signal. Either two choppers with different frequencies may be used, or a single chopper with a chopping wheel that permits chopping at two frequencies by radial symmetry. The two paths are then directed off of the table, to the STM to induce the pump and probe stimuli. Typically the optical pulses are incident on photoconductive switches that then generate voltage pulses applied to the junction by use of a transmission line sample (a). The STM used in this work was also originally intended to use an optical scheme modeled after the original work (b).

Though prosaic in nature, these practical challenges must be surmounted entirely for a successful instrument. Therefore the solutions devised, as well as the failures, are presented in the following sections.

5.7.1 Planned Design

In order to observe the dynamics of a vortex, there must be a pump and a probe applied. The classic transmission line sample lends itself to the excitation of vortex gyration with an in-plane current pulse. This design is commonly used to investigate microwave range ferromagnetic resonance.

The basic sample design involves a smooth transmission line with permalloy disks fabricated onto it. Down this transmission line, current (and consequently voltage) pulses may be sent. A large current pulse applied to the transmission line can introduce a field pulse to excite the gyrotropic mode, while a subsequent, smaller pulse can provide a voltage boost to mix with the modulation of the sample density of states excited in the sample. Ideally, the magnetic stimulus could be applied separately, to eliminate the boost to the tunnel current caused by the pump pulse itself. However, this is a challenging enhancement to the experiment. It is difficult to bring a transmission close enough to the junction to apply a few 100 A/m field without having it actually be the sample substrate. Efforts directed towards making optical triggers with off line stimuli were considered, however they were ruled out as it is again, difficult to fit something like a hard drive write head near by an STM tip. Ultimately the project gravitated towards the simplest possible sample design (Fig. 5.6).

5.7.2 The Createc STM

The instrument constructed for this work was based on a commercial Createc Low Temperature STM. The instrument is designed for stability and for minimizing the boil-off of liquid helium when operated at its base temperature. This makes the instrument excellent for investigation of well prepared samples on the atomic scale at low temperature, but provides a number of hurdles that must be overcome to apply the instrument more generally.

The microscope is a Besöcke-Beetle design (250, 251) and consists of a scan head suspended from a cryogenic reservoir by springs (Figs. 5.1 and 5.7 a). In a Besöcke-Beetle design, the scan piezo is mounted on a physically mobile slab. The slab has three identical radial ramps machined into it, and rests on top of three coarse piezos. The outer coarse piezos can use stick-slip motion to push the slab around in X and Y, and, by rotation, in Z. In pursuit of the ultimate stability, the microscope uses a ring of magnets mounted below the scan head to damp the motion of the head via eddy current damping. The magnets are arranged in

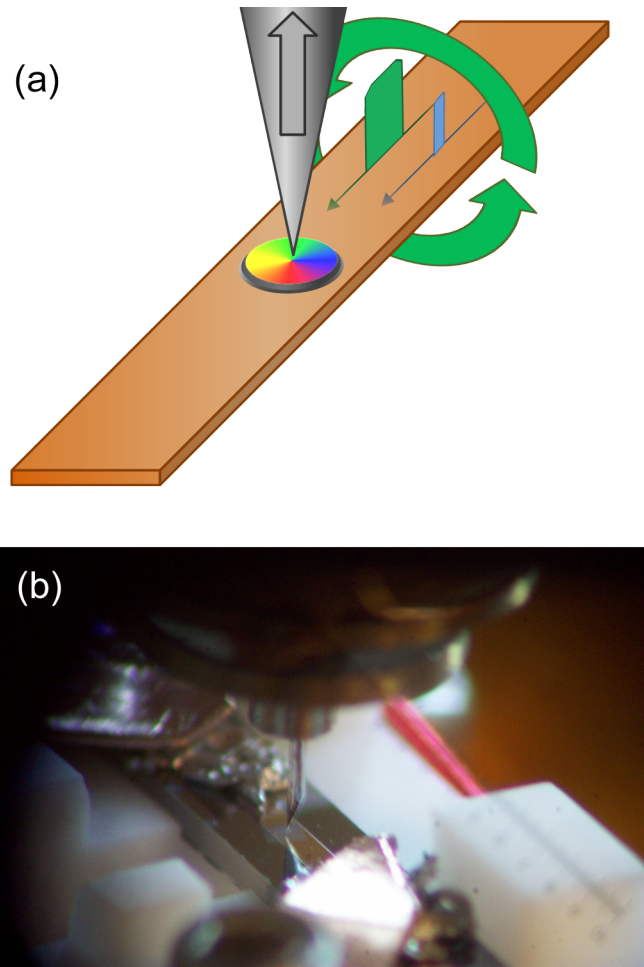


Figure 5.6: In the time-resolved SP-STMs design, a voltage pulse probe is used to detect dynamics excited in a disk sample via a large current pulse. The disks are fabricated on a transmission line that provides both electrical bias, and magnetic field for the sample (a). A large pulse (green) excites dynamics in the disk, while a smaller pulse (blue) follows and provides a bias spike to increase the number of states participating in tunneling. A spin polarized tip is used to observe the magnetic changes. Looking at a sample (sample no. 2), the transmission line, and tip are visible (b). An array of permalloy disks can be seen as a faint square aligned diagonally to the transmission line, underneath the tip.

a flux closed configuration, minimizing stray field at the sample. However, these magnets should be removed in order to safely apply a bias field, that may have a gradient, to the head⁵.

The base temperature of the microscope is 5 K. In order to achieve this, while still having the STM suspended by very soft springs and wires from a cryogen tank, great care must be taken in shielding the head from heat leaks. In the original instrument, all wiring was run down the side of the cryogen tank, to ensure it was at liquid helium temperature. Additionally, the microscope is encased in radiation shields connected to the tank. This prevents radiative heating from the warm surrounding environment. In standard operation, the tank is filled with liquid helium. With efficiency in mind, the instrument takes further steps to reduce the usage of helium. A second cryogenic tank surrounds, but is physically isolated from the inner tank. The outer tank is filled with liquid nitrogen. Additionally, there is a second set of shields suspended from the LN2 tank, providing radiative shielding for the inner shields (Fig. 5.7). These precautions allow the microscope to remain cold with as little as 60 L of liquid helium per month. For reference, some other cryogenic microscopes consume 100 L per day to reach temperatures of 25 K⁶. The shields are profoundly inconvenient. Optical access to the microscope head is sufficiently limited that two experienced operators might still discover they have no clue what is happening inside the microscope while installing a sample. The lack of optical access also makes directing lasers into the scan head very challenging. Despite these challenges, modifications to convert the instrument to a TR-SPSTM met with some degree of success.

5.8 Pump Probe Scheme

5.8.1 Optical Pump Probe Scheme

Initial plans for the microscope entailed the development of an opto-electronic pump-probe scheme as had been used in previous JM-STMs. This required the design of large current capable photo-switches, the construction of an optical pump-probe set-up adjacent to the STM, and coupling the laser pulses into the STM. Extensive work was performed pursuing this approach, however development was stopped when publications indicated that all-electronic approaches (229) were eminently capable of achieving the time resolution necessary for initial investigations of vortex dynamics. The infrastructure remains however, so

⁵Given the cost of the scan head, this was deemed too risky for initial investigations. If the instrument works with no bias field, it is possible the head will be modified.

⁶Make no mistake reader, this is no endorsement of this microscope. This machine is truly hungry for the hopes and dreams of graduate students, or any other optimist it encounters.

in principle conversion to an opto-electronic microscope or hybrid microscope would be possible. A summary of work done developing opto-electronic switches is available in Appendix I.

5.8.2 Electronic Pump Probe Scheme

The original reasoning for rejection of the electronic approach was the invasive rewiring required for the microscope. Fear of error was overcome in light of publications from other groups, motivating a rapid change in direction for the project. Principally, the issue with all STMs is the fact that wiring tends to be low bandwidth. Typically there is a trade off with electronic bandwidth and wire flexibility. For non time-resolved instruments, having flexible easy to work with wiring is much more important. In this case, bias wiring in the original microscope consisted of unshielded kapton coated wire, while the tunnel current wire was shielded twisted pair, with one of the twisted pairs soldered to the STM chassis. This wiring arrangement was wholly inadequate for high-speed measurements.

Wiring was largely a logistical challenge, and most details are skipped here. Very flexible coaxial wiring with a solid copper core, a kapton dielectric and a silver coated stainless steel braid for a shield was chosen from available wiring. Since no model information was marked on the storage spool, reflectometry was used to verify that the wire had 50Ω impedance and had good transmission properties, including low loss and low dispersion.

Equally important to the wiring is the use of matched connectors terminating the wiring. For all new wiring, double ended UHV compatible SMA feedthroughs (MDC/ISI 9252001) were added with UHV compatible connectors (Accu-Glass SMA 111027) inside the chamber. With the possibility of applying pulses using the tunnel current wire in mind, the length of the wires was minimized. This decreases the time constant of the resonant cavity formed by the high impedance tunnel junction and pre-amplifier, increasing bandwidth for tip pulses. The trade off for the short wires, is a corresponding reduction in the thermal heat sinking of the wires to the cryogen tanks resulting in a heat leak to the STM head.

The tunnel current wire is the most important wire. Effort was made to ensure no impedance mis-matches existed in the wire up to the tip. This included the transition to a short length of semi-rigid 50Ω coaxial wire to act as a feedthrough through the Besöcke-Beetle ramp. This allowed use of 50Ω matched shielded coaxial wire up to within a \sim mm of the tip.

The bias wires are less important, but still critical and, for the intended operation of this microscope, require higher bandwidth than the tip wire. The two coaxial cables are connected to the sample holder, using up four of the six sample contacts. Independent contacts are made for the centre and shield of each wire. This permits samples to be connected as a continuous section of the transmission line in either microstripline or coplanar geometry,

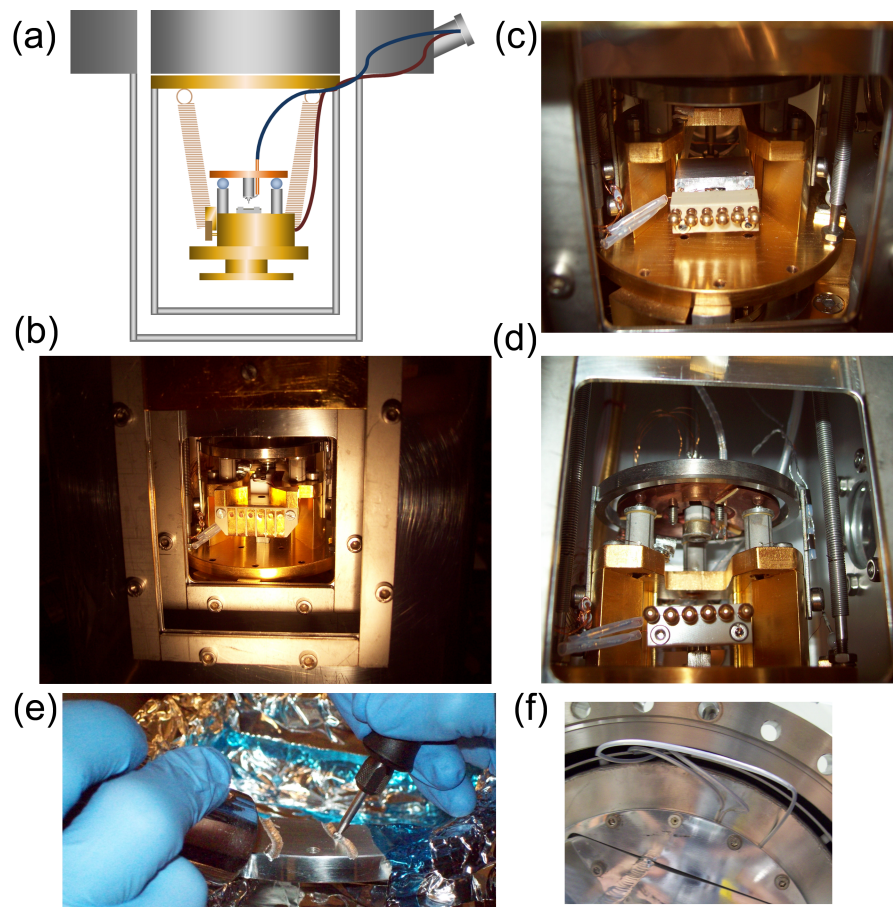


Figure 5.7: Extensive modifications added high speed bias and tunnel current wiring to the STM to enable electronic pump-probe experiments. A cartoon side view of the STM head suspended by springs from the cryogen tanks is shown (a). The added tunnel current wire is shown in blue, while the added bias wires are shown in red. The wires were added on high speed feed throughs on spare flanges close to the tunnel junction. Panels b to d show pictures of the modified scan head through the shield doors (from the left in the cartoon). The sample is installed through the doors (b) and sits on a block equipped with pogo pins (c). Close inspection shows the added bias wires passing through the stainless steel block that secures the sample holder (c), and the tunnel current wires passing through the Besöcke ramp (d). In order to minimize any additional heat leaks, troughs were machined in the cryogenic shields around the sample area in which the wires were embedded, (e) and (f).

minimizing the opportunity for creating a ringing or large reflections. Small, unavoidable reflections occur at the sample contacts (pogo pins).

5.8.3 RF Switched JM-STM

In the spirit of rapidly assembling the all-electronic version of the microscope, rather than reconstructing an electronic JM-STM as seen in recent work (224), here electronic chopping is used. This alternative approach was developed using immediately available electronic components. The method, named RF Switched JM-STM, employs a chopped delay in order to generate a signal representing only the time-resolved information at a frequency detectable by the pre-amplifier.

As in JM-STM, two trains of pulses are generated. One pulse is applied directly to the sample, and acts as a pump. The second pulse, acting as a probe, is passed through a circuit that uses a toggled RF switch to alternate between two different pathways of different electrical length. The RF switch is toggled with a low frequency square wave, which also serves as the reference signal for a lock-in amplifier reading the tunnel current. The signal detected by the lock-in amplifier represents the difference in average tunneling current for the two possible probe delays. This is directly proportional to the nonlinear enhancement of the tunnel current summing the probe with the local temporal dynamics for each delay. Given a dynamical response to the probe that decays in an orderly fashion back to equilibrium with in time Δt_d , a clear mapping of the response is possible by scanning the probe delay steadily. To do so the time difference between the two probe positions must be set $> \Delta t_d$, and the repetition period set to $> 2\Delta t_d$.

A more advanced version of this technique can be envisioned substituting a digital delay generator for the fixed delay between the two probe paths. Shifting only one probe time makes analysis less complex, and also permits repetition period to be reduced to $> \Delta t_d$. This would yield a $\sim 2\times$ boost in the measured signal.

In this case pulses are generated by a two output pulse generator (HP8131A) with variable delay between the outputs. The the pump pulse is fed directly to the STM sample, while the probe pulse is sent to a RF switch (MiniCircuits 15542) toggled at f_{chop} using a signal generator (Wavetek Model 184). The RF switch has one output passing down a 10 – 100 ns equivalent BNC cable delay line, while the other output passes through a variable attenuator (HP 8494B). The three pulse lines, pump and two probes, are recombined using passive combiners, and then passed through a bias tee (HP 11612A), used to apply an additional DC bias to the STM sample. The combined signal is applied to one side of the STM sample, and passed out to the other bias contact which is terminated in 50Ω to ground. A DC block (Minicircuits DC-89+) is also used to prevent the DC bias from generating

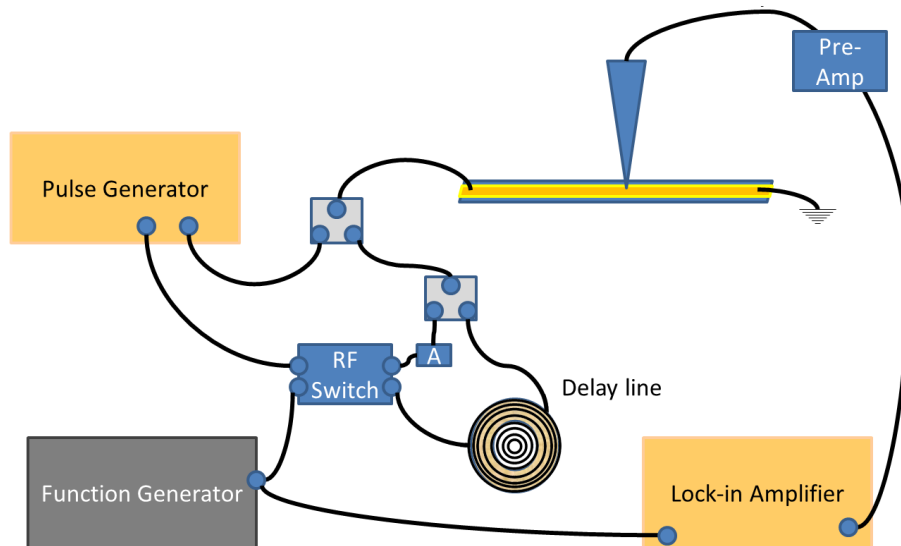


Figure 5.8: In RF switched JM-STM, time-resolved information is extracted by chopping the delay between the pump and probe pulses. The probe pulses are passed to an RF switch that toggles between a short path and a long path. An attenuator (A) is used to balance the pulse height on the short path. The probe pulse paths are recombined with a passive combiner, and that signal is then combined with the probe pulses before being applied to the tunnel junction. A lock-in amplified detects a signal at the chopping frequency.

a current across the transmission line. The tunnel current is fed from the pre-amplifier (either Femto DLPCA-200, or Ithaco 1211) to the STM feedback loop, as well as a lock-in amplifier (SRS SR830) that is referenced to f_{chop} .

5.9 Sample Preparation

In addition to the physical modifications to the STM, significant UHV infrastructure was developed to enable the fabrication of patterned magnetic elements *in situ* in order to ensure an STM quality surface. The sample additionally determines the method of stimulating magnetic dynamics. In this case, the simplest option is to place magnetic disks on an impedance matched transmission line that is able to apply both the pump and probe pulse. The pump pulse is quite large, and is intended to apply a magnetic field pulse to the disks, exciting the disk gyrotropic mode. The first necessary component is a suitable transmission line sample.

5.9.1 Transmission Line Sample

Previous attempts at junction mixing suffered from the use of rough films composing the transmission lines (221), making scanning quite challenging. In order to rectify this, a material was required that could produce exceptionally smooth, patterned films, as well as to withstand reasonable levels of heat treatment. To do so, metallic glass films developed in the Chemical Materials Engineering Department at the University of Alberta were employed (252).

The transmission lines were made out of a binary glass material $\text{Cu}_x\text{Hf}_{(1-x)}$ previously demonstrated to produce extremely smooth films (252) and to be easily patternable by standard lift off, or wet etch lithography. Additionally, under an oxygen free environment, the films were found to be stable up to 400°C under investigation by SEM. Thus initial work suggested the $\text{Cu}_x\text{Hf}_{(1-x)}$ would be an ideal sample substrate for the transmission lines.

Investigation of the $\text{Cu}_x\text{Hf}_{(1-x)}$ films under STM, however revealed that the films exhibit fundamental dynamics on a nanoscopic scale. Extensive work investigating these dynamics using STM was performed and is included here in Chapter 6. In summary, the films are composed of cluster like objects that hop stochastically at the surface for temperatures at least as low as 100 K. These dynamics are not desirable on the transmission line substrate. Hopping clusters present an opportunity to cause regular tip crashes, as well as to contaminate the tip itself. Therefore, the final samples used as TR-STM samples employed an additional capping layer of Au. Gold wets well to $\text{Cu}_x\text{Hf}_{(1-x)}$ films, preserving the smoothness, but inhibiting cluster dynamics. No dynamics were observed on films with such a capping layer.

The transmission lines used in experiments were made with $\text{Cu}_{80}\text{Hf}_{20}$ with thicknesses of either 100 nm or 300 nm as well as a 10 nm Au capping layer. The transmission lines were deposited on a $500\ \mu\text{m}$ thick silicon wafer, with an oxide layer ($\sim 30\ \text{nm}$). The transmission lines were made with widths varying from $250\ \mu\text{m}$ to 1 mm. Nominally, for the microstrip geometry⁷ on a $500\ \mu\text{m}$ thick Si wafer, a line width of $500\ \mu\text{m}$ yields approximately $50\ \Omega$ impedance. Narrower lines provide a higher magnetic field for a given current pulse, while thicker lines make it easier to land the STM tip on the transmission line without crashing. In practice good results were obtained with $450\ \mu\text{m}$ wide transmission lines.

The transmission lines were diced into 2 mm wide chips and were mounted on a custom macor block with a strip of copper coated kapton film (Pyrulux AP7164E) to serve as a ground plane. The sample block was attached to a holder equipped with semi-rigid coaxial cable. The shield of the semi rigid coaxial cable was soldered to the ground plane strip, while the centre was soldered to BeCu clips that make press contacts with the transmission line. To improve electrical contact, indium was placed underneath the clips. In this geometry, the transmission line acts as a continuous section of a $50\ \Omega$ cable connected as a microstrip line. In mounting a transmission line it is highly advisable to inspect the transmission properties, and the reflections prior to proceeding to any further steps. The clip contacts can cause significant reflections which may be removed with careful adjustments. Additionally, if the ground plane behind the microstrip is neglected, a cavity mode develops across the transmission line, resulting in a ringing effect which makes identification or dynamics more challenging (or identification of fake dynamics more likely).

5.9.2 Patterned Sample Fabrication *in situ*: Shadow Masking

Once a smooth transmission line has been developed, the next step is to prepare patterned magnetic elements with a UHV clean surface to allow good scan conditions. This is particularly important for spin polarized spectroscopy of density of states where contamination on a sample surface can annihilate any observable spin contrast. It is important to note that the usual heat treatments for STM samples involve extreme ($\sim 1000\ \text{K}$) heating which is likely to cause diffusion of any pre patterned micro-elements. Therefore, although the transmission line may be heated to some extent⁸, heating should be pursued prior to deposition.

To accomplish this, while still creating technologically pertinent fabricated structures, shadow masking was employed. As discussed in previous chapters, shadow masking is an excellent method for the production of clean structures. Here there is the additional advantage of having a patterning ‘layer’ that may be mechanically removed after deposition *in situ*.

⁷A transmission line on a substrate with a ground plane on the other side of the substrate.

⁸The limit on heating is set by the use of In contacts. Indium is UHV suitable, and has a low vapour pressure, but it melts at 156°C (253). Additionally the transmission line substrate itself does not require extreme heating, as it is not intended to be the scan surface from which spectroscopic data is collected.

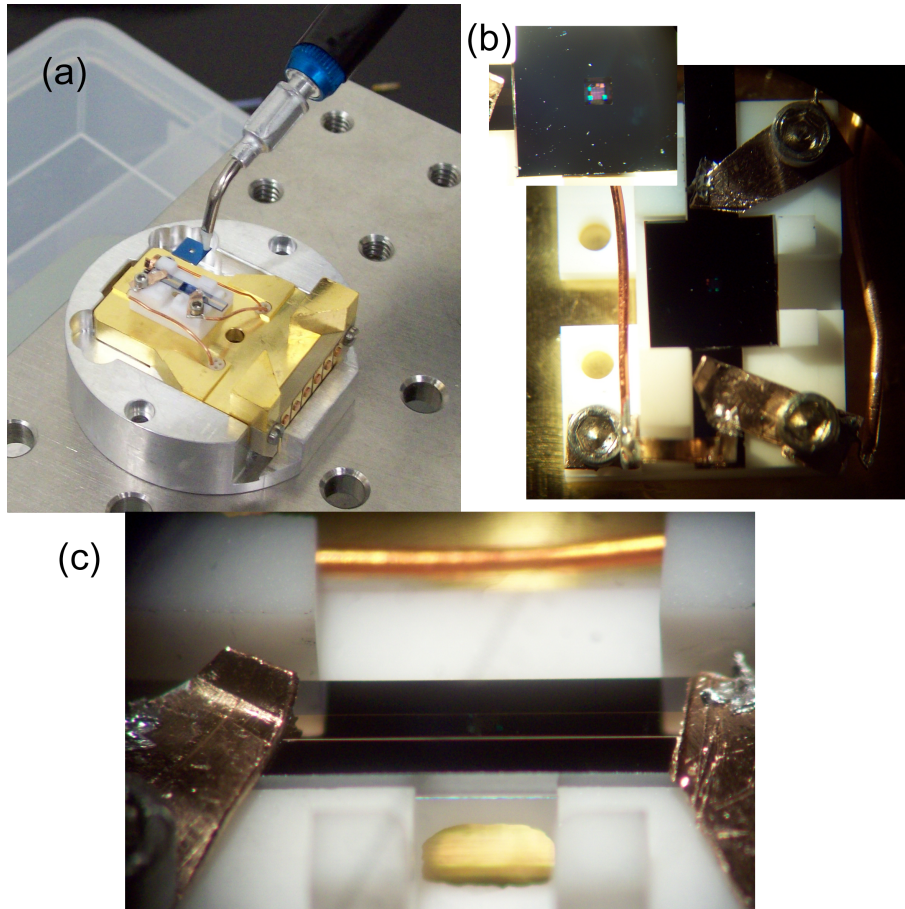


Figure 5.9: Disks are deposited onto the transmission line using a shadow mask placed directly onto the sample. A specialized holder, equipped with semi-rigid microwave compatible coaxial wires (a), and a sample block that accepts 5 mm square masks was constructed (b). Masks with patterned holes in membrane windows provide patterned samples (b). After removal of the mask *in situ*, the deposited pattern can be seen by looking for its diffraction pattern (c).

Initial designs called for the use of a custom silicon nitride membrane patterned with electron beam lithography (EBL) as the mask. Such windows were developed and produced, but the process never provided 100% yield and the resulting windows were exceptionally fragile. Subsequent trials used masks produced by focused ion beam (FIB) fabrication. The FIB method proved to be a time intensive process, however it yielded a useful mask almost 100% of the time with one complete TR-STM sample being produced and measured. During the project, it was found through a collaboration that the FIB process could have a significant effect on the magnetic properties of permalloy structures produced by shadow mask (254). Therefore final samples were produced using commercially available holey carbon film TEM grids (EMS CF-1/1-2C). Appendix C describes the process developed for producing EBL and FIB patterned windows.

5.9.3 Patterned Sample Fabrication *in situ*: UHV Deposition

Developing the deposition procedure was largely an exercise in simplification. Initial efforts using extremely valuable custom masks employed mask holding devices designed to be installed and removed *in situ*.

The masking approach devolved into simply placing the mask on the sample, and adding a collimator to the evaporator to reduce the deposition area to a ~ 2 mm diameter spot. This worked very well for SiN based masks with 5 mm square frames as the high speed holder is designed specifically to accommodate this form factor. For smaller TEM grid masks, turbo resonances in the load lock as well as jolts during transfer cause undesirable shifts. An *ad hoc* solution using added indium pillars as a loose corral was implemented to resolve this.

Similarly, the expected preparation of the sample was modified to suit what was practically possible. Prior to the deposition, transmission line substrates were stored in dry air, or nitrogen atmospheres. Subsequently, the samples were subjected to extended (> 48 hours) low heat $\sim 110^\circ\text{C}$ baking in the deposition chamber load lock using a UV bulb as a heat source.

Removal of the mask was originally intended to proceed via removal of a mask holding apparatus. This was found to be difficult, stressful, and to damage the sample surface. Therefore, with the change to having a simple bare mask resting on the holder, removal was also simplified. The holder has support pillars that corral the mask, tilting the sample holder such that the sample is butted up against such a pillar allows the mask to be dumped off while preventing it from sliding over the sample surface⁹. For TEM grids, the In pillars

⁹The sample holder worked as designed. Even more success, however, was had using a graduate student head as a blunt object to impact the transfer arm holding the sample. This caused the mask to be violently ejected vertically from the sample, resulting in remarkably few scratches. Despite the success, and ubiquitous availability of graduate student heads, this method is not recommended.

were slightly too effective for this. Therefore a needle like BeCu de-masker was made and used to flick the mask off of the sample.

5.9.4 Patterned Sample Fabrication *in situ*: Sample Transfer

The effort of sample preparation described above is pointless if the sample is then exposed to anything less than UHV conditions on its journey to the STM. Therefore a highly advanced, gigantic UHV vacuum suitcase was developed. The suitcase is extremely over engineered and is designed to interface with multiple chambers in addition to the STM. In practice, the suitcase traveled approximately 2-3 meters on each transfer, but did so admirably.

The key concept of this suitcase design was the use of a dual chamber system with all metal seals to preserve true UHV performance at all stages. The inner (sample) chamber provides a safe environment for the sample to be transferred in and is equipped with transfer arm for the sample, an ion pump, and a titanium sublimation pump (TSP)¹⁰. Separated by a UHV gate valve, the outer (buffer) chamber has a socket manipulator that enables sample exchange between the deposition and inner chamber, a turbo pump that can be valved off with a UHV gate valve, and a high power UV bulb for baking. The buffer chamber has an additional gate valve with a flexible bellows to connect to other chambers.

This design enables the suitcase to be plugged in to a dep chamber, baked (in its entirety), accept a sample, break vacuum on the outer chamber only, shift to a new chamber, perform a full bake of the outer chamber restoring UHV conditions, and subsequently transfer the sample to the new chamber.

In its final form, the suitcase used a 70 L/s turbo pump (Varian V-81-M), a 75 L/s ion pump (Varian Starcell 75L/s) and water cooling for the inner/sample chamber to mitigate extraneous heating during buffer baking. The base pressure for the suitcase was 4.5×10^{-11} mbar when cool, and an estimated 2×10^{-10} mbar (inside the sample chamber) while the buffer chamber was baking. More details, including a specific step by step instruction list for using the suitcase can be found in Appendix H.

5.9.5 Summary of Samples Made

The previous sections present a brief overview of STM sample production as a general concept. More detail is available in the appendices, however it is important to specifically state what samples were produced and how. Four samples in total were produced and observed.

¹⁰The TSP should never be fired while the sample is in the sample chamber.

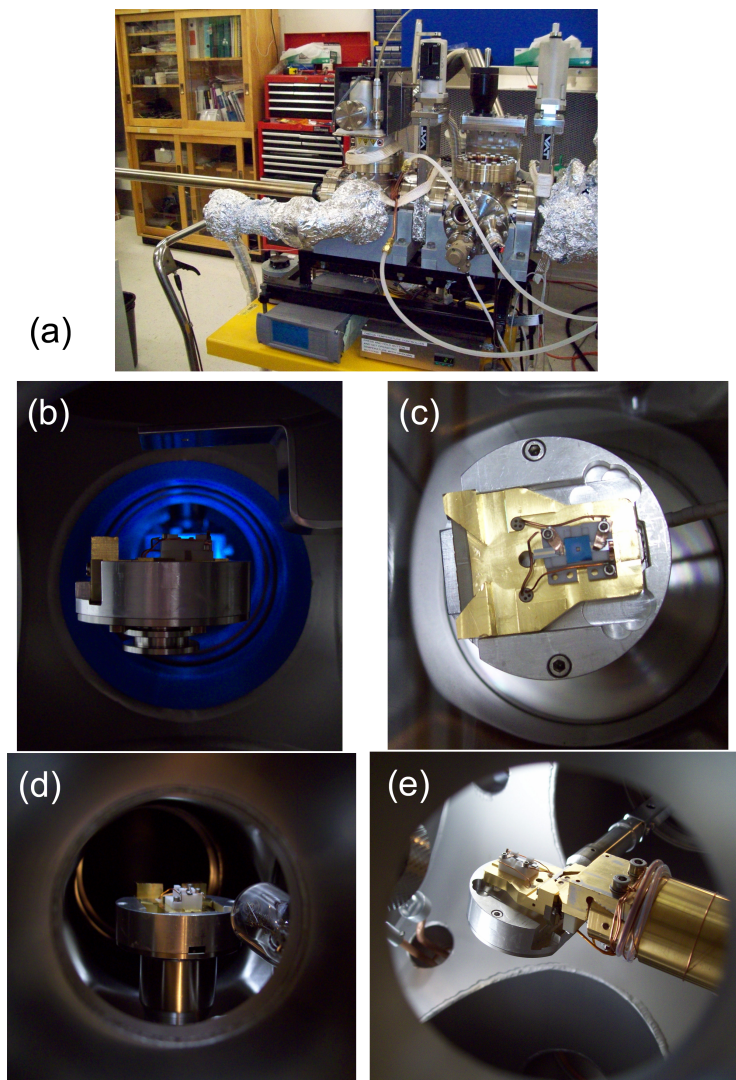


Figure 5.10: Samples are transferred from the deposition chamber to the STM using a custom built UHV suitcase. The suitcase is quite large (almost 1.8 m long), consisting of an outer chamber, and inner chamber and a long transfer arm capable of reaching the middle of the STM chamber. In home position it is plugged into the deposition chamber. Tinfoil is used as a heat shield during bake-out. The sample holder is held on a custom bed mounted on a platen transfer system on which it can be manipulated in the deposition chamber and suitcase. A physical block with a 2 mm hole is used to protect the sample holder from stray permalloy during deposition (b). The sample is transferred into the suitcase following deposition, (c) and (d). The suitcase is then disconnected from the deposition chamber, and moved to the STM. There, the sample is lifted out of its bed by the STM sample manipulator (e).

The first sample was a proof-of-concept sample for the shadow masking and transfer system. A standard sample holder was used with no high speed contacts. The sample was deposited onto a hydrogen passivated silicon wafer using a commercially available silicon nitride membrane with $2\ \mu\text{m}$ diameter holes on a $4\ \mu\text{m}$ pitch (Dura SiN DTM-25233). The sample holder was equipped with a small electro-magnet that could be used to apply few kHz AC fields, possibly enabling quasistatic measurements, or modulated field based SPSTM.

The second sample was a proof of concept sample for the operation of the TR-STM. This sample was used in air with a spare STM head to test high speed wiring configurations. A plain copper hafnium transmission line $300\ \text{nm}$ thick, and $750\ \mu\text{m}$ wide was used as the substrate. The same type of window with $2\ \mu\text{m}$ diameter holes was used for the deposition, with a target thickness of $20\ \text{nm}$ for the permalloy. For this sample, the custom high speed sample holder was used. This sample also served as a test bed of the suitability of magnetic field stimulation using the rather wide transmission lines. Fields on the order of $400\ \text{kA/m}$ were applied to do AC-MOKE measurements on the sample, enabling measurements of the magnetic hysteresis of the sample. These large thin disks exhibited a vortex like loop, however it is clear that not all disks were in the vortex state. No spin contrast was observed, and the in air stability limited any tests to noisy proof of concept tests for time resolution, however the sample did demonstrate the possibility of resolving and scanning permalloy separately on copper hafnium (Fig. 5.11).

The third sample constituted the first production sample on which time-resolved measurements were made in vacuum with the hope of observing spin dynamics. This sample was deposited using a custom FIB modified silicon nitride membrane (Norcada) to deposit a nominal $20\ \text{nm}$ permalloy onto a $300\ \text{nm}$ thick, and $500\ \mu\text{m}$ wide copper hafnium transmission line. At the time of the deposition, the evaporator was consistently delivering much thinner films than expected, and so the actual thickness was closer to $5\ \text{nm}$. This sample did not have the shield of the bias wires connected to a ground plane beneath the sample. Data from this sample tends to exhibit ringing as a result.

The final sample was produced in an attempt to resolve the issues with the previous sample. A holey carbon TEM grid featuring $1\ \mu\text{m}$ diameter holes on a $2\ \mu\text{m}$ pitch (EMS CF-1/1-2C) was used as the deposition mask, and the transmission line sample consisted of a $100\ \text{nm}$ thick $750\ \mu\text{m}$ wide transmission line. A capping layer of $10\ \text{nm}$ of Au was added. Measurements have not been performed in full on this sample at the time of this writing.

5.10 Spin Polarized Tips

The addition of a spin polarized tip to the STM is simple in concept, but non trivial in execution. Commonly, coated tips are used (255). However obtaining robust coatings is

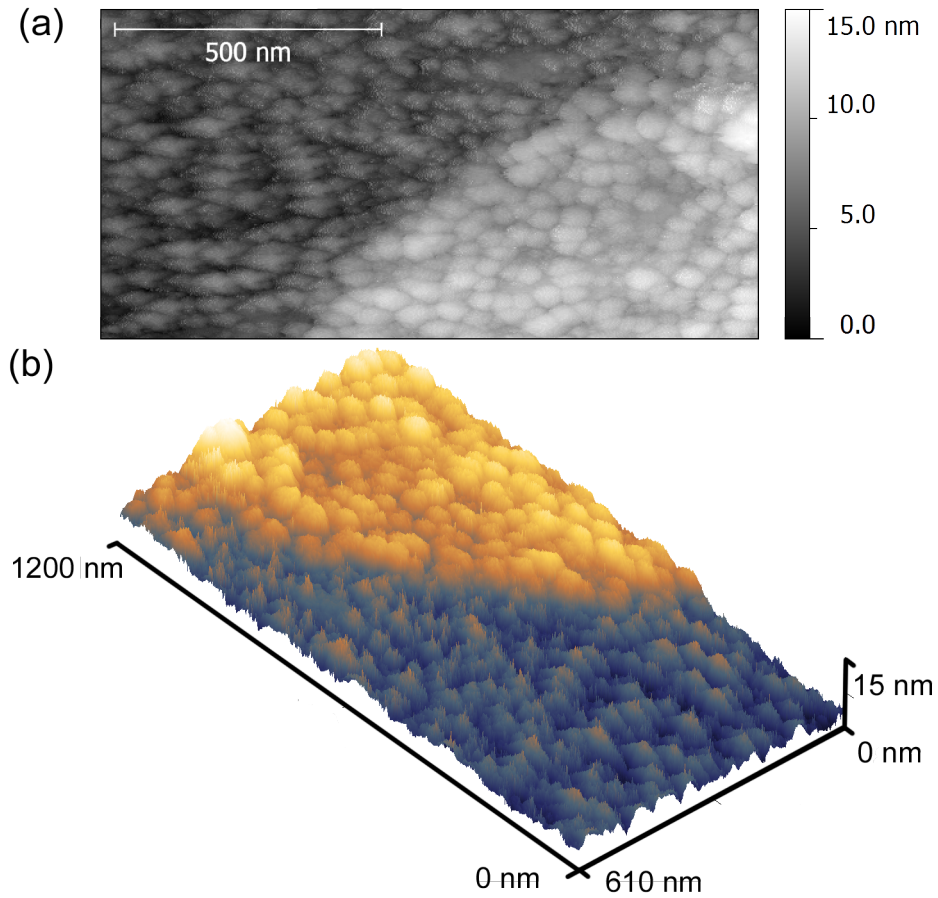


Figure 5.11: Observations of permalloy deposited on copper hafnium show distinct film structure, and a well defined edge in both 2D (a) and 3D views (b). The sample observed in air was useful in developing the RF switched technique, and in verifying the compatibility of permalloy and copper hafnium. This deposition was approximately 10 nm thick. Permalloy grains are easily visible, while the copper hafnium structure is both smaller, and less well defined. This sample was used for optical tests, resulting in slight oxidation of the copper hafnium, potentially explaining the poor appearance. This image was acquired with a 350 pA tunnel current and -48 mV bias voltage.

notoriously difficult (256). Bulk tips are usually very hard to work with, as ferromagnetic bulk tips almost always have stray field issues and antiferromagnetic materials are often very difficult to work with. Recent work has demonstrated the possibility of bulk chromium tips fabricated from custom wires (257).

Here an alternate approach to developing bulk chromium tips was used. The method is challenging and labor intensive, however it can produce high quality tips with sub 20 nm tip radius. In brief, the tips are hand machined from chromium rod to a dumbbell shaped precursor tip. Starting chromium rod is available from suppliers (either 2 mm diameter American Elements 99.9+% pure custom Cr rod or Goodfellow LS37 1513 J V1.0 mm diameter 99.7+% pure Cr rod). Following machining to the precursor, tungsten handles may optionally be spot welded to the dumbbell ends (highly recommended). This dumbbell is etched using a standard nominally 3 molar NaOH electrolytic etch on a modified Schrödinger's Sharpener (Obligato Objectives) tip etching apparatus¹¹. The tips are mounted in custom tip holders designed to accommodate large diameter tips of variable sizes. More detail can be found on the fabrication of the tips in appendix J.

Once in the STM, the tips are subjected to a standard set of tip treatments. First the tips are cleaned by electron bombardment to remove contamination (and possibly the top layer of material) from the tips. Second, the tips are treated by field emission. This follows standard recipes for the preparation of tungsten STM tips (258).

5.11 Proof-of-Principle Junction Mixing Results

Samples were successfully used in TR-STM experiments in atmosphere, and in vacuum. Time resolution of 500 ps, limited by the pulse generator employed while spatial resolution ranged between \sim nm to \sim 5 nm, limited by the quality of the tip and roughness of the sample. Contrast between the I-V properties of the underlying transmission line and the deposited elements was also observed, as was I-V contrast on the bare copper hafnium transmission line. However, no magnetic contrast has been observed. A summary of the major results is presented below.

5.11.1 Optimization of the Signal

A plethora of spurious noise sources make acquisition of time-resolved data challenging. Most notably, capacitive coupling of wires can provide alternate pathways for AC signals to leak from bias wires to the tunnel current wire. Care was required to ensure tunnel current signals are real.

¹¹The quality of this machine is perfectly matched with that of the Createc.

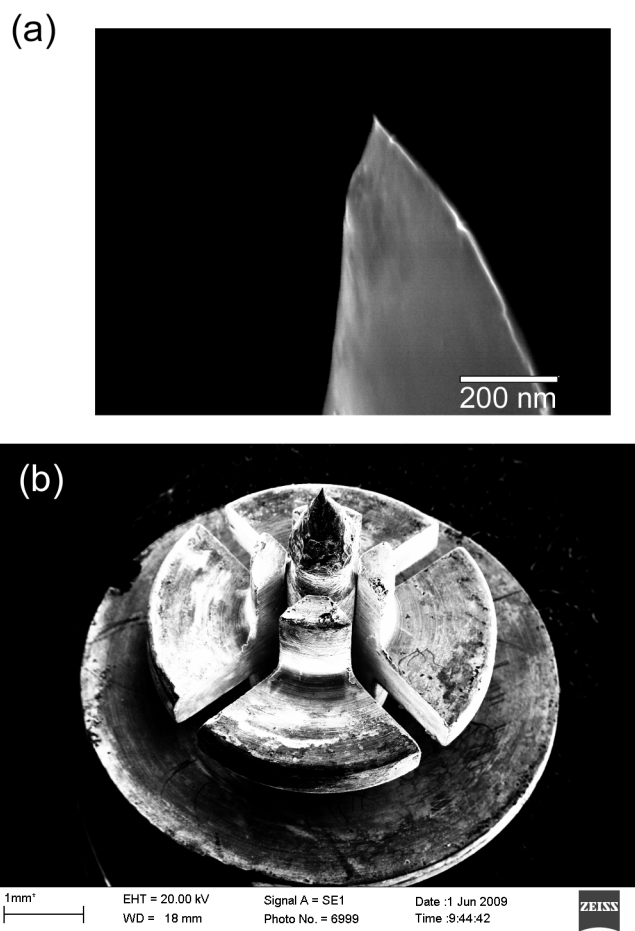


Figure 5.12: Bulk chromium tips were developed to provide a robust spin polarized tip for the STM. Hand machined tip precursors are mounted in custom designed holders that hold large tip diameters (~ 1 mm). Subsequently the precursors are electrochemically etched into tips. The tips were found to exhibit variable radii, largely due to the more rapid etching of chromium. Tips etched without errors exhibited very small tip radii, as low as ~ 10 nm.

Notably, capacitive signals can be diagnosed by comparison of the signal with the tip in range for tunneling, and out of range. If capacitive coupling cannot be eliminated, the mode of operation of the lock-in may be exploited to minimize its influence. Operating the lock-in in X-Y mode (quadrature mode rather than R- θ), pulling the tip out of range, locking in to the capacitive signal, and then shifting the lock-in phase by 90 degrees shifts the capacitive signal to the Y channel. Subsequently, after pulling into range, the signal in the X channel will represent only tunneling current signal. By contrast, locking in after pulling into range will result in a detection phase that maximizes the total signal and will only be a good representation of the tunnel current if capacitive coupling is far lower than the real signal. Non-linear elements involved in circuits connected in a capacitive, or pseudo capacitive fashion could lead to a time delay dependence in the extraneous signal. This is probably the most pathological situation imaginable, but this should always be cross checked with out of range time delay scans.

A very common, and difficult to exactly eliminate source of spurious signal is a subtle DC bias offset in the probe pulse. If any DC offset exists in the probe pulse channel, and if any difference in attenuation between the two probe pulse paths exist, then, in effect, a square wave bias voltage is applied to the junction at precisely the frequency of the RF switch chopping. This signal, however, is not delay dependent and may be eliminated by tuning the DC offset of the probe pulses at a delay and location such that no nonlinear coupling exists.

Other sources of noise are the usual STM modes. These are covered in a later section, Interpretation of TR-STM data.

5.11.2 Time Resolution

Operation of the STM in RF switched junction mixing mode at a single point will generate a time trace of the sample response. This first order experiment is valuable for a variety of reasons, including: determining time resolution, finding reflections or resonant modes on wires, or measuring point like dynamics. Spatial scans with time resolution can provide a more convincing demonstration of the measurement of dynamics, however due to the efficiency of data acquisition, the time traces are extremely useful as an initial probe.

In a simple JM-STM experiment, with no sample based dynamics, it is simply the non-linear boost to the tunnel current resulting from the summed bias voltages of the pump and probe pulses that may be measured. Effectively, this is an auto-correlation measurement of the convolved pump pulse modulated by the nonlinearity. In this work, no sample dynamics have been observed. A wide variety of pulse configurations were tested while searching for dynamics. Since the time scale of decay of the dynamics was only roughly known

($\sim 10 - 20$ ns), repetition rates between 10 and 50 MHz were used. Two example traces captured from the third sample (FIB mask based Py dots, observed in vacuum) are shown in Fig. 5.13. Limited by the bandwidth of the pulse generator (\sim rated at 500 MHz), the achievable time resolution in the microscope was approximately 700 ps measured by step rise time.

5.11.3 Spatial Contrast

Spatial contrast was achieved on bare copper hafnium, as well as between premalloy and copper hafnium. This is not surprising, and effectively repeats previous junction mixing results showing I-V contrasts of different materials (221, 222). I-V contrast arises between Py and CuHf, in a sense, from the conductivity differences of the two materials. Contrast within the CuHf itself, arises between different clusters and effects such as this have been seen on other metallic glasses (259).

Example data is shown in figure 5.14 and figure 5.15. Spatial imaging was particularly challenging to acquire. Accounting for the lock-in time constant necessitates that scans occur slowly (each pixel should require $>$ one time constant). This enhances the probability of drift or tip crashes interrupting a data set. Therefore, typically only a few scans at different delays could be acquired for any one region.

5.11.4 Interpretation of Results

Spatial time-resolved scans present some additional spurious effects that should be commented on for future work. Examining Fig. 5.14, the time-resolved signal has a remarkably sharp edge, actually sharper than the topography. This simply results from the fact that the topography represents the convolution of the sample shape and the tip profile, whereas the time-resolved signal, like any dI/dV based signal, simply reflects the I-V properties of the tunnel junction. The I-V signal is, for a uniform tip and sample, independent of what part of the tip is forming the tunnel junction and how tall the sample topography is. Hence, the absolute edges of imaged dots appear sharp in the time-resolved signal, but appear sloped and blurred in the topography.

Additionally, though the use of a lock-in technique mitigates spurious signals, stochastic jumps or spikes in the tunnel current constitute a broad band noise contribution to the tunnel current spectrum. Hence, any time there is an increase in the occurrence of spikes or jumps, the tunnel current signal measured at any given frequency will also spike. This leads to a gradient like imaging mode when scanning a rough sample too quickly, where the lock-in signal is higher along the edges of tall objects. This effect is easily picked out by

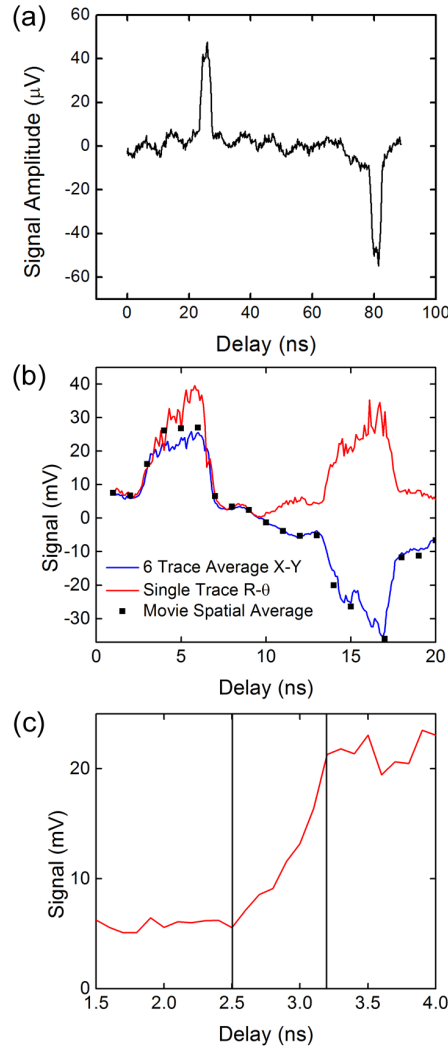


Figure 5.13: The constructed RF switched JM-STM exhibited ~ 700 ps time resolution. RF switched JM-STM measures the difference in signal at the two delays. This leads to positive or negative signal depending on the delay, and what the phase detection of the lock-in is set to. To measure dynamics, the fixed delay between the probe paths must exceed the length of the dynamical response, and the period between pumps must be at least twice the fixed delay. A long delay (a) exhibits signal with the pump and probe pulses overlap. Ringing is seen elsewhere, arising because the transmission line lacks a ground plane backing leading to a weak cavity mode. A short delay (b) shows how operating in quadrature (X-Y) or polar (R- θ) mode on the lock in affects the measured signal. This short delay pulse train was used to acquire the movie in Fig. 5.15. Averaged signal from the movie frames compares well with the time traces. Time resolution was found to be ~ 700 ps.

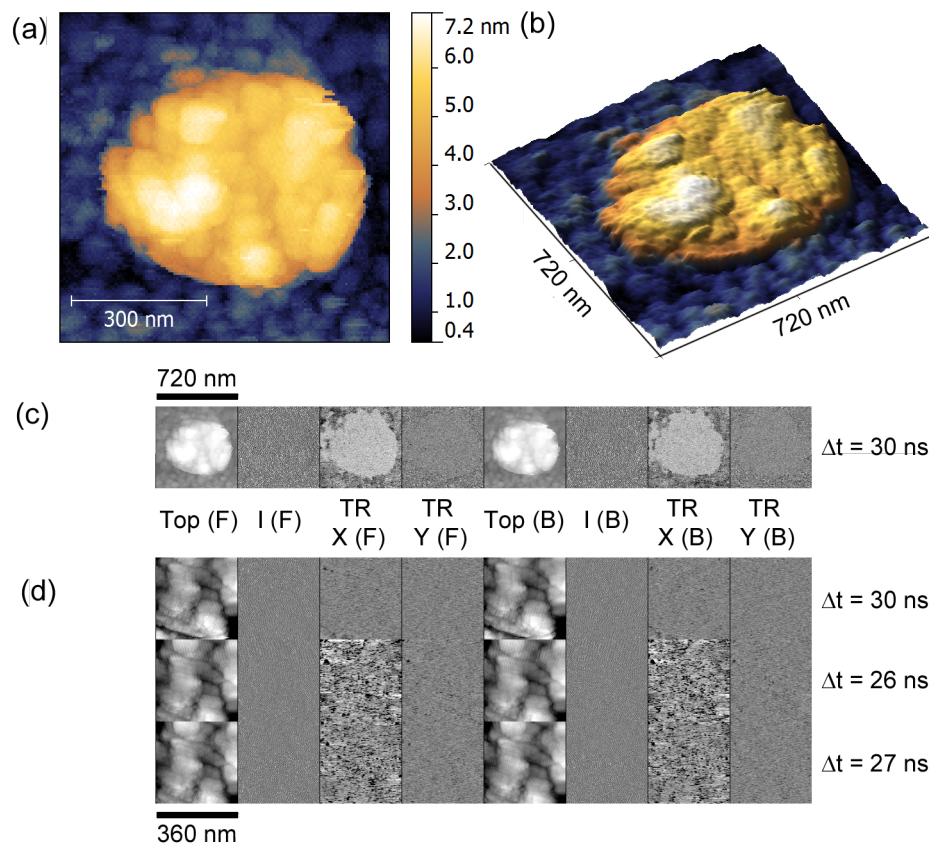


Figure 5.14: Permalloy showed delay dependent spatial contrast when compared with the transmission line. The third sample was an anomalously thin deposition (~ 5 nm). Disks showed a clear contrast, reflecting the generally lower conductivity of the permalloy (c). Attempts to make a movie while centred on a disk showed delay dependent contrast, but no identifiable magnetic dynamics. This data was acquired with a 50 pA tunnel current, a 180 mV bias voltage, a 20 ns fixed delay, a 100 nm rep rate, a 4 ns long pump, and 0.5 ns probe with voltage amplitudes applied to the transmission line of 500 mV and 250 mV respectively. The time trace in Fig. 5.13 (a) was taken under the same conditions.

comparing the forward and backwards scan images. One side of tall objects will be bright (high signal), while the other side will be dark (low signal); in the reverse scan, the sides will be switched. This can only be avoided by scanning more slowly, or by adjusting feedback loop parameters to enable faster feedback loop response.

5.12 Challenges

As discussed in the introduction, despite the progress and construction of each component necessary for this project, no magnetodynamics have been observed. A list of issues encountered is discussed in the subsequent sections. Emphasis is placed on issues not yet resolved.

5.12.1 Surface Roughness

Great effort was made to create samples representative of current research into technologically significant devices. This inherently means that the permalloy films are rough surfaces by STM standards. Under stable conditions, scanning of the permalloy was quite possible, though scanning onto and off of the disks could be quite dangerous as far as crashing goes. Much more complex fabrication methods yielding single-crystal transmission lines, or using template stripping (*260*) to produce smoother lines may reduce challenges in scanning.

More of a hindrance were the dynamics of the CuHf transmission line. At the time, fabrication of the transmission lines at a thickness of 300 nm was thought to be adequate for prevention of cluster hopping¹². However clusters were found to hop regularly, causing transient tip crashes increasing the challenge in performing measurements.

5.12.2 Spin Polarization

The principal issue with this project is the fact that spin polarization was never observed. On the third sample tested, spin contrast was expected, as successfully prepared chromium tips were used to observe UHV prepared magnetic disks. The vortex state additionally makes an ideal target, as no matter what the magnetization orientation of the tip apex, a portion of the sample will provide a parallel (or anti-parallel) section to provide contrast.

Two primary factors are conjectured to have suppressed the spin contrast. First, the measurements were performed at room temperature. By comparison the Néel temperature of

¹²As with almost all films, the feature size in metallic glasses tends to increase with film thickness.

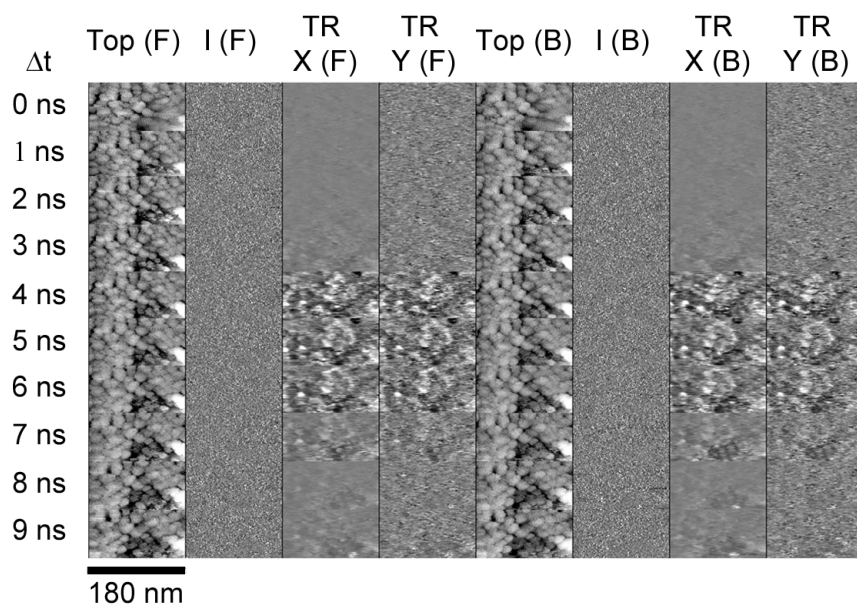


Figure 5.15: The IV contrast between surface features on copper hafnium allows the production of a spatially resolved movie. This data was acquired with a 110 pA tunnel current, a 284 mV bias voltage, a 12 ns fixed delay, a 30 ns rep rate, a 4 ns long pump, and 0.5 ns probe with voltage amplitudes of 1.75 V and 1 V respectively. The time trace in Fig. 5.13 (b) was taken under the same conditions. Spatial resolution in this movie, at this point, is limited by the tip that had been crashed multiple times.

chromium is ~ 310 K (261). Coupled with transient heating due to current spikes in time-resolved measurements, the tip may have been completely non-polarized. Another contributing factor is the use of a FIB processed mask in the sample production. This means the samples may be iron depleted, have altered film structure, and exhibit significantly suppressed magnetic properties (254).

For the final sample, the microscope has been cooled to liquid nitrogen temperatures (due to the heat leak, it is ~ 115 K). Additionally, a TEM grid with holes has been used to avoid the influence of implanted ions on the deposited permalloy. If spin polarization is still not observed in this final sample, there are a few possible remaining explanations. The tip itself may not be polarized, or contamination may interfere with the measurement of polarization. Given the precautions taken in cleaning the tip, and success in performing measurements without tip crashes, this is unlikely. More probable is an insidious combination of surface roughness and the magnetic structure of chromium.

Chromium tends to arrange into planes (100 planes) of aligned spins (262), with adjacent planes of opposite alignment. Since polarization depends only the apex atom, one can still obtain a strong spin polarized signal. However, on a rough surface, as scanning proceeds it is not guaranteed that the same atom is always responsible for the tunnel junction. Therefore the measured spin polarized signal may be averaged out, or be a patchwork of different contrasts. This issue could only be solved by making an atomically flat sample.

5.12.3 Unanticipated Problems

In re-wiring the microscope, heat leaks were anticipated. Operation at LN2 temperatures is cheap, however, and to ensure spin polarization of the tips, any temperature well below room temperature would be adequate. However, cooling the wiring proved a vexing problem. The wiring itself, having been chosen for good transmission qualities and shielding, is somewhat stiff. Consequently, when it cools and contracts, it pulls on the STM head. The STM ramp is still mobile, and the microscope operates well, however when the instrument is level, the head is pulled over such that it makes mechanical and electrical contact with the inner cryogenic shields of the instrument introducing terrible vibrational and electrical noise. Tilting the entire microscope chamber resolves this problem, however this is challenging to do so, particularly because the air legs supporting the chamber have a long settling time constant. Iterations over days and weeks are required in order to break the unintended contact. To resolve this, more flexible wiring, with intentional slack should be used to replace the tunnel current and bias wires¹³. The principal consequence of this unintended contact is noise. With the head shorted to the chamber, electrical noise (60 Hz and multiples) is

¹³Recommended: custom coaxial wire from Cooner Wire company.

extremely prominent, along with vibrational noise in the same frequency range (often 75 Hz). When re-leveled such that the head was no longer in contact, almost invariably, one of the air legs would be compressed or extended to its limit, effectively removing any damping capability. This introduced very strong low frequency noise (7.5 Hz) into the system. In both cases, noise was sufficient to make scanning images useless for analysis.

5.13 Conclusion

A time-resolved STM was successfully constructed and equipped with an antiferromagnetic tip, a transmission line sample and *in situ* fabricated magnetic elements. The microscope was found to function well in time-resolved mode, and the magnetic elements were imaged, and showed electronic (density of states) contrast compared to the transmission line. Despite the general success in construction of the instrument, no magnetodynamics or even magnetic contrast was observed. A large number of possible causes for the lack of magnetic signal were proposed and addressed. Experiments have not yet revealed whether these steps will enable time-resolved SP-STM inspection of fabricated thin film magnetic elements.

CHAPTER 6

Copper Hafnium:Structure and Dynamics¹

Often pursuit of novel research leads to unexpected discoveries in directions tangential to the originally intended work. Part of the challenge is determining which to pursue.

In the preparation of samples for time-resolved STM measurements, interesting properties of the chosen material, $\text{Cu}_x\text{Hf}_{(1-x)}$, were discovered and studied. In short, the films were found to be composed of highly mobile clusters. This type of cluster hopping dynamics had only recently been observed in other metallic glass films (263, 264). In exploring the dynamics, evidence for a reconstructed surfaces state as well as aging dynamics leading to this state were observed. Therefore, the investigation of the film structure developed into a component of this work.

6.1 Metallic Glasses

Glassy behavior is a near-universal phenomenon in highly disordered condensed matter systems (265). Dynamics in the deep-supercooled regime, well below the glass transition temperature, are of special interest as they modify the properties of these amorphous materials across all relevant time scales. Intense study is devoted to determine the nature, spatial and temporal properties of these dynamics to elucidate the process of aging. Of particular interest are the effects of heterogeneous dynamics (266) and the effects of geometrical constraints (267). Constraints provide a complication which can accelerate or slow dynamics (268). Recent results on film surfaces demonstrate clarifying evidence of accelerated aging to an equilibrium state having slow dynamics (269). In this chapter, the aging process of a metallic glass (MG). film is spatially resolved and controlled with a scanning

¹A version of this chapter has been prepared for publication.

tunneling microscope, revealing a distinct surface state as well as accelerated aging due to tip interaction.

At temperatures below the glass transition temperature, MGs are believed to be composed of clusters of constituent atoms which are then densely packed, often possessing some degree of medium range ordering (270). Well below the glass forming temperature, aging is dominated by β relaxation which is described as collective excitations (271) of the cluster units (272). Many of the properties of MGs are theoretically described in the context of models built on the dynamics of these clusters and have been currently reviewed (273). Recent scanning probe investigations have shed light on these amorphous systems including MGs (263) and amorphous silicon (264). Slow cluster hopping, interpreted as isolated β relaxations, has been observed in each case well below the glass forming temperature.

Alloys of copper and hafnium form a complex system with a wide variety of phases possible (274). The $\text{Cu}_x\text{Hf}_{1-x}$ system can form a binary MG with recent work showing this transition occurs at 23% atomic hafnium and above (275). Here the first STM observations on $\text{Cu}_x\text{Hf}_{1-x}$, a model binary MG, are presented. The surface is found to have hillock features with sizes dependent on concentration, and pervasive dynamics consistent with β relaxation hopping events of clusters. Lower hafnium concentration films exhibit an aged surface state with slower dynamics and larger clusters. The formation of this surface state is reproduced *in situ* via sputter cleaning a film, and then inducing accelerated dynamics and aging via scanning. This enables lithographic restoration of sections of the surface to semi-stable large clusters. This remarkable control of heterogeneous dynamics on the nanoscale demonstrates the possibility of watching the accelerated aging of an unstable amorphous film on a laboratory timescale.

6.2 STM Observations

The same Createc ultra high vacuum scanning tunneling microscope used for time-resolved experiments in Chapter 5 was applied to the investigation of $\text{Cu}_x\text{Hf}_{1-x}$ films. Due to extended operations using samples that were not always baked, the microscope was operated at a base pressure of 2×10^{-10} mbar. Electrochemically etched tungsten tips were used after *in situ* electron bombardment to remove any oxide, and subsequent field emission to reduce the tip radius. The tungsten tips were prepared in the same way as the Chromium tips, as described in Appendix J.

Five alloy concentrations were used: $\text{Cu}_{85}\text{Hf}_{15}$, $\text{Cu}_{81}\text{Hf}_{19}$, $\text{Cu}_{75}\text{Hf}_{25}$, $\text{Cu}_{63}\text{Hf}_{37}$, $\text{Cu}_{50}\text{Hf}_{50}$, listed by percent atomic composition. Each of the samples was prepared by co-sputtering a 50 nm layer of CuHf onto a Si(100) wafer in a high vacuum deposition system with a base

pressure ranging from 1×10^{-8} to 8×10^{-8} mbar. Each wafer was prepared with an oxidizing cleaning step employing a wet etch of H_2SO_4 and H_2O_2 (3:1) for 30 minutes, resulting in a thin oxide layer, ~ 10 nm, on the bare wafer surface. Extensive characterization of $\text{Cu}_x\text{Hf}_{1-x}$ films produced with this system has been conducted previously (252). With one exception, samples were transferred from the sputter chamber to the STM load lock under an inert gas (Ar or N_2) atmosphere. The 85/15 sample was transferred under a clean air atmosphere. In lieu of a typical load-lock bake, samples were stored under UHV conditions for >120 hrs to allow slow degassing while avoiding any thermally driven structural changes. The 75/25 sample was observed a second time after sputter cleaning the surface *in situ* using a typical Ar^+ cleaning process (Ionec IG70 sputter ion gun, 1.1 kV, Ar pressure 5×10^{-6} mbar, 20 minutes). No anneal was performed subsequent to the sputter cleaning.

6.3 Surface Structure

Topographic images of each sample are shown in figure Fig. 6.1. All samples exhibited a surface consisting of round hillocks arranged similarly to other previously observed amorphous materials (276–278). The three lower concentration hafnium samples (85/15, 81/19, 75/25) all yielded low-noise images with well-defined surface features clearly delineated from neighbors. These three samples showed two distinct populations of hillocks: one larger sized set defined the highest points of the surface, while a smaller sized second set was visible below, in gaps between upper layer hillocks (Fig. 6.1 a to c). The two highest hafnium concentration samples exhibited a fundamentally noisier surface with no second layer of smaller features (Fig. 6.1 d, e). Instead, the hillocks were less clearly defined, smaller and arranged in a tightly packed, smooth, single layer. This transition matches well with the theoretically predicted concentration of bulk glass formation at 23% at. Hf (275) and with experimental observations of bulk $\text{Cu}_x\text{Hf}_{1-x}$ glasses (279).

Size distributions were calculated from images of each sample using a watershed based algorithm (280, 281) with additional height thresholding to remove partially occluded hillocks. With the exception of the 85/15 sample, a monotonic reduction in hillock size was found (Fig. 6.1 f). The enlargement of surface features due to the bulk tip geometry was taken into account with a tip radius correction following the method in reference (282). The feature size of the 63/37 and 50/50 samples as well as the second layer features in the 81/19 sample agree with the expected cluster size of 1-2 nm in MGs (273, 283, 284) as well as the expected packing pattern (270). Previous work has shown that sputtered $\text{Cu}_x\text{Hf}_{1-x}$ films with % at. Hf as low as 10 % are amorphous (252). This results from the amorphous state being frozen in, due to the extreme effective quenching rate of the sputtered material which can exceed 10^{15} K/s (285). This is consistent with the STM observations here, where all

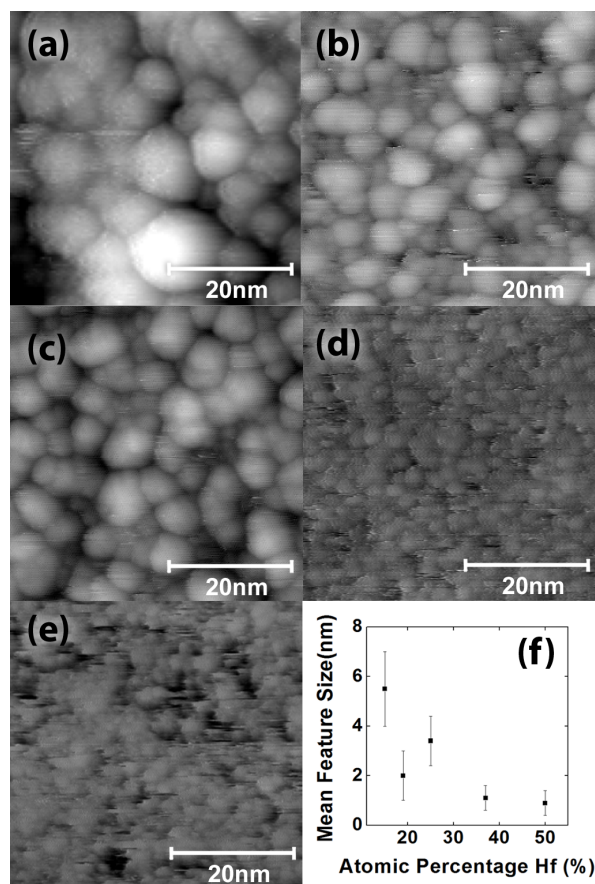


Figure 6.1: Topographic images of each film concentration: (a) $\text{Cu}_{85}\text{Hf}_{15}$ (19 pA, 1.7V), (b) $\text{Cu}_{81}\text{Hf}_{19}$ (20 pA, 2.6V), (c) $\text{Cu}_{75}\text{Hf}_{25}$ (20 pA, 2.4V), (d) $\text{Cu}_{63}\text{Hf}_{37}$ (20 pA, 2.6V), (e) $\text{Cu}_{50}\text{Hf}_{50}$ (20 pA, 2.2V). All images are shown with a linear grey scale corresponding to 3nm height difference between black and white. Small cluster substructure is visible particularly clearly in (b). Calculated cluster sizes corrected for estimated tip distortion are shown in (f).

films have amorphous structure, but those with Hf concentration below the bulk transition feature a surface reconstruction due to the less stable amorphous state.

6.4 Surface Dynamics

The STM revealed two types of dynamics on the $\text{Cu}_x\text{Hf}_{1-x}$ surface: motion of individual hillock structures (Fig. 6.2), and formation of large smooth structures spontaneously during scanning (Fig. 6.4). The former dynamics are highly reminiscent of the dynamics observed in recent work on other MG systems (263) and subsequently on amorphous silicon (264). Contrasting with previous observations, activity on these surfaces was pervasive, affecting the majority of the clusters over all time scales accessible by scanning (ms to minutes).

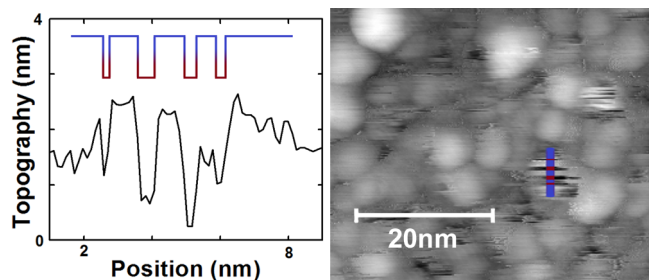


Figure 6.2: A particularly striking example of a cluster site repeatedly being filled and vacated during scanning on the 75/25 sample (19 pA, 2.2V). The fast scan direction is horizontal. A vertical profile (at left) shows the presence or absence of the cluster from scan line to scan line as indicated by trace showing the occupancy of the site.

Application of scanning probe microscopy techniques to noisy surfaces requires careful consideration of spurious noise sources. In this case, extraneous surface adsorbates could mimic the motion of clusters. However, surface structure and dynamics were found to vary with the concentration of the films, and no correlation was noted with sample transfer conditions between instruments. The concentration dependence of the dynamics was preserved on different samples transferred simultaneously. Furthermore, dynamics persisted through heating and sputtering surface treatments, and even through displacement of the top most layer of the surface via use of the STM tip. In both TEM and high resolution SEM inspections, dynamics of the films were visible, as well as in a second UHV STM. This provides very strong confirmation, from multiple independent sources, that contamination is not responsible for the observed surface structure or dynamics.

On short time scales, individual hillocks shifted within the time required for the transit of a tip over the domain itself (Fig. 6.2). Many showed multiple shifts, indicating a flicker-

ing mechanism with semi-reproducible hopping. On the three lower concentration samples, hopping was primarily limited to particular sites, often in gaps between larger hillocks. Typically, smaller sized features ranging between 1-5 nm in diameter dominated the dynamics. Larger features were observed to appear or disappear spontaneously, but not to flicker repeatedly. This clearly demonstrates the nanoscale heterogeneous dynamics that is expected on an amorphous surface. The semi-repeatable nature of the hopping events confirms that the hillock structures are clusters. On the two higher concentration samples, hopping was markedly faster, resulting in wide spread flickering noise. On all samples the extremely large number of hops presents a challenge to a quantitative extraction of hopping lifetimes. A general trend of decreasing hopping with repeated scanning of the same area was noted in some instances on the 85/15, 81/19 and 75/25 samples (Fig. 6.3).

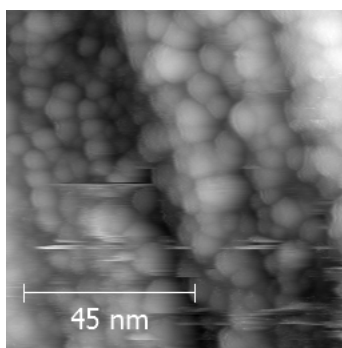


Figure 6.3: A topographic image of the 85/15 sample acquired at 20pA and 1.5V bias. The upper half of the image has been scanned extensively, while this is the first time the lower half of the image has been scanned. Similar effects were seen on the 81/19 and 75/25 sample indicating that all low concentration samples continued to age during observations. This image was also acquired in a region of the 85/15 sample featuring large ridges and with the small cluster substructure exposed between the ridges.

The other commonly observed dynamics were occasional changes in film structure beyond the apparent movement of hillocks. Clusters typically merged irreversibly into larger features (Fig. 6.4 a to f). Mergers ranged from very small, where a hillock would double in size, to exceptionally large where the resulting feature was up to 50 nm in size. Despite the extreme surface changes, often no corresponding tip change occurred, ruling out material being deposited from the tip, or tip crashes, as the cause. These events were unpredictable in nature and occurred under a wide variety of scanning parameters on all samples investigated, although mergers were less common, and much smaller on higher concentration hafnium samples.

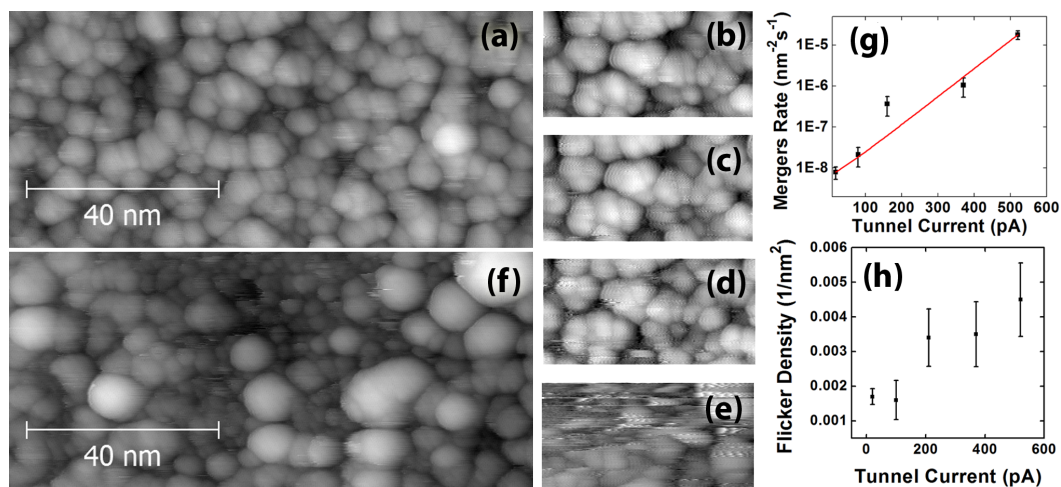


Figure 6.4: The effect of tunnel current on the 75/25 sample. (a) The initial scan (19 pA, 2.6 V) and (f) final scan (19 pA, 2.6 V) show extensive surface modification with the formation of numerous very large clusters and the movement of material away from the central scan area, exposing the subsurface small clusters. Images (b)-(e) show snapshots from the tunnel current ladder with currents 100 pA, 210 pA, 370 pA and 520 pA respectively (all at 2.6 V). Each sequence consisted of 5 images acquired over 3.5 minutes. Panel (g) shows the frequency of spontaneous surface cluster mergers as a function of tunnel current as calculated over available data from the 75/25 sample. Panel (h) shows the counted density of highly active (flickering) clusters present on the surface during tunnel current variation experiments.

6.4.1 Tunnel Current Dependence

A dramatic increase in surface activity was observed as the tunnel current set-point was increased. Panels 3 a to f show images from a tunnel current ladder sequence performed on the 75/25 sample during which no permanent tip changes were detected. The dominant effect of the highest tunnel current scans is clear, as are the distinct structural changes to the film. Evident here is the consequent exposure of the sub-layer of smaller hillocks. Qualitatively, the flicker activity in the freshly exposed subsurface is also significantly higher (Fig. 6.4 f), providing a direct visualization of heterogeneous dynamics just below the surface and confirming cluster structure and hopping dynamics are an intrinsic property of the $\text{Cu}_x\text{Hf}_{1-x}$ surface. Displacement of surface material and exposure of the subsurface structure was commonly seen with large mergers on the 75/25 surface. The volatility of the 85/15, 81/19 and 75/25 samples and exposure of the sub surface supports the previous conclusion that the samples with Hf concentrations near or below the bulk glass formation point are unstable and feature a relaxed surface of larger clusters.

Examining all data from the most thoroughly investigated sample, 75/25, a strong, approximately exponential, dependence of the merger rate on the tunnel current was found (Fig. 6.4 g). This contrasts to the weak current dependence of the areal density of hopping sites (Fig. 6.4 h). Data from other samples qualitatively support these trends. The vast majority of data was taken at extremely low tunnel currents as well as relatively high bias voltages, to mitigate possible physical tip interaction. Despite this, due to the high activity of the surfaces, the size of the hopping clusters and the fact that clusters are expected to hop extremely quickly (263), tunnel current spikes and transient physical interaction with the tip cannot be ruled out as the cause of mergers. When a cluster hops under the tip causing a large current spike, the heating may be sufficient to cause local crystallization as has been seen in TEM measurements (286) and nano-indentation (287). The exponential dependence on tunnel current fits with a thermally activated cause since the energy imparted to the surface in the tunnel current spike will be linearly proportional to the tunnel current set point. Cases of cluster formation (288) and alloying (289) operating by this type of mechanism have been seen in previous STM experiments.

6.5 Aging

The most interesting observations were gathered after Ar^+ sputter cleaning the 75/25 sample to disrupt the relaxed surface state. Measurements were pursued immediately after the cleaning with the same tip used to take reference images just before the cleaning. The surface was in constant flux, featuring short scars in the fast scan directions. Over multiple scans, the

surface coalesced into the familiar, more stable topography observed prior to the cleaning. Single pixel scars were replaced by multiple scan line width truncated images of clusters and cluster flicker, as seen on untreated surfaces. Increasing the scan range, however, revealed that it was only the scanned area with stable topography and slow dynamics (Fig. 6.5). This process was repeatable over multiple sequences. The lithographically defined sections were found to be stable on a long (>24 hour) time scale while no noticeable stabilization occurred outside the scanned areas. The emergence of identifiable hopping dynamics along with the enlarged surface clusters during scan sequences confirms that the surface was driven back to an unrelaxed state in the sputtering process, and that the subsequent effect was an accelerated aging process during which the surface was restored and hopping dynamics slowed ².

6.5.1 Noise Analysis

Knowing the flicker noise visible is due to hopping clusters, a more quantitative presentation of the aging can be made by extracting the power spectrum in the slow scan direction over successive scans (Fig. 6.5 e). The evolution of the dynamics is shown in figure 6.5 f where the noise floor is plotted as a function of elapsed scan time. Assuming a thermally activated hopping model for the surface dynamics, the expected telegraph noise spectrum may be written down as $S(f) = \tau / (2 + \pi^2 f^2 \tau^2)$ where $\tau = A_o^{-1} \exp(\Delta / (k_B T_f))$, Δ is the energy barrier for diffusion and A_o is the attempt frequency. A fictitious temperature $T_f(t) = T + T_f(0) \exp(-t/\Lambda)$ parametrizes the slowing of the dynamics as a thermalization process governed by a constant Λ (266). Plotting $S(f, t)$ for a high frequency, the variation of the noise floor with time can be fit to data in figure 6.5 f. Selecting Δ and A_o from typical parameters for β processes (263, 264, 272) ($\Delta \sim 0.5$ to 0.8 eV, $A_o \sim 0.01$ to 1 THz), good agreement is found for $T_f(0)$ of 325-360K and $\Lambda \sim 1$ hour. Within these ranges, specific values cannot be identified due to the sensitivity of the fit and large number of unknowns, however the model gives a good description of the dynamics for physically reasonable parameters. A representative fit is shown in figure 6.5 f.

This analysis greatly simplifies the physical situation by assuming a homogeneous fictitious temperature. Examining the data sequence, clusters become noticeably larger in scanned regions with slower dynamics. Therefore this fictitious temperature parameterizes the energy barrier change with cluster size, and hence a range of fictitious temperatures and evolution corresponding to the initial cluster size distribution would be expected. Additionally, the extreme bandwidth limitation of these STM measurements will affect apparent hopping

²The increase in stability of the 85/15, 81/19 and 75/25 films with scanning mentioned previously also fits with this interpretation. The effect was much less prominent, likely because of additional time and exposure to gases between sputtering and observations.

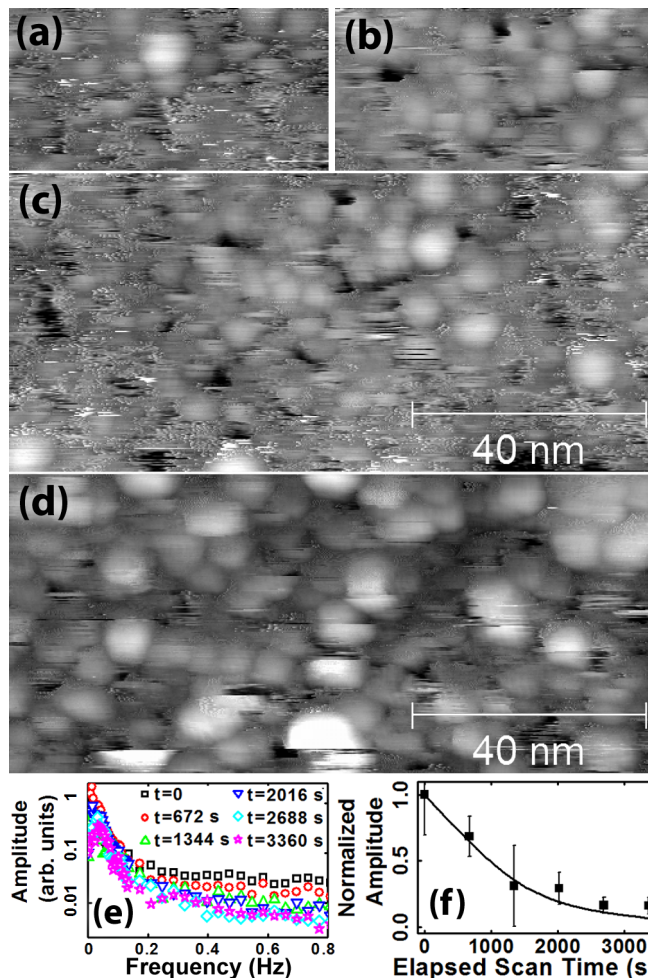


Figure 6.5: At top, (a) the first scan on the re-sputtered 75/25 surface is shown along with a scan captured of the same area 22 minutes later, (b). The previously scanned region is clearly visible nested within a zoomed out unscanned region (c). At bottom (d), the same area is shown after an additional 10 scans over 2.5 hours of scanning time. The surface has now stabilized in clusters. A 2.5nm linear grey scale was used in all images. All images were acquired at 20 pA and 2.2V. In (e), six power spectra taken in the slow scan direction show the change in the noise spectrum as the surface ages. At right (f) the noise floor extracted from each curve in (e) is fit with the calculated thermally activated noise at $f = 0.5$ Hz using a decaying fictitious temperature ($\Delta=0.8$ eV, $A_o = 1$ THz, $\Lambda=3000$ s, $T_f(0)=355$ K).

frequencies. The role of the tip in this process is not entirely clear. The absence of tip crashes, low tunnel current and high bias voltages used in imaging suggest a non-contact van der Waals interaction that acts as a weak, transient geometric constraint on the film. However the convolution of the tunnel current and tip-sample gap prevent conclusively ruling out heating induced by tunnel current spikes caused by hopping clusters. A full analysis of this problem requires more observations and development of new analysis techniques.

6.6 Temperature Dependence

A robust data set examining the telegraph noise was acquired as a function of temperature (Fig. 6.6). Using a sample of $\text{Cu}_{90}\text{Hf}_{10}$ three different temperatures were examined using limited time on a RHK variable temperature UHV STM. All other scan parameters were preserved between data sets, including scan speed, bias voltage and tunnel current set-point. Compared to the previously presented data, the tunnel currents used to acquire this data were significantly higher (150 pA at 1.0, 1.5 or 2.0 V). The reason for this is two-fold. First, the RHK feedback loop was unstable at low currents. Second, due to limited observational time and low activity at reduced temperatures, a higher tunnel current was considered advantageous in ensuring a more statistically significant data set was acquired in a short amount of time. The primary purpose of this data set was to determine if there was thermal activation present, rather than finding an accurate energy barrier. More data acquisition was planned, but experimental time with the RHK was cut short due to requirements for other experiments.

6.6.1 Measuring Cluster Lifetimes

Due to thermal drift, however, the same area could not be imaged at multiple temperatures precluding the usage of the power spectrum analysis method. Multiple images were acquired at each temperature to allow sufficient statistics to compute the observed distribution of telegraph noise dwell times and to compute the average dwell time of a flickering cluster. In order to extract this information from the image, a standard scar correction algorithm was used (280) where sudden jumps in data are detected as spikes which deviate from neighbouring points, both before and after, in the topographic derivative. Jumps more than one scan line in width identified using a second threshold applied to the detected derivative second jump back. This automated algorithm allows sufficient flexibility in tuning the width and detection thresholds to allow automated identification of flickering clusters. Some false positives are detected, such as some scan noise, or hillocks that appear, do not disappear or vice versa, however the dominant contribution is visually identifiable flickering (Fig. 6.6 b).

It is worth noting that the aspect ratio of the tip significantly impacts the performance of this algorithm. With a sharp tip, the sidewalls of the hillocks are very well defined, resulting in high levels of false positives. With a dull tip, only hopping events exceed the algorithm's first threshold resulting in much improved detection statistics. For instance, application of this algorithm to the variable current data set, yields results skewed by large false positives between clusters. In the analysis of the RHK data the first detection threshold was set at 2 times the RMS surface variation per pixel row while the second was set equal to the RMS surface variation. In order to properly capture fast dynamics at room temperature, the second threshold was dropped to 1/2 the RMS value. The detection of the transitions is performed, again, in the slow scan direction. Extracting a distribution of the widths of the flickering events then allows calculation of the distribution of lifetimes of clusters at preferential surface sites (Fig. 6.6).

6.6.2 Bandwidth Limitation for an Ensemble

Assuming an Arrhenius activation relation describing the hopping of the clusters, the decay distribution can be calculated with the approximate average lifetime τ as a decay parameter that is related to the energy barrier Δ .

$$P(\Delta t) \sim e^{-\frac{\Delta t}{\tau}}$$

where the decay parameter is given by

$$\tau = \frac{1}{\Gamma} = A_o^{-1} e^{\frac{\Delta}{k_B T}}$$

For the three different temperatures probed, 102K, 165K and 295K exponential distributions for the lifetimes were found as was expected from telegraph noise. All three temperatures were examined with identical scan parameters including tunnel current, bias and scan speed. Fitting for the decay parameter yields a measurement of the average lifetime. An Arrhenius plot relates the dependence of the average lifetime and the energy barrier (Fig. 6.6 d). An energy barrier of approximately 10 meV was found for the population of clusters participating in the observed hopping. This is a surprisingly low value for physical motion of clusters of material, but is actually fairly close to previous Arrhenius based estimates of cluster hopping on metallic glass surfaces (263). Two contributing reasons exist for the low energy barrier. First interaction with the STM tip will reduce the energy barrier. Assuming clusters are loosely bound and not chemically bonded to one another, interactions such as van der Waals would cause attraction to the tip. The second reason is that there is a large distribution of sizes of clusters participating in hopping which has previously been suggested

as a reason that the energy barrier appears suppressed with temperature variation observations (263). It is highly likely that the energy barrier is proportional to the mass and possibly the surface area of the cluster. Simultaneously, the bandwidth of the measurement is highly limited. Hence at each higher temperature, larger clusters participate in observable hops, while smaller ones become too fast. This suppresses the temperature trend by making observed activity more uniform.

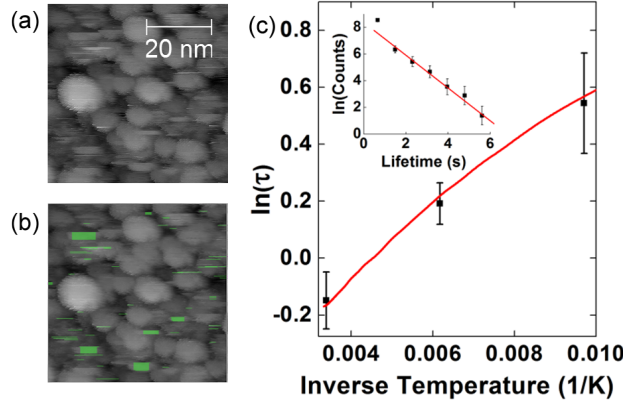


Figure 6.6: Jumping clusters can be identified using a scar detection algorithm, and life time distributions may be extracted to enable analysis. Clusters hopping on the time scale of scan lines show up as truncated clusters (a). Identifying scars allows measurement of the width of the hopping cluster, and hence the time it remained stable in one position (b). Observations on $\text{Cu}_{90}\text{Hf}_{10}$ show that lifetimes are thermally dependent, despite the influence of the tip (panel (c) inset). Analysis using the measured cluster size distribution, and an assumed van der Waals interaction, enables fitting of the observed hopping lifetimes to extract an interaction constant (c). The images were acquired with a tunnel current of 150 pA and a bias voltage of 1.5 V.

The effect of the bandwidth limitation and the distribution of energy barriers can be taken into account by determining a modified decay parameter. The case covering a bandwidth limited measurement of a single object exhibiting two level telegraph noise has been examined and treated fully in previous work (290). In the single object case, the decay lifetime is overestimated whenever the bandwidth is limited relative to the transition rate. The observed rate, Γ_{obs} can be expressed as a function of the intrinsic rate as such:

$$\Gamma_{obs} = \frac{2\Gamma + \Gamma_{bw}}{2} \left(1 - \frac{\Gamma\Gamma_{bw}}{(2\Gamma + \Gamma_{bw})^2}\right), \quad (6.1)$$

where Γ represents the intrinsic transition rate of the underlying hopping process and Γ_{bw} is the fastest rate detectable. This formula is for the simplified case where each state

participating in the telegraph noise has the same energy barrier; the general case may be found in the work of Naaman and Aumentado (290).

This result must be generalized to an ensemble of two level systems where the observed decay parameter is the average of the ensemble. To do so, an assumption must be made about the underlying form of the energy barrier. To proceed, an interaction proportional to surface area is assumed. This allows integration over the observed domain size distribution to be applied in lieu of an integral over the ensemble of energy barriers. Additionally one must assume that hopping of individual clusters is independent of all other hillocks, mobile or otherwise. The observed lifetime constant is then obtained as:

$$\int_0^{\infty} P_G(x)\Gamma_{obs}(x)dx, \quad (6.2)$$

where $P_G(x)$ is the normalized domain size distribution and the integral is performed over the variable x representing domain size. The function $\Gamma_{obs}(x)$ is the bandwidth corrected rate for a domain of size x with an intrinsic rate of $\Gamma(x) = A_o \exp \frac{-\alpha_v x^2}{k_B T}$ where α_v is a parameter describing the surface area interaction strength. This prescription for correction of the lifetime constant is general for any case where finite bandwidth is available and an ensemble energy barrier is dictated by an underlying variable that can be extracted independently. In this specific application the measured domain size distribution for $\text{Cu}_{90}\text{Hf}_{10}$ corrected for the estimated tip enlargement is employed for the probability distribution. Additionally an attempt frequency parameter of $A_o = 1 \text{ ps}^{-1}$ is assumed following estimates of similar cluster hopping attempt frequencies (263).

A good fit to the observed results is obtained for an α_v of 0.031 eV/nm^2 (Fig. 6.6). This implies an energy barrier of approximately 0.20eV for the typical cluster size. Recall that the RHK data sets were acquired at elevated tunnel currents compared to data taken with the Createc, providing at least a partial explanation of the disagreement in energy barriers. It is important to realize that numerous factors contribute to the bandwidth corrected fit for thermal dynamics, and so there is an implicitly large uncertainty in the application of the model. In particular, the shape of the distribution of domain sizes has a significant effect. In this case, an extracted distribution is available to work with, but has uncertainty due to the watershed algorithm employed as well as tip convolution. Tuning the shape of the distribution within uncertainty can result in a variation in α of an order of magnitude, but a variation in the calculated energy barrier of only $\pm 0.1\text{eV}$ since as the distribution is changed, the mean cluster size also changes.

6.7 Complementary Electron Microscopy

The dynamics observed on the CuHf films are only obvious with STM observations³. However, in the interest of identifying the dynamics and aging as a fundamental process that is not completely attributed to tip interaction, electron microscopy observations were undertaken. High resolution SEM provides confirmation of the structural changes of the films, such as enlarging clusters during scanning or the larger spontaneous formation of very large surface clusters. Hopping clusters proved to be too small for SEM. In order to verify hopping, the use of TEM is required, however the observations necessitate a change in substrate and film thickness.

6.7.1 SEM: Surface Aging

Use of scanning electron microscopy offers the opportunity to observe films identical to those observed in the STM. A sample composed of $\text{Cu}_{80}\text{Hf}_{20}$, 50 nm thick was transferred into a Hitachi S-5500 high resolution SEM immediately following deposition. The film structure reveals a very flat surface as expected, but also shows some sections where the topography exhibits larger smooth features protruding from above the rest of the surface. The more variable topography in these sections makes the film structure less stable, meaning that these areas are ideal locations to investigate for dynamics.

Indeed, in these areas, multiple types of surfaces changes were found. Upon scanning these features, the surface was found to planarize, and to convert from a smooth appearance into a pebbled texture. This corroborates the STM observations of aging. The SEM cannot image the extremely small amorphous clusters initially, however as scanning drives the unstable sections of the surface to rearrange, clusters grow and stabilize into the surface reconstruction observed with STM (Fig. 6.7). The clusters are lithographically enlarged with the beam, until they become large enough to be resolved by the SEM. This matches very well with the aging process observed following sputter cleaning of the STM samples.

6.7.2 SEM: Large Surface Changes

Additional shifts of material in varying quantities between locations were observed (Fig. 6.8). Holes enlarged or filled in the film surface, large cluster like objects appeared and disappeared. Periodically, a preferential site would begin to accumulate material rapidly, forming very large surface features (Fig. 6.8). These events match the large surfaces changes

³Or possibly with very good AFM, but no UHV AFM was available to test.

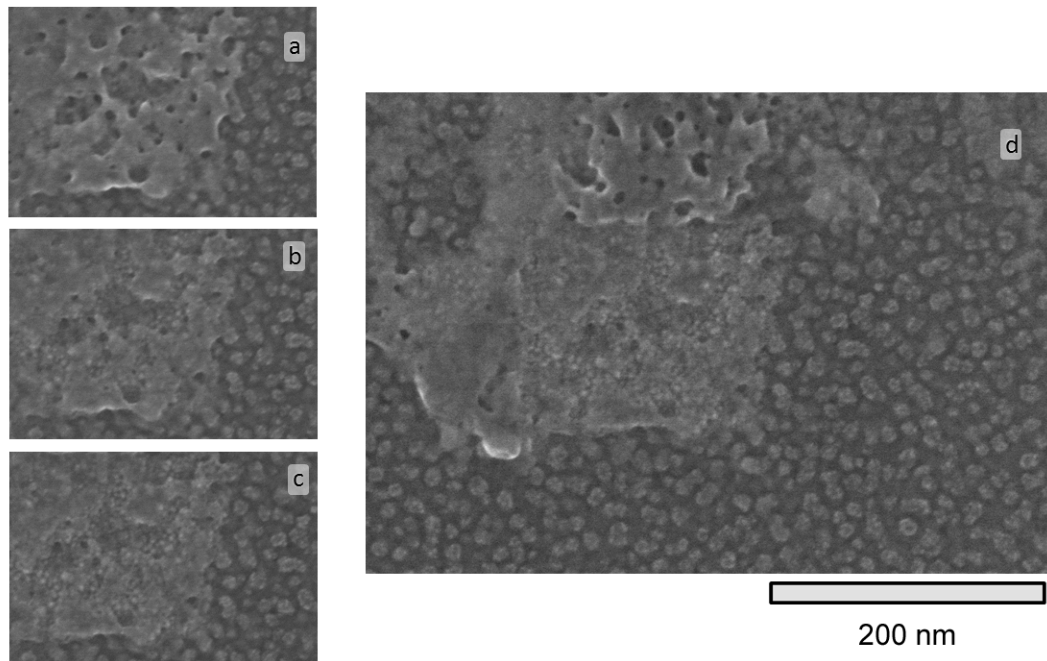


Figure 6.7: A reconstructed surface structure forms under the influence of the beam during SEM observations. Much as is seen in STM observations, within the scanning area pebble like surface features form, indicating the presence of clusters that enlarge steadily during observations (panel a through c are shown in order). In the case of SEM, this means the cluster features eventually become resolvable. Panel (d) offers a zoomed out view of the area where panels (a)-(c) were acquired, showing changes in the film are limited to the former scan area (at the centre of the image). Note that panels (a)-(c) use the same scale as panel (d).

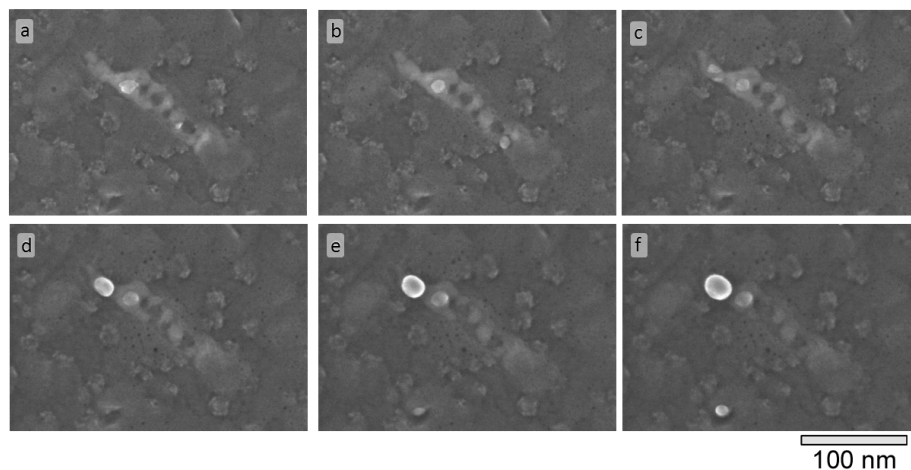


Figure 6.8: Rough sections of copper hafnium samples show dynamics observable with high resolution SEM. A large number of dynamical effects are visible over time (panel a through f are shown in order). Holes open up in formerly smooth sections of film. Large cluster like objects appear and disappear, and particular large clusters grow.

found in STM, including the observation of material surrounding the large feature disappearing in conjunction with the feature growing.

6.7.3 TEM: Hopping Clusters

The SEM observations did not have sufficient resolution to observe clusters sufficiently small that they exhibited stable hopping. Observations of films on TEM substrates also proved to be challenging, with no significant contrast detectable when looking directly through the film. Success was found using an unconventional technique. Films were sputtered onto carbon nano-tube substrates, coating the tubes with a very thin (5-15 nm) layer of $\text{Cu}_{80}\text{Hf}_{20}$. The coating of a 3D substrate affords the opportunity to look at sections of the film in profile, where fluctuations in thickness of the film are much more obvious. A caveat to this observational technique is the fact that the film is on a different substrate, is a different thickness, and has very different film geometry. However, this approach did allow TEM observation of hopping. A JOEL-2100 TEM was used.

Rare events, where a clear cluster like object spontaneously disappeared, and sometimes a possibly correlated cluster appeared elsewhere, were visible in fast scanning movies taken with TEM. The events were too rare for analysis, but did confirm hopping could occur in these films independent of STM observation.

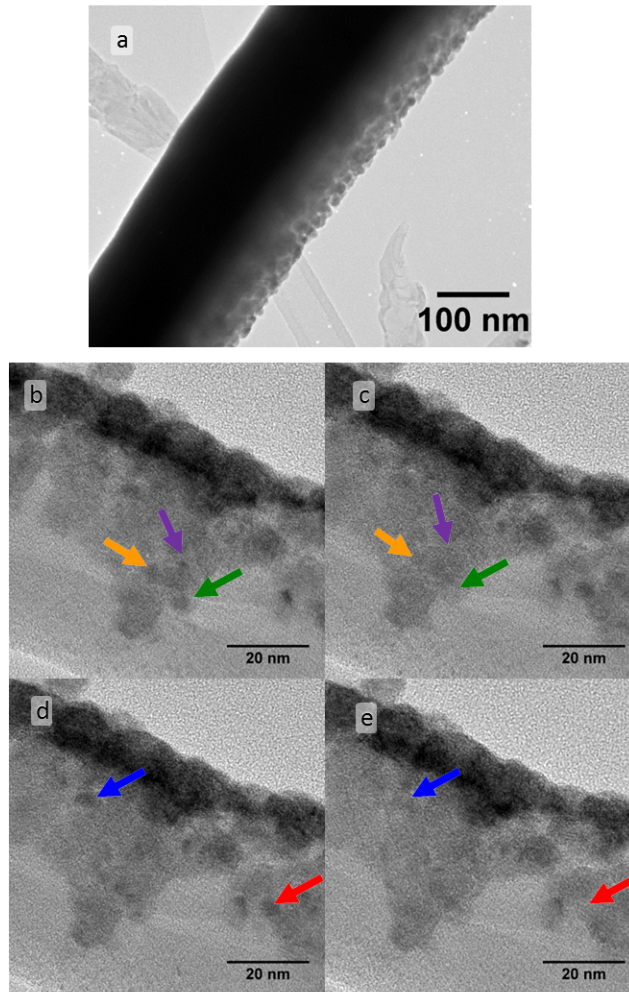


Figure 6.9: Under TEM observations of copper hafnium films in profile, occasionally nm scale sized clusters jump. Observations are made on films deposited on carbon nanotubes. At the edges of the tube, the film can be observed in profile. Jumps are rare, and difficult to spot. In the four panels shown, one cluster jumps between panel b-c-d in the middle left of the image, and another hops from d to e in the lower right hand area.

6.7.4 Beam Influence

In both STM and SEM observations, it is clear that the probe used has an influence on the film. The electron beam and STM tip are disparate types of probe however. One way each probe could have a similar effect is through heating, with the beam simply inducing heating, while transient tunnel current spikes induce heating during STM observations. However, as noted in the preceding sections, transient tunnel current spikes do not appear to be appropriate to describe all dynamics, particularly hopping. Comparing and contrasting the low energy, but close physical proximity influence of the STM tip against the high energy electron beam may provide significant insight into dynamics in more detailed future studies.

The robustness of the dynamics observed, with such different probes, provides a very strong confirmation that the dynamics and structure are endemic to the material and not due to contamination affecting the STM measurements. Extensive supporting work was performed also ruling out contamination, as summarized in the following section.

6.8 Cross Checks for Contamination

Numerous sources of noise can complicate STM measurements. This is a major issue that must be confronted when analyzing STM noise patterns for dynamical physical meaning. This is an emerging application of STM. The following extends the discussion of the identification of hopping in the main text.

The primary requirement is to distinguish hopping events from the other sources of noise. Mechanical or electrical noise can contribute periodic oscillations that are easy to identify, but can also result in stochastic noise which might mimic fast hopping noise. More commonly, an unstable tip or incorrect feedback loop settings can also lead to stochastic noise that appears as short “scars” in single scan lines, uncorrelated with features in neighboring lines along the slow scan direction. Feedback settings may also contribute scars that are multiple scan lines wide when the tip scans over large topographic features; these are readily identified by comparison of the forward and backward scan images: feedback artifacts will appear on opposite sides of the topographic feature. Bearing these possibilities in mind, it is possible to unambiguously discriminate the portion of the hopping event distribution which has no overlap with other sources of noise in the measurement.

6.8.1 Identification of Hopping Clusters

In this work hopping noise is identified rigorously by demanding, for a hop to be included in measurements, that a portion of the hopping cluster be imaged. Each event thereby included

as contributing to the glassy dynamics involves correlations within the image across multiple scan lines, and consistency between forward and backward scans (by examining the images it is easy to reject feedback effects near steep topography). These discrimination conditions fail for the sources of transient noise unrelated to the surface physics of interest. This constraint also limits identifiable hopping dynamics to sources that are localized to regions similarly sized to clusters in the fast scan direction, and look like clusters. The method does have the disadvantage of neglecting faster hops from analysis. Without further context, it is impossible to separate which fast scan noise represents hopping clusters.

There is one situation within the present work for which some further context is available: imaging of the active surface after sputter cleaning. Fast hopping is relevant in the frequency analysis of these data. In this case, imaging of sections previously scanned provides a control area within the scan, making it demonstrable that mechanical, electrical or tip noise are not contributing to the pervasive high frequency noise seen elsewhere. The emergence of identifiable hopping as the high frequency noise disappears during repeated scanning also supports the conclusion that the high frequency noise is fast hopping. The frequency-based analysis applied to the sputter cleaning sequence cannot be applied to other data in the manuscript for two reasons: no control areas where noise density drops considerably are available, and dynamics are so much slower that the frequencies involved in hopping overlap the topographic frequencies in the power spectrum.

6.8.2 Identification of Tip Artifacts

Numerous separate tips were utilized during the course of the experiments, in many cases specifically changing tips to rule out noise contributions from the tip in the observed dynamics. As discussed in the main text a detailed and reliable method of preparing tungsten tips in ultrahigh vacuum was employed. Typically a stable tip can be prepared that immediately yields atomic resolution on a crystalline surface. This also makes it very unlikely that the tips would consistently introduce a contaminant into the system.

Beyond contributing stochastic noise, tip conditions can contribute many other effects which need to be identified in STM data. Particularly important here are multiple tip effects, where more than one part of the tip contributes to the STM image. On rough surfaces, this is more likely. Most insidiously, it is possible to picture a single cluster being imaged by a second tip asperity and appearing to hop if that second tip is unstable. It is therefore critical to reject any data that has signs of multiple tips. These signs include double images, wispy features overlaid on the surface, or sudden disappearance of large, multi-cluster features.

Tip interactions with the surface, such as tip crashes, adsorption onto or deposition of material from the tip, can lead to changes such as the large hillock mergers described in

this work. These events are identified through sudden changes in the imaging signal which correspond to physical changes in the tip. When material is adsorbed (or desorbed) from the tip, the feedback loop shifts to compensate for the longer (or shorter) tip. This shows up as a step in the slow scan direction when a permanent change to the tip is made, or as a transient scar when something adsorbs onto the tip and desorbs a short time later. Typically a tip change results in a change in the imaging resolution, noise level, or a vertical and/or lateral shift of the image as a different part of tip becomes dominant in imaging. Surface dynamics information was not extracted from images failing the preconditions for tip stability. This prescription was used to evaluate the dynamics seen on the surface and determine that tip contact does not play a major role in the dynamics and evolution of the CuHf surface.

6.9 Surface preparation procedures unique to the study of amorphous films

Typically in STM experiments samples undergo extensive cleaning and annealing prior to measurements. This is impossible here because high temperature annealing would destroy the amorphous state and crystallize the film. Therefore extra steps are required to prevent and check for surface contamination or oxidation. The suite of additional tests for contamination and oxidation is described below. To restate what is said in the previous sections about contamination: surface structure and dynamics are persistent through all transfer conditions, persist on freshly exposed surface, persist after sputter cleaning, and depend on the concentration of the films. This presents a very clear indication that no contamination or oxidation played a role in the observations.

6.9.1 Thermal Treatments

After initial observations, all samples were heated and re-imaged. Two thermal treatments were used. Three samples (81/19, 63/37 and 50/50) were heated in UHV on the sample holder to ~ 390 K for 2 hours. The other samples were subjected to a 48 hour bake in the STM load lock at 400 K. No significant change in structure or imaging was noted for any sample following heating.

6.9.2 Current-Voltage Characteristics

A metallic surface and metallic tip have characteristic linear low bias current-voltage (I-V) relationships. All samples were tested for non-linearity in I-V curves at low bias voltages.

Particular attention was applied to the 85/15 sample as it was the only sample exposed to air. All samples yielded linear responses (Fig. 6.10). It is worth noting that obtaining I-V measurements were often affected by the activity of the surfaces, as would be expected. The I-V curves are acquired with the tip at constant height and the feedback loop temporarily disabled. Frequently, large jumps in tunnel current were detected, consistent with clusters hopping into and out of the tunnel junction during the measurement.

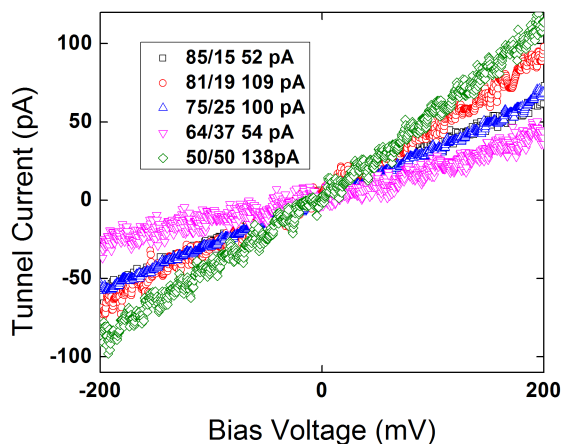


Figure 6.10: IV curves captured for each sample. The legend at top left shows the sample and the tunnel current set point used at the start of the measurement at 200 mV bias. Variable initial currents stem from using the largest stable current for that surface at 200 mV. Spectra were acquired with the STM feedback loop turned off and were therefore acquired rapidly (less than 0.5s) to reduce the influence of drift. However delay between issuing the command for spectrum acquisition, and actual data acquisition results in dead time where the feedback loop is off, allowing drift of the tip and leading to an effective reduction in the initial tunnel current for many of these spectra.

6.9.3 Second STM

Additional imaging on 85/15 and 75/25 samples was performed in a second UHV-STM system (RHK UHV 3000). The structure and dynamics were consistent with the data taken using the Createc microscope. The RHK microscope used platinum iridium tips, providing a confirmation of tip-independence.

6.9.4 Argon from Sputter Cleaning

A special case must be considered for the sputter-cleaned sample. Argon adsorbed on the surface will evaporate within minutes at temperatures as low as 200 K (291). Therefore none remains to interfere with scanning. The 1.1 keV argon ions do, however, penetrate copper to a depth of 2 - 3 nm (292) and some will remain implanted in the film. Even for low energy Ar ions such as these, argon defects are expected to remain stable up to temperatures well above room temperature (196).

Annealing typically removes most implanted argon left from sputter cleaning. However, in the case of CuHf films, annealing would destroy the amorphous state. Any argon remaining after the treatment could, in principle, interfere with scanning and cause a new source of surface noise. Given the high activity of the surface, it is conceivable that argon is released during scanning. The following order-of-magnitude estimates argue against this mechanism as a measurable source of tunnel current noise. If the released argon were visible in scans, it would need to remain in the junction long enough to provide a detectable current spike when averaged over the time constant of the pre-amp. An overestimated lifetime of Ar in the junction can be made by calculating the lifetime of a Xe atom in the junction at room temperature using the theory describing the capture barrier for manipulation of Xe via STM (293). Using a typical Xe attractive potential of 30 meV (294), a lifetime of ~ 6 ns is obtained. This is already far too short to contribute a tunnel current spike that is detectable when using a bandwidth of ~ 1 kHz for the preamp, before even accounting for the Ar lifetime in the junction being much shorter than for Xe, due to its lower mass and polarizability.

6.10 Conclusion

In summary, stable and unstable $\text{Cu}_x\text{Hf}_{1-x}$ amorphous films were examined with STM allowing direct observation of cluster structure in the films as well as β relaxation dynamics. Unstable films exhibited a relaxed surface state with features larger than expected cluster sizes on top of smaller features which match those observed in the stable amorphous films. Throughout the observations heterogeneous dynamics were observed in the form of preferential sites of high activity on the surface, increased activity in subsurface clusters, and most strikingly through controlled aging of the surface. Destroying the relaxed surface state allowed lithographic definition of aged sections of the surface simply via scanning. This clearly demonstrates the extreme range of heterogeneous dynamics possible in the aging process and confirms rapid surface aging of a sample to a stable surface reconstruction.

CHAPTER 7

Summary

The tendency of the magnetic vortex core to strongly interact with modulations in the magnetic properties of a device makes it an ideal candidate for use in a wide variety of information storage applications. The magnetic vortex in a disk serves as an excellent prototyping platform for magnetic computing elements. Moreover, with a stable vortex state confined within a circularly symmetric element, the system is sufficiently simplified that analytical descriptions may be pursued. This lends confidence to the physical interpretation of the results of the dynamical properties of vortices, and detailed energetic interactions with local film structure.

The potential technological and physical significance of the vortex state provides ample motivation for the study of magnetic disks. Three experimental techniques were applied in this work, supported by a robust analytical model, to study and understand the properties of the magnetic vortex.

Magneto-optical susceptometry was conceived and developed as a tool that has a unique method of measuring switching distributions of arrays. The AC-MOKE susceptometer constructed is a unique instrument, in application to fabricated micro-elements. It is particularly well suited to measurement of arrays, and as such, performs well at gathering large sets of data rapidly. The susceptometer was applied to elucidate the role of thermal dynamics in vortex annihilation at room temperature, separating it from the influence of the change of $M_S(T)$. Key to this analysis was an extension to analytical models describing the vortex susceptibility as a function of field. The instrument was successfully applied to extract energetic parameters describing the vortex decay for a variety of decay models (69). With much improved temperature ranges, such an instrument could be used to evaluate the influence of quantum tunneling on the decay of vortices.

Turning to smaller energetic transitions, measurements of interactions of a single vortex core with film defects were observed using a highly sensitive torsional magnetometer. This instrument enabled detection of minute shifts of the vortex core through measurement of the concomitant magnetization shift. This included the detection of thermally-driven switching between bistable pinned states. Coupled with a novel model of the disk that takes into account changes in energetic evolution during core interactions, the torsional magnetometer can be converted into a scanning vortex probe microscope (SVPM) that measures the energetic potential of the core interaction with the magnetic film with sub-nm accuracy. Measurement of the natural potential showed interactions as low as 500 meV, up to stronger interactions similar to those seen in dynamical measurements (89, 91). Investigations in two dimensions allowed a 2D reconstruction of a potential that generated matching hysteresis loops. Transition energy barriers separating bistable states were computed from thermal dynamics and were compared to barrier values extracted from the 2D model based reconstruction of the pinning potential. The model and experiment showed good agreement. The torsional magnetometry platform in conjunction with the model provide a method of measuring point-like energy changes in the film. This can be applied as a tool to study various methods of artificial pinning, calibrating pinning sites quantitatively, and guiding development of real-world devices. This was demonstrated by locating and measuring three artificial pinning sites added to the device by focused ion beam point implantation of gallium ions.

The torsional magnetometer has significant potential in four areas. First, it can be an invaluable tool for quantitative advancement of the understanding of magnetic pinning potentials. This is particularly important for ion implantation, which is not fully understood. Second, the observation of thermal hopping of the core indicates that, with sufficiently small pinning potentials, quantum tunneling-based depinning of the vortex core might be observed. This would verify recent possible observation of tunneling effects in arrays (48). These conditions may be obtainable in a single crystal sample, with no, or extremely small natural pinning, and very small artificially-induced pinning sites. Third, the hysteretic magnetization measurement applied here would be entirely compatible with simultaneous dynamical measurements. This could enable the extraction of even more information about the film. In particular, local damping measurements would be invaluable in understanding dissipation of energy. Last, the torsional magnetometer platform shows promise as a basis for real devices as well. A 2D array of very small pinning sites could provide a high density of states for a vortex core to occupy. NEMS has also been demonstrated to be highly integrable with existing computer technology. The 2D symmetry of the disk, on a sensitive detection platform may provide a novel functionality not realized in wire geometries.

The creation of a scanning vortex probe microscope, and effort in creating a method of accurately extracting the pinned core position, highlights the importance of developing

instruments that measure the vortex core position with sub nm accuracy, independent of any modeling. In particular, direct observation of dynamics with high spatial resolution has been elusive. To address this problem, a low temperature UHV STM was converted into a time resolved STM. It was also equipped with tips that, in theory, should be spin polarized in order to observe magnetic contrast. An infrastructure enabling the deposition of UHV clean permalloy disks onto the STM sample *in situ* was developed. This effort enabled time resolved measurements to be made on the disks. No magnetic contrast was observed, however scanning was possible and time resolution of ~ 700 ps was obtained. The instrument is fully functional. Challenges remain with diagnosing the lack of magnetic contrast and the general difficulty of scanning on relatively rough polycrystalline films.

The last component of this project was an offshoot of developing a smooth transmission line for time resolved STM measurements. In doing so, nanoscale dynamics were discovered in copper hafnium films. These dynamics were identified as thermally activated hopping amorphous clusters. Most remarkably, films below 20% hafnium were found to exhibit surface reconstructions of larger, possibly crystalline clusters. Destroying these clusters *in situ* using argon sputtering enabled observation of the formation of this surface state on a laboratory time scale. This may be the first movie of aging of a glassy material well below the glass transition temperature. All of the dynamics on the films were confirmed with electron microscopy, indicating that the results were not due to contamination or influence of the STM tip. Amorphous cluster dynamics analysis with an STM is a nascent field. Much work must be done to understand the role of the STM, and to compensate for the slow scan speed. However, much can also be learned from careful analysis of what would, in traditional STM measurements, usually be dismissed as noise.

Significant progress was made in this work towards quantitative magnetodynamics and to building a framework for rapid construction and prototyping of vortex based devices. A large part of this work involved developing instruments and theoretical frameworks that may now be applied in continued work to a wide variety of systems. The applications of torsional magnetometry, supported by the DVPM, and array measurements using AC-MOKE are virtually endless.

Bibliography

1. D. Mattis, *The Theory of Magnetism Made Simple* (World Scientific Publishing Company, 2006).
2. A. Einstein, W. J. de Haas, *Verh. Dtsch. Phys. Ges.* **17**, 152 (1915).
3. N. Bohr, *Niels Bohr Collected Works: II. The Doctor's Dissertation (Text and Translation)* (Elsevier, 1972).
4. H.-J. Van Leeuwen, *Journal de Physique et Le Radium* **2**, 361 (1921).
5. P. Weiss, *J. de Physique* **6**, 667 (1907).
6. H. Barkhausen, *Zeitschrift für Physik* **20**, 401 (1919).
7. C. Kittel, *Reviews of Modern Physics* **21**, 541 (1949).
8. W. Heisenberg, *Zeitschrift für Physik* **49**, 619 (1928).
9. O. W. Richardson, *Physical Review Series I* **26**, 248 (1908).
10. S. J. Barnett, *Science* **30**, 413 (1909).
11. J. C. Maxwell, *A Treatise on Electricity and Magnetism I* (Dover Publications, 1954).
12. J. C. Maxwell, *A Treatise on Electricity and Magnetism II* (Dover Publications, 1954).
13. S. J. Barnett, *Physical Review* **6**, 239 (1915).
14. A. Einstein, W. J. de Haas, *Proceedings Royal Acad. Amsterdam* **18**, 696 (1916).
15. S. J. Barnett, *American Journal of Physics* **16**, 140 (1948).
16. S. J. Barnett, *PNAS* **3**, 178 (1917).
17. J. Q. Stewart, *Physical Review* **40**, 100 (1918).

18. E. Beck, *Annalen der Physik (Leipzig)* **60**, 109 (1919).
19. V. Y. Frenkel, *Soviet Physics Uspekhi* **22**, 580 (1979).
20. W. Gerlach, O. Stern, *Zeitschrift für Physik* **9**, 349 (1922).
21. W. Pauli, *Zeitschrift für Physik* **31**, 373 (1925).
22. G. Uhlenbeck, S. Goudsmit, *Naturwissenschaften* **13**, 953 (1925).
23. W. Pauli, *Zeitschrift für Physik* **43**, 601 (1927).
24. E. Ising, *Zeitschrift für Physik* **31**, 253 (1925).
25. E. Ising, Contribution to the theory of ferromagnetism (1925).
26. F. Bloch, *Zeitschrift für Physik* **61**, 206 (1930).
27. L. Landau, E. Lifshitz, *Physikalische Zeitschrift der Sowjetunion* **8**, 153 (1935).
28. F. Bloch, *Zeitschrift für Physik* **74**, 295 (1932).
29. L. Néel, *Compt. Rend.* **241**, 533 (1955).
30. J. C. Slonczewski, *Journal of Magnetism and Magnetic Materials* **159**, L1 (1996).
31. A. Berger, S. Knappmann, H. P. Oepen, *Journal of Applied Physics* **75**, 5598 (1994).
32. S. Blundell, *Magnetism in Condensed Matter* (Oxford University Press, New York, 2001).
33. S. Chickazumi, *Physics of Ferromagnetism* (Oxford University Press, 1997), second edn.
34. A. Aharoni, *Introduction to the Theory of Ferromagnetism* (Oxford University Press, New York, 1996).
35. M. Beleggia, M. De Graef, *Journal of Magnetism and Magnetic Materials* **263**, L1 (2003).
36. S. Tandon, M. Beleggia, Y. Zhu, M. De Graef, *Journal of Magnetism and Magnetic Materials* **271**, 9 (2004).
37. S. Tandon, M. Beleggia, Y. Zhu, M. De Graef, *Journal of Magnetism and Magnetic Materials* **271**, 27 (2004).
38. E. C. Stoner, E. P. Wohlfarth, *Nature* **160**, 650 (1947).
39. T. L. Gilbert, *IEEE Transactions on Magnetics* **40**, 3443 (2004).

40. C. Herring, *Physical Review* **85**, 1003 (1952).
41. C. Herring, *Physical Review* **87**, 60 (1952).
42. S. A. Wolf, *et al.*, *Science* **294**, 1488 (2001).
43. D. A. Allwood, *et al.*, *Science* **309**, 1688 (2005).
44. I. Žutić, J. Fabian, S. Das Sarma, *Reviews of Modern Physics* **76**, 323 (2004).
45. S. S. P. Parkin, M. Hayashi, L. Thomas, *Science* **320**, 190 (2008).
46. S. Loth, S. Baumann, C. P. Lutz, D. M. Eigler, A. J. Heinrich, *Science* **335**, 196 (2012).
47. L. Bogani, W. Wernsdorfer, *Nature Materials* **7**, 179 (2008).
48. R. Zarzuela, S. Vélez, J. M. Hernandez, J. Tejada, V. Novosad, *Physical Review B Rapid Communications* **85**, 180401 (2012).
49. W. Wernsdorfer, *et al.*, *Journal of Magnetism and Magnetic Materials* **145**, 33 (1995).
50. W. Wernsdorfer, *et al.*, *Journal of Magnetism and Magnetic Materials* **151**, 38 (1995).
51. I. Tudosă, *et al.*, *Nature* **428**, 831 (2004).
52. E. Beaurepaire, J.-C. Merle, A. Daunois, J.-Y. Bigot, *Physical Review Letters* **76**, 4250 (1996).
53. G. P. Zhang, W. Hübner, *Physical Review Letters* **85**, 3025 (2000).
54. B. Koopmans, M. van Kampen, J. T. Kohlhepp, W. J. M. de Jonge, *Physical Review Letters* **85**, 844 (2000).
55. P. M. Oppeneer, A. Liebsch, *Journal of Physics: Condensed Matter* **16**, 5519 (2004).
56. G. P. Zhang, *Physical Review Letters* **101**, 187203 (2008).
57. G. P. Zhang, W. Hübner, G. Lefkidis, Y. Bai, T. F. George, *Nature Physics* **5**, 499 (2009).
58. U. Atxitia, O. Chubykalo-Fesenko, J. Walowski, A. Mann, M. Münzenberg, *Physical Review B* **81**, 174401 (2010).
59. T. Ostler, *et al.*, *Nature Communications* **3**, 666 (2012).
60. A. V. Kimel, R. V. Ivanov, B. A. and Pisarev, P. A. Usachev, A. Kirilyuk, T. Rasing, *Nature Physics* **5**, 727 (2009).

61. A. Kimel, A. V. Kirilyuk, A. Tsvetkov, R. V. Pisarev, T. Rasing, *Nature Physics* **429**, 850 (2004).
62. A. V. Kimel, *et al.*, *Nature* **435**, 655 (2005).
63. C. D. Stanciu, *et al.*, *Physical Review Letters* **99**, 047601 (2007).
64. B. Vodungbo, *et al.*, *Nature Communications* **3**, 999 (2012).
65. J. C. S. Davis, P. C. E. Stamp, *Physics In Canada* **67**, 126 (2011).
66. L. Thompson, P. C. E. Stamp, *Physical Review Letters* **108**, 184501 (2012).
67. L. Thompson, P. Stamp, *Journal of Low Temperature Physics* p. 1 (2012).
68. P. Fischer, *Materials Science and Engineering: R: Reports* **72**, 81 (2011).
69. J. A. J. Burgess, *et al.*, *Physical Review B* **82**, 144403 (2010).
70. Z. G. Liu, R. D. Sydora, M. R. Freeman, *Physical Review B* **77**, 174410 (2008).
71. J. A. J. Burgess, *et al.*, *Science* **339**, 1051 (2013).
72. J. P. Davis, *et al.*, *Applied Physics Letters* **96**, 072513 (2010).
73. J. P. Davis, *et al.*, *New Journal of Physics* **12**, 093033 (2010).
74. J. P. Davis, *et al.*, *Journal of Applied Physics* **109**, 07D309 (2011).
75. J. Losby, *et al.*, *Journal of Applied Physics* **111**, 07D305 (2012).
76. J. A. J. Burgess, J. E. Losby, M. R. Freeman, *arXiv:1208.3797 [cond-mat.mes-hall]* (2012).
77. R. P. Cowburn, D. K. Koltsov, A. O. Adeyeye, M. E. Welland, D. M. Tricker, *Physical Review Letters* **83**, 1042 (1999).
78. J. Raabe, R. Pulwey, T. Schweinböck, J. Zweck, D. Weiss, *Journal of Applied Physics* **88**, 4437 (2000).
79. T. Shinjo, T. Okuno, R. Hassdorf, K. Shigeto, T. Hono, *Science* **289**, 930 (2000).
80. K. L. Metlov, *arXiv:1210.5960 [cond-mat.mes-hall]* (2012).
81. A. B. Butenko, A. A. Leonov, A. N. Bogdanov, Rößler, *Physical Review B* **80**, 134410 (2009).
82. M. Im, *et al.*, *Nature Communications* **3**, 1 (2012).

83. D. H. Kim, *et al.*, *Nature Materials* **9**, 165 (2010).
84. R. D. McMichael, M. J. Donahue, *IEEE Transactions on Magnetics* **33**, 4167 (1997).
85. D. Toscano, S. A. Leonel, R. A. Dias, P. Z. Coura, B. V. Costa, *Journal of Applied Physics* **109**, 076104 (2011).
86. T. Uhlig, *et al.*, *Physical Review Letters* **95**, 237205 (2005).
87. J. P. Park, P. Eames, D. M. Engebretson, J. Berezovsky, P. A. Crowell, *Physical Review B* **67**, 020403 (2003).
88. R. L. Compton, P. A. Crowell, *Physical Review Letters* **97**, 137202 (2006).
89. R. L. Compton, T. Y. Chen, P. A. Crowell, *Physical Review B* **81**, 144412 (2010).
90. T. Y. Chen, A. T. Galkiewicz, P. A. Crowell, *Physical Review B Rapid Communications* **85**, 180406 (2012).
91. T. Y. Chen, M. J. Erickson, P. A. Crowell, C. Leighton, *Physical Review Letters* **109**, 097202 (2012).
92. J. S. Kim, *et al.*, *Physical Review B* **82**, 104427 (2010).
93. A. Aharoni, *Journal of Applied Physics* **68**, 2892 (1990).
94. N. A. Usov, S. E. Peschany, *Journal of Magnetism and Magnetic Materials* **118**, L290 (1993).
95. A. Wachowiak, *et al.*, *Science* **298**, 577 (2002).
96. B. E. Argyle, E. Terrenzio, J. C. Slonczewski, *Physical Review Letters* **53**, 190 (1984).
97. S. B. Choe, *et al.*, *Science* **304**, 420 (2004).
98. V. Novosad, *et al.*, *IEEE transactions on magnetics* **37**.
99. G. Mihajlovic, *et al.*, *Applied Physics Letters* **96**, 112501 (2010).
100. G. N. Kakazei, *et al.*, *Applied Physics Letters* **99**, 052512 (2011).
101. O. Tchernyshyov, G. Chem, *Physical Review Letters* **95**, 197204 (2005).
102. S. Savel'ev, F. Nori, *Physical Review B* **70**, 214415 (2004).
103. J. M. Shaw, M. L. Silva, T. J. and Schneider, R. D. McMichael, *Physical Review B* **79**, 184404 (2009).

104. K. Y. Guslienko, W. Scholz, R. W. Chantrell, V. Novosad, *Physical Review B* **71**, 144407 (2005).
105. K. S. Buchanan, *et al.*, *Nature Physics* **1**, 172 (2005).
106. H. Jung, *et al.*, *Scientific Reports* **1**, 1 (2011).
107. A. A. Thiele, *Physical Review Letters* **30**, 230 (1973).
108. K. Y. Guslienko, *et al.*, *Journal of Applied Physics* **91**, 8037 (2002).
109. G. M. Wysin, A. R. Völkel, *Physical Review B* **52**, 7412 (1995).
110. G. M. Wysin, W. Figueiredo, *Physical Review B* **86**, 104421 (2012).
111. A. S. Arrott, T. Templeton, B. Heinrich, A. Aharoni, *Journal Applied Physics* **50**, 2387 (1979).
112. A. S. Arrott, B. Heinrich, A. Aharoni, *IEEE Transactions on Magnetism* **15**, 1228 (1979).
113. A. Hubert, *Journal De Physique* **49**, 1895 (1988).
114. W. Scholz, *et al.*, *Journal of Magnetism and Magnetic Materials* **266**, 155 (2003).
115. K. Y. Guslienko, K. L. Metlov, *Physical Review B Rapid Communications* **63**, 100403 (R) (2001).
116. K. Y. Guslienko, V. Novosad, Y. Otani, H. Shima, K. Fukamichi, *Physical Review B* **65**, 024414 (2002).
117. K. Y. Guslienko, V. Novosad, Y. Otani, H. Shima, K. Fukamichi, *Applied Physics Letters* **78**, 3848 (2001).
118. K. L. Metlov, K. Y. Guslienko, *Journal of Magnetism and Magnetic Materials* **242**, 1015 (2002).
119. K. S. Buchanan, M. Grimsditch, F. Y. Fradin, S. D. Bader, V. Novosad, *Physical Review Letters* **99**.
120. K. Y. Guslienko, R. H. Heredero, O. Chubykalo-Fesenko, *Physical Review B* **82**, 014402 (2010).
121. F. A. Apolonio, W. A. Moura-Melo, F. P. Crisafuli, A. R. Pereira, R. L. Silva, *Journal of Applied Physics* **106**, 084320 (2009).
122. K. Y. Guslienko, A. N. Slavin, *Journal of Applied Physics* **87**, 6337 (2000).

123. D. X. Chen, E. Pardo, A. Sanchez, *Journal of Magnetism and Magnetic Materials* **306**, 135 (2006).
124. D. X. Chen, E. Pardo, A. Sanchez, *IEEE Transactions on Magnetics* **37**, 3877 (2001).
125. K. L. Metlov, *Physical Review Letters* **105**, 107201 (2010).
126. G. M. Wysin, *Journal of Physics:Condensed Matter* **22**, 376002 (2010).
127. J. Kerr, *Report of the British Association of the Advancement of Science* **5**, 85 (1876).
128. J. Kerr, *Philosophical Magazine* **3**, 321 (1877).
129. P. Weinberger, *Philosophical Magazine Letters* **88**, 897 (2008).
130. M. Parker, *Physica B* **86-88, Part 3**, 1171 (1977).
131. R. C. Gray, The Rev. John Kerr, f.r.s., Inventor of the Kerr Cell (1935).
132. P. N. Argyres, *Physical Review* **97**, 334 (1955).
133. W. H. Bragg, *Review of Modern Physics* **3**, 449 (1931).
134. A. Hubert, R. Schäfer, *Magnetic Domains: the Analysis of Magnetic Microstructures* (Springer, New York, 2000).
135. M. Freiser, A survey of magneto optic effects (1968).
136. A. Righi, *Annales de Chimie et de Physique* p. 433 (1885).
137. D. A. Allwood, G. Xiong, M. D. Cooke, R. P. Cowburn, *Journal of Physics D-Applied Physics* **36**, 2175 (2003).
138. K. W. Hipps, G. A. Crosby, *Journal of Physical Chemistry* **83**, 555 (1979).
139. J. Kranz, W. Drechsel, *Zeitschrift für Physik* **150**, 632 (1958).
140. H. J. Williams, F. G. Foster, E. A. Wood, *Physical Review* **82**, 119 (1951).
141. M. Zoladz, S. Knappmann, M. Otto, K. Röhl, T. Stobiecki, *Physica Status Solidi (a)* **189**, 791 (2002).
142. P. Möhrke, *et al.*, *Journal of Physics D: Applied Physics* **41**, 164009 (2008).
143. R. P. Cowburn, D. K. Koltsov, A. O. Adeyeye, M. E. Welland, *Applied Physics Letters* **73**, 3947 (1998).
144. W. A. Crossley, R. W. Cooper, J. L. Page, R. P. van Staple, *Physical Review* **181**, 896 (1969).

145. M. R. Freeman, R. R. Ruf, R. J. Gambino, *IEEE Transactions on Magnetics* **27**, 4840 (1991).
146. W. K. Hiebert, A. Stankiewicz, M. Freeman, *Physical Review Letters* **79**, 1134 (1997).
147. M. R. Freeman, W. K. Hiebert, A. Stankiewicz, *Journal of Applied Physics* **83**, 6217 (1998).
148. W. Hiebert, Experimental micromagnetic dynamics: Ultrafast magnetization reversal using time resolved scanning kerr effect microscopy, Ph.D. thesis, University of Alberta, Edmonton, AB (2001).
149. G. Garreau, M. Farle, E. Beaurepaire, K. Baberschke, *Physical Review B* **55**, 330 (1997).
150. C. S. Arnold, M. Dunlavy, D. Venus, *Review of Scientific Instruments* **68**, 4212 (1997).
151. W. F. Brown, *Physical Review* **130**, 1677 (1963).
152. L. Néel, *Comptes Rendus Hebdomadaires Des Séances De L'Académie Des Sciences* **228**, 664 (1949).
153. H. Shima, *et al.*, *Journal of Applied Physics* **92**, 1473 (2002).
154. H. F. Ding, A. K. Schmid, D. Q. Li, K. Y. Guslienko, S. D. Bader, *Physical Review Letters* **94**, 157202 (2005).
155. J. Li, J. Shi, S. Tehrani, *Applied Physics Letters* **79**, 3821 (2001).
156. A. Garg, *Physical Review B* **51**, 15592 (1995).
157. L. Gunther, B. Barbara, *Physical Review B* **49**, 3926 (1994).
158. M. M. Deshmukh, D. C. Ralph, M. Thomas, J. Silcox, *Applied Physics Letters* **75**, 1631 (1999).
159. M. Kolbel, *et al.*, *Nano Letters* **2**, 1339 (2002).
160. S. Pütter, N. Mikuszeit, E. Y. Vedmedenko, H. P. Oepen, *Journal of Applied Physics* **106**, 043916 (2009).
161. W. Wernsdorfer, Magnétométrie micro-squid pour l'étude de particules ferromagnétiques isolées aux échelles sub-microniques, Ph.D. thesis, Joseph Fourier University, Grenoble (1996).
162. D. Scholl, *et al.*, *Physical Review B* **43**, 13309 (1991).

163. E. Nazaretski, *et al.*, *Journal of Magnetism and Magnetic Materials* **310**, E941 (2007).
164. H. Min, R. D. McMichael, J. Miltat, M. D. Stiles, *Physical Review B* **83**, 064411 (2011).
165. D. A. Allwood, *et al.*, *Science* **296**, 2003 (2002).
166. J. H. Franken, H. J. M. Swagten, B. Koopmans, *Nature Nanotechnology* **7**, 499 (2012).
167. H. Min, R. D. McMichael, M. J. Donahue, J. Miltat, M. D. Stiles, *Physical Review Letters* **104**, 217201 (2010).
168. M. Eltschka, *et al.*, *Physical Review Letters* **105**, 056601 (2010).
169. J. Moreland, *Journal of Physics D: Applied Physics* **36**, R39 (2003).
170. J. M. Reynolds, *An Introduction to Applied and Environmental Geophysics* (Wiley-Blackwell).
171. H. N. Otis, *Review of Scientific Instruments* **4**, 681 (1933).
172. H. J. Williams, *Review of Scientific Instruments* **8**, 56 (1937).
173. C. Rossel, *et al.*, *Journal of Applied Physics* **79**, 8166 (1996).
174. P. A. Crowell, *et al.*, *Review of Scientific Instruments* **67**, 4161 (1996).
175. R. N. Kleiman, G. K. Kaminsky, J. D. Reppy, R. Pindak, D. J. Bishop, *Review of Scientific Instruments* **56**, 2088 (1985).
176. K. L. Ekinici, M. L. Roukes, *Review of Scientific Instruments* **76**, 061101 (2005).
177. K. C. Schwab, M. L. Roukes, *Physics Today* **58**, 36 (2005).
178. A. N. Cleland, *Foundations of Nanomechanics: From Solid State Theory to Device Applications* (Springer, 2003).
179. Y. Martin, H. K. Wickramasinghe, *Applied Physics Letters* **50**, 1455 (1987).
180. D. Rugar, C. S. Yannoni, J. A. Sidles, *Nature* **360**, 563 (1992).
181. D. Rugar, R. Budakian, H. J. Mamin, B. W. Chui, *Nature* **430**, 329 (2004).
182. C. L. Degen, M. Poggio, H. J. Mamin, C. T. Rettner, D. Rugar, *PNAS* **106**, 1313 (2009).
183. J. G. E. Harris, *et al.*, *Applied Physics Letters* **75**, 1140 (1999).
184. M. D. Chabot, J. Moreland, *Journal of Applied Physics* **93**, 7897 (2003).

185. M. Willemin, *et al.*, *Journal of Applied Physics* **83**, 1163 (1998).
186. X. Jander, J. Moreland, P. Kabos, *Applied Physics Letters* **78**, 2348 (2001).
187. Y. Wang, *et al.*, *Physical Review Letters* **97**, 227602 (2006).
188. T. M. Wallis, J. Moreland, P. Kabos, *Applied Physics Letters* **89**, 122502 (2006).
189. Norcada, a mems technology company (2013).
190. S. C. Masmanidis, *et al.*, *Science* **317**, 780 (2007).
191. N. Liu, *et al.*, *Nature Nanotechnology* **3**, 715 (2008).
192. M. R. Freeman, G. Nunes, *Applied Physics Letters* **63**, 1200 (1993).
193. R. P. Feynman, R. B. Leighton, M. L. Sands, *The Feynman Lectures on Physics: Volume 1* (Addison-Wesley, Reading, MA, 1963).
194. D. Antonio, H. Pastoriza, *Microelectromechanical Systems, Journal of* **18**, 1396 (2009).
195. J. Davis, J. Burgess, M. Freeman, *unpublished* (2008).
196. E. Kautto, J. Kuhalainen, M. Manninen, *Journal of Physics-Condensed Matter* **9**, 4365 (1997).
197. C. Chappert, *et al.*, *Science* **280**, 1919 (1998).
198. S. Khizroev, D. Litvinov, *Nanotechnology* **15**, R7 (2004).
199. J. Fassbender, J. McCord, *Journal of Magnetism and Magnetic Materials* **320**, 579 (2008).
200. T. Devolder, H. Bernas, *Topics in Applied Physics* **116**, 227 (2010).
201. F. Marquardt, S. M. Girvin, *Physics* **2**, 40 (2009).
202. M. Rahm, R. Höllinger, V. Umansky, D. Weiss, *Journal of Applied Physics* **95**, 6708 (2004).
203. M. Rahm, J. Stahl, W. Wegscheider, D. Weiss, *Applied Physics Letters* **85**, 1553 (2004).
204. S. Kim, *et al.*, *Nature Nanotechnology* **7**, 567 (2012).
205. S. Kasai, *et al.*, *Physical Review Letters* **101**, 237203 (2008).
206. L. Bocklage, *et al.*, *Physical Review B* **78**, 180405 (2008).
207. D.-H. Kim, *et al.*, *Journal of Applied Physics* **99**, 08H303 (2006).

208. W. Chao, J. Kim, S. Rekawa, P. Fischer, E. H. Anderson, *Opt. Express* **17**, 17669 (2009).
209. H. Jung, *et al.*, *Applied Physics Letters* **97**, 222502 (2010).
210. G. Binnig, H. Rohrer, C. Gerber, E. Weibel, *Applied Physics Letters* **40**, 178 (1982).
211. G. Binnig, H. Rohrer, C. Gerber, E. Weibel, *Physical Review Letters* **49**, 57 (1982).
212. G. Binnig, H. Rohrer, C. Gerber, E. Weibel, *Physical Review Letters* **50**, 120 (1983).
213. G. Binnig, H. Rohrer, *Reviews of Modern Physics* **71**, S324 (1999).
214. M. R. Freeman, G. Nunes, *Applied Physics Letters* **63**, 2633 (1993).
215. G. Nunes, M. R. Freeman, *Science* **262**, 1029 (1993).
216. S. Weiss, D. F. Ogletree, D. Botkin, M. Salmeron, D. S. Chemla, *Applied Physics Letters* **63**, 2567 (1993).
217. R. H. M. Groeneveld, H. van Kempen, *Applied Physics Letters* **69**, 2294 (1996).
218. G. M. Steeves, A. Y. Elezzabi, R. Teshima, R. A. Said, M. R. Freeman, *IEEE Journal of Quantum Electronics* **34**, 1415 (1998).
219. M. R. Freeman, A. Y. Elezzabi, G. M. Steeves, N. G., *Surface Science* **386**, 290 (1997).
220. G. M. Steeves, A. Y. Elezzabi, M. R. Freeman, *Applied Physics Letters* **70**, 1909 (1997).
221. G. M. Steeves, Junction mixing scanning tunneling microscopy, Ph.D. thesis, University of Alberta, Edmonton, AB (2001).
222. N. N. Khusnatdinov, T. J. Nagle, G. Nunes, *Applied Physics Letters* **77**, 4434 (2000).
223. D. A. Yarotski, A. J. Taylor, *Applied Physics Letters* **81**, 1143 (2002).
224. I. Moulton, M. Herve, Y. Pennec, *Applied Physics Letters* **98**, 233103 (2011).
225. T. L. Cocker, *et al.*, *Submitted* (2012).
226. O. Takeuchi, *et al.*, *Applied Physics Letters* **85**, 3268 (2004).
227. H. Shigekawa, O. Takeuchi, M. Aoyama, *Science and Technology of Advanced Materials* **6**, 582 (2005).
228. Y. Terada, S. Yoshida, O. Takeuchi, H. Shigekawa, *Nature Photonics* **4**, 869 (2010).
229. S. Loth, M. Etzkorn, C. P. Lutz, D. M. Eigler, A. J. Heinrich, *Science* **329**, 1628 (2010).

230. M. Julliere, *Physics Letters A* **54**, 225 (1975).
231. M. Johnson, J. Clarke, *Journal of Applied Physics* **67**, 6141 (1990).
232. R. Wiesendanger, H.-J. Güntherodt, G. Güntherodt, R. J. Gambino, R. Ruf, *Physical Review Letters* **65**, 247 (1990).
233. R. Wiesendanger, H. Güntherodt, G. Güntherodt, R. Gambino, R. Ruf, *Zeitschrift für Physik B Condensed Matter* **80**, 5 (1990).
234. R. Wiesendanger, *et al.*, *Science* **255**, 583 (1992).
235. R. Wiesendanger, *Reviews Modern Physics* **81**, 1495 (2009).
236. A. F. Otte, *et al.*, *Nature Physics* **4**, 847 (2008).
237. S. Loth, K. von Bergmann, M. Ternes, A. F. Otte, A. J. Heinrich, *Nature Physics* **6**, 340 (2010).
238. R. A. Serway, C. J. Moses, C. A. Moyer, *Modern Physics*, Saunders Golden Sunburst Series (Thomason Learning, Harcourt, ON, 1997).
239. D. J. Griffiths, *Introduction to Quantum Mechanics* (Pearson, Prentice Hall, Upper Saddle River, NJ, 2005).
240. J. Bardeen, *Physical Review Letters* **6**, 57 (1961).
241. C. J. Chen, *Introduction to Scanning Tunneling Microscopy* (Oxford University Press, New York, 1993).
242. J. Tersoff, D. R. Hamann, *Physical Review B* **31**, 805 (1985).
243. C. J. Chen, *Physical Review Letters* **65**, 448 (1990).
244. J. C. Slonczewski, *Physical Review B* **39**, 6995 (1989).
245. J. G. Simmons, *Journal of Applied Physics* **34**, 238 (1963).
246. J. G. Simmons, *Journal Applied Physics* **34**, 1793 (1963).
247. A. Sommerfeld, H. Bethe, *Elektronentheorie der Metalle* (Springer-Verlag, 1967).
248. R. Holm, *Journal of Applied Physics* **22**, 569 (1951).
249. R. H. Fowler, L. Nordheim, *Proceedings of the Royal Society of London. Series A* .
250. J. Frohn, J. F. Wolf, K. Besocke, M. Teske, *Review of Scientific Instruments* **60**, 1200 (1989).

251. G. Meyer, *Review of Scientific Instruments* **67**, 2960 (1996).
252. E. J. Lubber, B. C. Olsen, C. Ophus, V. Radmilovic, D. Mitlin, *Nanotechnology* **20**, 345703 (2009).
253. R. C. Weast, *CRC Handbook of Chemistry and Physics, 51th Edition* (CRC Press, 1970), 51st edn.
254. J. Bates, Y. Miyahara, J. A. J. Burgess, O. Iglesias-Freire, P. Grütter, *Accepted to Nanotechnology* (2013).
255. A. Kubetzka, M. Bode, O. Pietzsch, R. Wiesendanger, *Physical Review Letters* **88**, 057201 (2002).
256. G. Rodary, *et al.*, *Applied Physics Letters* **98**, 082505 (2011).
257. A. Li Bassi, *et al.*, *Applied Physics Letters* **91**, 173120 (2007).
258. A. Lucier, Preparation and characterization of tungsten tips suitable for molecular electronics studies, Ph.D. thesis, McGill University, Montréal, QC (2004).
259. A. Oreshkin, *et al.*, *JETP Letters* **94**, 58 (2011).
260. P. Nagpal, N. C. Lindquist, S. Oh, D. J. Norris, *Science* **325**, 594 (2009).
261. S. A. Werner, A. Arrott, H. Kendrick, *Physical Review* **155**, 528 (1967).
262. G. Allan, *Surface Science* **74**, 79 (1978).
263. S. Ashtekar, G. Scott, J. Lyding, M. Gruebele, *Journal of Physical Chemistry Letters* **1**, 1941 (2010).
264. S. Ashtekar, G. Scott, J. Lyding, M. Gruebele, *Physical Review Letters* **106**, 235501 (2011).
265. L. Berthier, G. Biroli, *Reviews of Modern Physics* **83**, 587 (2011).
266. R. Richert, *Physical Review Letters* **104**, 085702 (2010).
267. K. Watanabe, T. Kawasaki, H. Tanaka, *Nature Materials* **10**, 512 (2011).
268. R. Richert, *Dynamics of Nanoconfined Supercooled Liquids* (Annual Reviews, Palo Alto, 2011), vol. 62 of *Annual Review of Physical Chemistry*, p. 65.
269. A. Sepulveda, *et al.*, *Physical Review Letters* **107**, 025901 (2011).
270. H. W. Sheng, W. K. Luo, F. M. Alamgir, J. M. Bai, E. Ma, *Nature* **439**, 419 (2006).

271. G. Adam, J. H. Gibbs, *Journal of Chemical Physics* **43**, 139 (1965).
272. J. Hachenberg, *et al.*, *Applied Physics Letters* **92**, 131911 (2008).
273. M. W. Chen, *Mechanical behavior of metallic glasses: Microscopic understanding of strength and ductility* (Annual Reviews, Palo Alto, 2008), vol. 38 of *Annual Review of Materials Research*, p. 445.
274. M. A. Turchanin, P. G. Agraval, *Powder Metallurgy and Metal Ceramics* **47**, 223 (2008).
275. Y. Y. Cui, J. H. Li, Y. Dai, B. X. Liu, *Journal of Applied Physics* **108**, 063510 (2010).
276. S. G. Mayr, M. Moske, K. Samwer, *Physical Review B* **60**, 16950 (1999).
277. S. Vauth, C. Streng, S. G. Mayr, K. Samwer, *Physical Review B* **68**, 205425 (2003).
278. D. E. Burgler, *et al.*, *Physical Review B* **59**, 10895 (1999).
279. G. Duan, D. H. Xu, W. L. Johnson, *Metallurgical and Materials Transactions a-Physical Metallurgy and Materials Science* **36A**, 455 (2005).
280. D. Nečas, P. Klapetek, *Central European Journal of Physics* **10**, 181 (2012).
281. P. Klapetek, *et al.*, *Acta Physica Slovaca* **53**, 223 (2003).
282. K. I. Schiffmann, M. Fryda, G. Goerigk, R. Lauer, P. Hinze, *Fresenius Journal of Analytical Chemistry* **358**, 341 (1997).
283. J. D. Stevenson, P. G. Wolynes, *Nature Physics* **6**, 62 (2010).
284. Q. Wang, C. T. Liu, Y. Yang, Y. D. Dong, J. Lu, *Physical Review Letters* **106**, 215505 (2011).
285. J. P. Chu, Y. W. Lai, T. N. Lin, S. F. Wang, *Materials Science and Engineering a-Structural Materials Properties Microstructure and Processing* **277**, 11 (2000).
286. G. Wilde, H. Rosner, *Applied Physics Letters* **98**, 251904 (2011).
287. J. J. Kim, Y. Choi, S. Suresh, A. S. Argon, *Science* **295**, 654 (2002).
288. H. J. W. Zandvliet, W. Wulfhekel, B. L. M. Hendriksen, B. J. Hattink, B. Poelsema, *Physical Review B* **57**, 1356 (1998).
289. M. Nielinger, H. Baltruschat, *Chemphyschem* **4**, 1022 (2003).
290. O. Naaman, J. Aumentado, *Physical Review Letters* **96**, 100201 (2006).

291. J. Unguris, L. W. Bruch, E. R. Moog, M. B. Webb, *Surface Science* **109**, 522 (1981).
292. J. F. Ziegler, M. D. Ziegler, J. P. Biersack, *Nuclear Instruments and Methods in Physics Research Section B-Beam Interactions with Materials and Atoms* **268**, 1818 (2010).
293. R. E. Walkup, D. M. News, P. Avouris, *Journal of Electron Spectroscopy and Related Phenomena* **64-5**, 523 (1993).
294. X. Bouju, C. Girard, H. Tang, C. Joachim, L. Pizzagalli, *Physical Review B* **55**, 16498 (1997).
295. M. Scheinfein, A. Elizabeth, *LLG Micromagnetics Simulator Version 2.46 User Manual* (llmicro@mindspring.com, 2002).
296. K. S. Buchanan, *et al.*, *Physical Review B* **74**, 064404 (2006).
297. R. F. L. Evans, *et al.*, *Physical Review B* **85**, 014433 (2012).
298. J. R. Oppenheimer, *Physical Review* **13**, 66 (1928).
299. A. D. Gottlieb, L. Wesoloski, *Nanotechnology* **17**, 1 (2006).
300. L. D. Landau, E. M. Lifshitz, *Quantum Mechanics, Non-relativistic Theory*, Volume 3 of Course of Theoretical Physics (Pergamon Press, Oxford, 1958).

APPENDIX A

Micromagnetic Simulations

This appendix has two purposes. First, it allows the inclusion of some simulation parameters used throughout this work, but considered insignificant to the results of the simulation, and therefore left out of the main text. Second, a few issues not covered in the LLG manual (295) are discussed for the benefit of future LLG users.

A.1 LLG Software

All simulations described in this work were performed using the commercially available micromagnetic simulation package, LLG Micromagnetics Simulator v2.56d by M. Scheinfein. The software is quite capable, with a wide variety of simulation methods. It is, however a quirky program with a number of idiosyncrasies as well as an occasionally challenging black-box nature. Particularly in cases where the manual for the program is incomplete, great care must be taken to ensure that simulations are physically reasonable, and meaningful.

The software is based on a finite difference formulation of the LLG equation. Effectively, one can think of the discrete site based sums for exchange energy etc. as described in the introduction, but applied to giant spins distributed over the simulation grid. Computation of the various energies and evolution according to the LLG equation may be performed using a forward time integration. Other modes of solution, based on energy minimization, are available, however these typically fail for experimentally pertinent simulation sizes.

Two types of simulation were performed in this work. Quasi-static simulations, run with artificially high damping, were used to compute hysteresis loops. Realistic damping was used to compute dynamics.

A.2 Quasi-Static Simulations

Field sweeps on laboratory time scales involve, often, sweep rates on the order of 150 A/m per second (or 1.5×10^{-7} A/m per ns). For the time scales of dynamical effects (ps to ns), the sweeps are effectively quasi-static. This is problematic for simulations as integration steps must be performed, usually, on ps time scales making sweep based simulation impractical. An alternative approach, is to assume the quasi-static nature of the sweep means that dynamics will play no significant role in the simulated hysteresis. Under this assumption, if a very large (~ 1) damping factor is used, dynamics will be almost completely suppressed. Instead, time integration through the LLG equation will function as a critically, or over damped steepest decent search for the minimum energy for any given simulation. This permits reasonable integration times while avoiding excitation of physically unreasonable dynamics.

Quasi-static field sweeps are accomplished by setting series of mini simulations at incremented (or decremented) field steps. Each field step is initialized from the previous state, and then integrated for either a set number of iterations, or until a convergence parameter is satisfied.

A.2.1 Typical Simulation Parameters

For each individual simulation, dimensions and saturation magnetization varied. These parameters are stated where simulation results are presented within this work. Other parameters remained fixed from simulation to simulation. Most notably, simulations were run using a second order integrator, reducing the computation cost of directional derivatives taken over the grid, and speeding up integration, and were run with a high damping factor always set equal to 1. Temperature was set to zero for quasi-static simulations.

A.2.2 Grid

Grid sizes were typically chosen to be 5×5 nm in x and y , with a single layer over the thickness of the disk. Variations in grid size were made in a few isolated circumstances. Typically, for quasistatic vortex behaviour, grid sizes of 5×5 nm are considered adequately fine (89, 164, 296). For very large elements (eg. $3.6 \mu\text{m}$ diameter disks), grid sizes of 10×10 nm were used in order to circumvent the memory limitation imposed by the LLG software (2 GB). Additionally, for pinning simulations cross-checking simulations using 2.5×2.5 nm grids were run in order to check for grid size effects. Most notably, it was considered

possible that core distortions would not be adequately resolved on the larger grid, and play a significant role in the pinning process. No significant effects were found.

Technically, LLG is capable of a grid coarseness correction. This interpolates the square edges of the simulation grid to be terminated in diagonals across the empty grid spaces. However, enabling this ubiquitously lead to bizzare integration errors including alpha numeric energies. This is regrettable, as the option can be critical to realistic simulations of smooth edged disks.

A.2.3 Consequences of Over-Damping

One disadvantage of the high damping approach to quasi-static field sweeps is the possibility of trapping the simulation in a local minimum energy state, preventing the simulation from actually reaching the real ground state. This is particularly evident in simulations aiming to recreate the vortex state via a sweep down from high field. Commonly, on large disk sizes, $\sim 1.5 \mu\text{m}$ or larger depending on film thickness, simulations may ‘freeze’ in a buckled state, failing to nucleate a vortex. This is, in a sense, similar to super-cooling of a transition. Pathways between buckled states and vortex nucleation depend on the defects at the disk edge where buckling patterns have domain-wall like features intersecting the boundary. The quasi-static sweep down enforced by use of a high damping constant is equivalent to a very fast (often equivalent to 15 A/m per ns) sweep down of the field with an artificial suppression of dynamical effects. The suppression of dynamics is realistic, as in real world hysteresis loops the field is swept on a time scale where all field induced dynamics would be damped out or barely present due to the slow (quasi-static) field sweep. However, high damping also serves to suppress thermal dynamics. Thermal dynamics are included as spin waves (295), or rather fluctuations, randomly excited on the grid. Thus they are directly, and immediately, impacted by the damping factor. This pseudo-elimination of thermal effects, combined with the limited integration time for each field step (ie the fast field sweep) serve to remove the thermally activated pathways for transitions from buckled states to vortex states.

A.2.4 Convergence

One strategy that can mitigate the impact of thermal dynamics suppression is to run simulations with a low convergence factor. The convergence factor is a parameter that will indicate that the simulation is fully converged, and no further changes will take place. In field sweeps, the convergence parameter can be used to determine when to switch from one field step to the next. At each simulation iteration, the value of the convergence parameter is compared to the value of the change in the angle of the direction cosines of the magnetization

for each cell computed by the simulation for the next field step. Guidelines suggest a convergence parameter of 1×10^{-4} (295). However, in practice 1×10^{-7} were generally found to be adequate, and values as low as 1×10^{-9} were used when integration time was not an issue.

Setting a low convergence helps to compensate for the lack of thermal excitations, in accessing path ways to lower energy states that feature no or very low energy barriers. It cannot, however, make up for the ability for thermal dynamics to access states with large energy barriers. Low convergence also helps to avoid field steps that, at default convergence values, would be detected as completely converged on the first iteration, despite having a changed applied field.

A.3 Dynamics

Dynamics simulations are, in some ways, more straight forward to describe. In general, the approach to dynamics outlined in the manual is successful. Dynamical simulations were undertaken with similar parameters (grid sizes etc.) to the quasi-static simulation. Large grid sizes (> 5 nm) were avoided except in cases where simulation was impossible due to memory constraints. Otherwise simulations were performed using a 4th order integrator and a low damping factor (0.0005 to 0.002).

A.3.1 Thermal Stretching

In a limited set of dynamic simulations, an unexpected effect, where an easily identified oscillation (eg. the gyrotropic mode) showed a period stretch over time. The cause of this effect is unconfirmed at this time. Suggestions include an integration error, or time step error in the simulation. However, simulations featuring this effect commonly included temperature dynamics. In particular, the first noted occurrence of this effect was found by initializing with a zero temperature starting state into a dynamical simulation with temperature turned on (~ 300 K). Suggesting the slowing of dynamics is a representation of rapid thermalization within the magnetic film itself, accurately accounted for by the program, is conjecture at this point. A thorough investigation would need to be undertaken to confirm this.

APPENDIX B

Electron Beam Evaporator

Depositions of permalloy films used in this project were all performed using a modified electron beam evaporator. The deposition system was specifically designed for the production of very smooth, very clean films, and to interface with the vacuum suitcase for sample transfer to the STM.

The evaporator is a modified Omicron EFM3 UHV electron beam gun. It is designed to provide a narrow collimated beam of evaporant with slow deposition rates. The design of the instrument is a simple collinear arrangement of a ring filament and a rod of evaporant material that is clamped in place and charged with a positive voltage. Heating the filament in vacuum results in thermionic emission of electrons, which are then accelerated towards the rod, preferentially heating the end, and allowing for evaporation. Evaporant then escapes from the inner chamber, passing back through the filament centre and through a tube which provides a collimated beam with approximately 1.8° divergence. For shadow masking, this is highly advantageous, reducing the possibility of enlarged features due to a large mask/substrate gap. By contrast, sputtering films can lead to evaporant being driven underneath the mask creating a continuous film that simply has bumps instead of defined features.

A particular detail of this design, in the context of permalloy (and many other materials), is the fact that the evaporated Ni and Fe atoms will carry a positive charge, and thus be accelerated away from the rod. This makes the design more efficient, but it also means that evaporant molecules will be accelerated towards the sample. As a result, resputtering of material is expected at the growth surface. This is a complex scenario and full understanding of the effects of accelerated deposition were not performed in this work. It is conjectured that the resputtering is a contributing factor to the high degree of smoothness found in films produced by this evaporator. Additionally, the resputtering process may create voids, or

reduce the overall film density leading to a suppressed saturation magnetization.

The gun is mounted on a large UHV chamber (Kurt J. Lesker Rapid Sample Transfer Station aka "The Rapi") that maintains a base pressure of 4×10^{-11} mbar. The base pressure can degrade over time, particularly when depositing on thermally sensitive samples which are not baked in the load lock. This leads to deposition base pressures usually ranging between 1×10^{-10} mbar and 1×10^{-9} mbar. During deposition, the deposition pressures typically range between 4×10^{-10} mbar and 1×10^{-9} mbar.

The evaporator uses a flux collection based method for calibration of deposition rate. In the end of the deposition unit, an electrode collects the flux due to the, in general, positively charged atoms of evaporant incident on the electrode. This gives a rough measurement of the rate of evaporation. This method of thickness monitoring is notoriously unreliable. Electrons emitted from the filament can be collected on the flux electrode or neutralize evaporant atoms. Stray deposition within the gun can also mask the measured flux, changing the calibration over time. Regular maintenance of the gun, cleaning evaporant out of the evaporation chamber whenever the filament is replaced, is important. Scraping the barrel clean with clean tools is usually sufficient. When the calibration fails, it can be impossible to detect until the sample is inspected. The most common, preventable cause of calibration error is incorrect placement of the evaporant rod with respect to the filament. If the rod is too far extended, and actually intersecting the plane of the filament, the rod will evaporate from its sides, resulting in a preferential deposition to the inside of the e-gun, rather than out of the nozzle.

In using the e-gun, some confidence is needed in controlling the position of the rod. Typically the rod moves down very slightly during the deposition. However, occasionally, the flux drops precipitously requiring a large shift in the rod position. This is conjectured to coincide with the complete melting of the end of the rod, which results in the formation of a bulb, and consequent shortening of the rod. Tracking the deposition and deciding how to move the rod is best accomplished by monitoring the emission current (current between filament and evaporant rod). Maintaining a constant filament current, and constant emission current will provide a good control of the flux. After a fresh filament is installed, and a fresh rod of evaporant, the required filament current and emission current will rise over time. This is caused by the bulbous rod and aging of the filament. For consistent operation, careful records of the required emission and filament current necessary to maintain flux must be maintained to provide good starting points for each subsequent deposition.

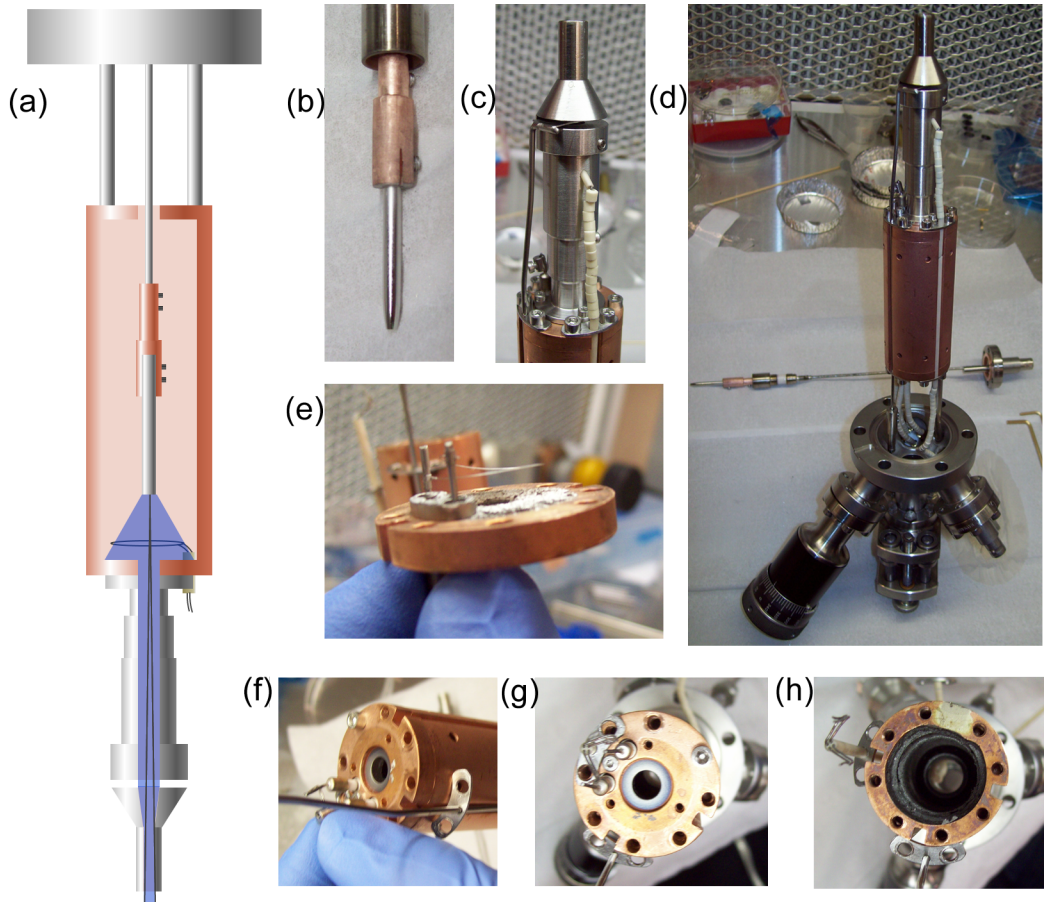


Figure B.1: The evaporator is a colinear design. A cut away schematic of the e-gun shows the rod of evaporant clamped to its support (a). Below a filament provides a source of electrons that are accelerated towards the charged rod. The long barrel of the gun provides tight collimation. The evaporant in its holder (b). The collimating nozzle (c) featuring the rotatable shutter. The filament is mounted on fragile ceramic feedthroughs passing through a copper plate (e). Replacement of the filament requires spotwelding to these supports. Panels (f) to (h) depict the removal of the filament plate, which allows access to the barrel of the e-gun for cleaning.

APPENDIX C

Shadow Mask Fabrication

Four types of shadow masks were used in this project, two custom developed, and two commercial. Fundamentally each one shared the same basic design of a frame supporting a membrane with patterned holes in it. The two commercial types of masks were patterned silicon nitride membranes mounted on square silicon frames (Dura SiN DTM-25233, and Dura SiN DTM-25232), and carbon films supported on copper grids (EMS CF-1/1-2C).

C.1 EBL Shadow Masks

Significant effort was directed towards fabricating shadow masks using electron beam lithography as a patterning tool for silicon nitride membranes. Key challenges in this endeavor included: spinning resist uniformly onto small chips, performing lithography on an insulating substrate, and most critically, developing an etch which preferentially removed silicon nitride over the resist. A specialized chuck was constructed to allow membranes to sit off centre from the axis of rotation of the resist spinner, nested in a square corner machined so that the edge of the corner is the same height as the mask. This, in a sense, extends the surface of the chip, improving resist spinning quality. The electron beam lithography itself followed a standard recipe for silicon and PMMA resist, and was the least challenging aspect of mask production. Developing the etch was exceedingly challenging. An alternative chemistry etch, employing CHF_3 , as opposed to the usual CF_4 etch that is standard for nitride, was used. This etch proved to be slow, and, while it made mask production possible, the membranes were often extensively thinned, and extremely fragile.

All fabrication was performed in the University of Alberta Nanofab. The Raith 150 EBL unit, the Headway resist spinner, the Trion Reactive Ion etch Unit, and the Micro Etch *Betty*

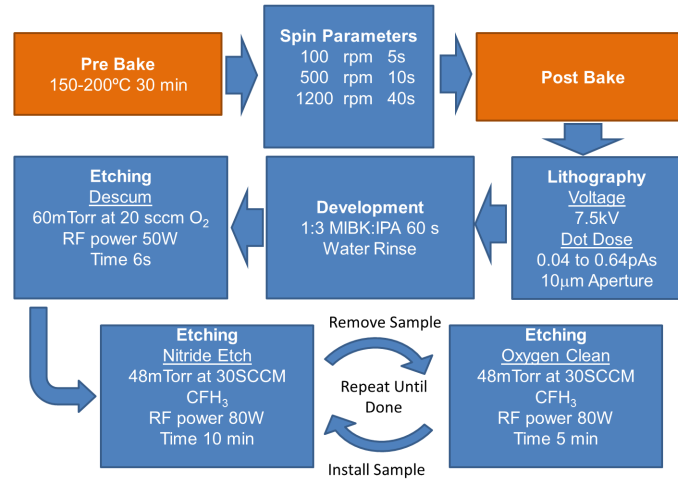


Figure C.1: The process flow is a complicated set of procedures. Specific parameters for the University of Alberta Nanofab equipment are included. SCCM stands for standard cubic cm per minute.

were used. Fabrication starts with a clean membrane. Following the process flow in figure C.1, resist is spun on at low speeds using the specialized off centre chuck. Usually two drops of PMMA 495 A2 or PMMA 950 A2 is an adequate amount of resist. Masks tend to fly off of the chuck. This may be remedied by having a thin film of residue resist dropped into the corner of the chuck. Following this, the resist is baked. For bilayer resist, after the bake the next layer may be spun on and followed by another bake. Lithography and development then proceeds by using standard silicon parameters for the use of PMMA. Though it will remove some resist in unexposed areas, a descum step can help to ensure that any hard baked resist left in the exposed areas following development is removed entirely. The last step is a long, iterative etch. Up to 10 minute long bursts of etching may be executed using the CHF_3 etch. During this time, the DC bias applied to accelerate the etching plasma will drop significantly due to the formation of a poorly characterized polymer coating. A 5 to 10 minute oxygen clean (with the sample removed) restores the electrodes. The cycle of etching and cleaning should be pursued until the sample is ready, or destroyed. Often this takes 50 to 80 minutes of total etching time. When the etch is complete, a 10 minute clean should always be run out of consideration for the next user.

Produced masks were successfully used. Due to the etching process, holes tended to be somewhat rough and only approximately circular. Additionally, though the CHF_3 etch improved on the standard etch, providing a selectivity of nitride over PMMA of 3:1 for bare SiN and PMMA, small patterned features tended not to etch as fast. Completed windows tended to have no PMMA remaining, and to have been thinned, making the windows fragile.

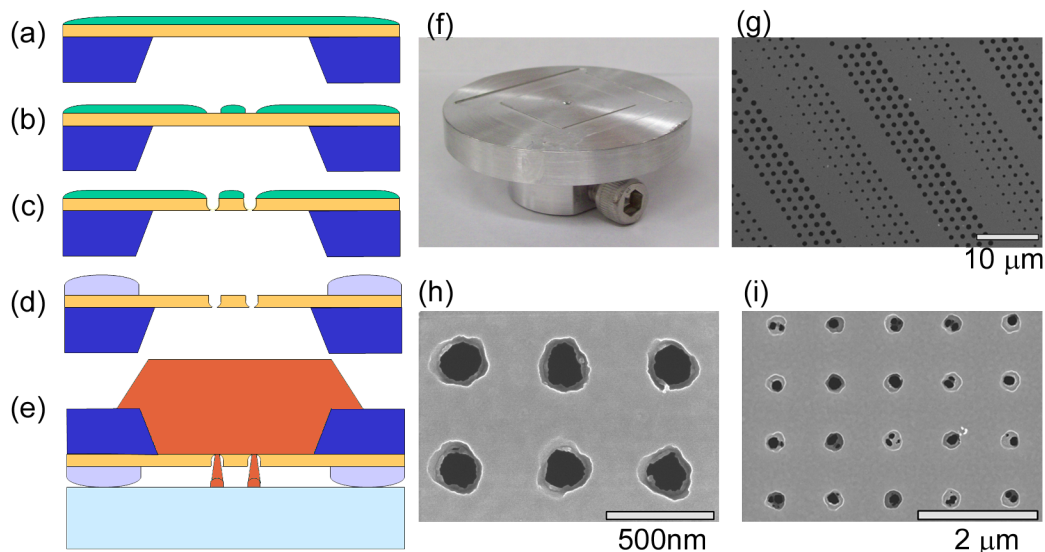


Figure C.2: Shadow masks were successfully fabricated using electron beam lithography. Resist was spun, patterned, developed, etched, on some masks aluminum spacers were deposited, and finally the masks were used to fabricate samples (a) to (e). A specialized spinning chuck was devised to allow small samples to sit nested in a corner for more effective resist spinning (f). Large area patterning was possible, and did not require prohibitively long electron beam exposures (g). However, holes in the etched windows tended to be rough edged, (h) and or, for small holes, not entirely etched (i). The inconsistency of the process and fragility of the resulting windows resulted in moving to alternative mask types.

Exploratory work was performed using different resists, however no success was forthcoming before the project shifted to the use of FIB produced shadow masks.

C.2 FIB Shadow Masks

To prepare a large scale shadow mask for deposition of permalloy elements *in situ* onto an STM transmission line substrate, a Focused Ion Beam (FIB) mill was used. This is the same instrument as was used to prepare the torsional paddles on silicon nitride membranes: a Zeiss NVision 40 dual column Focused Ion Beam mill. The mill was used to write large ($\sim 1,000,000$) arrays of point exposures. To ensure that this process did not use up time during the usual work day of the FIB, the exposures were done over night. This proved to be a technical challenge, due to drift of the patterning stage over night. However drift is not so much of an issue when the goal is simply to have an enormous number of dots.

Small errors in spacing, or occasional overlap of dots are acceptable. The point exposures were performed using a beam current of 300 pA and accelerating voltage of 30 kV with dwell times of 200 ms for dot exposures to result in holes in the membrane with a diameter of approximately 400 nm.

The membrane used was a $500 \times 500 \mu\text{m}$, 100 nm thick silicon nitride membrane on a $5 \times 5 \text{ mm}$, $200 \mu\text{m}$ thick silicon frame (189) designed as an X-ray substrate. Prior to exposure it was coated with a thin gold coating to prevent charging.

Following deposition using the FIB prepared mask, TEM inspection was performed on it. The mask showed signs of film structure change near the holes. This structure change has recently found to be correlated with a suppression of magnetization in the deposited permalloy film (254). Therefore, this method of mask production was abandoned in favour of commercial masks. The convenience and low cost of commercial masks outweighed the lack of flexibility offered in the different hole densities available.

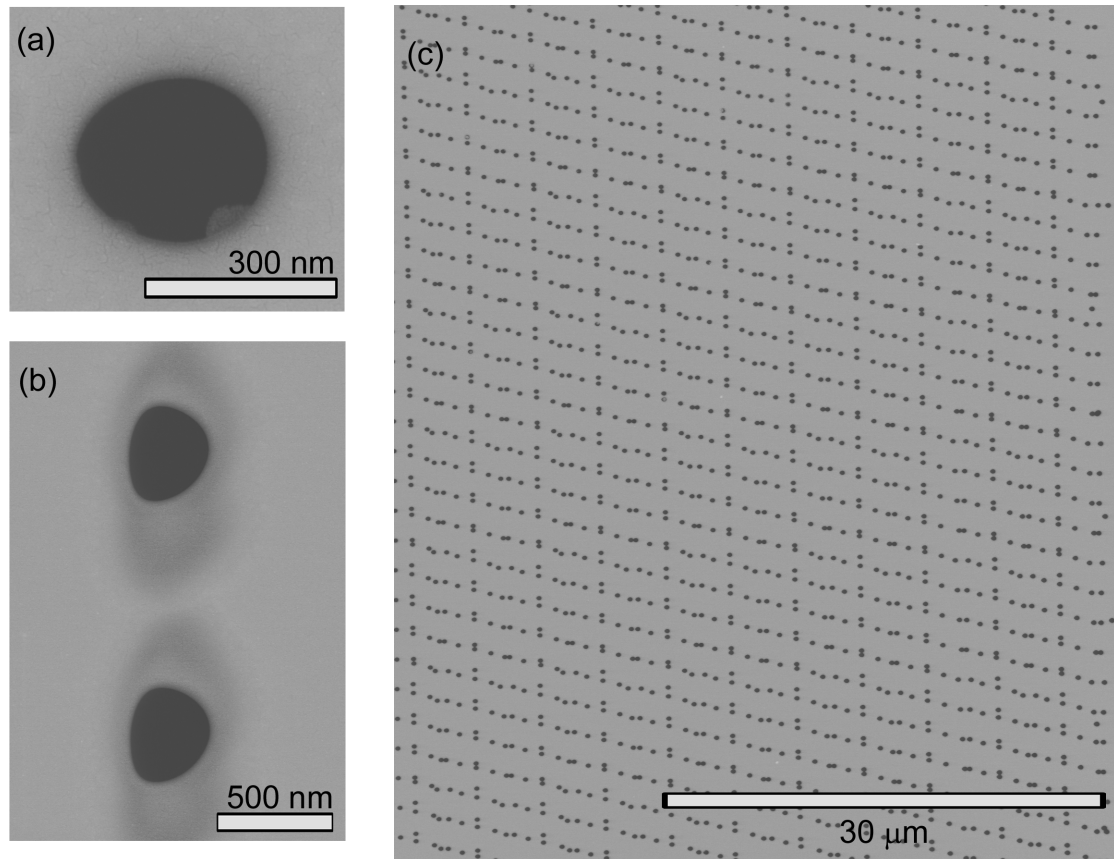


Figure C.3: Images of the FIB fabricated shadow mask. The pattern was exposed in multiple sessions over $100\ \mu\text{m}$ square regions. Typical hole size was found to be 400 nm in diameter. After use with a permalloy deposition, change in film structure is visible near the holes punctured in membrane. This likely indicates influence of the electric field of the implanted ions in the membrane on the permalloy growth.

APPENDIX D

Shadow Mask Deposition

Shadow masking (*158*) is an excellent technique for the production of low volume research or prototype samples. It provides a method of cleanly patterning films (Fig. D.1). No resist is used and a variety of sensitive samples can be used as substrates by creating a spacing between the mask and sample. Shadow masks are not without drawback, however. Principally, it is challenging to align two chips precisely, and it can be quite challenging to keep two chips together securely, or to remove the mask without damaging the sample. Geometrical considerations also lend a unique shape to the shadow masked samples, and make depositions sensitive to the gap between mask and substrate.

In resist based techniques like lift-off, resist is in contact with the sample, or for bilayer techniques, suspended above the sample by the thickness of the lower layer of resist ($\sim 100 - 2000$ nm). This makes effects from the angular dispersion of the arriving evaporant immaterial, or, often leading to rounded edges on the sample. By contrast shadow masks may feature gaps on the scale of multiple microns, or even more depending on what is used to space the mask above the sample. Effectively, it is inevitable that some dust, or scraps of chipped silicon wafer will provide a 'natural' and possibly unwanted spacer. In cases where this is detrimental, mask mounting should be done in a clean room. Bits of dust can be enormous, on the scale of 25 or more μm . A large gap such as this can result in a significant enlargement of the deposited pattern.

For a finite source, consider evaporant being emitted isotropically from a large number of point sources. Considering the point sources at the edges of the finite source, and considering a distant hole in a mask, with a substrate some distance below it, this leads to a geometry where not all of the source has line of site to the deposited feature on the substrate. This leads to an edge region that receives less evaporant (Fig. D.2). This, coupled with a gradual

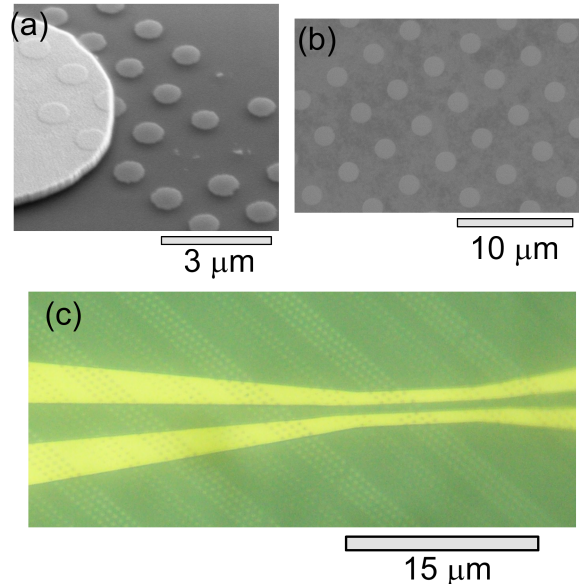


Figure D.1: Figures (a) and (c) show the results of custom EBL fabricated shadow masks. Panel (a) shows a deposition of permalloy disks near a large gold alignment mark. Panel (c) is an optical micrograph of disks deposited onto a coplanar transmission line sample. Panel (b) shows TR-STM sample number 2, which had $2\ \mu\text{m}$ diameter disks deposited onto a CuHf transmission line using a commercial mask.

clogging of the holes during deposition, leads to an approximate linear profile to the edge of the sample dependent on the gap, and clogging rate (159).

Challenges in manipulating shadow masks safely can be overcome with some fore thought and effort. Manipulation using vacuum tweezers is very effective, particularly when the vacuum tweezers are mounted on a three axis stage. This eliminates shakes and errors that go along with manual handling. This style of manipulator has been named a Batesian shadow masking manipulator after J. Bates from McGill University.

Simply moving masks around with the vacuum tweezers allow for much safer, and more precise manipulation. This is very important for expensive masks, such as those that have been patterned by extensive FIB work. However, the real power in the technique is enabling precise alignment of mask and sample. Under a microscope, with a great deal of persistence, patience, and at least some luck, it is possible to attain alignments on the micron scale. The Batesian style manipulator constructed in this work incorporated a three axis micrometer stage, and a rotational stage (Fig. D.3). The rotational stage was challenging to use as it is quite difficult to centre the sample on the sub-mm scale. Under a good microscope¹,

¹Thank you to Mark Salomons and the Wolkow lab for use of their long working distance microscope.

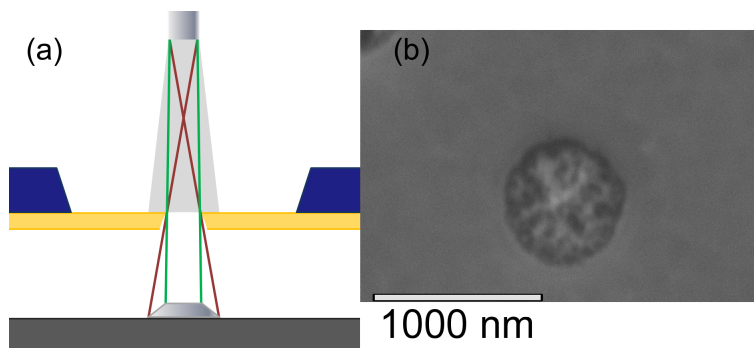


Figure D.2: Finite size, and line-of-sight contribute to the potentially large sloped edge, and overall enlargement, of shadow masked dots (a). Clogging also provides a reduction in the deposition area with time, contributing to the slope. A completely clogged hole is shown in (b).

alignment of shadow masks to prefabricated torsional paddles on silicon chips was possible. Targeting a single device, alignment of $4\ \mu\text{m}$ accuracy was relatively easy. Taking rotation into account, multiple device could be aligned, however, not perfectly. The yield would be approximately 10% for $2\ \mu\text{m}$ deposited onto $6\ \mu\text{m}$ paddles. Further improvements to the manipulator, including two point vacuum contacts, and a more easily centred rotation stage would significantly improve this process.

The best approach to alignment of the mask is to align approximately, drop the mask until it is almost touching, realign, then bring the mask into firm contact. As the mask is brought into contact, it will slide, disrupting the alignment. Repeating this, and attempting to predict the slide can provide remarkable results. It can also ruin a sample easily. A gap must be ensured to prevent scratches destroying the sample as the mask slides. In the case where samples are plentiful, it may be permissible to rely on luck and dust. However in other cases, it is likely worth while to sprinkle silica particles (or some other uniform sized particle) on the surface to provide random spacing, or to deposit feet onto the mask. Practice using sacrificial chips with easily identifiable features is strongly advised prior to any alignment attempt.

Once the mask is firmly in contact, it must be clamped, and the tweezers released. This must be done with purely vertical motion. The very tip of a beryllium copper clip works well for this purpose. Using a screw to tighten the clip down tends to result in a rotational shift of the clip, usually pushing any clamped mask. Therefore it is best to either lower pre-tensioned clips with set screws that hold individual tines of a clip up, or to use a second clip off to the side, to push the tines of the first clip down. A generic shadow masking holder was built with a wide distribution of tapped holes for this purpose.

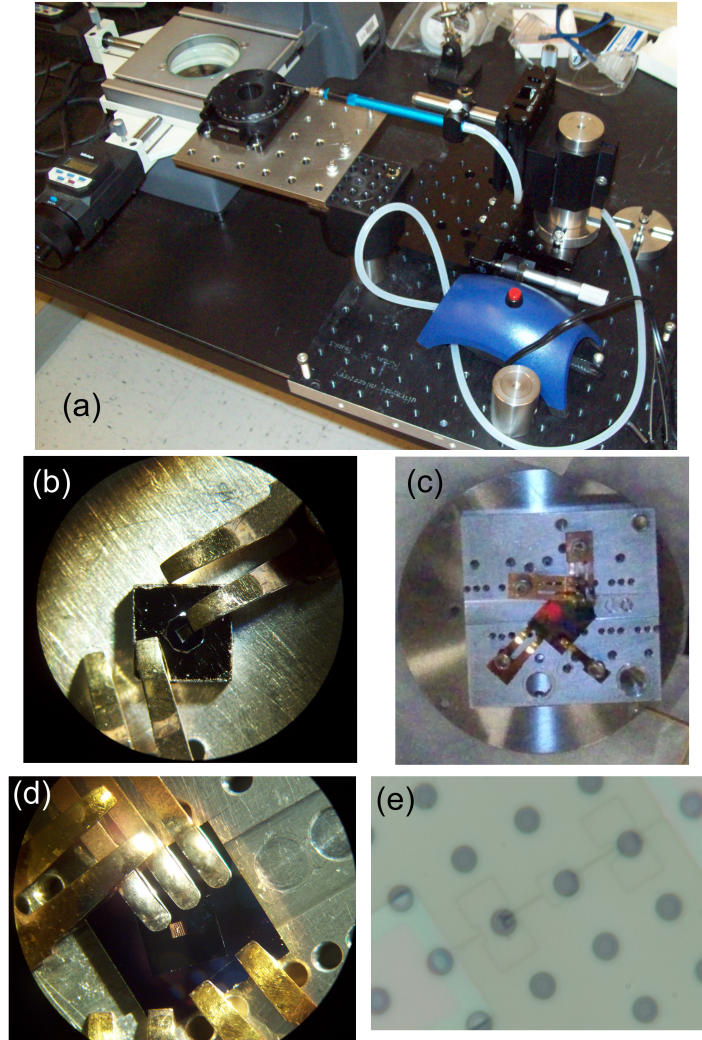


Figure D.3: The bulk manipulator is made of typical mechanical optics components mounted on a bread board (a). The very tip of a beryllium copper clip turned upside down makes an excellent point contact (b). A simple slab holder with a variety of tapped holes, 2-56 for fine lifting set screws, and 4-40 for larger clamping screws allows flexible general use mask mounting (c). Lifting or compressing the clips that actually hold the mask down using a second set of adjacent clips reduces rotational motion of the clamping mask (c) and (d). Excellent alignment can be obtained. Shown in (e), a mask with $2\ \mu\text{m}$ diameter holes is aligned to a fabricated NEMS device.

APPENDIX E

Vortex Creation¹

Concurrently with the experiment measuring annihilation of vortices described in Chapter 3, another experiment was performed measuring creation. This experiment is included in an appendix because, while it is related to this body of work, and should be discussed for completeness, it is not considered a core component of this thesis.

The experiment was performed on a single magnetic disk $1\ \mu\text{m}$ in diameter and $42\ \text{nm}$ thick mounted on a torsional resonator identical to the one described in Chapter 4. The paddle device measured was actually the same device used to acquire data in Chapter 4. The torsional magnetometer apparatus was an older design featuring a much larger vacuum chamber with better vacuum pressure ($\sim 10^{-9}\ \text{mbar}$), but having no temperature control. Bias fields were applied with the same permanent magnet mounted on rail configuration as used for Chapter 3 and Chapter 4. The interferometer apparatus was made with the same components as in Chapter 4, but mounted in a slightly different configuration to accommodate the different chamber design.

Primarily the experiment was designed to be a statistical investigation of the creation and annihilation process. In particular, with a single disk, the focus was on the creation process which cannot be studied in an array. The trade off of the single disk approach is that in order to study a statistically significant number of annihilations, a large number of measurements must be made compared to single measurements made on an array. Annihilation for the single disk was found to vary very little, with a decay distribution width (approximated as a Gaussian) of $80\ \text{kA/m}$ and a weak dependence on sweep rate (Fig. E.1 a). By contrast, creation events were found to vary wildly based on sweep rate with some sweep rates yielding tight distributions similar to the annihilation distribution, and other sweep rates yielding

¹This appendix describes work carried out in reference (73), related to, but not considered part of this thesis work.

multiple distribution peaks and sporadic events not correlated with any strong distribution (Fig. E.1 b). The dependence of the creation process on the sweep rate was interpreted as supercooling of a phase transition, as predicted by Nori (102).

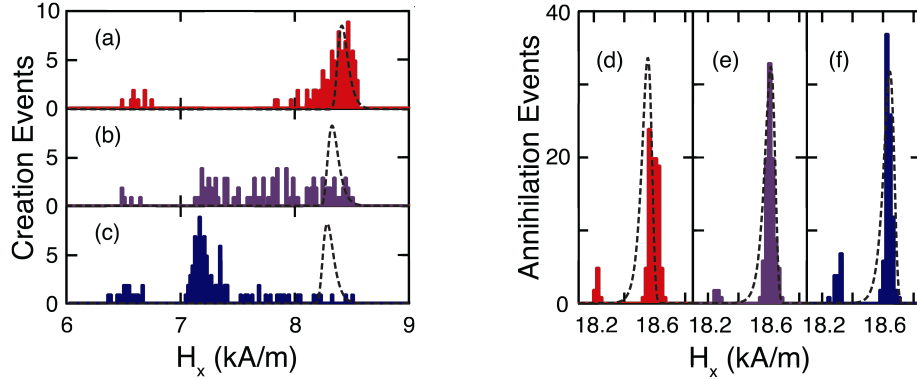


Figure E.1: Creation and annihilation statistics vary greatly in qualitative behaviour with sweep rate. Annihilation fields maintain a tight distribution with a weak dependence on sweep rate (d-f), consistent with a thermally activated model. Small secondary distributions indicate annihilations of vortices of the opposite chirality. By contrast creation field distributions (a-c) vary widely in shape with sweep rate. Some sweep rates yield tight distributions, similar, to the annihilation distributions. Other sweep rates feature broad distributions of vortex creation events with no discernible pattern. The distributions in red, purple and blue were taken for a sweep rates of 20 A/m per second, 140 A/m per second, and 430 A/m per second respectively. This figure is adapted from reference (73) with permission.

Upon rotation of the magnetic field the sweep rate dependence of the creation events could be completely suppressed, while the annihilation distribution could be shifted slightly. Rotations as small as 0.5 degrees, subtending an arc length of 4 nm at the disk edge, were found to have a significant effect. This indicates that the grain structure (~ 5 nm in width) is strongly correlated with the creation and annihilation process. This corroborates earlier work, noting the necessity of inclusion of disk roughness in simulations of annihilation and creation in much smaller disks (70). For annihilation, this fits well with the observed statistics. Using the decay model discussed in Chapter 3, the data was fit well with a decay parameter of $3/2$, indicating a depinning process. Certainly the last pinning site the vortex core interacted with prior to annihilation would influence the apparent energy barrier, and therefore, the annihilation field. Applying this logic to the creation process is more speculative. In simulation, commonly in micron scale disks, a vortex annihilating in a disk generates two edge defects. These defects have field dependent positions at the edge of the disk (See Fig. 2.4 in Chapter 2), and propagate along the edge of the disk as field changes. When the vortex is recreated, it is typically through a process where multiple vortices are generated

from these defects. Often there are preceding buckled states (See Fig. 2.4 in Chapter 2). It is quite reasonable to speculate that the influence of the grains or other edge structure in the disk will affect the supercooling discussed by Nori (102). As the defects shift along the edge of the disk, the sweep rate dictates how long the magnetic defects reside at different points along the edge of the disk. Magnetodynamically, the sweep rate is adiabatically slow, but for thermal dynamics this experiment, as well as the one in Chapter 3 (and previous work (70)), show that laboratory time scale effects are very important. Ergo, the sweep rate can change the probability of the nucleation of a buckled state for the defects existing at various locations along the edge of the disk. Variable sweep rates could affect the probability of accessing different buckled states, and therefore nucleation pathways. Similarly, changing the direction of the field changes what sections of the disk perimeter the magnetic defects traverse. A section that has a very strong nucleation point will result in variability being killed, and collapse of creation to a single distribution (a sort of depinning of a virtual vortex in some sense). Note that only one defect needs a strong nucleation point, once a vortex or portion of a buckled state is nucleated on one side of the disk, the energetic balance of the other side is inevitably changed, eliminating the other defect, or inducing additional nucleation from it. All together, the picture of sweep rate, film structure at the disk edge, and thermal dynamics provides an explanation for the variability.

The speculation above is compelling, however to substantiate it would require extensive low damping, dynamics capable simulations of adiabatically slow field sweeps. This is not possible with LLG simulations ². Experimentally, it would be ideal to look at the temperature and sweep rate dependence of the creation process simultaneously, as was done for annihilation in Chapter 3. This would allow resolution of the thermal dynamics speculated to be participating in the details of the supercooling process. However, the temperature controlled apparatus described in Chapter 4 was too unstable for extended sets of experiments (~1000s of data runs).

One other notable effect was found in this experiment. The first hints of disorder potential were visible in this experiment, and indicated that the device being studied nucleated the same chirality of vortex 92% of the time, and the opposite chirality only 8% of the time. This is easily visualized by looking at the annihilation distribution. The less common chirality gives a smaller, distinct peak.

²It may be possible with LLB (Landau Lifshitz Bloch) (297) simulations which may account for thermal dynamics on long time scales.

APPENDIX F

Torsional Paddle Fabrication

The torsional paddles used in this experiment were fabricated in a four step process from silicon nitride membranes with deposited permalloy disks (Fig. F.1). The process is designed with the idea of creating very clean, uncontaminated samples on a easy to handle substrate with minimal fabrication steps. The first step is to make a shadow mask that will define the magnetic elements. This can be done a variety of ways including electron beam lithograph, focused ion beam milling, or optical lithography. See Appendix C for an overview of the three approaches to making shadow masks. If a suitable hole size, shape, and spacing are available, the most efficient way to make a shadow mask is to purchase a TEM grid which has a holey membrane. The second step is to prepare a clean silicon nitride membrane chip. These chips are commercially available as either TEM sample substrate, or X-ray sample substrates. The two chips are clamped together such that the mask and membrane are in close contact. The next step is to deposit the magnetic film through the holes onto the membrane. See Appendix B for details on electron beam deposition, and Appendix D for the shadow masking procedure . The last step is to fabricate the torsional device using a Focused Ion Beam (FIB) mill. Prior to milling, it is helpful to put an anti-charging layer (< 10 nm of Au) on the opposite side of the membrane to reduce distortions in the exposure due to charging. A dual column FIB, one that is equipped with an SEM, provides the advantage of imaging and registering the pattern to the magnetic elements without using the FIB beam, preventing excess Ga ion implantation. Additionally, the exposure should be performed on the opposite side of the membrane from the magnetic elements. This means that the magnetic material is protected from the Ga ions by the membrane, preventing any damage from the Gaussian tails of the beam or mishaps. Simulations demonstrate that 100 nm of silicon nitride provides excellent shielding for the permalloy (Fig. F.2) even for, brief, direct exposure through the membrane.

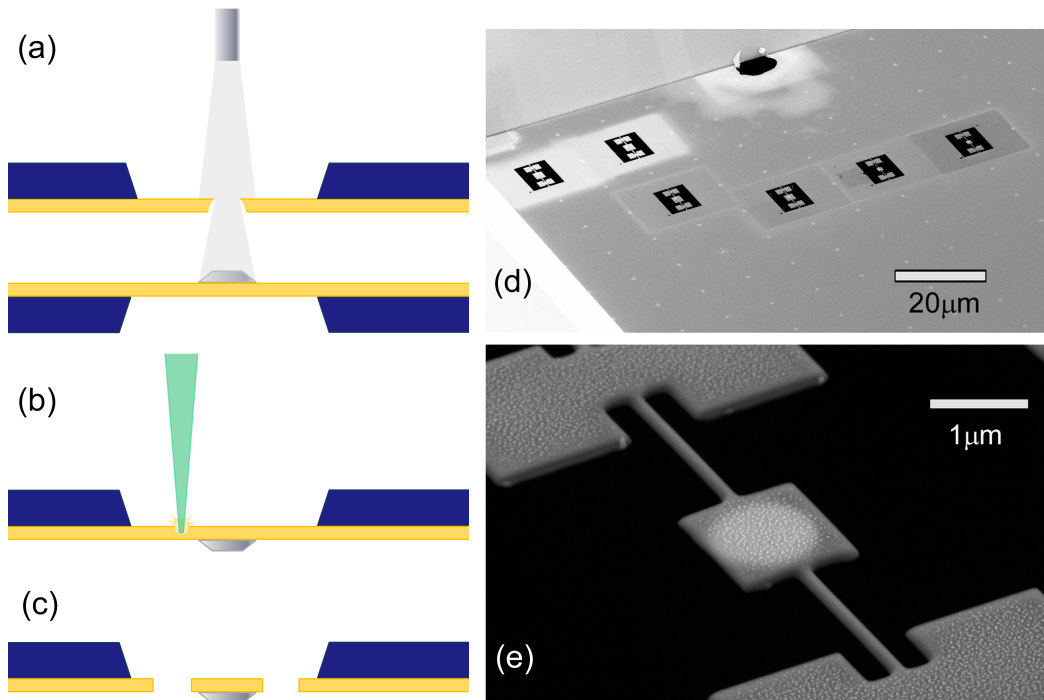


Figure F.1: Magnetic elements are fabricated on the membrane by shadow mask deposition, or by other means. Subsequently, the membrane is flipped, and the backside is coated with a metallic anti-charging layer (here chrome-gold). Following this, the focused ion beam is used to cut out the shapes of paddles by rastering the beam (b). This leaves devices largely separated from the membrane complete with magnetic elements (c). An array of paddles fabricated around dots (d). A zoomed in view of a successful device. (Figures d and e courtesy of D. Vick and J. Davis.)

Specifically, for the fabrication of this device a Zeiss NVision 40 dual column Focused Ion Beam mill was used with a beam current of 150 pA and accelerating voltage of 30 kV. Based on estimates from exposures, the beam is approximately 30 nm wide (estimating by the full width half max). The FIB is equipped with a Raith laser interferometric stage that translates the sample with nm precision allowing raster scanning to define a complex exposed pattern. The challenge in fabricating the paddle is to avoid damaging the magnetic disk. The dual column feature was exploited in order to do this. The second column on the FIB is a high quality scanning electron microscope, which allows non destructive imaging of the sample. However the SEM is offset from the FIB beam. This makes aligning features with the two tricky. Prior to exposing a paddle design, points well away from the disk were identified using SEM imaging as alignment targets. Targeting these points with the FIB enabled registration of two beams.

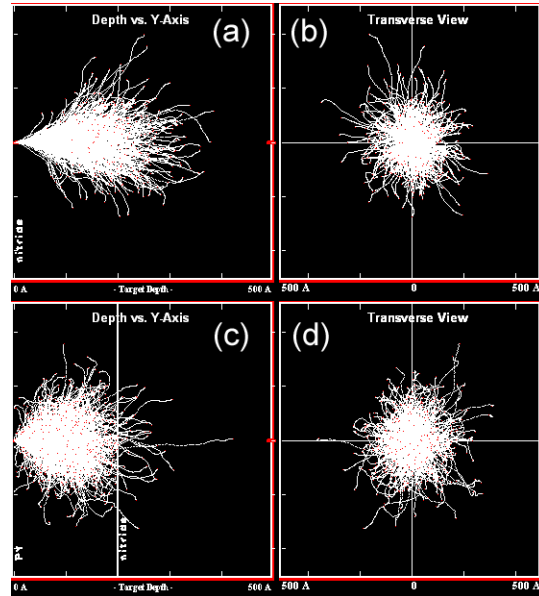


Figure F.2: Simulation with SRIM allows estimation of the depth and spread of implanted ions in the paddles. In silicon nitride, the depth profile shows that ions may penetrate up to 30 nm (a) while the lateral spread is approximately 40 nm (b). In permalloy, the penetration depth is approximately 20 nm (c) with a similar spread. The simulations only take into account the ballistic implantation of the ions. No diffusion is considered after the ions come to rest. Simulation images courtesy of D. Vick.

Initial devices used a $250 \times 250 \mu\text{m}$, 100 nm thick silicon nitride membrane $5 \times 5 \text{ mm}$, 200 μm thick silicon frame (Norcada NX5025C) designed as substrate for X-ray samples. Later the design was shifted to a 3 mm diameter, 300 μm thick, octagonal (standard TEM size) frame,

with a 3×3 array of $\sim 100 \times 100 \mu\text{m}$ membrane windows (Norcada TA301C). The device discussed here was fabricated on one of the TEM frames. As far as cleaning is concerned, these commercial membranes are delivered individually packaged, and 'fabrication quality clean' from the company that produces them. In this case, cleanliness is assured, as Norcada produces these membranes in the Nanofab at the University of Alberta through a commercial partnership. Hence the fabrication process and conditions are easily verified.

APPENDIX G

The Modified Bardeen Approach

The Modified Bardeen Approach is one of the most successful theoretical descriptions of the STM. In Chapter 5 much of the 'Modified' portion of the MBA is left uncovered. The reality is that the part of the approach modified from Bardeen's original work covers the detailed evaluation of the tunneling matrix elements and secondary effects such as image forces. This Appendix does not aim to cover this material. Rather, this appendix aims to fill in a few small, but potentially challenging gaps in the justification of the application of time dependent perturbation theory in the MBA. The material here follows closely the treatment of Chen (241), using the same notation for clarity, but with some additional steps and assumptions highlighted.

The MBA is based on time dependent perturbation theory performed under an unusual approximation developed by Oppenheimer (298). The potential energy of the sample and tip is separated into two somewhat arbitrary potentials denoted U_S and U_T under the condition that the total potential be equal to the sum, and the product of the two equals zero everywhere (Fig. 5.2). For each potential, it is assumed there is a complete orthonormal set of wave functions, denoted χ_ν and ψ_μ for the tip and sample respectively, that provide the stationary solution to the Schrödinger equation for energies E_ν and E_μ . The time dependence is considered through the introduction of the tip portion of the potential: at $t < 0$, the tip potential is off, at $t = 0$, the tip potential is turned on. Critical to applying time dependent perturbation theory here is the condition that $U_S U_T = 0$ everywhere. This ensures that the stationary wave function solutions for the tip and sample have small overlaps and permits the use of Oppenheimer's expansion method for time dependent perturbation theory where the small parameter exploited to allow accurate low order approximations is the overlap of the wave functions rather than the size of the coupling potential (298).

The full description of the problem is given by the time dependent Schrödinger equation for

the total wave function Ψ .

$$i\hbar \frac{d\Psi}{dt} = (T + U_S + U_T)\Psi \quad (\text{G.1})$$

Solution to the problem proceeds by considering the evolution of the wave function from $t = 0$. Since tip wave functions constitute a complete orthonormal basis, the total wave function may be expressed as:

$$\Psi = \sum_{\nu} a_{\nu}(t) \chi_{\nu} e^{-\frac{iE_{\nu}t}{\hbar}} \quad (\text{G.2})$$

If at $t = 0$, one considers the total wave function to be given by a single sample wave function, ψ_{μ} , the coefficients $a_{\nu}(t)$ may be written down:

$$a_{\nu}(t) = \langle \chi_{\nu} | \psi_{\mu} \rangle e^{-\frac{i(E_{\mu} - E_{\nu})t}{\hbar}} + c_{\nu}(t).$$

Then the coefficients introduced here, $c_{\nu}(t)$, describe the time dependent occupancy of the tip states themselves. In the context of considering a single sample wave function, these coefficients describe the probability that the sample wave function has decayed to a tip wave function. In the consideration of starting in a single sample state, then the condition $c_{\nu}(0) = 0$ exists for all ν . Substituting equation G.2 into equation G.1, these unknown coefficients may be solved for.

More compactly, the form of the solution for the total wave function can be equivalently written:

$$\Psi = \psi_{\mu} e^{-\frac{iE_{\mu}t}{\hbar}} + \sum_{\nu} c_{\nu}(t) \chi_{\nu} e^{-\frac{iE_{\nu}t}{\hbar}} \quad (\text{G.3})$$

Equation G.3 may be substituted into equation G.1 to solve for the evolution of the coefficients $c_{\nu}(t)$. The left hand side of the expanded equation reads:

$$E_{\mu} \psi_{\mu} e^{-\frac{iE_{\mu}t}{\hbar}} + \sum_{\nu} \left(i\hbar \frac{dc_{\nu}}{dt}(t) + E_{\nu} c_{\nu}(t) \right) \chi_{\nu} e^{-\frac{iE_{\nu}t}{\hbar}}$$

The right side, after exploiting the fact that ψ_{μ} and χ_{ν} are solutions to the separate stationary wave equations for the tip and sample and therefore satisfy $(T + U_S)\psi_{\mu} = E_{\mu}\psi_{\mu}$ and $(T + U_T)\chi_{\nu} = E_{\nu}\chi_{\nu}$, reads:

$$E_\mu \psi_\mu e^{-\frac{iE_\mu t}{\hbar}} + U_T \psi_\mu e^{-\frac{iE_\mu t}{\hbar}} + \sum_\lambda (E_\lambda + U_S) c_\lambda(t) \chi_\lambda e^{-\frac{iE_\lambda t}{\hbar}}$$

Some convenient cancellation can be performed to yield:

$$\sum_\nu i\hbar \frac{dc_\nu(t)}{dt} \chi_\nu e^{-\frac{iE_\nu t}{\hbar}} = U_T \psi_\mu e^{-\frac{iE_\mu t}{\hbar}} + \sum_\lambda U_S c_\lambda(t) \chi_\lambda e^{-\frac{iE_\lambda t}{\hbar}}$$

Taking the inner product of both sides with $\langle \chi_\eta |$ provides an equation that may be solved for the coefficients $c_\eta(t)$:

$$i\hbar \frac{dc_\eta(t)}{dt} = \langle \chi_\eta | U_T | \psi_\mu \rangle e^{-\frac{i(E_\mu - E_\eta)t}{\hbar}} + \sum_\lambda \langle \chi_\eta | U_S | \chi_\lambda \rangle c_\lambda(t) e^{-\frac{i(E_\lambda - E_\eta)t}{\hbar}}. \quad (\text{G.4})$$

This result is in a sense, an exact equation for the solution for the problem. However that is not entirely fair, as implicit in the construction of the problem was the assumption that the coefficients $c_\eta(t)$ are the sole contribution to the transition probability. Taking an inner product of $\langle \chi_\eta |$ with equation G.3, it is apparent the validity of this assumption depends on $\langle \chi_\eta | \psi_\mu \rangle$ being small compared to the modulus of the corresponding coefficient. This assumption was summarized as the overlap of the tip and sample wave functions is small, and is made more likely (but not guaranteed) by demanding the tip and sample potentials have a product of zero over all space. So, the equation actually gives an approximate solution only for weak overlap of the junction wave functions. However, that does not make it any easier to solve. In order to proceed, a second major condition must be imposed. Supposing that tunneling rates are very slow, then, for a short period of time, the coefficients $c_\lambda(t)$ will all be very small for that time period (~ 1 ps is adequate (299)). Additionally, while tip states may have significant spatial overlap, this overlap occurs inside the tip region, where $U_S = 0$ minimizing any contribution from the sum terms. These broad assumptions greatly simplify equation G.4 and yield the solution:

$$c_\eta(t) = \frac{\langle \chi_\eta | U_T | \psi_\mu \rangle e^{-\frac{i(E_\mu - E_\eta)t}{\hbar}}}{E_\mu - E_\eta}. \quad (\text{G.5})$$

This allows computation of the approximate probability of transition to the tip states as $|c_\eta(t)|^2$:

$$|c_\eta(t)|^2 = \frac{|M_{\mu\eta}|^2 4 \sin^2 \left[\frac{(E_\mu - E_\eta)t}{2\hbar} \right]}{(E_\mu - E_\eta)^2} = \frac{2\pi}{\hbar} |M_{\mu\eta}|^2 t \delta(E_\mu - E_\eta). \quad (\text{G.6})$$

where following the treatment of the usual Golden Rule in Landau and Lifshitz (300), the second half of the equation is valid only for large t . This finally yields the transition rate at large t :

$$W_{\mu\eta} = \frac{2\pi}{\hbar} |M_{\mu\eta}|^2 \delta(E_\mu - E_\eta), \quad (\text{G.7})$$

and the form of the Golden Rule has been found.

APPENDIX H

The UHV Suitcase

In the ideal case, STM samples need to be sputter cleaned and annealed at high temperature in order to provide atomic resolution surfaces. Some samples do not require this, but these are exceptions, rather than the norm. In developing patterned microstructures using polycrystalline films, high heat treatments are impossible due to interdiffusion of separate component metals, and spatial diffusion of patterned elements. Therefore, it would be ideal to form patterned elements *in situ*, and scan on the elements without exposure to any possible surface contamination, eliminated the requirement for surface treatments.

Adding a deposition unit to the STM is the simplest method of introducing *in situ* fabrication. However concerns over magnetic contamination of the chamber, physically unbalancing the chamber with a separate deposition chamber, and possibly ruining the STM transfer arm during deposition ruled this out. Instead, another UHV chamber was refurbished and used for the deposition, and a portable vacuum suitcase was designed and constructed to transfer the sample.

The suitcase is simple in its design concept. Sample motion through the suitcase is linear, accomplished by a long magnetically coupled transfer arm. A platen/fork system (MDC CAB-FAST) is used, with the sample holder resting in a bed mounted on a platen. The transfer arm is equipped with a fork that snaps onto the bases of the platen allowing pick up and drop of along a line. The suitcase is a two chamber system. The inner chamber has the transfer arm, a viewing window, an ion pump and a titanium sublimation pump. The inner chamber is separated from the outer chamber by a UHV gate valve. The outer (buffer) chamber is equipped with a turbo pump mounted on an elbow that maybe be valved off by a UHV gate valve, a second UHV gate valve, a quartz lamp for baking, an ion gauge, two viewing windows, and a platen-accepting socket mounted vertically on a heavy duty linear manipulator. The socket accepts the bottom of the platens and providing a method

of removing the platen from the transfer arm without the use of an orthogonal fork. The second gate valve opens to a flexible edge-welded bellows. This bellows allows connection of the suitcase to other chambers.

The size of components of the suitcase is dictated by the need to move the STM sample holder, which is rather large. The minimum standard flange size that will comfortably fit the sample holder (using oversized copper gaskets) is the 4.5 inch CF flange size. Unfortunately, the 4.5 inch size is quite uncommon, making components expensive. Instead, the more prevalent 6 inch standard was used to reduce cost. This results in a suitcase 178 cm long, and weighing over 130 kg. The suitcase is mounted on a scissor lift cart chassis that allows the chamber to move up and down with over 30 cm of range. Three nested steel tubes equipped with bolts provide brakes to prevent the suitcase from sagging on its hydraulic lift over time. Fine leveling screws allow small adjustments between the suitcase and the cart in the case of a non level floor (adjust only if absolutely necessary). Besides the quartz lamp on the buffer chamber, all other heating for baking is accomplished with heater tapes.

The procedure for a transfer is somewhat involved. Typically, the suitcase starts connected to the deposition chamber after being baked extensively ¹. Under these conditions, the turbo pump on the suitcase is normally running, or valved off, while the buffer chamber is open to the deposition chamber, and the inner chamber is valved off. While the sample is in the deposition chamber, the titanium sublimation pump (TSP) on the deposition chamber should be shut down. Following deposition, the sample is transferred into the suitcase. The UHV Rapid system is also equipped with a platen fork. The sample is transferred into the buffer chamber and installed on the socket. Immediately before opening the inner chamber, the TSP on the inner chamber should be fired. Subsequently, the sample is picked up with the suitcase transfer arm and moved into the inner chamber. Following this, the inner chamber valve should be closed, the buffer chamber valve to the rapid should be closed, and the turbo pump on the buffer should be valved off, turned off and vented with nitrogen. Finally, the valve between the rapid and the suitcase attachment point is also closed, and the edge-welded coupling bellows may be vented by asymmetrically undoing the nuts. Use of nitrogen for venting the bellows would be ideal, however it is impractical. Once the suitcase is disengaged and all unnecessary wiring removed, it may be, carefully moved to the STM suitcase port. Strictly speaking, only the ion pump needs to be powered during the move. The ion gauge should be turned off. Particular attention should be paid to the ion pump cable which must not be bent at a sharp angle.

At the STM, the suitcase must first be set to the correct height. The hydraulics should always be pumped up prior to disengaging the brakes. Failure to do so will result in the suitcase dropping rapidly, and possibly tipping over. As mentioned the suitcase is heavy,

¹See UHV suitcase logbook for baking temperatures, variac voltages, and typical bake pressure profiles.

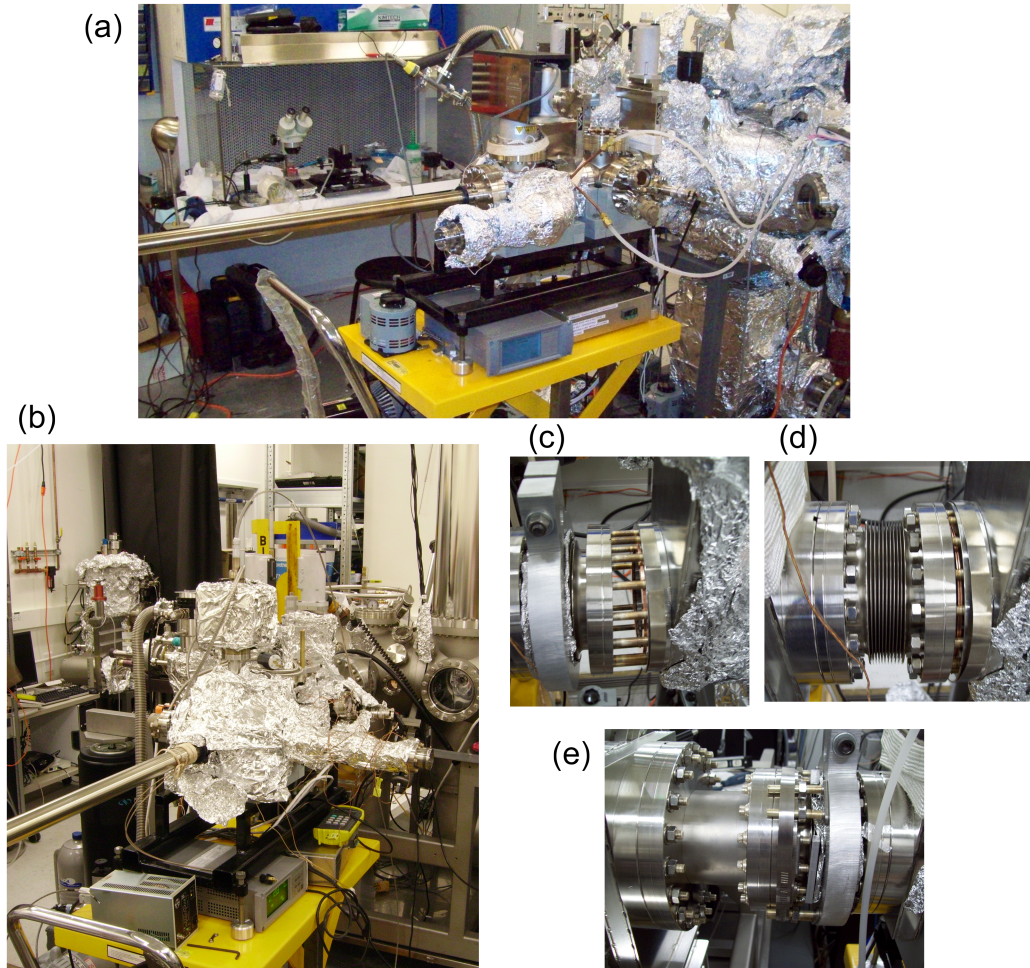


Figure H.1: The suitcase home position is connected to the rapid deposition chamber (a). The trip to the STM is very short, and mostly a 90 degree turn (b). Connecting the bellows, (c) to (e) is an intricate and frustrating process that must be followed in order, with the assistance of at least one other experienced operator. Early application of nuts (d) and addition of the home made port aligner (e) are critical steps.

and caution should *always* be used. Once the suitcase is freely supported by the hydraulic alone, the deck must be pumped up to the correct height². The suitcase must now be pushed forward carefully and extremely slowly to shift the flange of the bellows onto the studs of the gate valve on the STM suitcase support. Two people are required for this³. One needs to hold a fresh gasket in place and guide the bellows, while the second performs the manipulation of the cart. Once the flange and studs are aligned, due to clearance issues with the edge weld, nuts must be put onto the studs prior to pushing the suitcase in all the way.

Once the bellows flange is tightened, a very important precaution must be taken. When pumped out, the bellows *will* collapse. The pressure will exert sufficient force to shift the suitcase, even independently of the cart if the cart cannot move. Therefore a crude port aligner must be constructed using sets of studs and plate nuts held in place by large hose clamps in order to hold the bellows apart. This must be done, *every* time. As before, if the suitcase falls off the cart, significant damage, and possible injury, will be incurred.

With the bellows tightened, the buffer chamber may be pumped out. First, the elbow should be evacuated to low vacuum with the scroll pump. Then the buffer chamber may be opened to the elbow. The buffer and elbow should be vented with nitrogen before being opened to the bellows. The buffer chamber can now be pumped to high vacuum, before being baked. The baking procedure for the buffer alone is designed to avoid heating the inner chamber. Therefore fewer heating tapes are used, a lower temperature is used, and chilled water should be run through a cooling coil that is wrapped around the inner chamber. Once the buffer is baked and cooled, the buffer chamber may be opened to the STM, and to the inner chamber. The sample may, at last, be transferred into the STM. Prior to using the STM, the suitcase should be disengaged using the same procedure as used to disengage from the deposition chamber. It is then advisable to re-install the suitcase onto the deposition chamber to prevent slow leaks through gate valves from degrading base pressure.

²Usually this requires several cycles of pumping up and slowly lowering the suitcase with the release in order to attain the correct height within a few mm.

³One Greg Popowich, or one David Fortin is highly recommended for this task.

APPENDIX I

Gallium Arsenide Optoelectronic Switches

I.1 GaAs Photoswitches

Initial efforts to develop a TR-STM were directed at a traditional optical JM-STM using optoelectronic switches to apply pulses to the STM tunnel junction. This was a quite logical first choice, as all previous work (*215, 219–222*) used optical techniques. Additionally, the use of photoswitches on the sample holder or sample itself eliminates the need for high speed bias wiring by allowing generation of pulses at the sample and subsequent dissipation of the pulses into lossy wiring or terminations to ground.

With the idea of applying a magnetic field pulse using a transmission line, a fairly large current pulse may be required. Therefore a set of large area opto-electronic switches was developed in an attempt to deliver a higher amplitude pulses. The switches are effectively interdigitated thin film capacitors fabricated on an optically active substrate that allows rapid discharging when the substrate is temporarily rendered conductive by photo excited electrons (and holes). As long as the full switch area is illuminated, discharge time remains fast, while providing a larger charge build up in the switch, as well as a larger number of photo excited carriers.

The switches were made using standard optical lift-off lithography with a bi-layer resist recipe (included later in this appendix). High resistivity gallium arsenide wafers (Epistone Epi-Ready A Grade 100 oriented GaAs wafers), 625 μm thick were used as substrates. A layer of 300 nm thick copper was deposited to create the electrodes. The switches were designed to sit at the top of a coplanar transmission line, therefore requiring the bond/contact pads of the switches to be spaced less than 1 mm apart. Additionally, broad-band impedance

matching was included in the switch design by incorporating 10:1 tapers¹. For a microstrip geometry, a transmission line width of $465\ \mu\text{m}$ yields an impedance of $50\ \Omega$ for the GaAs substrates.

Preliminary results were obtained with limited testing. The size of the switch did not have a significant influence on the pulse height, or on measured pulse duration. Pulses were all approximately 200 ps in width, as measured by a 2 GHz inductive current probe (Tektronix CT-6). However the low bandwidth of the probe blurs out the actual duration of the pulses, reducing the apparent peak, and increasing the duration. The relative peak height is still a useful measurement of the amplitude of the current pulses, however. Within the tested data set, it appeared that switches with the highest density of fingers, and relatively small gaps, provided the optimal results. In other words, the highest capacitance switches functioned optimally. This indicates that, rather than the number of excited carriers, the capacitance of the switches was the limiting factor in the pulse height. Increasing the voltage to increase the stored charge was not a viable option in this case. The integrated DC current had a clear contribution independent of the pulses. This was conjectured to be the result of thermally excited photocarriers permitting the maintenance of a steady current even without incident photons. The kink in the DC current measurement (Fig. I.1) is likely due to a pause in measurement taking, resulting in a slight cooling of the sample. Two solutions to the DC voltage problem were proposed. First, synchronizing a high voltage pulser (up to 1000 V) to provide a \sim microsecond long square pulse voltage to the switch would allow gating of the DC current. If the DC current is eliminated during the time when no pulse is incident, then cooling must occur, preventing the current from becoming self sustaining. The second solution was to create a new generation of photoswitches on a thin film of GaAs. The thick wafers used may have allowed photoexcitation well into the bulk of the wafer contributing carriers that diffused to the electrodes over a long period of time, contributing to the DC current. A thin GaAs film on a non-photoactive substrate would eliminate this.

The optimal size of photoswitch was not precisely determined due to insufficient testing. The optoelectronic design was abandoned while switches were still being tested. Experiments were also slowed by challenging conditions. The deposited copper on the switches tended to oxidize rapidly under intensive pulsing, increasing resistance, heating and accelerating the oxidation. Stable testing was possible only after constructing a constant flow nitrogen hood over the switch sample holder with a window for the laser. Many samples of each variation of switch made remain intact, allowing testing to be completed in future.

¹A reduction of width of size X was implemented over a distance of $10X$.

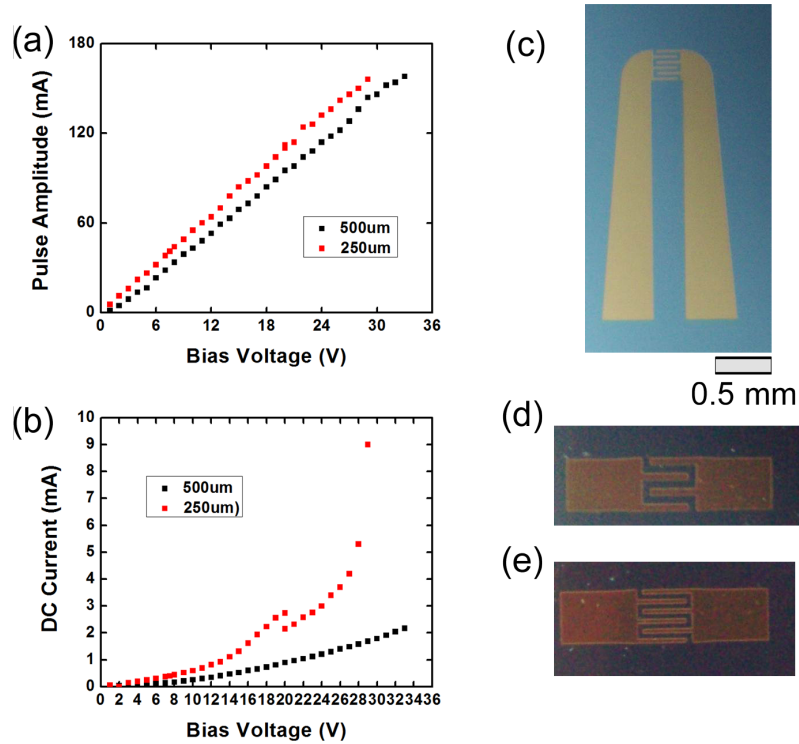


Figure I.1: Photoswitches were subjected to initial tests. Pulse height was found to vary linearly with voltage, unsurprisingly (a). The integrated total DC current (b) was found to vary non-linearly with voltage (b). Two sizes of photoswitches were created: one with an active area of 265 μm square (c), and one with a 500 μm square area (d). For both sizes, the number, width and spacing of the interdigitated fingers was varied. Under large amplitude pulses, pulse height was found not to depend strongly on the switch size. Data is shown here for an eight finger 265 μm switch and a four finger 500 μm switch.

I.2 GaAs Integrated Samples

A set of test samples incorporating photoswitches into integrated STM transmission line samples was prepared as a test concept. One sample was designed to apply an out of plane field pulse, however the spacing and size of the transmission lines in th design would result in a miniscule pulse. This design could work quite well if the location of the transmission lines was known for tip approach (i.e. an SEM was pointed at the tip and sample). The second style of sample incorporates a simple dual switch design to apply two pulses to the transmission line serving as the STM target. On this chip, a large area photoswitch is included with bond pads to allow an off chip stimulus such as a hard drive read head.

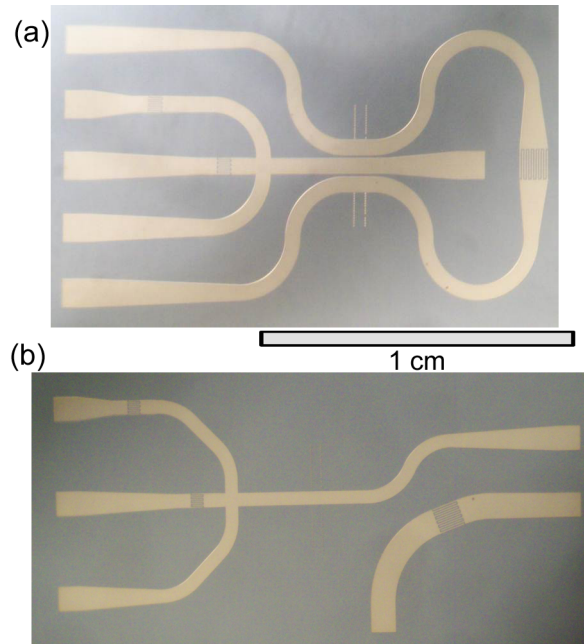


Figure I.2: At top (a) the out-of-plane field pulse sample is shown. A central line has dual switches for classic junction mixing experiments. The outer line is designed to have act as a co-planar transmission line applying an out-of-plane field pulse between the two lines. At bottom (b), the off chip stimulus sample is shown.

APPENDIX J

Fabrication of Bulk Chromium Tips

J.1 Machining

Chromium is a brittle material that is difficult to make wires out of or to machine. The brittle nature of the metal limits the diameter of wire commercially available to rods > 1 mm. This is quite large for electro-chemical etching, posing a challenge. To reduce etching to a more reasonable time frame, reduction of the rod diameter by physical machining targeting a particular location along the rod, the etching point, is desirable. Unfortunately, chromium is also extremely hard (8.5 on Mohs scale) meaning that any machining should be performed with diamond tooling.

A basic design of a dumbbell was developed as the simple precursor shape for tips (Fig. J.1). The obvious method for machining a cylindrically symmetric object such as this is using a lathe, however using a rigidly mounted tool rapidly and ubiquitously resulted in snapping the chromium rod rather than cutting it. Only a very small amount of lateral pressure may be applied. This means that very high speed rotation is desirable to make up for the minimal amount of cutting possible on each revolution of the rod. A rotary tool was used as a high speed miniature lathe, holding the rod and revolving it. Diamond grit coated tools were then held to the rod, by hand, as it spins. Note that inverting this approach and holding bits of chromium against a tool is a sure fire way to cause burns to the machinist's fingers, and quite possible cuts, despite the relative safety of grit based tooling.

The precursor is machined down in diameter to fit into the the customized large diameter tip holders (see Fig. 5.12). For 1 mm rod, the ends of the rod must simply be tapered slightly, and the tip holders may need to be gently clamped with tweezers, slightly closing

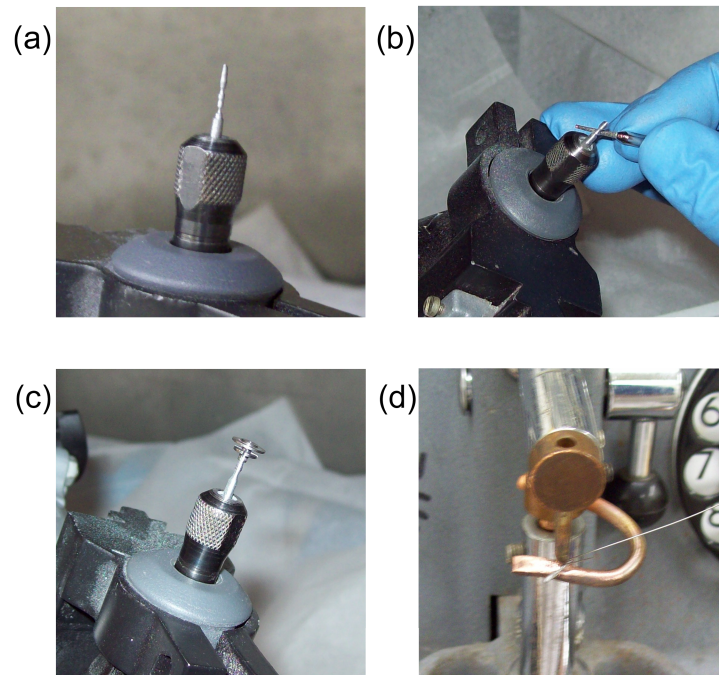


Figure J.1: The dumbbell precursor is quite fun to machine, but challenging and aggravating in the case of repeated errors (a). The 'softness' of human held tools is important in preventing breakage (b). Testing the tip holder must be done before parting off the precursor (c), otherwise adjustments are virtually impossible to make. Spot welding wire to the precursor is much less fun (d), much more difficult, and highly likely to break the precursor in the event of clumsiness.

the opening¹. For larger rod much more machining is required. Testing the fit with the tip holder prior to parting the precursor off is highly advised. The rest of the machining is simple. Two narrow sections are machined into the rod, one is the etch point, separating the upper and lower tips. The second is a parting point used to separate the precursor from the rod when machining is completed.

In preparation for etching, it is very useful to spot weld a tungsten wire onto one of the two dumbbell halves. The tungsten wire should be sanded gently and rinsed prior to spot welding. This is difficult, and dangerous for the fragile precursor, but massively improves etching. Oxidation is a common side effect.

More detailed instructions may be pointless. Ultimately, no description will suffice to describe the learned softness of touch necessary for the machining. All that can be said, is, that as the rod becomes thin at the etch point, ensure that the break point for the precursor is thinner, increasing the odds that an accidental break will happen at the intended location, even if it is premature.

Safety precautions are required in this endeavor. Safety glasses are necessary. Additionally, chromium has some carcinogenic properties. Therefore gloves should be worn during machining, as should a good quality dust mask. Out of consideration for others, machining should be done in a 'dirty fume hood'². Clean up of any dust is also required. Laying out large lab wipes in the work area makes this easy, and also provides a convenient white backdrop to locate dropped pieces of chromium.

J.2 Etching

Following machining, the precursor must be etched. A two ring tip etcher is used. A thin NaOH film is suspended in the rings by dipping the rings in a beaker of 3M nominal NaOH solution. Following this, the tip is mounted such that the etch point is in the film of the top ring, and the lower half of the precursor, or ideally the spot welded wire passes through the lower ring (Fig. J.2). The top half of the tip should be mounted in a tip holder for convenience. However care should be taken to keep the etch solution from seeping or wicking into the crevices of the tip holder. Subsequently, a voltage is applied between the tip and the tip ring, driving an electrochemical reaction that etches away the chromium. The lower ring serves to detect the voltage applied to the tip, allowing rapid shut off of the etching

¹Squeezing the tip holders should be done with extreme caution. Only a slight compression of the clamps is required, and the tip holders are very challenging to make. Each one is very valuable.

²Specifically a fume hood designed for good ventilation while sanding, spray painting, or doing some other coarse activity requiring ventilation. Use of one designed for wet processing, in a clean area is not an acceptable alternative

voltage as soon as the tip breaks³. Despite the machining, it is highly unlikely that the etch point was thinned sufficiently that one round of etching results in completed tips. It is likely the films will need to be refreshed five to ten times. When the NaOH films break, or become too saturated, rinsing the tip and rings, followed by re-immersion in the NaOH beaker is effective in restoring fresh films.

Chromium etches very quickly, which is good in the context of etching through the thick etch point. However, it is bad for the production of sharp tips. Stopping the etch rapidly is incredibly important, and can make the difference between a 200 nm and a 10 nm radius of curvature on the tip. This is the primary reason that addition of a spot welded wire is important. It significantly improves the chances of the sense circuit functioning correctly.

Once the etch is completed, there is a chance that the lower tip is recoverable. It may be suspended in the lower ring, or a captured in tip catcher placed below (a pit with a depth and with less than the length of the tip). Often the lower tip is of excellent quality making the effort in picking the tip up, mounting it in a tip holder, and clipping off excess tungsten wire, worth while. The top tip, already in a holder, is much easier to recover and handle. Both tips should be rinsed in distilled water, acetone, methanol, IPA and finally water again. Residues invisible to the eye, or under an optical microscope can ruin a tip easily. Finally the tip should be dried with clean dry air, or nitrogen. Following this, the tip should be inspected, at the very least, under an optical microscope to ensure it is of sufficient quality to merit installation in the STM. Bent tips, or extremely dull tips are common, and can be identified even under an optical microscope.

J.3 Field Emission

The final stage of tip preparation takes place in the UHV chamber of the STM. Tips are degassed by using electron bombardment for heating. Thermally emitted electrons from a filament are accelerated towards the charged tip holder on the STM manipulation arm. The back side of the tip holder is heated first, followed by the tip itself. Pulses of current up to five seconds long are used. Standard procedure calls for steady increasing of current to a standard 1.5 A for the back of the tip, with an accelerating voltage of 500 V. Once at this point, pulses are repeated until pressure spikes caused by the heating have diminished to a negligible rise (low 1×10^{-10} mbar up to low 1×10^{-9}) mbar. This process is repeated for the frontside (tip), with the rather more cautious filament current of 1.25 A. This reduces the chance of destroying the tip by electron heating induced evaporation.

After cleaning, the quality of the tip is tested, and occasionally improved, by field emission. A transfer arm tipped with magnets was added to the STM preparation chamber. The

³In theory.

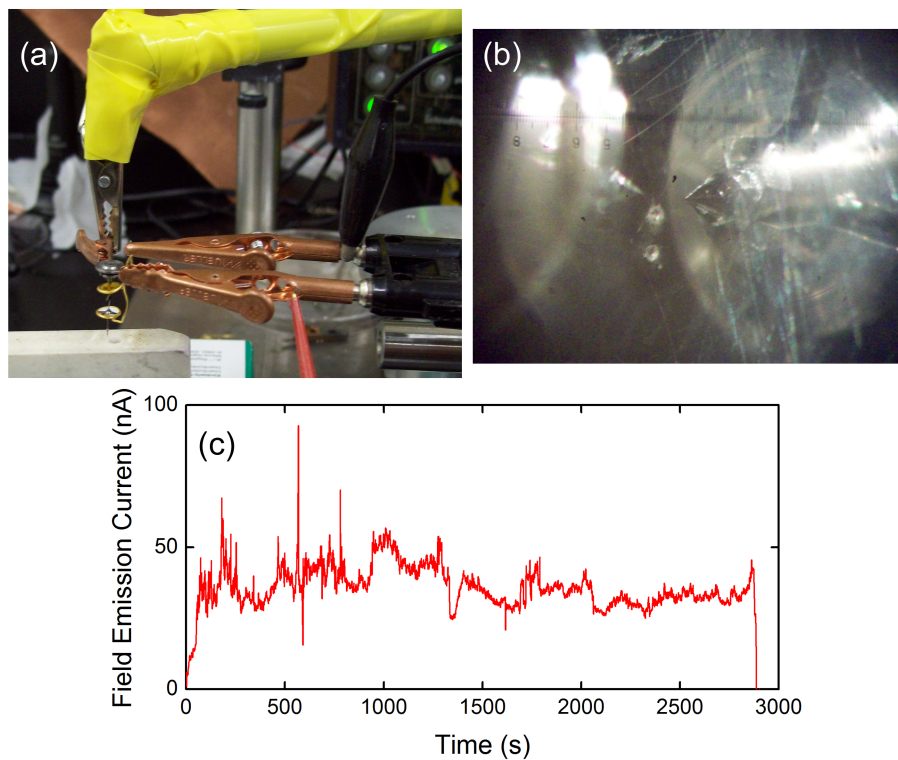


Figure J.2: Chromium tips should be mounted in a tip holder, and passed through the double ring structure of the tip etcher (a). A spot welded wire on the lower half of the precursor allows the tip to penetrate the lower ring, while minimizing weight and reducing chromium use. A lighter lower tip also reduces the chance of fracture. Field emission is accomplished by bringing tips near to a mirror and applying a voltage between the tip and mirror (b). Accidents involving sudden arcing result in pits in the mirror. An example field emission current trace (c) acquired from a dull Cr tip at 3250 V, reduced to 3190 V by the end of the trace. Better tips field emit at the same distance at voltages as low as 600 V.

tip may be installed on this arm, and subsequently approached to a polished electrode. A high voltage is applied across the gap, inducing tunneling field emission (258). The current disturbs tip atoms, and can cause ad atom diffusion, reshaping the tip. As the tip shift and changes, the tunneling field emission current changes as the electric field at the sharp tip varies. As the tip become sharper, the current increases. Chromium tends to exhibit a lack of stability compared to tungsten tips. Therefore relatively low field emission currents (50-150 nA) are most effective. Sharpening of the tip may be noted as a decrease in the voltage necessary to maintain an approximate target current. Typically, voltages are stepped down throughout a field emission run as the tip improves. Good tips usually field emit in the high 100s of volts when a distance of the order a 1-4 mm away from the mirror electrode. Bad tips, but still potentially usable, may require up to 4 kV to field emit at the same range.